Solidification de l'océan de magma lunaire et dynamique des cumulats

Line Colin

ENS DE LYON

THESE

pour l'obtention du grade de Docteur, délivré par

l'ECOLE NORMALE SUPERIEURE DE LYON

Ecole Doctorale N°52
PHAST - Physique et Astrophysique

Discipline : SCIENCES DE L'UNIVERS (Sciences de l'Univers)

Soutenue publiquement le 26 février 2026, par :

Line COLIN

Solidification de l'océan de magma lunaire et dynamique des cumulats

Solidification of the lunar magma ocean and dynamics of the cumulates

---

Après avis de :

Gaël CHOBLET, Directeur de recherche, Université de Nantes / CNRS	Rapporteur
Julien MONTEUX, Chargé de recherche - HDR, Université Clermont-Auvergne / CNRS	Rapporteur

Devant le jury composé de :

Cathy QUANTIN-NATAF, Professeure des universités, Université Claude Bernard Lyon 1	Présidente
Gaël CHOBLET, Directeur de recherche, Université de Nantes / CNRS	Rapporteur
Julien MONTEUX, Chargé de recherche - HDR, Université Clermont-Auvergne / CNRS	Rapporteur
Henri SAMUEL, Chargé de recherche, Université Paris Cité / CNRS	Examinateur
Chloé MICHAUT, Professeure des universités, ENS de Lyon	Directrice de thèse
Stéphane LABROSSE, Professeur des universités, ENS de Lyon	Co-directeur de thèse

Mam'selle Bulle avait un rêve un peu spécial
Pour une bulle quitter la Terre c'est peu banal
[...]
Et c'est dans la voie lactée que Mam'selle décida d'habiter
Ainsi dans le ciel depuis des millions d'années
Madame la Terre observe cette bulle illuminée
Chaque soir quand la nuit vient à tomber
Mam'sellle Bulle sur nous veille jusqu'à ce que le soleil l'interpelle
Mam'selle Bulle!

Mam'selle Bulle - Les Ogres de Barback

Résumé

La croûte lunaire est principalement composée d'anorthosite, une roche de faible densité qui cristallise à basse pression ($\sim$ 1 GPa). L'enrichissement en anorthite de la croûte lunaire, mis en évidence grâce aux échantillons des missions Apollo, a apporté des preuves en faveur de la formation de la Lune par un impact géant entre la proto-Terre et un corps de la taille de Mars. De plus, la croûte lunaire présente une dichotomie marquée : sur la face visible, son épaisseur varie entre 20 et 30 km tandis que sur la face cachée elle atteint 50 à 60 km. À partir d'un simple diagramme de phase eutectique, nous avons développé un modèle décrivant la solidification de l'océan magmatique lunaire (LMO) en deux étapes de cristallisation. Ce modèle nous a permis d'estimer un intervalle de temps pour la solidification du LMO, en tenant compte de la teneur initiale en anorthite, de la composition eutectique et de la conductivité thermique de la croûte. En combinant cet intervalle avec les vitesses de refroidissement dérivées des roches lunaires, nous avons estimé une plage de temps pour la formation de la Lune comprise entre 4400 et 4560 Ma. Dans un second temps, nous avons étudié le retournement mantellique lunaire d'un point de vue thermique, lié au profil de température instable en fin de seconde étape de cristallisation. En supposant un changement de phase par fusion et/ou cristallisation à l'interface entre le manteau et le LMO, nous montrons qu'un retournement rapide de degré un peut survenir au début de la seconde étape. La présence de ce retournement pourrait affecter la cristallisation de la croûte par un flux thermique différentiel à la surface du manteau ou par la persistance d'une perturbation de degré un.

Abstract

The lunar crust is mostly composed of anorthosite, a low-density rock that crystallizes at low pressure ($\sim$ 1 GPa). The enrichment in anorthite within the lunar crust, revealed by Apollo mission samples, provided evidence for the formation of the Moon through a giant impact between the proto-Earth and a Mars-sized body. Furthermore, the lunar crust is characterized by a significant dichotomy: on the near side, the crustal thickness ranges from 20-30 km, whereas on the far side it reaches 50-60 km. Using a simple eutectic phase diagram, we developed a model for the solidification of the Lunar Magma Ocean (LMO) in two stages of crystallization. With this model, we estimated a range for the solidification timescale of the LMO, taking into account the initial composition in anorthite content, the eutectic composition, and the thermal conductivity of the crust. Combining this timescale with cooling rates derived from lunar rocks, we estimated a range for the formation of the Moon between 4400 and 4560 Myr. Secondly, we investigated the lunar mantle overturn from a thermal perspective, driven by the unstable temperature profile at the end of the second crystallization stage. Assuming phase changes by melting and/or crystallization at the interface between the mantle and the LMO, we show that a rapid degree-one overturn can occur at the beginning of the second stage. The presence of such an overturn could affect crustal crystallization through differential heat flux at the surface of the mantle or through the persistence of degree-one perturbations.

Remerciements

Ce n'est pas une chose si facile que de remercier toutes les personnes qui ont fait partie de près ou de loin de ces années de thèse tant il y aurait de choses à dire, et j'espère n'oublier personne dans ces quelques lignes.
Tout d'abord je ne peux que remercier chaleureusement mes deux directeur · ice · s de thèse Chloé et Stéphane, sans qui tout cela n'aurait pas été possible. Merci à vous deux pour votre confiance pour ce projet de thèse. Merci pour votre accompagnement, pour votre présence au cours de ces trois ans et demi et aussi lors de mon stage de master. Grâce à vous, j'ai pu apprendre énormément, et bien que mes étourderies aient parfois posé souci, je ne vous remercierai jamais assez pour tout ce que vous m'avez apporté au cours de cette thèse. Je souhaiterais aussi remercier les membres de mon jury, Gaël Choblet, Julien Monteux, Henri Samuel et Cathy Quantin-Nataf, pour avoir accepté de relire et d'évaluer mon travail. Les questions que vous avez pu me poser ont été très enrichissantes et j'espère qu'elles mèneront à de futurs projets. Enfin, merci de m'avoir octroyé le titre de docteur.
Ces années n'auraient pas été pareilles sans toutes les belles personnes de ce labo. Tout d'abord, l'équipe Cruslid, Valentin, Alexandra, Kathryn et Swann. Merci pour la chaleureuse ambiance, surtout lors de notre passage à San Francisco. Merci à mes co-bureaux, même si nous n'avons pas le même point de vue sur la lumière, partager ce thésarium avec vous a été super, et je vous laisse vous battre pour savoir qui récupérera mon bureau. Enfin, je ne pourrais finir cette partie sans remercier les permanents du labo, Marie-Jeanne, Manue, Mathieu, Jérémy, Bruno, Francis, Salomé et tous les autres (désolé · e pour tous · tes ceux · elles que j'ai oublié · e · s), votre présence égaye les repas du midi.
Merci à tous les copain · nes ! Marie, tu es celle qui est là depuis le plus longtemps. On se souviendra toujours de notre voyage en Allemagne. Et comme tu l'as si bien dit "From the collège to the thèse". Les copain · nes de la Colok Nomade, Joules Aïe, Niko, Marc, Kiki, Nico, Hugo, Victor, je n'ai pas toujours été là, j'ai parfois disparu, mais on a toujours réussi à se retrouver comme si le temps n'était jamais passé ! Merci pour les soirées, les week-ends bourbiers, les fous rires et pour votre joie de vivre et votre bonne humeur sans faille. Et surtout merci d'être venus le jour de ma soutenance. Les copines de Brest, sans qui ces deux années de master n'auraient pas été pareilles, et merci pour ce chouette voyage en Martinique ! Et enfin, les copain · es de Lyon Camille, Marine et Mariane, Baptiste, Bebou (Laura) et Mathias, passer ces quelques mois/années avec vous

a été génial et a grandement contribué à ce que ces quatre années à Lyon aient été moins dures. Je n'oublierai pas nos week-ends, nos soirées au bar et j'espère que tout cela n'est pas fini. Bebou, tu as ensoleillé ma vie lors de ton passage, les pauses café et les tartines de beurre n'ont plus la même saveur sans toi. J'espère qu'on aura bientôt un nouveau vélo toutes les deux pour qu'on puisse repartir rouler dangereusement sur la nationale et dans des paysages incroyables. Mathias, mille mercis ne suffiraient pas, pour ta présence pendant ces derniers mois, ta bienveillance et ta relecture (parfois compliquée) de mes fautes d'orthographe. Tu es un petit être humain merveilleux et je suis heureuse de t'avoir rencontré.
Merci à ma famille de m'avoir permis de faire des études qui m'ont amenée ici aujourd'hui. Je ne vous remercierai jamais assez d'avoir été présents, pour votre humour décalé et pour toutes nos discussions et votre ouverture d'esprit. Merci Papa de m'avoir donné envie de faire des sciences en mangeant une glace sur un banc à Draguignan. Merci Maman pour la relecture de mon introduction et la correction de mes (trop) nombreuses fautes d'orthographe, et même si tu n'es pas d'accord avec ça, merci de m'avoir appris plein de choses, qu'elles soient parfois plus ou moins utiles mais toujours très précieuses. Et le meilleur pour la fin merci Clem ! Merci d'être là et d'être qui tu es. Merci pour nos discussions sans fin, même si t'es chiante, je t'aime et je suis très fière d'être ta sœur. Merci Maud, Fred, Thibaut, Antoine, Julie, Louis et Mamie d'avoir été présents le jour de ma soutenance. Et on n'oublie pas Pipe la plus mignonne des chachats !

Je ne pourrais finir ces remerciements sans avoir une pensée pour toi Pépé, qui m'a montré les étoiles, bien trop tôt les matins, lorsque j'étais petite. Je garde précieusement ces souvenirs en mémoire, et sans le vouloir, tu as certainement contribué au fait que j'en sois ici aujourd'hui. Je pense toujours fort à toi.

Contents

Préambule

Pleine Lune du 9 août 2025. On distingue aisément les *maria*, les grandes tâches sombres, et les hautes terres, les surfaces claires et brillantes. Crédit Auriane Keromnes.

À l'aube des premières civilisations humaines, la Lune occupait déjà une place centrale dans l'histoire de l'humanité. Parfois associée à une divinité, elle est aussi l'objet de nombreux mythes, légendes et autres croyances populaires. Elle transformerait les hommes en loup à la pleine lune, favoriserait la pousse des cheveux, ou bien serait habitée par un lapin géant. Cette dernière croyance est liée à une paréidolie, qui consiste à voir un lapin dans les *maria*. Sa présence marquée dans la peinture, le cinéma ou bien la musique, illustre son rôle central dans les sociétés humaines. Elle est aussi le seul corps du système solaire, hormis la Terre, à avoir été foulée par des humains.

La Lune exerce une influence directe sur la Terre puisqu'elle est à l'origine des marées. Après le Soleil, elle est l'astre le plus visible dans le ciel. Bien que ce dernier soit environ 400 fois plus grand que la Lune, il est aussi 400 fois plus éloigné, ce qui confère à ces deux astres une taille similaire pour un observateur terrestre. Cette coïncidence est à l'origine des éclipses totales de Soleil, lorsque la Lune recouvre entièrement le disque solaire. La Lune n'est pas une planète, mais le satellite naturel de la Terre, un des deux seuls corps telluriques du système solaire à en posséder. Elle n'est éloignée en moyenne que de 360 000 km de la Terre, une distance réalisable avec une voiture équipée d'un bon moteur. Avec un rayon de 1737 km et une densité moyenne de $3.3 \times 10^3\,\mathrm{kg\,m^{-3}}$, la Lune est le cinquième plus grand satellite du système solaire et la deuxième lune la plus dense après Io, une des lunes de Jupiter. Sa rotation synchrone avec la Terre fait que nous observons toujours la même face depuis notre planète. Il faut attendre la course à l'espace pendant la guerre froide pour avoir les premières images de la face cachée de la Lune.

Bien que la Lune ne soit pas une planète, elle constitue un objet d'étude unique pour comprendre la formation des planètes telluriques. L'absence d'atmosphère et de tectonique des plaques a permis la préservation de la croûte, archive de sa formation. Celle-ci conserve les traces de sa différenciation interne et offre des indices uniques sur les processus à l'œuvre lors de la formation et de l'évolution thermique des corps telluriques.

Chapter 1

Introduction

1.1 Histoire de l'observation de la Lune

1.1.1 De la Préhistoire au XVI^{e} siècle

Les premières représentations connues des phases lunaires remontent au Néolithique, il y a 5000 ans. En Irlande, sur le site néolithique de Knowth, un monument est entouré de pierres gravées. L'une d'elles (K52, fig. 1.1) est interprétée comme l'un des plus anciens calendriers astronomiques identifiés (Prendergast, 2017). Cette pierre gravée pourrait aussi correspondre aux premières représentations descriptives des *maria*, *mare* au singulier, où elles sont représentées par des arcs de cercle (fig. 1.1b, Stooke, 1994). Cette pierre gravées (K52) n'est pas la seule où les gravures sont interprétées comme des représentations des mers lunaires sur ce site néolithique[1]. Bien plus tard, le philosophe

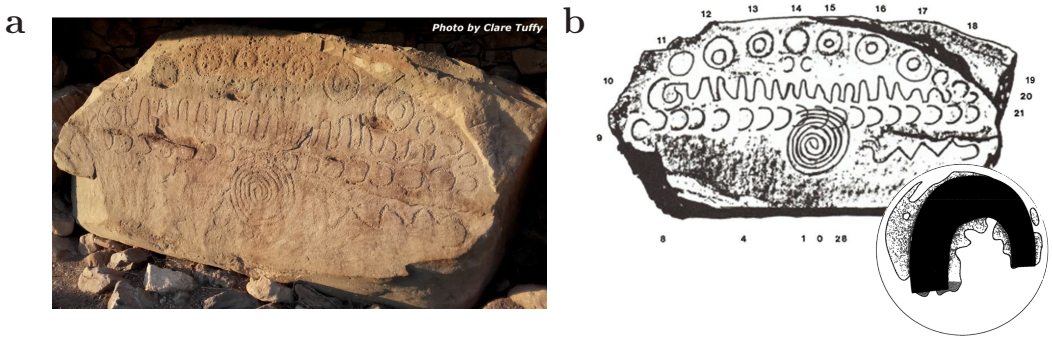

Figure 1.1: **a**- Pierre gravée K52 à Knowth en Irlande et **b**- représentation schématisée des gravures (Prendergast, 2017; Stooke, 1994).

[1]Le site https://www.knowth.com/lunar-maps.htm fournit de nombreuses informations sur ce site archéologique.

grec *Anaxagoras* ($\sim$ 500 av. J.C) est considéré comme le premier à avoir donné une explication aux éclipses. Des tablettes d'argile témoignent aussi, au V^{e} siècle avant J.C., d'une compréhension avancée des cycles lunaires, avec notamment l'enregistrement de la périodicité des éclipses sur environ 18 ans, un cycle connu aujourd'hui sous le nom de *Saros* (Aaboe et al., 1991). Au fil du temps, les observations de la Lune ont nourri de nombreuses découvertes. Entre le VI^{e} et le IV^{e} siècle avant J.C., des astronomes chinois établissent que la clarté de la Lune ne lui était pas propre mais provenait de la lumière solaire qu'elle reflète (Hummel, 1960, p.227). Peu après, l'astronome Habash al-Hāsīb parvient à estimer la distance Terre–Lune ainsi que le diamètre lunaire, ouvrant la voie à une première quantification de ses dimensions (Langermann, 1985). Bien plus tard, à la Renaissance, Léonard de Vinci réalisa les premières cartes détaillées de la surface lunaire (Reaves et al., 1987).

1.1.2 Du XVII^{e} siècle à la guerre froide

Le début du XVII^{e} siècle est marqué par une avancée décisive dans l'observation de la Lune avec le perfectionnement des premières lunettes astronomiques par Galilée. Pour la première fois, il devient possible de cartographier avec précision la surface de sa face visible et d'en révéler le relief (Galilei, 1610, fig. 1.2). Dans les décennies qui suivent, de nombreuses cartes détaillées sont réalisées, permettant non seulement de décrire les grandes structures lunaires mais aussi de nommer les cratères les plus remarquables. Cette pratique a progressivement conduit à la nomenclature encore en usage aujourd'hui, où la plupart des cratères portent le nom de scientifiques et de savants célèbres.

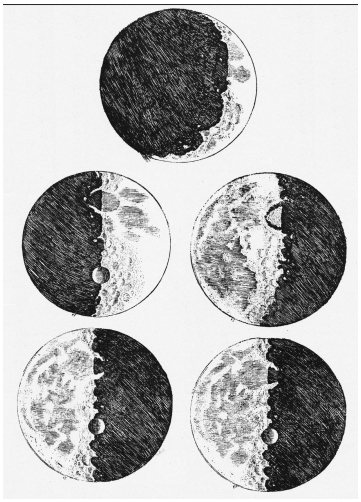

Figure 1.2: Croquis de la surface visible de la Lune à l'aide d'une lunette astronomique en fonction des différentes phases de la Lune (Galilei, 1610).

1.1.3 Durant la guerre froide

La guerre froide marque un tournant décisif dans la connaissance de notre satellite. La course à l'espace entraîne en effet une accélération spectaculaire des progrès en exploration

spatiale, et en particulier lunaire avec la mise en place de 89 missions (réussies et échouées) entre 1958 et 1976. En octobre 1959, la sonde soviétique *Luna 3* transmet les premiers clichés de la face cachée de la Lune. Bien que leurs résolutions soient faibles, ces images révèlent environ 70% d'une région jusque-là inconnue. Elles montrent notamment que la face cachée diffère fortement de la face visible : elle apparaît beaucoup plus cratérisée et dépourvue de mers basaltiques. La guerre froide est marquée par de nombreuses histoires d'espionnage, et les missions spatiales n'ont pas échappé à la règle. Deux mois après son lancement, l'URSS envoie une reproduction du module de *Luna 3* au Mexique pour une exposition. Avec la complicité du gouvernement mexicain, les services américains parviennent à détourner temporairement le camion qui transportait le module, afin de l'étudier clandestinement avant de le restituer pour l'exposition publique (Harvey, 2007). Cela a permis aux services américains de photographier l'entièreté du module. Il faut attendre la mission *Ranger 7*, 5 ans plus tard pour avoir les premières images en hautes résolutions de la face cachée de la Lune.

L'apogée de la course à l'espace survient en juillet 1969, lorsque la mission *Apollo 11* réussit le premier alunissage habité, avec Neil Armstrong, Buzz Aldrin et Michael Collins à bord. Les missions *Apollo* suivantes (jusqu'à *Apollo 17* en 1972) rapportent au total plus de 300 kg d'échantillons lunaires, qui constituent encore aujourd'hui une ressource scientifique majeure. Si la motivation première des missions *Apollo* reste politique, leur impact scientifique est considérable, et a encore des retombées aujourd'hui puisque les échantillons des missions *Apollo* sont toujours étudiés. Leurs études ont permis de nombreuses avancées dans la compréhension de la Lune. Les analyses minéralogiques montrent que la croûte lunaire est dominée par l'anorthosite, une roche peu dense qui se forme à faible pression. Les datations géochronologiques ont affiné la chronologie des surfaces lunaires, tandis que les rapports isotopiques révèlent une similarité avec ceux de la Terre. Enfin, les échantillons indiquent que la Lune est appauvrie en éléments volatils, et les mesures géophysiques des missions *Apollo* montrent que son noyau est de petite taille (Crawford, 2012). De plus, cela a permis de mettre au point le scénario classique de solidification de l'océan de magma lunaire (voir section 1.2.3).

Toutefois, les missions *Apollo* ont également laissé une empreinte durable à la surface lunaire. En plus des modules et instruments scientifiques, plusieurs objets insolites, comme la célèbre balle de golf frappée par Alan Shepard lors d'*Apollo 14*, témoignent de l'activité humaine. Ces déchets soulèvent la question de l'impact anthropique sur les environnements planétaires et de la nécessité d'une réflexion sur la préservation des surfaces planétaires (Glavin et al., 2004).

1.1.4 De la fin de la guerre froide à nos jours

À la suite de la guerre froide, l'exploration lunaire est progressivement délaissée au profit de Mars et des autres planètes du système solaire. Il faut attendre les années 1990 pour que de nouvelles missions consacrées à la Lune voient le jour. En 1990, le Japon devient la troisième nation à placer un orbiteur autour de notre satellite. Quelques années plus tard, la mission américaine *Clementine* (1994) fournit les premières cartes globales de composition et de topographie de la Lune à partir d'images acquises dans le visible et l'infrarouge (Nozette et al., 1994). En combinant les données topographiques et gravimétriques, cette mission permet également d'estimer pour la première fois l'épaisseur de la croûte lunaire, proche de zéro sous *Mare Crisium*, et plus de 100 km sur la face cachée, au niveau du bassin Korolev (Zuber et al., 1994). En 1998, la mission *Lunar Prospector* (Binder, 1998) affine cette cartographie globale en mesurant la composition chimique de la surface, le champ magnétique et le champ de gravité. Elle met notamment en évidence une abondance d'hydrogène, interprétée comme la présence de glace d'eau dans les régions polaires, et permet de cartographier la distribution du composant KREEP (K - potassium, REE - terres rares et P - phosphore), riche en éléments traces, ainsi que des principaux types de roches lunaires. Les mesures du champ magnétique révèlent par ailleurs des anomalies localisées, notamment aux antipodes de *Mare Serenitatis* et *Mare Imbrium*, tandis que les données gravimétriques confirment l'existence d'un noyau de petite taille (∼300 km) enrichi en fer. Plus récemment, la mission *GRAIL* (Gravity Recovery and Interior Laboratory, 2013) a fourni une vision sans précédent du champ de gravité lunaire (Zuber et al., 2013). Elle montre que les anomalies gravitationnelles sont en grande partie liées à la topographie. La topographie sur la face visible est nettement plus basse que celle de la face cachée. Cette variation de degré un dans la topographie est attribuée à une variation dans l'épaisseur de la croûte, celle-ci étant nettement plus fine sur la face visible (20 à 30 km) que sur la face cachée (50 à 60 km) (Wieczorek et al., 2013). Les données ont également mis en évidence des structures auparavant invisibles, telles que des failles, des reliefs volcaniques ou encore des structures d'impact comme des pics centraux au centre des cratères.

Ces missions ont eu comme principal objectif d'étudier la surface et l'intérieur de la Lune. D'autres ont ciblé des aspects différents, comme la mission *LADEE* (Lunar Atmosphere and Dust Environment Explorer, 2013) dédiée à l'étude de la poussière et de l'atmosphère lunaire. Le retour d'échantillons n'est pas non plus l'apanage des missions *Apollo* : les missions soviétiques *Luna 20* à *Luna 23* ont également rapporté des échantillons lunaires. Plus récemment, la mission chinoise *Chang'e 5* a permis le retour de nouveaux échantillons, suivie de *Chang'e 6* qui a rapporté pour la première fois des échantillons en provenance de la face cachée de la Lune. Dans un avenir proche, le programme

Artemis prévoit quant à lui d'envoyer à nouveau des humains sur la Lune (fig. 1.3). En 2023, la NASA revèle les quatre astronautes choisis pour participer à cette nouvelle exploration de la Lune par les humains, avec notamment Victor Glover et Christina Hammock Koch, temoignant une volonté de diversité dans les programmes spatiaux alors que les précédentes missions *Apollo* n'avaient envoyé que des hommes blancs.

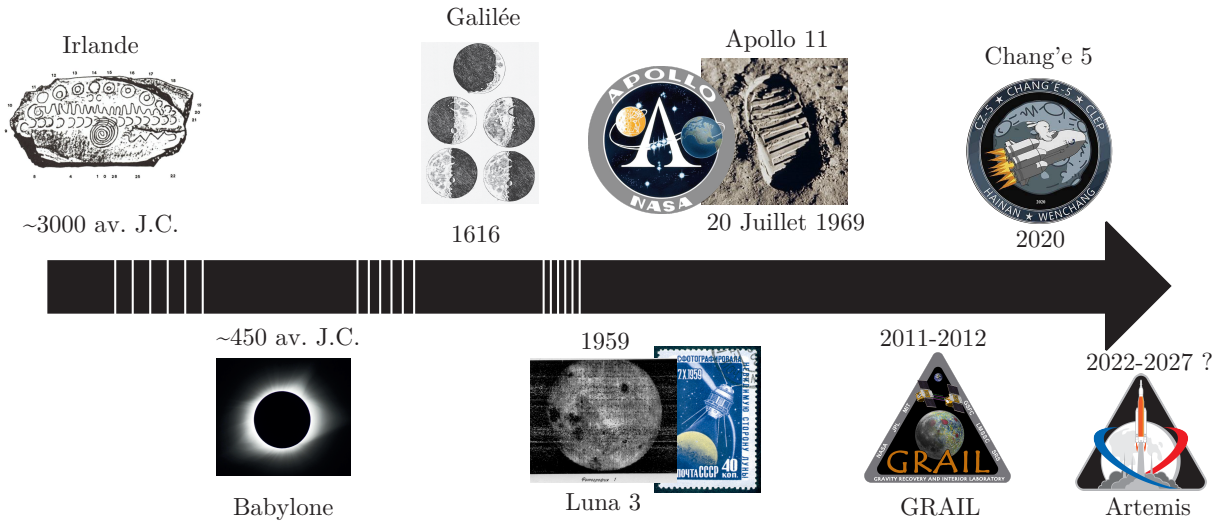

Figure 1.3: Frise chronologique de certaines des grandes observations de la Lune du Néolithique à nos jours.

1.2 Formation de la Lune

1.2.1 Les premières hypothèses

Plusieurs hypothèses ont été formulées concernant la formation de la Lune. L'une des premières est la *théorie de la formation simultanée* proposée par Roche (1873). Dans ce scénario, la Terre et la Lune se seraient formées à partir d'une même source de débris qui se seraient agglomérés pour donner naissance, d'un côté, à la Terre et, de l'autre, à la Lune. Peu après, George Darwin (1879), fils de Charles Darwin, avance la *théorie de la fission*. Il propose que la Terre était une masse en fusion animée d'une rotation rapide, cette rotation aurait entraîné la formation d'une protubérance qui se serait détachée pour former la Lune. Au début du XX^{e} siècle, une troisième hypothèse est proposée par See (1909), la *théorie de la capture*. Elle suppose que la Lune se serait initialement formée dans une autre région du Système solaire avant d'être capturée par la Terre sous l'effet de l'attraction gravitationnelle. Le corps capturé aurait ensuite été fragmenté après avoir franchi la limite de Roche, les débris se réassemblant pour former la Lune. Ce sont

finalement les missions spatiales de la guerre froide qui ont permis de développer le scénario le plus accepté actuellement : la formation de la Lune suite à un *impact géant*.

1.2.2 L'impact géant

Les analyses d'échantillons lunaires ont révélé une forte similarité isotopique entre la Terre et la Lune. De plus, les roches magmatiques lunaires présentent des similitudes avec celles du manteau terrestre, à la différence près que la Lune est enrichie en éléments réfractaires (à haute température de vaporisation) et appauvrie en éléments volatils (à faible température de vaporisation) (Taylor et al., 2006). Ces résultats ont conduit à la formulation de la théorie de l'impact géant à la fin des années 1970 (fig. 1.4), selon laquelle la Lune se serait formée à la suite d'une collision entre la proto-Terre et un corps différencié de la taille de Mars, nommé Théia en référence à la titanide mère de Séléné, déesse de la Lune (Hartmann et al., 1975).

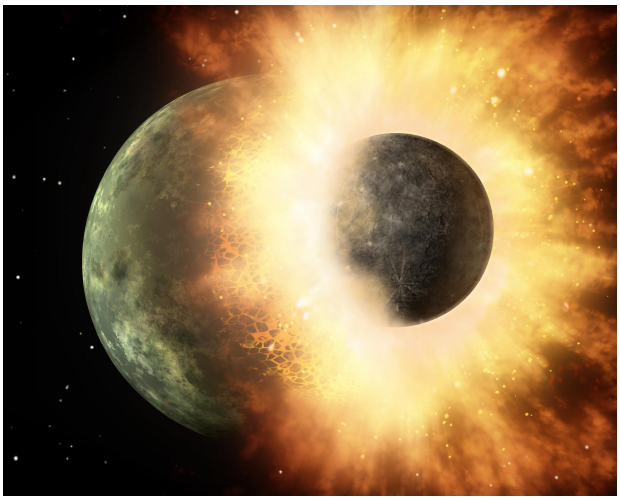

Figure 1.4: Représentation artistique de l'impact géant qui a conduit à la formation de la Lune. Crédits : NASA/JPL-Caltech.

Le matériau éjecté par cet impact aurait formé un nuage de débris chauds en orbite, dont l'accrétion progressive aurait donné naissance à la Lune. Toutefois, la similarité isotopique Terre-Lune est difficile à expliquer si l'on considère que la Lune s'est formée majoritairement à partir du matériel de l'impacteur. Des travaux plus récents proposent que la proto-Terre était en rotation très rapide au moment de l'impact (Ćuk et al., 2012), ou encore que l'impacteur avait une masse comparable à celle de la Terre (Canup, 2012). Ces scénarios permettent de concilier l'hypothèse de l'impact géant avec l'homogénéité isotopique observée entre la Terre et la Lune. Une autre proposition avancée pour résoudre cette difficulté est le modèle de la synestia. À la suite d'un impact très énergétique, la Terre et l'impacteur auraient formé une structure en rotation rapide, composée d'un mélange de liquide et de vapeur de silicates. Lors du refroidissement, la Terre se serait progressivement reconstituée au centre, tandis que des condensats se seraient formés dans les régions externes. L'accrétion de ces condensats dans la vapeur environnante aurait alors conduit à la formation de la Lune (Lock et al., 2017; Lock et al., 2018). Ce

processus permet aussi d'expliquer l'appauvrissement en éléments volatils de la Lune.

1.2.3 L'océan de magma

Le concept d'océan de magma n'est pas récent. Dès le XIX^{e} siècle, Kelvin (1863) proposait que la Terre s'était refroidie à partir d'un état initialement chaud et incandescent. Cependant, ce sont les échantillons rapportés par les missions *Apollo*, et en particulier l'abondance d'anorthosites, qui ont conduit à l'hypothèse d'un océan de magma lunaire (Lunar Magma Ocean-LMO). Sur Terre, l'anorthosite se forme dans des chambres magmatiques à faible pression et sa faible densité favorise sa flottabilité. Produire une telle quantité d'anorthosite sur la Lune implique donc une source de magma conséquente. C'est à partir de ces observations qu'a émergé le modèle classique de solidification du LMO, qui permet notamment d'expliquer la formation des hautes terres. Dans ce scénario, les cristaux d'olivine et de pyroxène précipitent en premier et sédimentent au fond, constituant le manteau lunaire (fig. 1.5). Ensuite, l'anorthite commence à cristalliser et, en raison de sa faible densité, flotte à la surface de l'océan de magma pour former une croûte de flottaison (Wood, 1970, fig. 1.6). Les dernières phases du LMO sont riches en éléments incompatibles et producteurs de chaleur, KREEP, et les dernières couches du manteau lunaire se composent de minéraux denses, en particulier l'ilménite.

Néanmoins, de nombreuses incertitudes subsistent concernant cet océan de magma, notamment concernant sa profondeur initiale qui est encore débattue. Les travaux sur la formation de la Lune suggèrent plutôt que la Lune a été initialement totalement fondue, en particulier au vu de l'énergie libérée par l'impact géant (Pritchard et al., 2000). De plus, l'épaisseur actuelle de la croûte est utilisée pour contraindre la profondeur initiale de l'océan de magma. En effet, si la croûte correspond à environ 8% de la masse totale de l'océan de magma, ce dernier pourrait atteindre une profondeur d'environ 1000 km (Elkins-Tanton et al., 2011; Snyder et al., 1992). En revanche, si la croûte constitue une fraction plus importante de l'océan de magma, celui-ci doit être plus mince, de l'ordre de $\sim$ 500 km à 800 km afin de rester compatible avec les épaisseurs crustales observées, comprises entre 34 km et 43 km (Rapp et al., 2018; Charlier et al., 2018). Cependant, la présence d'eau dans le manteau lunaire (Lin et al., 2017) permet de former une croûte plus fine à partir d'un océan de magma global en retardant l'apparition de l'anorthite dans la séquence de cristallisation.

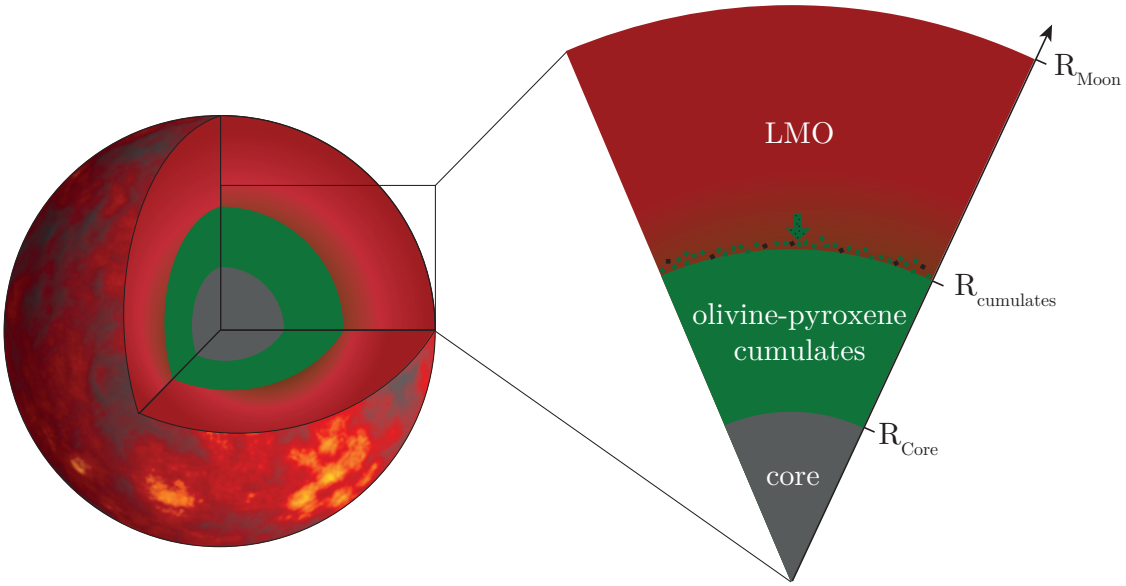

Figure 1.5: Schéma du modèle classique de solidification de la Lune lors de la première étape de cristallisation. L'olivine-pyroxène sédimentent au fond pour former les cumulats (en vert) lors de la solidification de l'océan de magma (rouge). Le noyau est représenté en gris foncé.

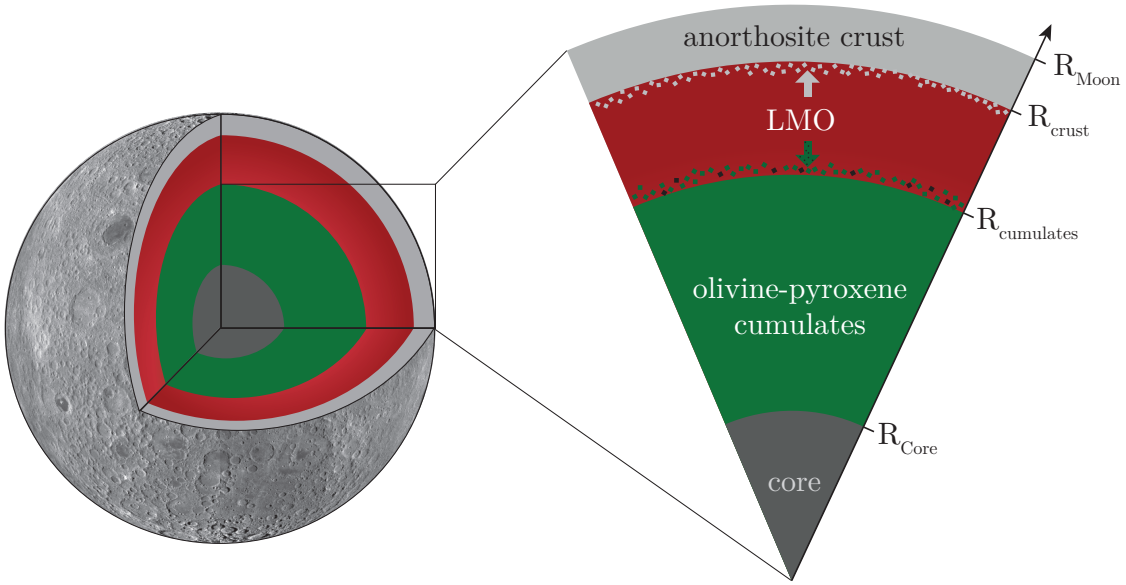

Figure 1.6: Schéma du modèle classique de solidification de la Lune lors de la cristallisation simultanée d'olivine-pyroxène et d'anorthite. L'olivine-pyroxène sédimente au fond pour former les cumulats (en vert), l'anorthite flotte en surface pour former la croûte (gris clair) lors de la solidification de l'océan de magma (rouge). Le noyau est représenté en gris foncé.

1.3 Structure de la Lune

Comme toutes les planètes telluriques, la Lune est un corps différencié qui se compose d'un noyau interne, d'un manteau et d'une croûte.

1.3.1 La croûte

Les roches de la croûte lunaire peuvent être divisées en deux grandes catégories aisément observables à l'oeil nu (fig. 1.7a). La première correspond aux grandes étendues claires et brillantes, les hautes terres ou *terrae*. Elles représentent plus de 80% de la surface de la Lune. Elles s'apparentent à la croûte primaire formée par flottaison des cristaux d'anorthite en surface de l'océan de magma comme expliqué précédemment. La seconde correspond aux tâches sombres, les *maria*, qui représentent environ 17% de la surface et sont principalement situées sur la face visible. Elles correspondent à des épanchements de magma suite à des impacts, d'où leur forme plutôt circulaire. Trois grands terrains peuvent être définis à la surface de la Lune (Jolliff et al., 2000, et fig. 1.7) :

- Terrains du bassin Aitken au Pôle Sud (South-Pole Aitken Terrane SPAT) qui correspond au plus vaste et au plus profond bassin d'impact lunaire connu. Il s'agit également du plus ancien, et l'impact a excavé une part significative de la croûte.
- Terrains feldspathiques des hautes terres (Feldspathic Highland Terrane FHT) qui est la croûte primaire constituée d'anorthosites.
- Terrains Procellarum riche en KREEP (Procellarum KREEP Terrane PKT) interprété comme le produit éruptif du liquide résiduel enrichi en éléments incompatibles (K-Potassium, REE-Terres Rares, P-Phosphore) lors des derniers stades de solidification de l'océan de magma

Bassin Aitken au Pôle Sud

Le bassin Aitken se situe sur la face cachée, et constitue la plus vaste structure d'impact connue du Système solaire, avec un diamètre estimé à environ 2600 km et une profondeur topographique d'environ 12 à 13 km (Spudis et al., 1994). Les analyses spectrales indiquent que les matériaux de surface y présentent une teneur moyenne en fer plus élevée que celle de la croûte lunaire feldspathique, ainsi qu'un enrichissement modéré en titane (Jolliff et al., 2000). Cette signature géochimique pourrait témoigner de la présence de matériaux issus de niveaux profonds de la croûte ou du manteau supérieur, voire d'un composant KREEP résiduel localisé sous le bassin (Ivanov et al., 2018). Toutefois, malgré la profondeur de l'excavation et le fort amincissement de la croûte, il y a peu de traces

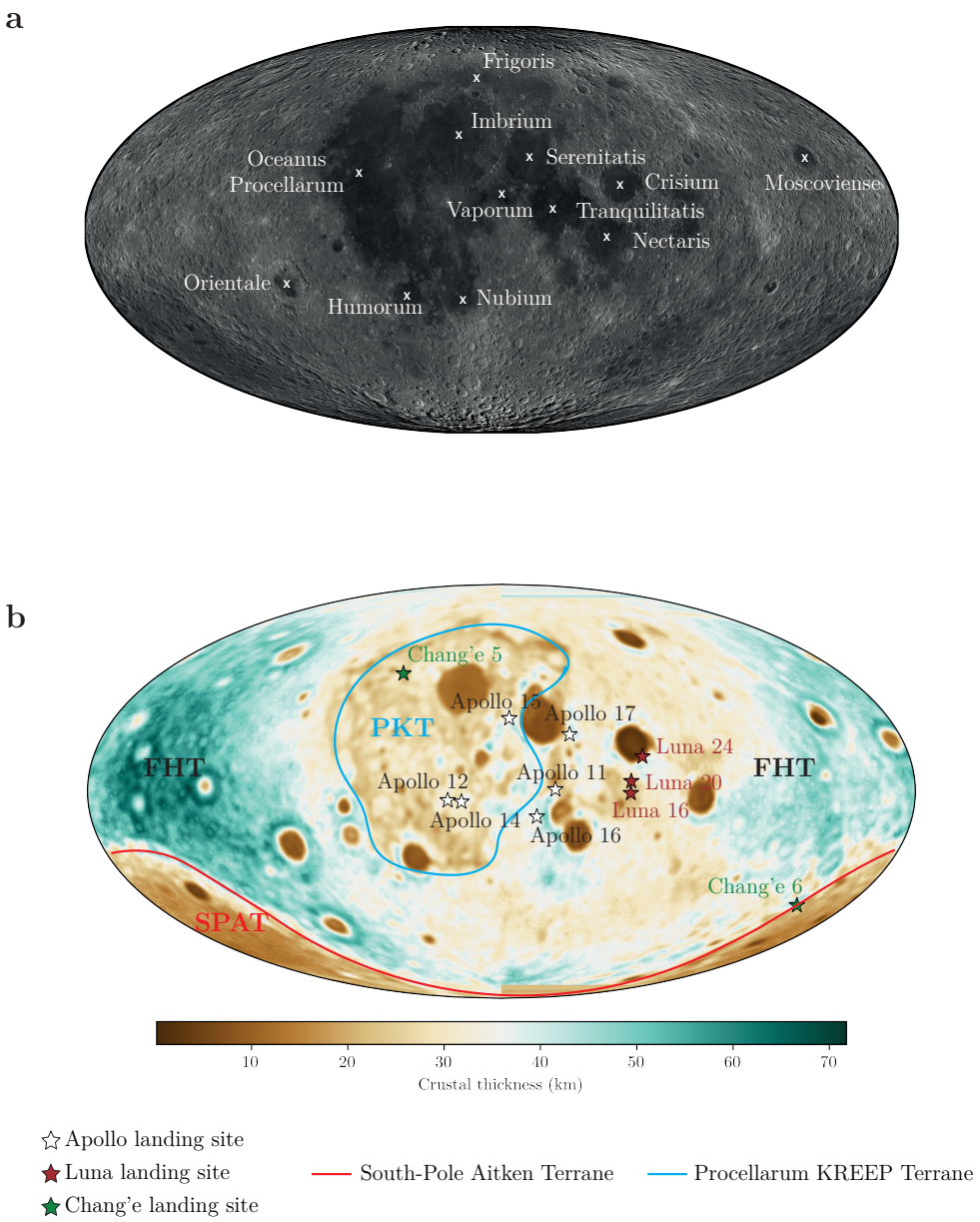

Figure 1.7: **a**- Image de la surface de la Lune en projection Mollweide centrée sur la face visible avec le nom des principales mers basaltiques. **b**- Carte de l'épaisseur de croûte d'après Wieczorek et al. (2013) en projection Mollweide, centrée sur la face visible, avec les délimitations des terrains définis par Jolliff et al. (2000), SPAT (ligne rouge), PKT (ligne bleu) et les FTH (correspondent au reste), et les sites d'atterissages des missions avec retour d'échantillons, *Apollo* (étoiles blanches), *Luna* (étoiles oranges) et *Chang'e* (étoiles vertes).

d'olivine, ce qui peut s'expliquer par la fusion de matériel suite à l'impact (Yamamoto et al., 2010). Ce bassin se serait formé tôt dans l'histoire de la Lune, probablement avant le retournement du manteau (Nakamura et al., 2009).

Hautes terres

Les hautes terres couvrent la plus grande majorité de la surface lunaire. Elles correspondent aux surfaces les plus anciennes et sont fortement cratérisées en particulier sur la face cachée. Elles témoignent des premiers stades de différenciation de l'océan de magma. La grande majorité des anorthosites résulte de la cristallisation de l'océan de magma lunaire, au cours duquel des cristaux légers de plagioclase riche en calcium (anorthite, $CaAl_2Si_2O_8$) ont flotté en surface pour former une croûte primitive globalement homogène (Wood, 1970, fig. 1.6). Ces roches se sont formées relativement tôt avec des âges compris entre 4,52 et 4,35 milliards d'années (Ga) ce qui en fait les roches les plus anciennes de la croûte lunaire (Borg et al., 2023). Elles ont aussi la particularité d'être enrichies en europium (Eu), tandis que les roches basaltiques en sont au contraire appauvries.

Un type de roche particulier est aussi présent dans ces hautes terres, il s'agit de la suite magnésienne. Elles témoignent des premières intrusions magmatiques dans la croûte primaire. Il s'agit de roches qui sont à la fois enrichies en magnésium donc témoignent d'une formation au début de la solidification de l'océan de magma mais sont parfois aussi enrichies en éléments KREEP, qui témoignent cette fois-ci d'une cristallisation plutôt tardive. Elles sont datées entre 4,3 et 4,6 milliards d'années (Borg et al., 2023). Leur origine demeure incertaine et peut résulter de processus dynamiques au sein du manteau lunaire.

Maria et KREEP

Les mers lunaires forment un vernis relativement mince, recouvrant la croûte primaire anorthositique de la Lune, avec des épaisseurs généralement comprises entre quelques centaines de mètres et 4 km dans les grands bassins (Taylor et al., 2009; Michaut et al., 2016). Elles représentent environ 17% de la surface lunaire et peuvent ainsi être considérées comme une croûte secondaire. Principalement situées sur la face visible, elles sont facilement observables à l'œil nu, tandis que celles présentes sur la face cachée sont rares et associées à de grands bassins d'impact tels que *Mare Moscoviense*, *Mare Orientale* ou encore *Mare Ingenii* (fig. 1.7a). Contrairement aux provinces basaltiques terrestres ou aux surfaces volcaniques de Vénus et Mars, les mers lunaires se caractérisent par leur planéité et l'absence de volcans boucliers. Leur mise en place résulte de plusieurs épisodes éruptifs distincts, majoritairement datés entre 3,8 et 3,0 Ga, bien que des âges plus anciens datés à 4,380 Ga et plus récents de 2,030 Ga aient également été identifiés

(Taylor et al., 2009; Snape et al., 2018; Li et al., 2021a). Les mers basaltiques présentent des hétérogénéités et un enrichissement en fer important en comparaison aux basaltes terrestres principalement issus de la croûte océanique. Elles sont aussi caractérisées par un enrichissement en terres rares et un appauvrissement en europium, ce qui confirme que les mers basaltiques proviennent de la fusion partielle d'un manteau différencié (Taylor et al., 2009).

Les KREEP constituent une composante particulière des basaltes lunaires, fortement enrichie en éléments incompatibles, et sont principalement concentrés dans la région d'*Oceanus Procellarum* (fig. 1.7). Les datations isotopiques Sm-Nd (samarium -néodyme) et Lu-Hf (lutécium-hafnium) indiquent un âge de cristallisation de 4345 ± 26 Ma, antérieur à celui de la majorité des autres mers basaltiques (Borg et al., 2023). Le composant KREEP est interprété comme le liquide résiduel de l'océan magmatique lunaire, cristallisé à partir des derniers $\sim 2\%$ de liquide restant après la cristallisation de l'olivine-pyroxène et de l'anorthite, et sont particulièrement riches en éléments incompatibles. Ce composant résulte des derniers liquides de la cristallisation de l'océan de magma, où le liquide riche en éléments compatibles a été piégé entre les cumulats sous-jacents et la croûte.

1.3.2 Le manteau

Données sismologiques

Les principales contraintes sur la structure du manteau proviennent des données sismologiques acquises par les missions *Apollo*. Celles-ci ont permis d'enregistrer environ 1800 impacts de météorites, 28 séismes peu profonds et très énergétiques, ainsi que près de 7000 séismes profonds de plus faible énergie (Wieczorek, 2009). Les séismes profonds proviennent de sources regroupées sur environ 300 sites (ou « nids ») et semblent être principalement liés aux effets de marée. L'ensemble de ces événements n'a toutefois été détecté que sur la face visible de la Lune. Par ailleurs, aucune onde sismique n'a été enregistrée à des profondeurs supérieures à 1200 km, laissant une incertitude sur l'intérieur profond. Enfin, la qualité des données disponibles est inégale, certains enregistrements présentant des incertitudes de temps d'arrivée supérieures à 10 secondes (Wieczorek, 2009).

Les profils de vitesse utilisés pour contraindre la structure du manteau lunaire proviennent de l'inversion des temps d'arrivée des ondes P (ou premières, il s'agit d'ondes de compressions) et S (ou secondaire, il s'agit d'ondes de cisaillements, qui ne se propagent pas dans les milieux liquides). Ces vitesses sismiques fournissent des informations précieuses sur la structure interne du manteau et permettent de construire des modèles de structure interne analogues au PREM (Preliminary Reference Earth Model) établi pour la Terre. Garcia et al. (2011), proposent un modèle préliminaire de la structure interne

de la Lune, VPREMoon. D'autres modèles plus anciens montrent la présence d'une discontinuité sismique autour de ∼400-750 km de profondeur (Goins et al., 1981; Nakamura, 1983; Khan et al., 2000; Lognonné et al., 2003). Cependant, cette discontinuité n'est pas présente dans le modèle de Garcia et al. (2011). L'idée de cette discontinuité a été abandonnée, les différences entre les modèles peuvent être liées à une mauvaise couverture des rayons sismiques à ces profondeurs, ainsi qu'aux incertitudes dans la determination des temps d'arrivée (Lognonné et al., 2015). La présence d'une zone partiellement fondue à la base du manteau a été suggérée pour expliquer l'atténuation des ondes S en profondeur (Nakamura et al., 1973). L'analyse des données sismiques d'Apollo par Weber et al. (2011) suggère aussi la présence d'une zone partiellement fondue, dont le sommet se situe à un rayon d'environ 480±15 km à la base du manteau (fig. 1.8). La mission *Artemis*, devrait permettre de déposer un nouveau sismomètre à la surface de la Lune, ce qui permettra d'apporter de nouvelles informations. Outre la sismologie, des mesures électromagnétiques issues des missions *Apollo* (12 et 15) ainsi que de la mission orbitale *Explorer 35* révèlent une augmentation de la conductivité électrique avec la profondeur (Banerdt et al., 2014). Cette tendance peut être reliée à une élévation de température en profondeur, mais aussi à une teneur accrue en fer ou à la présence d'eau, deux facteurs susceptibles d'accroître la conductivité. Dans le cas où une zone partiellement fondue existerait, elle pourrait résulter d'un enrichissement local en matériaux plus denses et producteurs de chaleur, issus de la déstabilisation des couches supérieures du manteau (Stegman et al., 2003a).

Séismes profonds

La présence de séismes profonds uniquement sur la face visible de la Lune demeure énigmatique et contre-intuitive. En effet, l'occurence des séismes profonds est associée à la présence de matériel froid et cassant. Cependant, la face visible est marquée par la présence des *maria* ainsi qu'une possible zone partiellement fondue à la base du manteau ce qui suggère au contraire un manteau chaud. Plusieurs explications ont été proposées pour expliquer l'occurence de ces séismes. Il pourrait s'agir d'un biais d'observation car toutes les stations ont été installées sur la face visible. Il est possible qu'il y ait une zone d'atténuation dans l'intérieur profond de la Lune, ce qui empêche d'observer des séismes lunaires profonds (Nakamura, 2005). De même, la présence d'une zone partiellement fondue compliquerait la détection des séismes profond (Weber et al., 2011). La corrélation entre la localisation des séismes profonds et celle des *maria* a également été proposée. Les mers basaltiques résulteraient de la fusion, en profondeur, d'un mélange olivine–pyroxène–ilménite issu du retournement compositionnel. Des instabilités dans cette couche favorisent la remontée puis l'éruption de ce matériel, qui, une fois refroidi,

s'enfonce de nouveau. En présence d'eau et de volatils, ce matériau peut alors se fracturer plus facilement sous l'effet des forces de marée terrestres (Qin et al., 2012). Enfin, malgré les températures élevées à la base du manteau, la rupture et donc la sismicité pourraient être favorisées par rapport à une simple déformation ductile, en raison des contraintes de marée (Kawamura et al., 2017).

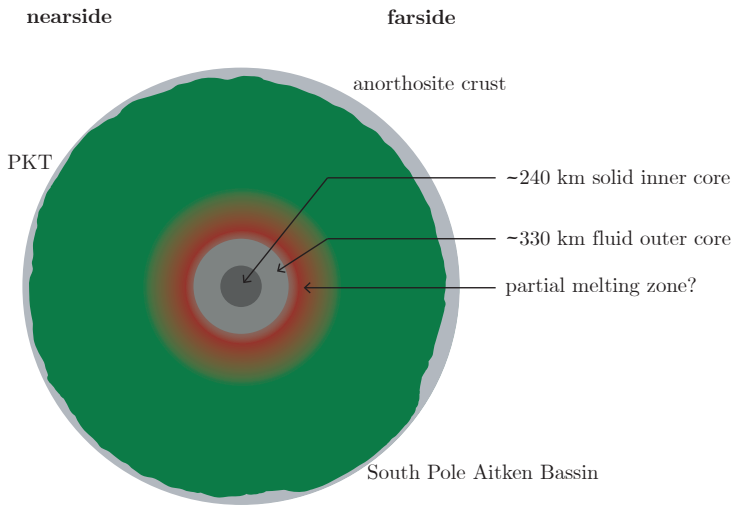

Figure 1.8: Représentation schématique de l'intérieur de la Lune aujourd'hui.

1.3.3 Le noyau

Toutes les planètes telluriques et certains satellites de glace possèdent un noyau métallique, représentant généralement près de la moitié de la taille de leur corps parent. Les analyses de masse du rayon et du moment d'inertie suggère la présence d'un noyau métallique, mais dont la taille est faible en comparaison à la taille de la Lune. Les études basées sur le moment d'inertie, sensible aux variations de densité avec la profondeur, estiment que si le noyau est riche en fer alors le rayon de ce noyau est d'environ 460 km (Wieczorek, 2009). Différentes mesures géophysiques, permettent aussi de donner des estimations de la taille du noyau. Par exemple, à partir des données du champ magnétique, il est possible d'obtenir la conductivité électrique qui donne des informations sur la structure interne de la Lune. La conductivité électrique est obtenue en comparant le champ magnétique variable dans le temps à la surface de la Lune avec celui d'un satellite distant (Banerdt et al., 2014). Avec ces méthodes, la mission *Lunar Prospector* a permis d'estimer que le rayon du noyau lunaire est de 390 ± 90 km (Banerdt et al., 2014). Plus récemment, les données géophysiques de la mission Kaguya estiment cette limite à 290 km (-120 km, + 60 km), avec une limite haute possible de 400 km (Shimizu et al., 2013). Les données

sismiques permettent elles aussi d'estimer le rayon du noyau, bien que les ondes soient atténuées en profondeur, ce qui rend la tâche plus complexe (voir section 1.3.2). Weber et al. (2011) suggèrent que le noyau est, comme sur Terre, composé d'une graine solide et d'un noyau liquide, ayant pour rayon 240 ± 10 km et 330 ± 20 km respectivement. Ce noyau serait peut-être entouré d'une zone partiellement fondue de 140 km d'épaisseur riche en matériel dense (voir section 1.3.2 et fig. 1.8). Garcia et al. (2011) estiment le rayon du noyau à 380±40 km, pour une densité moyenne du noyau de 5,2±1.0 $\mathrm{kg\,cm^{-3}}$.

Champ magnétique

La Lune ne présente pas de champ magnétique global aujourd'hui. Toutefois, elle en a possédé un par le passé, comme en témoignent les échantillons de roches lunaires qui conservent une magnétisation rémanente indiquant l'existence d'un champ magnétique ancien. Celui-ci aurait persisté jusqu'il y a environ 2 milliards d'années, avec des variations d'intensité : un champ initialement fort et proche de l'intensité du champ magnétique terrestre actuel (>50 µT), entre 4,2 et 3,5 milliards d'année (Ga), qui a considérablement baissé vers 3,2 Ga ($\lesssim$5 µT), puis s'est encore atténué après 1 Ga (<0.1 µT, Cai et al., 2025). Les mécanismes pouvant générer un champ magnétique sur la Lune restent incertains, notamment pour expliquer un champ à la fois intense et de longue durée, en accord avec les mesures des échantillons. La Lune étant petite, il a été montré que l'extraction de chaleur du noyau n'est pas suffisante pour produire un champ magnétique pendant plus de quelques millions d'années (Konrad et al., 1997). Toutefois, cette dynamo peut être entretenue par un retournement du manteau riche en éléments producteurs de chaleur, ce qui limite le refroidissement du noyau (Stegman et al., 2003a). De plus, le refroidissement du noyau dû à sa cristallisation peut soutenir une dynamo relativement longue (Laneuville et al., 2014). Le refroidissement rapide du noyau par des cumulats denses et froids peut également prolonger la dynamo lunaire (Evans et al., 2022). D'autres scénarios, tels qu'une rotation différentielle entre le noyau et le manteau induite par la précession de l'axe de rotation (Dwyer et al., 2011), ou par des variations de la vitesse de rotation du manteau liées à des impacts (Le Bars et al., 2011), ont aussi été proposés.

1.4 Asymétrie face visible et face cachée

1.4.1 Observations de l'asymétrie

La Lune présente une asymétrie marquée entre sa face visible et sa face cachée. Sur le plan morphologique, la première est caractérisée par l'abondance des *maria*, tandis que la seconde montre une surface beaucoup plus cratérisée (fig. 1.9a). Cette différence se reflète

également dans l'âge des terrains. Les *maria*, plus jeunes, contrastent avec la croûte anorthositique face cachée, supposée plus ancienne au vu de l'importance du nombre de cratères. Elle se manifeste aussi dans l'épaisseur crustale, qui varie de 20 à 30 km sur la face visible contre 50 à 60 km sur la face opposée (Wieczorek et al., 2013, et fig. 1.9b). Enfin, elle concerne aussi la composition, puisque des éléments tels que le titane (Ti) ou le thorium (Th) sont principalement concentrés dans la région d'Oceanus Procellarum (fig. 1.9c).

Principalement visible en surface et au niveau de la croûte, cette dichotomie pourrait également concerner l'intérieur de la Lune. Par exemple, les séismes profonds n'ont été détectés que sur la face visible, sans qu'on puisse exclure leur présence sur la face cachée, les observations pouvant être limitées par des biais lié à la localisation des stations des missions *Apollo* et l'atténuation des ondes sismiques en profondeur. Ainsi, les contrastes observés dans la croûte pourraient résulter de processus internes suggérant une asymétrie plus profonde, au sein du manteau lui-même. En particulier, l'asymétrie peut être thermique. C'est ce que suggère la récente étude de Park et al. (2025). A partir des données de la mission GRAIL, les auteurs calculent les nombres de Love de la Lune k_{lm}, qui permettent de caractériser les variations temporelles du champ de gravité pour chaque harmonique sphérique de degré l et d'ordre m, et reflètent la déformation tidale. La valeur obtenue en particulier pour k_3 est bien plus élevée que celle attendue pour un corps symétrique, ce qui suggère une anomalie de température de l'ordre de 100-200 °C entre la face visible et la face cachée. Ce résultat est appuyé par les analyses de la mission *Chang'e 6*. La mission *Chang'e 6*, a récémment permit de prélever et ramener des échantillons de la face cachée de la Lune. L'analyse de ces échantillons suggère que les minéraux qui composent ces échantillons se sont refroidis à des températures inférieures ($\sim 100\,°C$) à ceux de la face visible. Cela suggère que l'asymétrie lunaire n'est pas restreinte à la croûte mais touche aussi l'intérieur plus profond (He et al., 2025).

1.4.2 Mécanismes proposés pour expliquer la dichotomie

Depuis les années 1970, plusieurs mécanismes ont été proposés pour expliquer cette dichotomie. Une première hypothèse est celle d'un bombardement précoce ayant aminci une partie de la croûte, ce qui aurait entraîné une redistribution des masses et une réorientation de la Lune. Une croûte amincie favorise par ailleurs les éruptions de lave en surface (Wood, 1973). L'impact géant responsable de la formation du bassin Pôle Sud–Aitken a également été envisagé comme origine de l'asymétrie (Jones et al., 2022). L'énergie dégagée aurait pu induire une hétérogénéité dans le manteau et conduire à la ségrégation des éléments producteurs de chaleur du côté de la face visible. Une autre hypothèse met en avant la position précoce de la Lune par rapport à la Terre, dans son stade d'océan

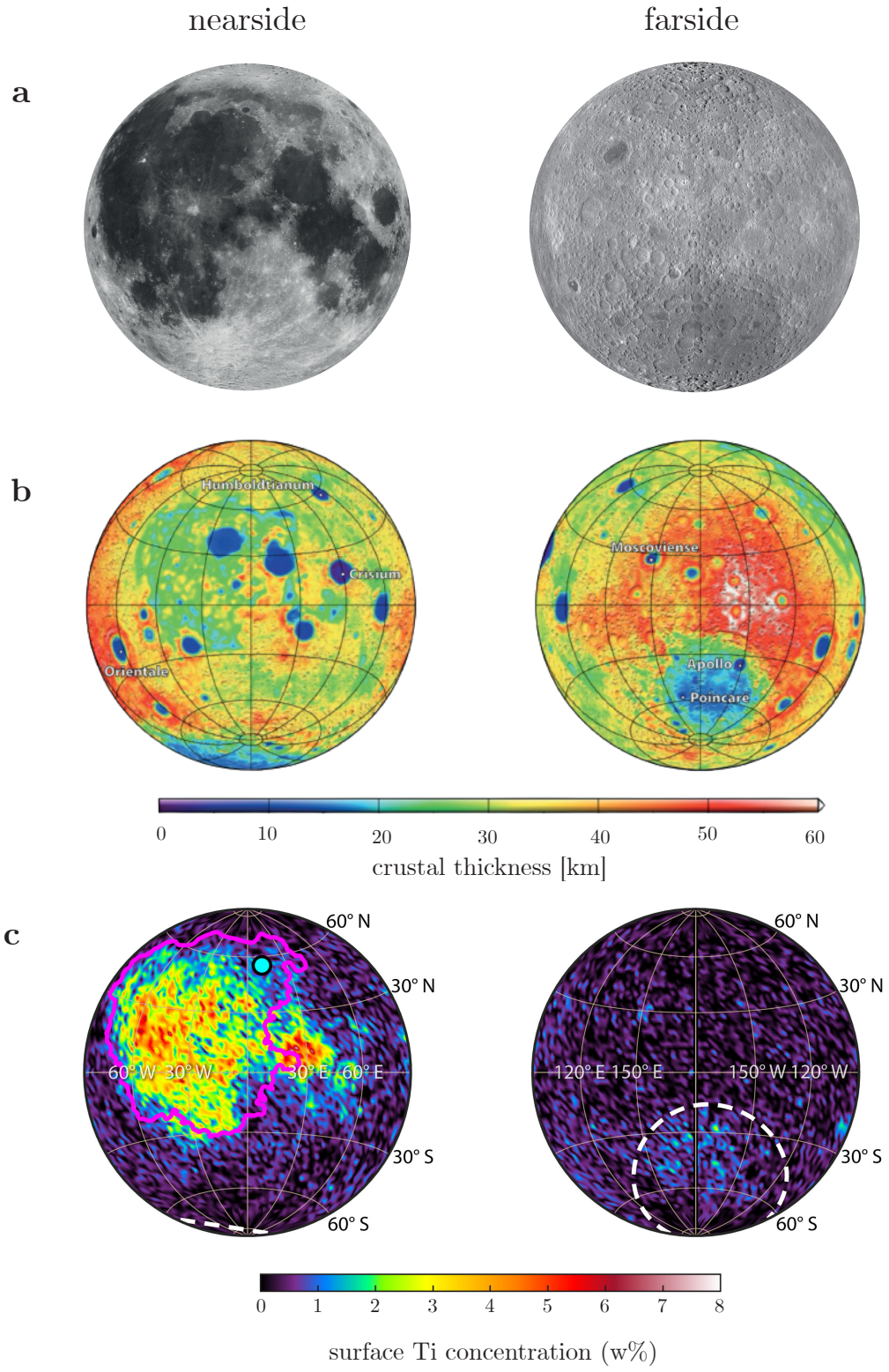

Figure 1.9: **a**- Photographies de la face visible (à gauche) et de la face cachée (à droite), crédits : NASA/JPL. **b**- Carte de l'épaisseur de croûte sur les faces visible et cachée (Wieczorek et al., 2013). **c**- Carte de la concentration du titane (Ti) à la surface de la Lune en $w\%$ (Jones et al., 2022).

de magma. Ce scénario impliquerait un chauffage différentiel entre les deux hémisphères, aboutissant à une croûte plus fine sur la face visible (Roy et al., 2014). La cristallisation de l'océan magmatique elle-même a également été invoquée pour générer une asymétrie particulière dans le manteau (Wasson et al., 1980). La croissance instable d'une couche stagnante au-dessus d'un manteau partiellement fondu ou d'un océan de magma avec cristaux en suspenssion (slushy magma ocean) est également évoquée (Watson et al., 2022a). La ségrégation d'une couche enrichie en éléments KREEP, piégée entre manteau et croûte, pourrait aussi expliquer l'amincissement de la croûte sur la face visible (Laneuville et al., 2013). Cependant, si cette hypothèse rend compte de la différence d'épaisseur crustale, elle ne précise pas comment l'asymétrie initiale à la base de la croûte s'est mise en place.

Evolution dynamique du manteau

Une piste pour expliquer l'asymétrie entre la face cachée et la face visible est la dynamique du manteau lunaire. De nombreuses études s'accordent sur le fait que la Lune a connu une phase de retournement du manteau, résultant de la solidification tardive d'une couche dense située à faible profondeur. En effet, la stratification du manteau lunaire est directement héritée de la cristallisation du LMO. Au fur et à mesure de la solidification des cumulats, qui s'effectue de la base vers la surface par sédimentation, le liquide résiduel du LMO s'enrichit en éléments incompatibles. Lorsque la cristallisation du LMO atteint environ 89-95% (Elkins-Tanton et al., 2002), les phases riches en éléments denses, tels que l'ilménite, et producteurs de chaleur commencent à se former dans les dernières couches de cumulats (Snyder et al., 1992; Elkins-Tanton et al., 2011; Lin et al., 2017; Charlier et al., 2018; Rapp et al., 2018). Cette couche enrichie se retrouve alors piégée entre les cumulats et la croûte de flottaison, créant une situation gravitationnellement instable (Hess et al., 1995; Parmentier et al., 2002). Selon la rhéologie du manteau lunaire, cette couche peut soit se déstabiliser et s'enfoncer, soit demeurer confinée sous la croûte (Elkins-Tanton et al., 2002; Maurice et al., 2024).

Dans le scénario où la couche dense plonge et se retrouve à la frontière noyau-manteau, sa densité élevée la rend à priori stable et empêcherait tout développement de convection. Cependant, cette couche est fortement enrichie en éléments producteurs de chaleur par rapport aux cumulats situés au-dessus. Plusieurs études suggèrent ainsi, que la couche dense pourrait alors se déstabiliser, et entraîner des mouvements convectifs (Hess et al., 1995; Zhong et al., 2000b; Stegman et al., 2003a). En particulier, si cette couche se destabilise en prenant la forme d'une harmonique sphérique de degré un, cela peut produire naturellement une asymétrie globale (Zhong et al., 2000b).

Les modèles d'évolution thermique du manteau qui étudient la convection se placent

généralement après la phase de retournement. À ce stade, les couches denses situées sous la croûte se sont déjà déstabilisées et la Lune est entièrement solidifiée. Ces modèles reposent sur l'hypothèse d'une solidification rapide de l'océan de magma lunaire. Ils montrent alors que la convection mantellique a pu s'établir. Ce processus pourrait expliquer l'origine des mers basaltiques ainsi que la longue durée du volcanisme lunaire, dont les basaltes les plus récents sont datées de 2030±4 Ma (Li et al., 2021b). La Lune étant un petit corps, son refroidissement aurait pu être rapide. Cependant, la présence d'une lithosphère froide isolant le manteau, permet de maintenir une convection et d'expliquer la durée d'éruption des mers basaltiques (Ziethe et al., 2009). Cette convection peut persister encore de nos jours avec des vitesses inférieures à 1 cm an^{-1} (Ziethe et al., 2009). L'approfondissement progressif de la zone de fusion partielle pourrait expliquer la diminution de la teneur en titane des mers lunaires les plus jeunes (Spohn et al., 2001), tandis que la remontée de la couche dense riche en éléments producteurs de chaleur contribuerait également à l'alimentation du volcanisme basaltique (Zhang et al., 2017). Cependant, ces modèles ne permettent pas d'expliquer la présence des *maria* uniquement sur la face visible.

Dynamique des cumulats en présence d'un océan de magma

À l'exception de l'étude de Maurice et al. (2020) and Maurice et al. (2024), les travaux portant sur la dynamique des cumulats lunaires se placent dans un contexte de solidification complète de la Lune, et négligent donc les interactions potentielles avec l'océan de magma encore en cours de cristallisation.

Morison et al. (2019) se sont intéressés au temps de mise en place de la convection dans les cumulats lunaires, alors que ces derniers s'épaississent au cours du temps. Leur approche repose sur une étude de stabilité linéaire avec un profil initial de température dépendant de la composition et de la pression. La spécificité de leur modèle réside dans l'introduction d'une condition aux limites mécanique perméable entre l'océan de magma liquide et les cumulats solides. En effet, les études classiques de la convection dans les cumulats imposent généralement des conditions de glissement libre et non-pénétratives aux limites : la contrainte tangentielle y est nulle et la vitesse normale est imposée à zéro. Cela néglige la possibilité de la formation d'une topographie dynamique à l'interface. Il s'agit d'une hypothèse raisonnable, puisque le poids de la topographie limite son amplitude. Cependant, une telle topographie peut avoir le temps de se développer, et ces reliefs dynamiques à l'interface solide/liquide peuvent être rapidement effacés par des processus de fusion et de cristallisation par le transport de chaleur latente dans l'océan de magma (fig. 1.10). Cela a notamment été proposé à l'interface graine solide/noyau liquide terrestre (Deguen, 2013; Alboussière et al., 2010). Une topographie positive du solide pénétrant dans le liquide tend à fondre, tandis qu'une topographie négative est comblée par solidi-

fication (fig. 1.10). En introduisant cette condition aux limites de changement de phase, Morison et al. (2019) montrent que la convection mantellique pourrait démarrer très tôt durant la solidification de l'océan de magma lunaire. De plus, la condition de changement de phase favorise le fait que convection puisse se developper en prenant la forme d'une harmonique sphérique de degré un (Morison et al., 2019; Morison et al., 2024, fig. 1.10).

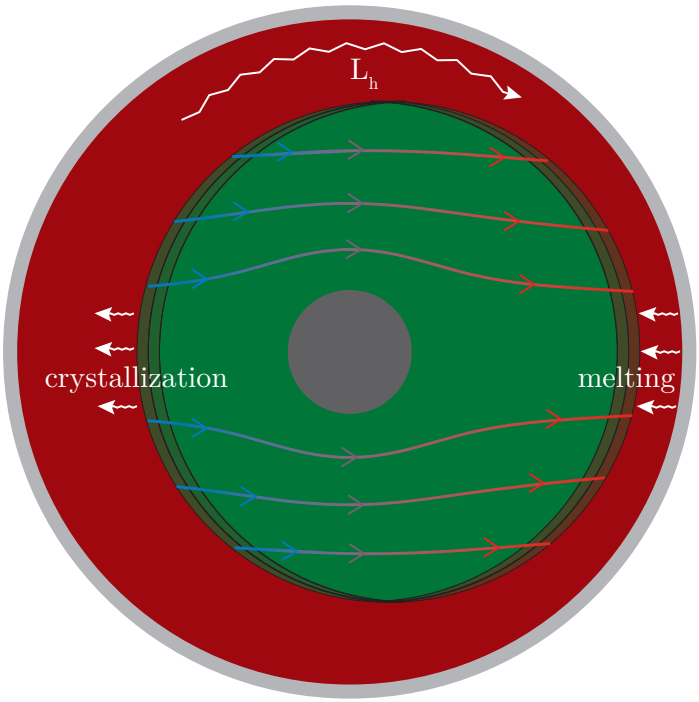

Figure 1.10: Représentation schématique du changement de phase à l'interface cumulats/océan de magma. La noyau est représenté en gris foncé, les cumulats en vert, l'océan de magma en rouge et la croûte en gris clair. Les lignes en zigzag correspondent à la chaleur latente libérée par la cristallisation dans les zones « creux » topographiques et transportée par convection dans l'océan de magma pour la fusion des cumulats dans les « sommets » topographiques. Les flèches rouges-bleues représentent les lignes de flux à l'intérieur des cumulats.

1.5 Problématique et plan

Les études du temps de solidification ont souvent argumenté en faveur de temps courts, de l'ordre de 10 Ma (Elkins-Tanton et al., 2011). Cependant, l'étude récente de Maurice et al. (2020) propose des temps de solidification beaucoup plus longs, atteignant plus de 200 Ma. Cela conduit à la question suivante : quelle est la durée de solidification de l'océan de magma ? Les études portant sur la dynamique des cumulats se basent généralement sur

l'hypothèse d'un temps de solidification rapide de l'océan de magma et s'intéressent donc à la dynamique des cumulats lorsque l'océan de magma est totalement solidifié, en négligeant les interactions possibles entre les cumulats et l'océan encore présent. Les travaux de Boukaré et al. (2018) et Maurice et al. (2024) montrent que, dans le cas d'un océan de magma à durée de vie longue, des instabilités thermiques peuvent se développer dans les cumulats avant la fin de la solidification. En tenant compte d'un changement de phase à l'interface entre les cumulats et l'océan de magma, le développement des instabilités est facilité et le degré préférentiel de ces instabilités correspond alors à une harmonique sphérique de degré un. Ces résultats amènent alors à formuler une nouvelle question : quel est le temps caractéristique du développement de ces instabilités thermiques ? Et est-ce que la durée de solidification de l'océan de magma lunaire est suffisamment longue pour que le retournement des cumulats se produise avant la fin de la solidification de l'océan de magma lunaire ? Si ces instabilités peuvent effectivement se développer avant la solidification complète, quel est le temps d'initiation d'un retournement dans les cumulats et quelle est sa durée ? Selon quel degré d'harmonique sphérique ce retournement va-t-il se développer ?

Dans un premier temps, j'ai étudié le temps de solidification de l'océan de magma. En effet, des estimations du temps de solidification de l'océan de magma lunaire existent déjà. Par exemple, Elkins-Tanton et al. (2011), proposent un temps de cristallisation relativement rapide de l'ordre de 10 Ma, mais sans prendre en compte la faible conductivité thermique de la croûte, la production de chaleur radiogénique, ni un océan de magma global. À l'inverse, Maurice et al. (2020), obtiennent des temps de solidification beaucoup plus longs atteignant plus de 200 Ma, en prenant en compte la faible conductivité de la croûte anorthositique, la production de chaleur radiogénique, mais ne prennent pas en compte un océan de magma global. Pour estimer le temps de solidification de l'océan de magma lunaire global, j'ai développé un modèle 1D basé sur la conservation de la chaleur dans l'océan de magma à partir d'un diagramme de phase simple avec un eutectique. Ce modèle permet de contraindre le temps de solidification de la Lune en étudiant l'effet de différents facteurs : l'épaisseur finale de la croûte, la composition eutectique, qui contraint le moment où l'anorthite commence à cristalliser, et la conductivité thermique de la croûte. Ce travail constitue l'objet du Chapitre 2.

Dans un second temps, je me suis intéressée à la dynamique des cumulats lors de la solidification de l'océan de magma lunaire en prenant notamment en compte une condition aux limites pénétrative à la frontière cumulats/océan de magma. Dans le chapitre 3, je détaille les méthodes numériques utilisées pour étudier la dynamique des cumulats, en partant d'un cas simple. En utilisant à la fois une étude de stabilité linéaire et des simulations numériques directes, j'étudie la convection dans les cumulats en prenant en

compte une condition de changement de phase à l'interface. Dans le Chapitre 4, j'applique les méthodes développées dans le chapitre 3 au cas spécifique de la Lune. Pour cela, les conditions initiales découlent directement du modèle de solidification du LMO développé dans le Chapitre 2, et je prends en compte le refroidissement séculaire du noyau à la base des cumulats.

Dans la suite de ce manuscrit, je me suis intéressée à l'application du modèle d'évolution thermique à Mars. La question d'une couche primaire anorthositique formée de la même manière que sur la Lune a souvent été écartée sur Mars. Cependant, les missions spatiales orbitales ont permis de mettre en évidence des traces d'anorthosites sur Mars (Carter et al., 2013). C'est pourquoi dans le Chapitre 5, je propose d'estimer l'épaisseur maximale d'une croûte primaire anorthositique sur Mars ainsi que le temps nécessaire à sa formation.

Enfin, dans le Chapitre 6 de ce manuscrit, j'explore les éventuelles conséquences d'un retournement de degré un dans les cumulats sur la cristallisation de la croûte. J'étudie aussi la possibilité de la mise en place de la convection dans la croûte en prenant en compte un changement de phase à la base de la croûte.

Chapter 2

Thermal evolution of the lunar magma ocean

Le chapitre suivant a fait l'objet d'un article publié en Novembre 2024 dans la revue Earth and Planetary Science Letter (Colin et al., 2024). Dans cet article nous présentons un modèle pour la solidification de l'océan de magma lunaire basé sur un diagrame de phase anorthite/olivine-pyroxène avec un eutectique. A partir de ce diagrame de phase, il est possible de diviser la solidification de l'océan de magma en deux étapes. (1) L'olivine-pyroxène cristallisent et sédimentent au fond de l'océan de magma pour former les cumulats. (2) Une fois l'eutectique atteint, il y a cristallisation simultanée d'olivine-pyroxène qui continuent de faire croître les cumulats, et d'anorthite qui flotte en surface pour former une couche de flotaison isolant l'océan de magma. A partir de la conservation de la chaleur dans l'océan de magma pendant ces deux étapes, nous pouvons suivre la croissance des cumulats et de la croûte et ansi, estimer le temps de solidification de l'océan de magma lunaire en fonction de différents paramètres. Nous étudions aussi l'influence d'un retournement des cumulats sur le temps de solidification de l'océan de magma lunaire.

abstract

The energy of the giant impact was large enough to generate an initially fully molten Moon. During the solidification of this lunar magma ocean (LMO), an anorthosite crust formed by flotation of light anorthite crystals. Lunar anorthosites show crystallization ages as young as 4.360 Gyr, suggesting a long-lived LMO or a rather young Moon. Existing models for LMO solidification are for a specific phase diagram based on one compositional model. However, the LMO solidification timescale depends on the lunar bulk composition and on the appearance of anorthite in the crystallization sequence.

Here, we propose a physically robust 1D model for LMO evolution based on a simple anorthite-olivine eutectic phase diagram. Cumulates first settle at the ocean base for about a thousand years. This first stage results in an unstable thermal profile for the cumulates that can lead to their overturn. In the second stage, simultaneous crystallization of anorthite and cumulates leads to the formation of a buoyant lid that considerably slows down LMO cooling.

We explore the impact of an initially hydrated composition, which reduces the stability of plagioclase, of the eutectic position and the crust thermal conductivity. We show that cumulates overturn may reduce or extend the LMO solidification time depending on its duration. The total LMO solidification timescale ranges between 45 and 250 Myr. Given the most reliable age of 4.360 Gyr for FAN sample 60025, which derives from more than 99% of crystallization, we estimate an age of 4400 to 4560 Myr for the Moon.

2.1 Introduction

The energy from the giant impact between the proto-Earth and a Mars-sized body was sufficient to give rise to an initially hot Moon with a global magma ocean (Pritchard et al., 2000; Canup, 2012; Ćuk et al., 2012; Nakajima et al., 2014). A global magma ocean appears particularly inevitable if the formation of the Moon occurred in a Synestia, a planetary structure resulting from a high-energy, high-angular momentum giant impact, as recently suggested (Lock et al., 2017; Lock et al., 2018). The lunar Highlands, forming the pale and bright regions on the Moon's surface, are remnants of the initial crust formed by the cooling and crystallization of this lunar magma ocean (LMO). Samples collected by astronauts during the Apollo missions, meteorite samples, and remote-sensing studies indicate that the lunar Highlands are predominantly made of anorthosite, containing more than 90% of Ca-rich anorthite (Warren et al., 1979; Ohtake et al., 2009). In the LMO solidification scenario, this primary crust is formed by aggregation of buoyant anorthite minerals floating on the surface and insulating the magma ocean beneath while, cumulates form by sedimentation of dense olivine and pyroxene crystals (Wood et al., 1970)

(fig. 2.1c). Fractional crystallization of the LMO would have resulted in the formation of a residual liquid, highly enriched in incompatible elements (K: Potassium, REE: Rare Earth Elements and P: Phosphorus), which could explain the singular composition of the Oceanus Procellarum KREEP terrane. LMO fractional crystallization would also lead to an unstable density profile in the cumulates, resulting both from the decrease in the LMO liquidus temperature and its progressive enrichment in iron as crystallization proceeds (Hess et al., 1995; Parmentier et al., 2002; Boukaré et al., 2018; Morison et al., 2019).

Dating of ferroan anorthosite, believed to be the oldest crustal rock type on the Moon, yield ages ranging from 4.29 to 4.55 Gyr (Alibert et al., 1994; Borg et al., 2020; Marks et al., 2019; Nyquist et al., 2006), hence spanning over $\sim$ 250 Myr. It has been argued that these ages may not reflect the true crystallization ages of anorthosites as different chronometers do not always give overlapping results (Borg et al., 2015). The intense early bombardment of the lunar crust could have perturbed the crystallization and metamorphic history of these rocks (Carlson, 2019). Nonetheless, the sample FAN 60025 shows one of the youngest ages of 4.360 Gyr, consistent for several radiometric systems (Borg et al., 2011). Borg et al. (2011) proposed that this age could reflect a relatively late formation of the Moon, more than 100 Myr after Solar System formation. Numerous studies summarized in Borg et al. (2023) have also shown that many lunar rocks show ages that cluster around 4.33-4.360 Gyr suggesting rapid cooling of a magma ocean. These observations were used to argue that the Moon formation took place shortly before 4.360 Gyr. The debate about the age of the Moon has been ongoing since then and is closely tied to the timescale of solidification of the LMO, approximately 200 Myr after the formation of the Solar System. Indeed, this young age for a ferroan anorthosite can also imply that the LMO took longer to solidify than previously thought (Maurice et al., 2020) or that the lunar crust did not form by flotation but by a process closer to serial magmatism (Longhi, 2003; Borg et al., 2011; Gross et al., 2014), for instance by extraction of melts from a slushy magma ocean which cools down over a longer time-scale than in the classical LMO solidification scenario (Michaut et al., 2022).

Existing models provide variable estimates for the solidification time in its classical scenario, from 10 Myr (Elkins-Tanton et al., 2011) to 100-200 Myr (Maurice et al., 2020; Zhang et al., 2021b). These models are based on only one specific phase diagram associated to the compositional model of Elkins-Tanton et al., 2011. However, the shortest estimate does not account for the production of radioactive heat. In this model, anorthite appears rather late in the crystallization sequence, when 80% of the lunar magma ocean has solidified. Other fractional crystallization experiments have been carried out, based on slightly different bulk compositions for the Moon, or different LMO depths (considering a whole magma ocean rather than a shallower one as in Elkins-Tanton et al., 2011).

They notably differ in the overall final proportion of anorthite and the specific point in the crystallization sequence when anorthite emerges (Snyder et al., 1992; Elkins-Tanton et al., 2011; Charlier et al., 2018). Adding water to the bulk composition of the Moon reduces the stability of plagioclase and delays its appearance in the crystallization sequence (Lin et al., 2017). Such differences in composition not only result in different final possible thicknesses for the anorthosite crust, they also affect the time at which the flotation crust starts to insulate the magma ocean beneath, and hence the total amount of latent and radioactive heat that must be conducted away through this lid. In some models, anorthite starts to form when only ∼66-70% of the LMO has crystallized (Lin et al., 2017; Rapp et al., 2018; Johnson et al., 2021; Schmidt et al., 2022), i.e. notably earlier in the crystallization sequence than in the model of Elkins-Tanton et al. (2011), which could prolong the lifetime of the LMO.

To evaluate the consequences of different compositional models as well as the consequences of an overturn of the cumulate layer on the LMO solidification timescale, we propose a physically robust 1D model for the evolution of the Moon in its magma ocean stage. Our model is based on a simple anorthite/olivine-pyroxene eutectic phase diagram, which naturally results in a two-stage cooling process for the LMO. Before anorthite becomes a stable phase, the LMO cools down rapidly by radiative loss of heat at its surface (Solomatov, 1999). In the second stage, the simultaneous crystallization of anorthite and olivine-pyroxene cumulates leads to the formation of a buoyant anorthositic lid that considerably slows down the cooling of the magma ocean (fig. 2.1c). We solve for heat conservation in the different layers of the lunar body to follow the evolution of the crust, LMO and cumulates thicknesses and temperatures and evaluate the LMO final solidification time.

2.2 Compositional Model

2.2.1 Phase diagram and mass conservation

We consider a simple binary eutectic phase diagram with two components: anorthite on the one hand and olivine-pyroxene on the other. The liquidus temperature $T_{\mathrm{Liq}}(t)$ is assumed to be linearly related to the mass fraction in anorthite component $C(t)$ of the liquid (fig. 2.2a):

$$T_{\mathrm{Liq}}(t) = T_{\mathrm{OL}} - mC(t), \tag{2.1}$$

where T_{OL} is the liquidus temperature for the olivine-pyroxene component and $m = \frac{T_{\mathrm{OL}} - T_{\mathrm{E}}}{C_{\mathrm{E}}}$ characterises the liquidus slope. T_{E} and C_{E} correspond respectively to the eutectic temperature and composition. As the LMO convects vigorously, it is well-mixed and we

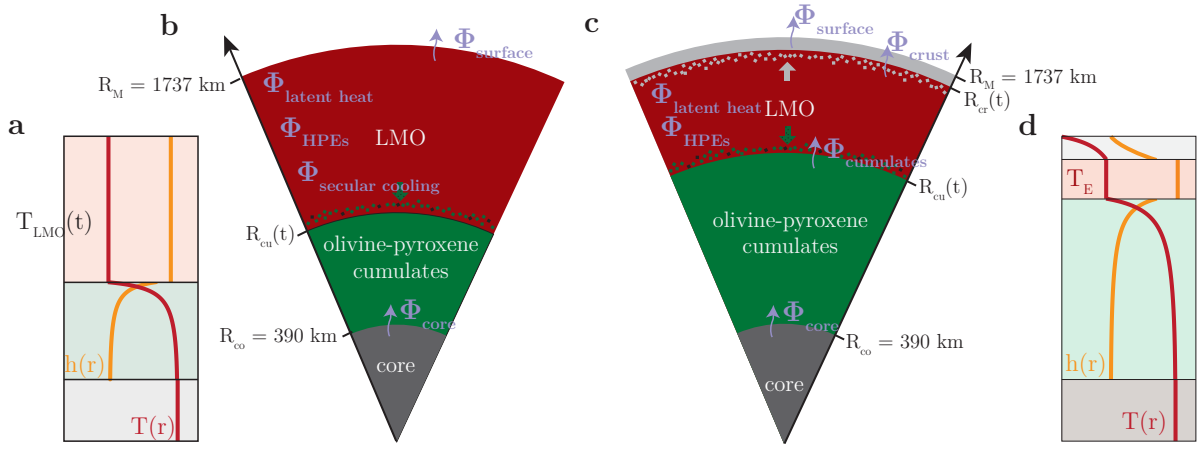

Figure 2.1: Schematic representation of the two stages of crystallization of the lunar magma ocean. Left two panels (**a**, **b**): first, "radiative", stage. Right two panels (**c**, **d**): second, "conductive", stage. **a** and **d**: Radial profiles of the temperature and heat-producing element concentration during the first and second stage respectively. **b** and **c**: Schematic of the structure of the Moon, the heat sources and fluxes in the first and second stage, respectively. The core is shown in dark gray, the olivine-pyroxene cumulates in green, the LMO in red, and the conductive crust in light gray.

assume that its temperature is uniform and equal to the liquidus temperature $T_{\mathrm{LMO}}(t) = T_{\mathrm{Liq}}(t)$. Considering the onset of crystallization as the initial time for our calculation, we note C_0 the initial LMO content in anorthite component and T^0_{LMO} the corresponding liquidus temperature. The pressure range inside the LMO is small because of the low lunar gravity, in particular during the second stage where the thickness of the LMO at the beginning of the second stage varies between 250 and 50 km (see section 2.4.2); we thus neglect the effect of pressure on the phase diagram, which would have a second order influence on our results.

Two stages of crystallization naturally appear from this simplified phase diagram (fig. 2.2a). In the first stage, as the magma ocean cools down along the liquidus, dense crystals of olivine and pyroxene settle at the bottom leading to a crystallization of the LMO from the bottom-up. The LMO becomes richer in anorthite component as it crystallizes until it reaches the eutectic composition C_{E} and temperature T_{E}. Conservation of the anorthite component provides a relation between the upper radius of the cumulate layer $R_{\mathrm{cu}}(t)$ and the LMO content in anorthite component $C(t)$:

$$\left(R_{\mathrm{M}}^3 - R_{\mathrm{co}}^3\right) C_0 = \left(R_{\mathrm{M}}^3 - R_{\mathrm{cu}}^3(t)\right) C(t), \tag{2.2}$$

where R_{M} is the radius of the Moon and R_{co} that of the core, and where, for simplicity, we consider a uniform average density for the different layers of the Moon. At the end of the

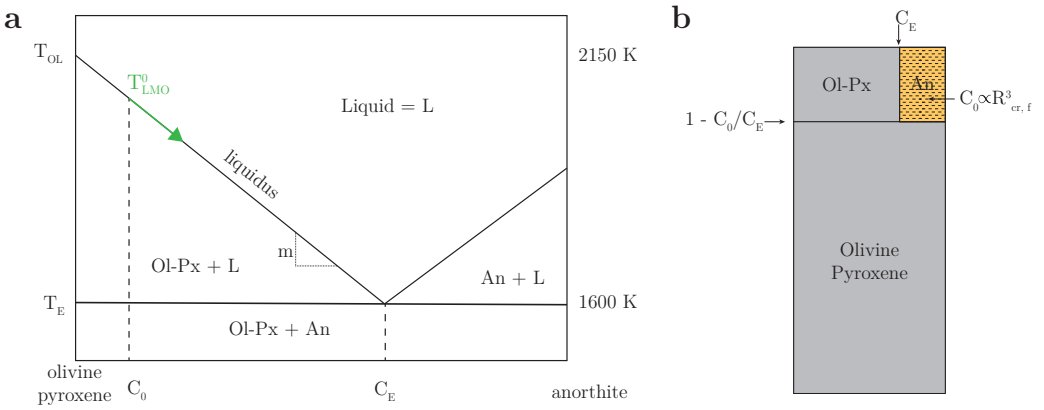

Figure 2.2: **a**- Simplified olivine-pyroxene/anorthite phase diagram with liquidus $T_{\mathrm{liq}}(C) = T_0 - mC(t)$ as a function of anorthite content of the liquid $C(t)$, where $T_{\mathrm{OL}} = 2150$ K is the liquidus temperature of the olivine-pyroxene component, $T_{\mathrm{E}} = 1600$ K is the eutectic temperature, $C_{\mathrm{E}} \in [0.2, 0.7]$ the eutectic composition and m represents the slope of liquidus. The initial conditions are $C_0 \in [0.05, 0.1]$ and the corresponding initial temperature of the LMO T^0_{LMO}, adapted from O'Driscoll et al., 2010. **b**- Simplified solidifying mantle mineral assemblage adapted from Elkins-Tanton et al. (2011).

first stage $C(t) = C_{\mathrm{E}}$ and the ratio $(C_{\mathrm{E}} - C_0)/C_{\mathrm{E}}$ thus corresponds to the total percentage of LMO crystallized at that time. Equations (2.1) and (2.2) can be used to obtain an analytical expression for the temperature variation in the cumulates as a function of the radial coordinate, assuming that diffusion is negligible because this first stage is short. During stage 1, the temperature profile in the cumulates is thus considered frozen and depends on the radius as the temperature at the cumulates-LMO boundary evolves along the liquidus (fig. 2.2):

$$T_{\mathrm{cu}}(r) = T_{\mathrm{OL}} - mC_0 \frac{R_{\mathrm{M}}^3 - R_{\mathrm{co}}^3}{R_{\mathrm{M}}^3 - r^3} \quad \text{for} \quad R_{\mathrm{co}} \leq r \leq R_{\mathrm{cu}}. \tag{2.3}$$

As the LMO crystallizes, the cumulate temperature profile becomes super-isentropic and thus prone to instability and overturn.

When the eutectic composition is reached in the LMO, anorthite starts to crystallize and olivine-pyroxene crystals continue to form in eutectic proportions. This constitutes the second stage of the thermal evolution. Light anorthite crystals then form a floating crust, while the LMO remains at the eutectic temperature T_{E}. Conservation of the anorthite component gives the final radius of the crust $R_{\mathrm{cr,f}}$:

$$\left(R_{\mathrm{M}}^3 - R_{\mathrm{cr,f}}^3\right) = \left(R_{\mathrm{M}}^3 - R_{\mathrm{co}}^3\right) C_0, \tag{2.4}$$

where we assume that all available anorthite floats to form a pure anorthositic crust. This buoyant and conductive lid then insulates the LMO, which significantly slows down its

rate of crystallization.

2.2.2 Parameters of the phase diagram

The parameter C_0 represents the available amount of anorthite. As we assume all available anorthite reaches the crust, C_0 controls the final thickness of the crust. This parameter depends on the exact composition of the bulk silicate Moon, its water content in particular, as water tends to delay and diminish the appearance of anorthite. To estimate a range for C_0, we refer to the various phase diagrams published in the literature (Snyder et al., 1992; Elkins-Tanton et al., 2011; Lin et al., 2017; Charlier et al., 2018; Rapp et al., 2018; Johnson et al., 2021; Schmidt et al., 2022); these studies suggest the overall range $C_0 \in [0.05, 0.1]$. The larger C_0, the thicker the anorthositic crust, the slower the heat conduction through the lid and the longer it takes to solidify the LMO. Assuming a global magma ocean, a water concentration of 1600 ppm in the LMO, corresponding to a value of $C_0 = 0.075$, may be necessary to explain the reduced crustal thickness of the Moon, as constrained from gravity and topography data (Wieczorek et al., 2013; Lin et al., 2017). This appears significantly larger than available estimates based on the water content measured directly in lunar rocks (Saal et al., 2008; Hauri et al., 2011; Hauri et al., 2015). Alternatively, a fraction of anorthite crystals may have not reached the lunar crust and remained trapped in the cumulates ; the parameter C_0 then represents the effective concentration of anorthite forming the lunar primary crust. The second key parameter of the phase diagram is C_{E} which represents the percentage of anorthite component crystallizing during the second stage. As C_{E} decreases, more olivine and pyroxene crystallize during the second stage and more latent heat must be evacuated through the floating crust. While C_{E} varies from ~ 0.3 to 0.5 among the different proposed compositional models (table 2.1), we explore the wider range $[0.2 - 0.7]$ based on the phase diagram of O'Driscoll et al. (2010).

Table 2.1: Values of C_0, C_{E}, percentage of LMO crystallized at the end of the first stage, initial LMO depth and final crustal thickness for different studies.

study	C_0	C_{E}	% crystallization	initial LMO depth [km]	crustal thickness [km]
Snyder et al. (1992)	0.088	0.4	78	400	28
Elkins-Tanton et al. (2011)	0.089	0.43	80	1000	49
Lin et al. (2017) (no water)	0.1	0.31	68	700	47
Lin et al. (2017) ($\sim$ 3000 ppm)	0.06	0.2	78	700	27
Charlier et al. (2018)	0.1	0.5	78	600	43
Rapp et al. (2018)	0.1	0.37	74	1347	60
Johnson et al. (2021)	0.084-0.92	0.27-0.36	70-75	1347	50-55
Schmidt et al. (2022)	0.14	0.3-0.5	72	600-1150	60-82

2.2.3 Heat Producing Elements (HPEs)

The decay of radioactive Heat Producing Elements (HPEs) contributes to a non-negligible source of heat during the magma ocean evolution and must be considered. Uranium (^{235}U and ^{238}U), Thorium (^{232}Th), and Potassium (^{40}K) are the main HPEs in the LMO. These highly incompatible elements tend to remain in the liquid phase as their solid/liquid partition coefficients are low (Sun et al., 2017). For simplicity, we consider all of these elements as a single one with a given radiogenic decay constant λ and distribution coefficient D between the liquid phase l and the crystallized layer s:

$$D = \frac{[HPE]_\mathrm{s}}{[HPE]_\mathrm{l}}. \tag{2.5}$$

HPEs are assumed to be homogeneously distributed in the LMO, but not in the solid layers, where their distribution varies radially and is calculated based on eq. (2.5) and on the rate of crystallization (see section 2.3.2). We track the radial distribution of the heat production from HPEs $h_i(t)$ during magma ocean crystallization, in the two solid layers i, where index i stands for crust (cr) or solid cumulates (cu).

During the first stage, as the cumulates grow with time, the total content of the LMO in HPEs decreases. Morison et al. (2019) and Boukaré et al. (2018) give an analytical solution for the radial distribution of the heat production from HPEs as a function of the radius of the cumulates, which can be converted in a function of the radial position in the cumulate r:

$$h_\mathrm{cu}(r) = h_0 \left(\frac{R_\mathrm{M}^3 - R_\mathrm{co}^3}{r^3 - R_\mathrm{co}^3} \right)^{1-D} \quad \text{for} \quad R_\mathrm{co} \leq r \leq R_\mathrm{cu}, \tag{2.6}$$

with h_0 the heat production rate per unit volume of the initial LMO. This expression neglects radioactive decay during the first, very rapid, stage. The actual heat production as a function of time in the second stage is obtained by taking into account radioactive decay as $he^{-\lambda t}$, with λ an effective mean radioactive decay constant. We call h_0 and h_cu heat production coefficients for the initial magma ocean and the cumulates, which are the products of the concentration in HPEs by their heat production rates.

During the second stage, the concentration in HPEs increases in the LMO as the two solid layers grow. Conservation of HPEs gives the variation of the heat production coefficient in the LMO induced by LMO solidification:

$$\frac{\mathrm{d}h_\mathrm{LMO}}{h_\mathrm{LMO}} = (1 - D)\frac{\mathrm{d}V_\mathrm{cryst}}{V_\mathrm{LMO}}, \tag{2.7}$$

where V_LMO is the LMO volume and $-\mathrm{d}V_\mathrm{cryst}$ its volume variation. We follow the evolution in radiogenic heat production in the LMO from eq. (2.7), and compute that in the crust

and cumulates from the partition coefficient (see section 2.7).

2.3 Thermal model

2.3.1 Stage 1

Surface temperature

The LMO forms a spherical shell of outer radius R_{M} and inner radius $R_{\mathrm{cu}}(t)$, which increases with time as the LMO cools down and solidifies. During the first stage, the heat flux lost by radiation at the surface is balanced by the flux supplied by convection in the LMO. We parameterize the convective heat flux following the boundary layer theory which assumes that convection near one boundary is independent of processes near the other boundary and which provides a simple relationship between the Nusselt number Nu and the Rayleigh number Ra:

$$Nu = \gamma Ra^{\beta}, \tag{2.8}$$

where Nu is the ratio between the convective heat flux and the characteristic conductive flux in the LMO, γ the scaling prefactor and, $\beta = 1/3$ is the exponent given by the thermal boundary layer theory at the limit of weakly rotating convection (Gastine et al., 2016). The Rayleigh number Ra characterises the strength of convection and is defined as:

$$Ra = \frac{\alpha \rho g \left(T_{\mathrm{LMO}} - T_{\mathrm{s}}\right) d^3}{\kappa \mu} \tag{2.9}$$

where α is the thermal expansion coefficient, ρ the LMO density, T_s the surface temperature, $d = R_{\mathrm{M}} - R_{\mathrm{cu}}$ the LMO thickness, κ the thermal diffusivity, and μ the LMO viscosity, $\alpha, \rho, \kappa, \mu$ being assumed constant. As T_{LMO} and d decrease with time, the Rayleigh number is time-dependent. From eqs. (2.8) and (2.9), the surface equilibrium between the radiative and convective heat fluxes is expressed as:

$$\epsilon \sigma \left(T_{\mathrm{s}}^4 - T_{\infty}^4\right) = k \frac{T_{\mathrm{LMO}} - T_s}{d} \gamma Ra^{\beta}, \tag{2.10}$$

where ϵ is the emissivity, σ the Stephan-Boltzman constant, k the thermal conductivity. T_∞ is the equilibrium temperature, derived from the equality between the solar flux absorbed by the Moon and the radiative heat flux it emits:

$$T_\infty = (1 - A)^{1/4} T_{\odot} \sqrt{\frac{R_{\odot}}{2D_{\odot}}}, \tag{2.11}$$

Table 2.2: List of the parameters and variables of the model.

Symbol	Description	Value	References
Parameters			
R_{M}	Radius of the Moon	1737 km	
R_{co}	Radius of the core	390 km	
T_{OL}	Liquidus temperature for the ol-px component	2150 K	O'Driscoll et al. (2010)
T_{E}	Eutectic temperature	1600 K	O'Driscoll et al. (2010)
m	Liquidus slope	$m = \frac{(T_{\mathrm{OL}} - T_{\mathrm{E}})}{C_{\mathrm{E}}}$	
h_0	Initial heat production	25 pW kg^{-1}	Taylor (1982)
	Initial uranium abundance	33 ppb	Taylor (1982)
	Initial thorium abundance	125 ppb	Taylor (1982)
	Initial potasium abundance	400 ppb	Taylor (1982)
λ	Effective radiogenic decay constant	5.8×10^{-10} Myr^{-1}	
D	Solid/liquid partition coefficient of HPEs	10^{-3}	Sun et al. (2017)
g	Gravity acceleration	1.62 m s^{-2}	
ρ	Density	3.3×10^3 kg m^{-3}	
c_{p}	Heat capacity	1×10^3 J kg^{-1} K^{-1}	
L	Latent heat	5×10^5 J kg^{-1}	Weill et al. (1980)
σ	Stefan-Boltzman constant	5.67×10^{-8} J K^{-1}	
ε	Emissivity	1	
A	Albedo	0.12	
$T_{\odot}$	Sun surface temperature	5780 K	
$R_{\odot}$	Sun radius	700×10^3 km	
$D_{\odot}$	Moon-Sun distance	1495×10^5 km	
T_{∞}	Black body equilibrium temperature (eq. (2.11))	270 K	
α	Thermal expansion coefficient	10^{-5} K^{-1}	Maurice et al. (2020)
μ_{LMO}	Viscosity	1 kg m^{-1} s^{-1}	
k	Thermal conductivity of the LMO	4 W m^{-1} K^{-1}	
k_{cu}	Thermal conductivity of cumulates	4 W m^{-1} K^{-1}	Maurice et al. (2020)
β	Thermal boundary layer coefficient	1/3	Gastine et al. (2016)
γ	Scaling prefactor	0.07	Gastine et al. (2016)
$c_{\mathrm{p,\,co}}$	Heat capacity of the core	840 J kg^{-1} K^{-1}	Maurice et al. (2020)
ρ_{co}	Density of the core	7.2×10^3 kg m^{-3}	
Explored parameters			
C_0	Initial content in anorthite component	$\in [0.05, 0.1]$	
C_{E}	Eutectic composition	$\in [0.2, 0.7]$	
κ_{cr}	Thermal diffusivity of the crust	$\in [5.5, 8.2]\ 10^{-7}$ m^2 s^{-1}	Roy et al. (2021)
k_{cr}	Thermal conductivity of the crust	$\in [1.8, 2.7]$ W m^{-1} K^{-1}	Branlund et al. (2012) Roy et al. (2021)
Q	Energy released at the beginning of the overturn	$\in [3 \times 10^{14}, 2 \times 10^{12}]$ W	
τ_{ov}	Overturn time	$\in [1.8, 180]$ Myr	
Variables stage 1			
$T_{\mathrm{LMO}}(t)$	LMO temperature	eq. (2.1)	
$R_{\mathrm{cu}}(t)$	Radius at the top of the cumulates	from eq. (2.13)	
$T_{\mathrm{s}}(t)$	Surface temperature	eq. (2.10)	
$h_{\mathrm{cu}}(t)$	HPEs concentration in the cumulates	eq. (2.15)	
Variables stage 2			
$R_{\mathrm{cu}}(t)$	Radius at the top of the cumulates	eq. (2.24)	
$R_{\mathrm{cr}}(t)$	Radius at the base of the crust	eq. (2.23)	
$T_{\mathrm{cr}}(t, r)$	Temperature in the crust	eq. (2.15)	
$T_{\mathrm{cu}}(t, r)$	Temperature in the cumulates	eq. (2.15)	
$h_{\mathrm{cr}}(r)$	HPEs production in the crust	eq. (2.7) and 2.7	
$h_{\mathrm{cu}}(r)$	HPEs production in the cumulates	eq. (2.7) and 2.7	

where $T_{\odot}$ is the surface temperature of the Sun, $R_{\odot}$ the radius of the Sun, $D_{\odot}$ the Moon-Sun distance, and A the surface albedo of the Moon.

Heat budget in the magma ocean

During the first stage, only olivine and pyroxene cumulates crystallize (see section 2.2). We neglect pressure effects and assume a homogeneous temperature for the LMO. As the first stage is very rapid ($\sim$ 300 yr, which is verified a posteriori), we neglect heat conduction in the cumulates.

In the LMO, the heat lost by radiation into space at the surface is balanced by the sum of the latent heat released by crystallization of olivine-pyroxene cumulates, the heat produced by radiogenic decay and secular cooling of the LMO, that is written as in Lister et al. (1995) ; we neglect the heat flux associated to compositional changes in the LMO:

$$\begin{aligned}\epsilon\sigma 4\pi R_{\mathrm{M}}^2\left(T_{\mathrm{s}}(t)^4 - T_{\infty}^4\right) &= \rho L\frac{\mathrm{d}V_{\mathrm{cryst}}}{\mathrm{d}t} + h_{\mathrm{LMO}}(t)V_{\mathrm{LMO}}(t)\\ &\quad - \rho c_{\mathrm{p}}\left(\int_{R_{\mathrm{cu}}(t)}^{R_{\mathrm{M}}}\frac{\partial T_{\mathrm{LMO}}}{\partial t}\,4\pi r^2 dr\right),\end{aligned} \tag{2.12}$$

where L is the latent heat of crystallization, $h_{\mathrm{LMO}}(t)$ the LMO radioactive heat production per unit volume, c_{p} the heat capacity. As the LMO temperature is uniform, the third term representing secular cooling on the right hand side of eq. (2.12) can be simplified using the expression of T_{LMO} from eq. (2.3). Given eq. (2.3) and eq. (2.12), the heat budget can be simplified as:

$$\begin{aligned}4\pi R_{\mathrm{M}}^2\sigma\epsilon(T_s(t)^4 - T_{\infty}^4) =& 4\pi R_{\mathrm{cu}}^2\frac{\mathrm{d}R_{\mathrm{cu}}}{\mathrm{d}t}\left[\rho L + (T_{\mathrm{OL}} - T_{\mathrm{LMO}}(t))\,\rho c_{\mathrm{p}}\right]\\ &+ h_{\mathrm{LMO}}(t)\frac{4}{3}\pi\left(R_{\mathrm{M}}^3 - R_{\mathrm{cu}}^3(t)\right).\end{aligned} \tag{2.13}$$

Equations (2.10) and (2.13) are solved numerically to calculate the temporal evolution of the cumulates radius R_{cu} and of the surface temperature T_{s} during the first stage. At the end of the first stage, the amount of heat stored in the cumulates that can be released during an overturn episode is calculated from:

$$\begin{aligned}E_{\mathrm{cu}} &= \rho c_{\mathrm{p}}\int_{R_{\mathrm{co}}}^{R_{\mathrm{cu}}} 4\pi(T_{\mathrm{cu}}(r) - T_{\mathrm{E}})r^2 dr\\ &= \rho c_{\mathrm{p}}\frac{4}{3}\pi\left[(T_{\mathrm{OL}} - T_{\mathrm{E}})(R_{\mathrm{cu}}^3 - R_{\mathrm{co}}^3) - mC_0(R_{\mathrm{M}}^3 - R_{\mathrm{co}}^3)\ln\left(\frac{R_{\mathrm{M}}^3 - R_{\mathrm{co}}^3}{R_{\mathrm{M}}^3 - R_{\mathrm{cu}}^3}\right)\right],\end{aligned} \tag{2.14}$$

where we use eq. (2.3).

2.3.2 Stage 2

Heat conduction in the crust and cumulates

In the second stage, cooling of the LMO occurs by diffusion of heat through the floating anorthositic lid. Diffusion of heat in the cumulates is not negligible anymore and we solve for the 1D time-dependent conduction equation in both the crust and cumulates to obtain their temperature profiles as a function of time:

$$\frac{\partial T_{\rm i}(t,r)}{\partial t} = \frac{\kappa_{\rm i}}{r^2}\frac{\partial}{\partial r}\left(r^2\frac{\partial T_{\rm i}(t,r)}{\partial r}\right) + \frac{h_{\rm i}(t,r)e^{-\lambda t}}{\rho c_{\rm p}}, \tag{2.15}$$

where index i stands for crust or solid cumulates, $\kappa_{\rm i} = \frac{k_{\rm i}}{\rho c_{\rm p}}$ is the thermal diffusivity and $h_{\rm i}(r)$ the heat production coefficient per unit volume, computed from the partition coefficient D, eq. (2.5) (see section 2.2.3).

For the anorthositic crust, the boundary conditions are $T|_{r=R_{\rm cr}} = T_{\rm E}$ and $T|_{r=R_{\rm M}} = T_s$ (see section 2.2), where T_s is given by the balance between the radiative and conductive fluxes at the surface:

$$\epsilon\sigma(T_{\rm s}^4 - T_\infty^4) = -\,k_{\rm cr}\left.\frac{\partial T_{\rm cr}(t,r)}{\partial r}\right|_{r=R_{\rm M}}. \tag{2.16}$$

For the solid cumulates, we use: $T|_{r=R_{\rm co}} = T_{\rm co}$ and $T|_{r=R_{\rm cu}} = T_{\rm E}$ (see section 2.2). The diffusion equation is solved using a fully implicit finite volume scheme on a regular grid with a front-fixing method to deal with the growth of the solid layers with time (section 2.7).

Core

The core is considered as a sphere of uniform temperature $T_{\rm co}$. Heat conservation in the core gives the evolution of $T_{\rm co}$:

$$\rho_{\rm co}c_{\rm p,co}\frac{4}{3}\pi R_{\rm co}^3\frac{{\rm d}T_{\rm co}}{{\rm d}t} = -4\pi R_{\rm co}^2 q_{\rm co}, \tag{2.17}$$

where $\rho_{\rm co}$ is the core density and $c_{\rm p,co}$ the heat capacity and the heat flux out of the core $q_{\rm co}$ is deduced from the temperature gradient at the base of the cumulates:

$$q_{\rm co} = -\,k_{\rm cu}\left.\frac{\partial T_{\rm cu}}{\partial r}\right|_{r=R_{\rm co}}. \tag{2.18}$$

Equation (2.17) is used to calculate the thermal evolution of the core, which gives the boundary condition at the base of the cumulates eq. (2.18).

Conservation of heat in the LMO in stage 2

In stage 2, the magma ocean is a spherical shell of inner radius $R_{\rm cu}(t)$ and outer radius $R_{\rm cr}(t)$. Heat conservation in the LMO requires that the heat flux evacuated by conduction through the anorthositic lid balances the sum of the heat fluxes coming from the diffusion of heat in the cumulates, latent heat released by crystallization in the LMO and radiogenic decay of HPEs (fig. 2.1c):

$$S_{\rm cr} q_{\rm cr} = S_{\rm cu} q_{\rm cu} + \rho L \frac{{\rm d}V_{\rm cryst}}{{\rm d}t} + h_{\rm LMO} e^{-\lambda t} V_{\rm LMO}. \tag{2.19}$$

$S_{\rm cr} = 4\pi R_{\rm cr}^2(t)$ is the surface of the LMO-crust interface, $S_{\rm cu} = 4\pi R_{\rm cu}^2(t)$ is the surface between the LMO and the cumulate layer, $q_{\rm cr}$ and $q_{\rm cu}$ are respectively the heat flux conducted away by the crust and the heat flux brought by conduction in the cumulates. These conductive fluxes are given by:

$$q_{\rm i} = - k_{\rm i} \left. \frac{\partial T_{\rm i}}{\partial r} \right|_{r=R_{\rm i,\ i=cr,\ cu}}, \tag{2.20}$$

and are computed at each time step from the temperature profiles in the crust and cumulates (section 2.3.2). We also consider the case of a thermal overturn of the cumulates and then modify the heat flux from the cumulates $q_{\rm bot}$ as described in section 2.3.3. $V_{\rm LMO}$ and $h_{\rm LMO}$ depend on time as the LMO crystallizes and concentration of HPEs increases (section 2.2.3). $\frac{{\rm d}V_{\rm cryst}}{{\rm d}t}$ is the total rate of crystallization, which is the sum of the rate of crystallization of anorthite and olivine-pyroxene components. Since anorthite and olivine-pyroxene are in eutectic proportion, we have:

$$\frac{{\rm d}V_{\rm An}}{{\rm d}t} = C_{\rm E} \frac{{\rm d}V_{\rm cryst}}{{\rm d}t} = -4\pi R_{\rm cr}^2 \frac{{\rm d}R_{\rm cr}}{{\rm d}t}, \tag{2.21}$$

$$\frac{{\rm d}V_{\rm Ol\text{-}Px}}{{\rm d}t} = (1 - C_{\rm E}) \frac{{\rm d}V_{\rm cryst}}{{\rm d}t} = 4\pi R_{\rm cu}^2 \frac{{\rm d}R_{\rm cu}}{{\rm d}t}. \tag{2.22}$$

Using eq. (2.21) into eq. (2.19), we obtain an equation for the evolution of $R_{\rm cr}$ as a function of time:

$$-\frac{{\rm d}R_{\rm cr}}{{\rm d}t} = \frac{C_{\rm E}}{\rho L} \left(- k_{\rm cr} \left. \frac{\partial T_{\rm cr}}{\partial r} \right|_{r=R_{\rm cr}} - \frac{R_{\rm cr}^3 - R_{\rm cu}^3}{3R_{\rm cr}^2} e^{-\lambda t} h_{\rm LMO} + k_{\rm cu} \frac{R_{\rm cu}^2}{R_{\rm cr}^2} \left. \frac{\partial T_{\rm cu}}{\partial r} \right|_{r=R_{\rm cu}} \right). \tag{2.23}$$

In case of an overturn, the last term on the right-hand-side is modified according to section 2.3.3. The evolution of $R_{\rm cu}$ is then derived from eqs. (2.21) and (2.22):

$$\frac{{\rm d}R_{\rm cu}}{{\rm d}t} = - \left(\frac{1 - C_{\rm E}}{C_{\rm E}} \right) \frac{R_{\rm cr}^2}{R_{\rm cu}^2} \frac{{\rm d}R_{\rm cr}}{{\rm d}t}. \tag{2.24}$$

2.3.3 Case of cumulates overturn during the stage 2

At the end of the first stage, the temperature profile in the cumulates is super-isentropic and can induce a thermal overturn. The timescale for the onset of cumulates overturn may be short, as short as several thousand years (Elkins-Tanton et al., 2011; Boukaré et al., 2018; Morison et al., 2019), which is however longer than the first stage of LMO solidification (see section 2.3.1). Consequently, heat released by the overturn can be considered in the second stage only and heat conservation in the LMO eq. (2.19) then writes:

$$S_{\text{top}} q_{\text{top}} = \Phi_{\text{ov}}(t) + \rho L \frac{\mathrm{d}V_{\text{cryst}}}{\mathrm{d}t} + h_{\text{LMO}} e^{-\lambda t} V_{\text{LMO}}, \tag{2.25}$$

where Φ_{ov} represents the rate of heat released at the surface of cumulates during overturn and varies with time as the overturn progresses. As the onset time of overturn is likely short compared to the timescale of the second stage of LMO solidification (thousands of years compared to millions of years), and to explore the effect of overturn decay time, we parameterise this rate of heat released with an exponential decay function:

$$\Phi_{\text{ov}}(t) = Q e^{-\frac{t}{\tau_{\text{ov}}}}, \tag{2.26}$$

where Q is the heat flux from the overturn at the start of stage 2, and τ_{ov} its characteristic decay time. Assuming that the additional heat stored in the cumulates is fully released during the overturn, we have:

$$E_{\text{cu}} = \int_0^\infty \Phi_{\text{ov}}(t) dt = Q \tau_{\text{ov}}. \tag{2.27}$$

The total overturn energy available, E_{cu}, is determined by the choice of phase diagram through eq. (2.14). The values of Q and τ_{ov} can then vary with the constraints that their product must equal E_{cu}, eq. (2.27).

2.4 Results

2.4.1 Reference case

We first show the thermal evolution of a reference case, considering an initial global magma ocean, a final crustal thickness of 44 km and 80 % of crystallization at the end of the first stage (i.e.: $C_0 = 0.075$, $C_{\text{E}} = 0.37$), no overturn in the cumulates and a low thermal conductivity for the crust, $k_{\text{cr}} = 2\,\text{W}\,\text{m}^{-1}\,\text{K}^{-1}$, corresponding to a thermal diffusivity of $\kappa_{\text{cr}} = 6.06 \times 10^{-7}\,\text{m}^2\,\text{s}^{-1}$ (Branlund et al., 2012; Roy et al., 2021).

Stage 1

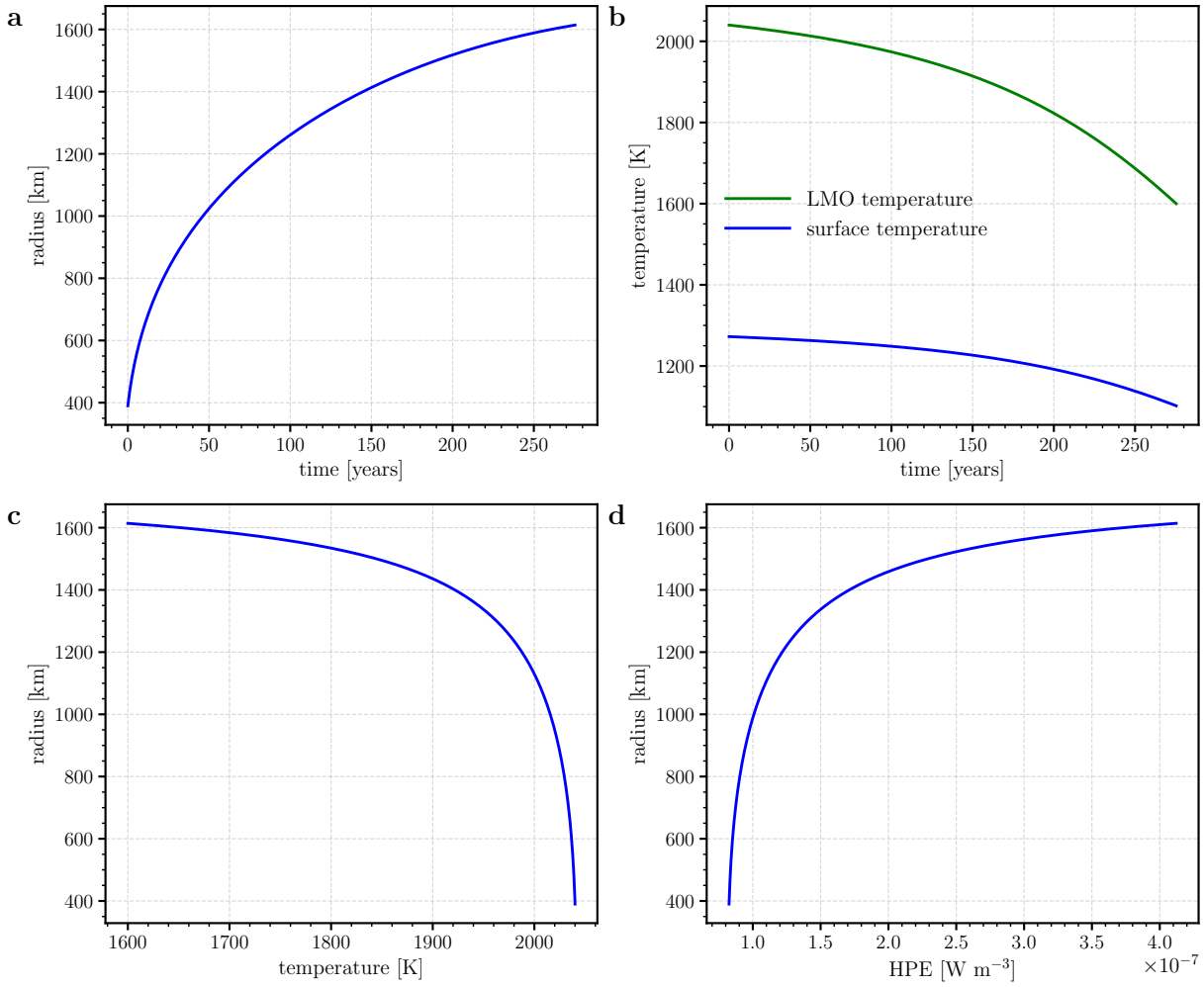

Figure 2.3: Temporal evolution of **a** the radius of the cumulates and **b** the surface temperature in blue and the LMO temperature in green. Radial evolution of **c** the temperature in the cumulates and **d** the heat production in the cumulates.

The first stage is very fast: in 275 yr, 80% of the LMO is crystallized and the eutectic temperature is reached (Figure 2.3a). This timescale is much shorter than the diffusion timescale in the cumulates, it is also shorter than the onset time for cumulates overturn (Morison et al., 2019; Hess et al., 1995; Elkins-Tanton et al., 2011); this justifies that we neglect the heat flux from the cumulates for this stage. The temperature in the cumulate layer decreases with radius following the decrease of the LMO temperature with time, which is associated to its gradual enrichment in anorthite (fig. 2.3 b and c). As the LMO solidifies, its concentration in HPEs increases and therefore the concentration in the cumulates increases with radius (fig. 2.3d).

Stage 2

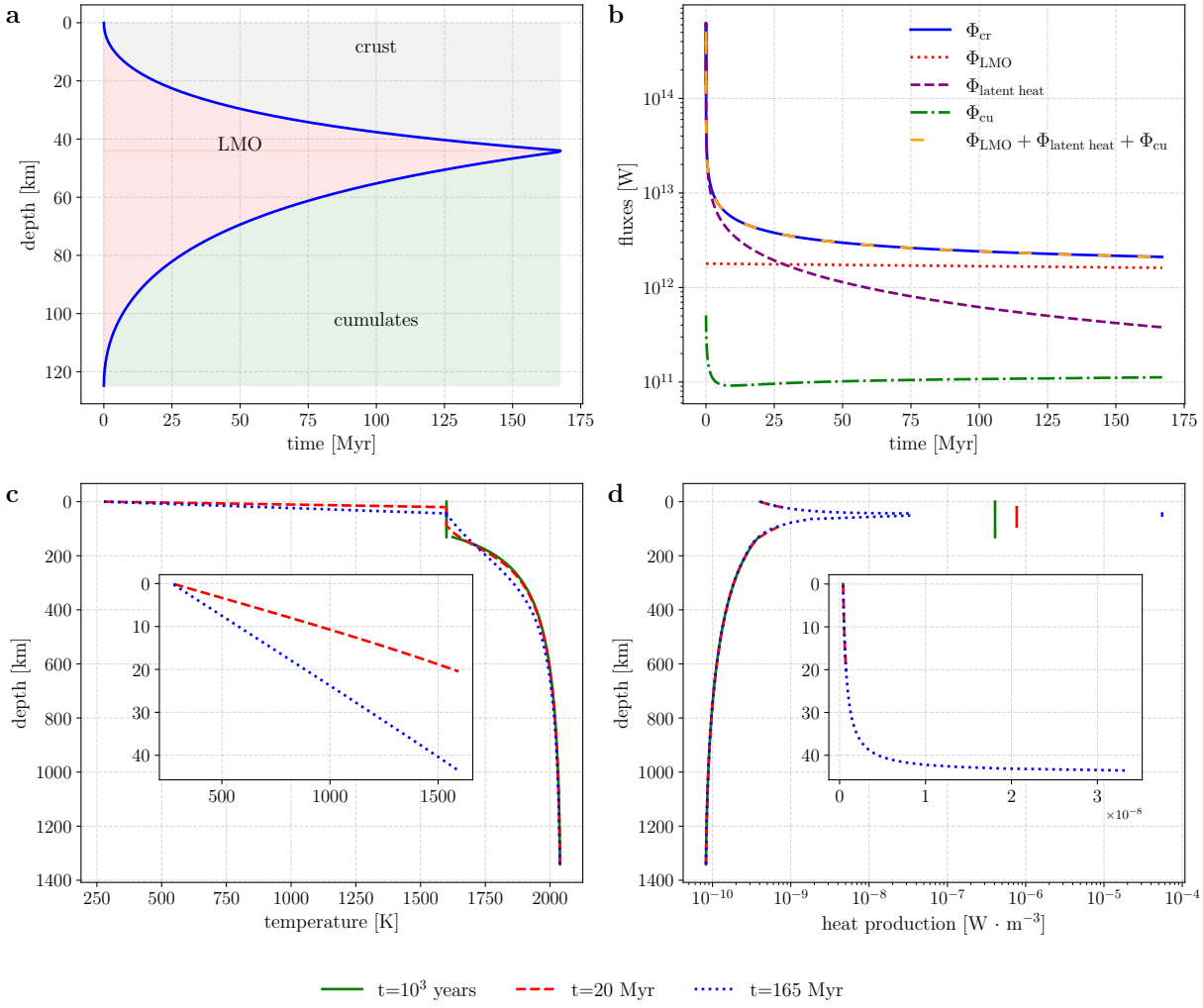

Figure 2.4: Temporal evolution of **a** the crustal radius and cumulates radius, **b** the various contributions to the LMO heat budget: conductive flux at the base of the crust Φ_{cr} (blue solid line), heat flux from radioactive decay of HPEs in the LMO Φ_{LMO} (red dotted line), latent heat flux $\Phi_{\text{latent heat}}$ (dashed purple line), conductive flux from the cumulates Φ_{cu} (dash-dotted green line), sum of Φ_{LMO}, $\Phi_{\text{latent heat}}$ and Φ_{cu} (dash-dotted green line). **c** Full temperature profile at times $t = 275\,\text{yr}$ (green line), $t = 20\,\text{Myr}$ (in red dashed line) and at $t = 165\,\text{Myr}$ (blue dotted line). Temperature profiles in the crust are shown in the inset. **d** Heat production distribution as a function of radius at the same times as in panel **c** The inset shows the radial heat production distribution in the crust.

The total solidification time at the end of the second stage is 166 Myr in the reference case (fig. 2.4a). Owing to the presence of the conductive lid, the heat loss from the LMO is significantly reduced compared to stage 1 (fig. 2.4a and b). The temperature profile within the crust gradually approaches a linear conduction profile (inset in fig. 2.4c), typical of steady-state conduction in a thin shell with negligible heat production. In the cumulates,

the larger heat production in the solid at the end of LMO crystallization tends to curve the temperature profile with time (fig. 2.4c). As the crust thickness increases, its basal heat flux decreases and the growth rate of both the crust and cumulates decreases over time, which implies a decrease of the latent heat release (purple curve on fig. 2.4b). The heat flux due to radioactive heat production in the LMO remains quasi-constant throughout the solidification process and, although latent heat released by crystallization first dominates the LMO heat budget, radioactive heat production prevails after 25 Myr (red dashed line fig. 2.4b). Thus, radioactive heat production must be taken into account to properly compute the solidification time of the LMO.

2.4.2 Exploration of the model parameters

Having presented a typical evolution for the reference case, we now explore the effects of varying the main control parameters: initial composition C_0, or equivalently final crust thickness, eutectic composition C_E, and thermal conductivity k_cr (or equivalently thermal diffusivity κ_{cr}), within the range given in table 2.2.

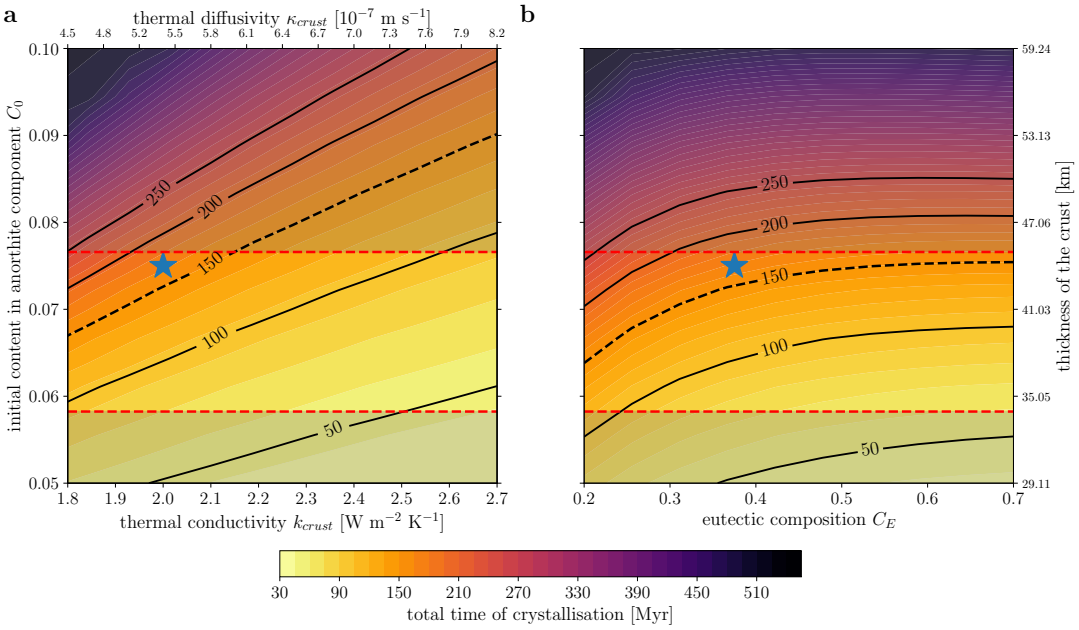

Figure 2.5: **a** LMO solidification time as a function of initial anorthite content C_0 and crust thermal conductivity k_cr for a fixed eutectic composition corresponding to $C_\mathrm{E} = 0.37$ of crystallization at the end of the first stage. **b** Total crystallization time as a function of initial anorthite content C_0 and eutectic composition C_E for a fixed value of $k_\mathrm{cr} = 2$ W m^{-1} K^{-1}. The bright area between the red dashed lines is the acceptable range of crustal thickness as estimated from the inversion of topography and gravity data by Wieczorek et al. (2013). The dashed lines corresponds to the estimated values of the solidification time according to Fu et al. (2023). The blue star corresponds to our reference case.

As the LMO solidification time is controlled by the timescale for diffusion of heat through the crust, $\tau_{\text{diff}}^{\text{cr}} = (R_{\text{M}} - R_{\text{cr}})^2 \rho_{\text{cr}} c_{\text{p}} / k_{\text{cr}}$, it strongly depends on the crustal conductivity and final crustal thickness. As shown by Maurice et al. (2020) and Zhang et al. (2021b), the lower the conductivity k_{cr} and the diffusivity κ_{cr}, the more difficult it is to extract heat through the crust and the longer it takes for the LMO to crystallize (fig. 2.5a). The thermal conductivity of anorthosites does not appear to depend on temperature (Roy et al., 2021), we thus use a constant value. Thermal conductivity measurements on anorthosites vary between 1.5 and 2.5 $\text{W m}^{-1} \text{K}^{-1}$, while the thermal diffusivity range between 5×10^{-7} and 8×10^{-7} m^2 s^{-1} (Roy et al., 2021; Clauser et al., 1995). We thus vary k_{cr} between 1.8 and 2.7 $\text{W m}^{-1} \text{K}^{-1}$, which gives values for κ_{cr} between 5×10^{-7} and 8×10^{-7} m^2 s^{-1} given our chosen density and heat capacity value (see table 2.1). Increasing k_{cr} from 1.8 to 2.7 $\text{W m}^{-1} \text{K}^{-1}$ the solidification timescale decreases by 160 Myr (going from 250 Myr to 90 Myr) for a 45 km thick crust (fig. 2.5a). The LMO solidification time increases with the initial anorthite content C_0 (fig. 2.5a and b) because the larger C_0, the thicker the anorthositic crust, the slower the heat transfer through the crust is. For a crustal thickness increasing from 34 to 45 km, the range of crustal thicknesses compatible with the inversion of gravity and topography data (Wieczorek et al., 2013), the LMO crystallization time increases from 70 to 170 Myr using $k_{\text{cr}} = 2 \text{ W m}^{-1} \text{K}^{-1}$ and $C_{\text{E}} = 0.37$.

The LMO solidification time also increases as the anorthite eutectic composition C_{E} decreases: if C_{E} is smaller, more olivine and pyroxene crystallize during the second stage because the crust starts to form earlier for a given value of C_0 (i.e. a given final crustal thickness), and more latent heat must be extracted through the anorthositic lid. For instance, decreasing by 0.2 the value of C_{E} in our reference case, which corresponds to the estimated difference between the compositional models of Charlier et al. (2018) and Lin et al. (2017) (see table 2.1), makes the total solidification time increase from 160 Myr to 200 Myr for a final crustal thickness of 45 km (fig. 2.5b).

Overall, the solidification time can range between 44 Myr and 250 Myr.

2.4.3 Effect of an overturn

Here, we examine the effect of cumulates overturn considering the same parameters as in our reference case. The heat flux from the cumulates is then not diffusive but decreases exponentially with time (section 2.3.3). Using the phase diagram of our reference case, we estimate that the additional heat stored in the cumulates that can be released during overturn is of 1.8×10^{28} J, eq. (2.14). This is significantly larger than the total amount of latent heat released during the second stage, which is 0.7×10^{28} J, showing that, depending on its amplitude and decay rate, cumulate overturn may induce melting of the crust. Given our parametrisation, the initial heat flux Q increases as the characteristic decay time of

the overturn decreases following eq. (2.27). We explore decay times between 1.8 and 180 Myr. For a short-lived overturn such that $\tau_{ov} \lessapprox 5$ Myr, the solidification time of the LMO is reduced when accounting for an overturn compared to our reference case because the heat released by the overturn is quickly evacuated through the initially very thin crust, marked by a large temperature gradient and basal heat flux (fig. 2.6b). The growth rate of the crust remains negligible for the first million years and then follows the trend of the reference scenario (fig. 2.6a) once the overturn has died out. When the crust is thicker and more insulating, no conductive heat flux remains to be evacuated on the contrary to the reference case, which explains the shorter solidification time for a short-lived overturn. For decay times smaller than ∼1.8 Myr, the heat flux Q becomes too large to be evacuated through the initially thin crust and can melt it, possibly entirely if the overturn proceeds quickly enough. This would increase the heat flux at the LMO surface and accelerate even more its cooling. If, on the contrary, the decay time of the overturn exceeds 5 Myr, a significant fraction of the heat stored in the cumulates is then released when the crust becomes thick and insulating, and this can significantly prolong the LMO solidification time: for $\tau_{ov} = 100$ Myr, the LMO solidification timescale reaches 388 Myr (fig. 2.6).

2.5 Discussion

2.5.1 LMO solidification time

The LMO solidification time depends strongly on the crustal conductivity, initial anorthite content and eutectic composition. For a crustal thickness of 44 km, a percentage of crystallization of 80 % at the end of the first stage, as in Elkins-Tanton et al. (2011), and using $k = 2\,\mathrm{W\,m^{-1}\,K^{-1}}$, the LMO solidification time is 166 Myr. This is much larger than the timescale of $\sim$ 10 Myr estimated by Elkins-Tanton et al. (2011), who neglect heat production by radioactive decay, an important heat source in the LMO energy budget (fig. 2.4b), and assume an initial LMO depth of 1000 km and a larger thermal diffusivity of $10^{-6}\,\mathrm{m^2\,s^{-1}}$ corresponding to a crustal conductivity of $k_{cr} = 3.3\,\mathrm{W\,m^{-1}\,K^{-1}}$ in our model. Neglecting the heat flux from the cumulates, radioactive heat production and assuming a steady-state conduction in the crust, an analytical solution for the total solidification time τ_{sol} can be obtained (section 2.8):

$$\tau_{sol} = -\frac{\rho L}{R_M k_{cr} \Delta T} \frac{1}{C_E} \left[\frac{R_M R_{cr,\,f}^2}{2} - \frac{R_{cr,\,f}^3}{3} - \frac{R_M^3}{6} \right]. \tag{2.28}$$

Using $C_E = 0.37$, $R_{crust,final} = 1693$ km and $k_{cr} = 3.3\,\mathrm{W\,m^{-1}\,K}$, this solidification time is $\sim$ 30 Myr, which is still significantly larger than in Elkins-Tanton et al. (2011). Results

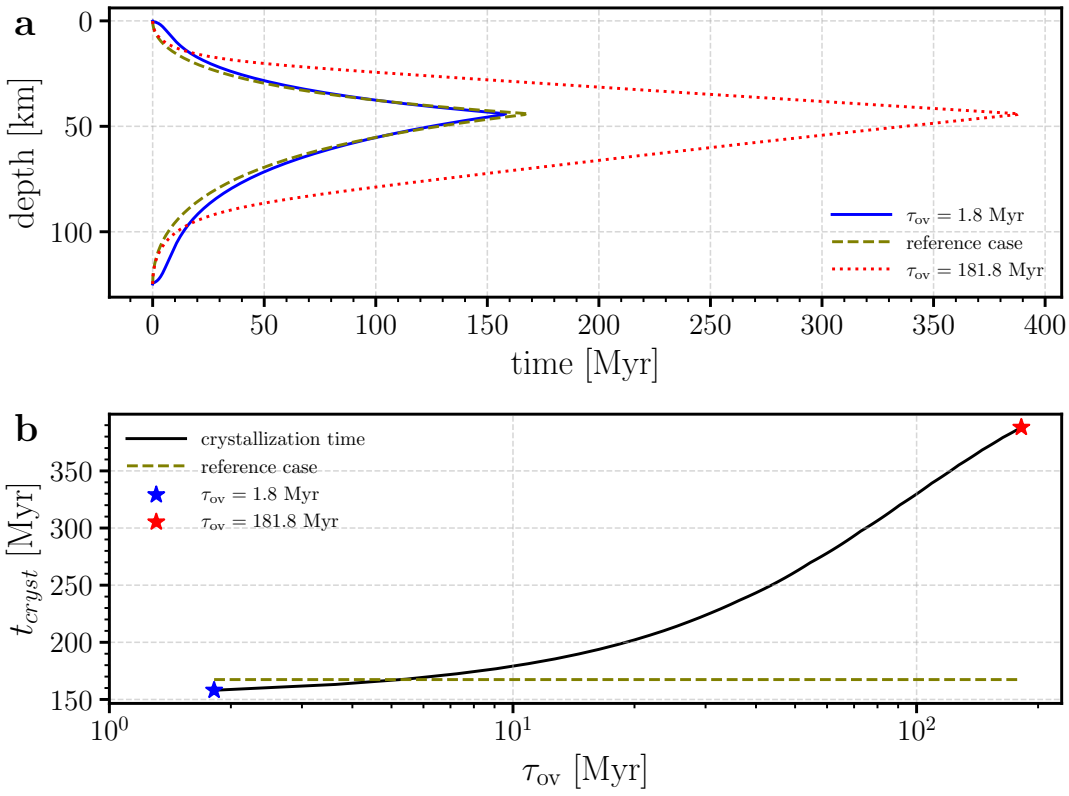

Figure 2.6: **a** Temporal evolution of the crustal radius and cumulates radius, in the reference case assuming a conductive heat flux from the cumulates fig. 2.4a (olive green dashed line), in the case of a short-lived overturn (blue line), and for a long-lived overturn (dotted red line). The parameters are the same as for the reference case, *i.e.*: $C_0 = 0.075$, $k_{cr} = 2\,\mathrm{W\,m^{-1}\,K^{-1}}$ and $C_E = 0.37$. **b** Crystallization time (black line) as a function of τ_{ov} the decay time of the overturn. The olive green dashed line corresponds to the LMO solidification time in the reference case and the blue and red stars correspond to the extremums of **a**.

for our reference case are very similar to that of Maurice et al. (2020), who use the more complex, i.e. pressure-dependent, version of the phase diagram of Elkins-Tanton et al. (2011): for a magma ocean extending down to the core and accounting only for heat conduction in the cumulates as assumed here, their solidification timescale is 165 Myr fig. S6 of Maurice et al., 2020, which is very close to our estimate. Small differences arise from the variation of the phase diagram with pressure, which corresponds to a variation of C_E during the second stage, as well as from a different distribution in heat producing elements, whose partition coefficient is not constant and depends on the crystallizing minerals in Maurice et al. (2020). The influence of the pressure-dependence of the phase diagram or of a varying HPEs partition coefficient during LMO solidification are thus clearly of second order given our current knowledge of the average lunar crust thickness, crust bulk conductivity and phase diagram (fig. 2.5). Our simplified, though physically

robust, approach, with a binary eutectic phase diagram, appears thus of appropriate complexity to estimate the LMO solidification timescale.

With a range of LMO solidification time between 45 and 250 Myr for crustal thicknesses between 34 and 45 km (fig. 2.5), the lifetime of the LMO appears increased compared to initial estimates by Elkins-Tanton et al. (2011). Our results show that the crustal conductivity value as well as the occurrence and timescale of cumulates overturn can significantly affect estimates of the LMO solidification time. The thermal conductivity of anorthosites is low compared to other crustal rocks (Clauser et al., 1995) which increases LMO insulation. Analyses of GRAIL gravity data additionally shows that the lunar crust is highly porous, with an average porosity of $\sim 12\%$ over a few tens of kilometers depth (Wieczorek et al., 2013). Accounting for such a large porosity would significantly decrease the crustal conductivity and prolong the LMO duration (Zhang et al., 2021b). However, the lunar megaregolith most likely formed after LMO solidification, concommittantly to large basins through impacts and ejectas (Li et al., 2023). Impacts large enough to deeply fracture the crust and forge a megaregolith may in fact create holes in a flotation crust, which would accelerate the cooling of the underlying LMO (Perera et al., 2018).

The LMO solidification time can be significantly extended if the overturn has a long duration (fig. 2.6). However, the impact of the overturn is highly sensitive to its lifetime, it may even reduce the LMO solidification time by ~ 10 Myr if its characteristic decay timescale is smaller than 5 Myr, because all the heat from the cumulates is then quickly evacuated through the thin floating crust. Furthermore, the decay timescale of the thermal overturn is not likely to be several orders of magnitude longer than its initiation timescale, which is likely to be less than 1 Myr (Morison et al., 2019; Boukaré et al., 2018).

Studies of LMO solidification often use an initial depth of 1000 km, based on a potential seismic discontinuity (Khan et al., 2000; Lognonné, 2005). Using our model and varying the initial LMO depth still leads to a solidification time larger than 50 Myr (fig. 2.7), using $k_{\mathrm{cr}} = 2\,\mathrm{W\,m^{-1}\,K^{-1}}$, as it mainly depends on the final crustal thickness. Our results thus suggest a long-lived LMO and show that this classical scenario, which explains a wide range of lunar crust characteristics, from the large feldpar enrichment of the lunar crust to the formation of the KREEP Province, can also explain the age range of anorthosites, in particular given dating uncertainties (Borg et al., 2023). By comparison, the model of Michaut et al. (2022), which propose that anorthosites form by extraction of melts in a stagnant lid from a slushy magma ocean could lead to even longer crustal formation timescales and account for the compositional heterogeneities of anorthosites, a characteristic that is more difficult to explain with the flotation scenario (Gross et al., 2014; Russell et al., 2014). More data on lunar rocks are thus needed to fully understand the lunar crust formation scenario.

2.5.2 Formation age of FAN 60025 and age of the Moon

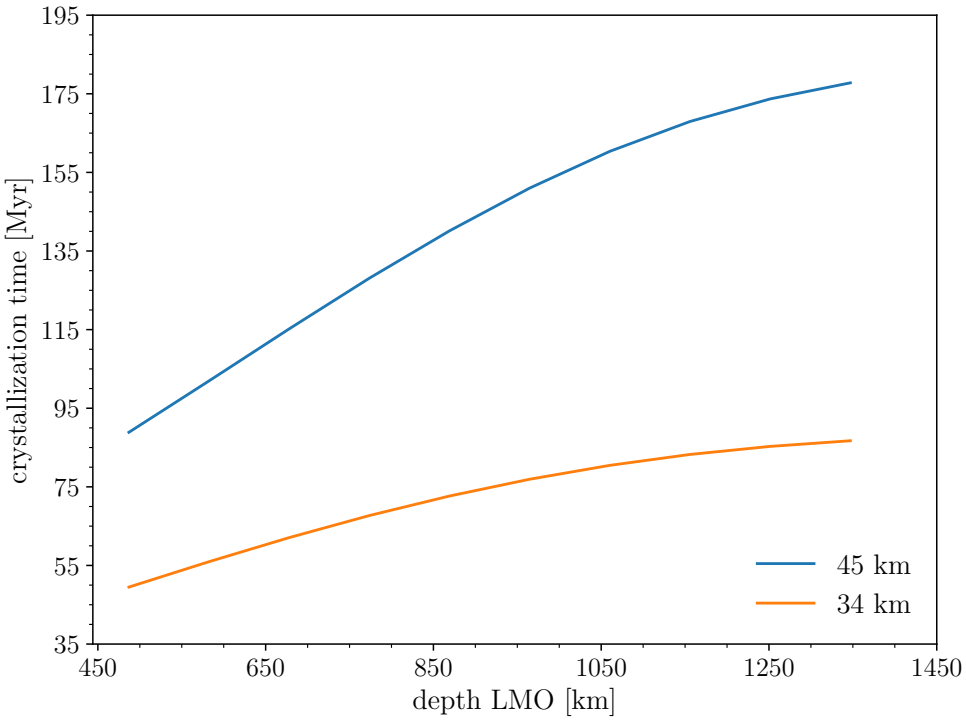

Figure 2.7: LMO solidification time as a function of initial LMO depth for the two extreme values of average crustal thickness according to Wieczorek et al. (2013): a 45 km thick crust (blue line) and a 34 km thick crust (orange line). $C_{\mathrm{E}} = 0.37$, $k_{\mathrm{cr}} = 2\,\mathrm{W\,m^{-1}\,K^{-1}}$ and C_0 is calculated using eq. (2.4).

Based on the compositional profiles of pigeonite and augite, McCallum et al. (1996) estimated a maximum cooling rate of $18\,\mathrm{K\,Myr^{-1}}$ for ferroan anorthosite sample 60025. Using our model, we calculate the cooling rate in the crust as a function of depth and time (fig. 2.8). Cooling rates are initially large, of the order of a few hundreds of $\mathrm{K\,Myr^{-1}}$ and decrease with time as the crust thickens. Calculated cooling rates are consistent with the upper limit given by McCallum et al. (1996) and show that sample 60025 formed at depths larger than 15 km and at least 20 Myr after the onset of LMO crystallization for a closure temperature ranging between 1070 K and 1300 K.

Fu et al. (2023) argued that the Ca and Mg isotopic composition of anorthosite sample 60025 is compatible with this sample marking the end of LMO differentiation and indicates a formation after more than 99% of solidification. Such a large percentage of crystallization is reached after at least 40 Myr, in the configuration of the shortest solidification timescale (fig. 2.8b), and up to 200 Myr after Moon formation (longest crystallization time, fig. 2.8a). Anorthosites crystallizing after 99% of LMO solidification would form at

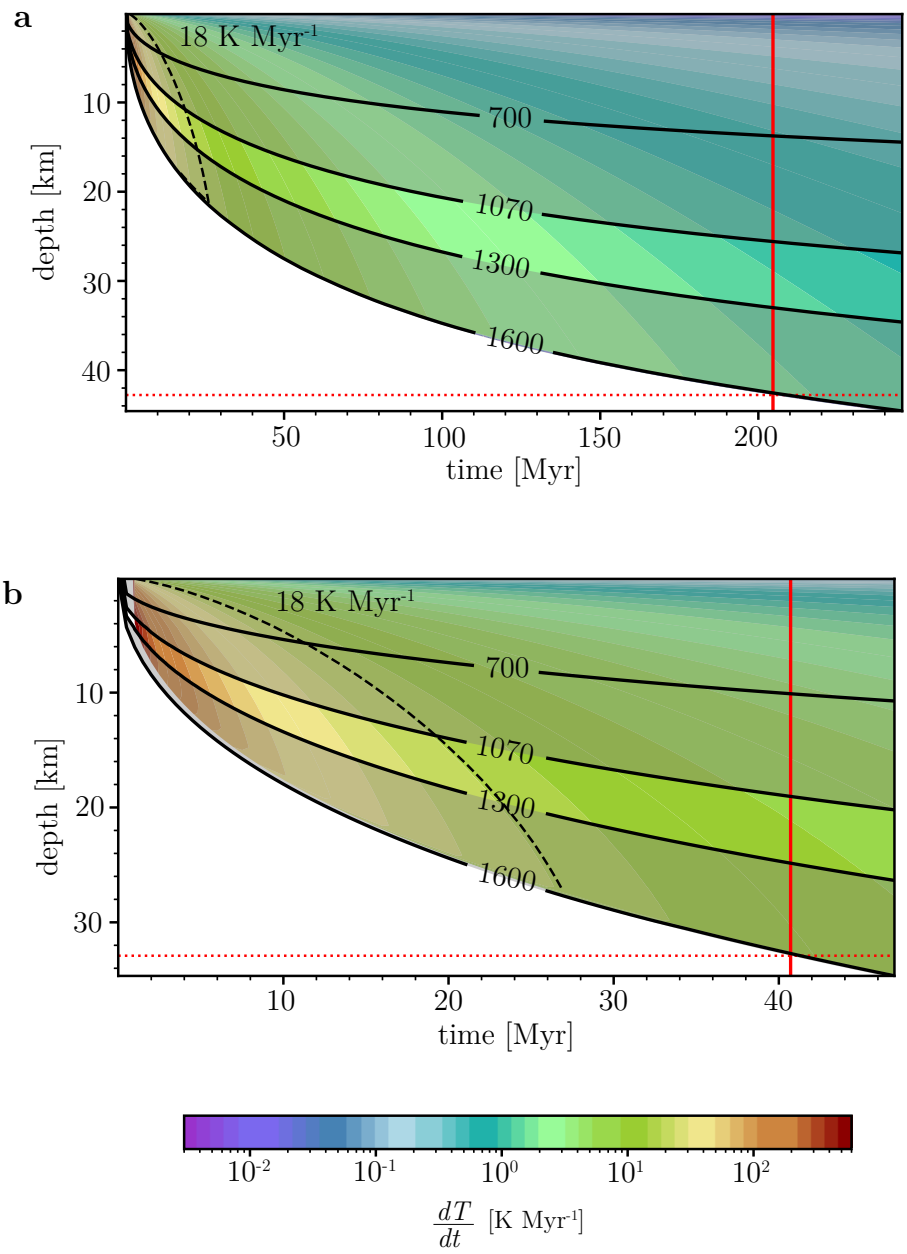

Figure 2.8: Cooling rate as a function of depth and time **a**- for the "longest scenario" where the final crustal thickness is 45 km and the total solidification time is 246 Myr, and where we use $C_0 = 0.0765$, $C_E = 0.37$ and $k_{cr} = 1.8\,W\,m^{-1}\,K^{-1}$ and **b**- for a thinner crustal thickness of 35 km and a shorter LMO solidification time of 47 Myr, and where we use $C_0 = 0.06$, $C_E = 0.37$ and $k_{cr} = 2.7\,W\,m^{-1}\,K^{-1}$. This cases correspond to the shortest and longest total solidification time (fig. 2.5). The black dashed line corresponds to the maximum cooling rate of $18\,K\,Myr^{-1}$ inferred for FAN sample 60025 by McCallum et al. (1996). The solid black lines represent different isotherms and the range of temperatures corresponding to the cooling rates determined by (McCallum et al., 1996) are shown in the brighter area. The red solid and dotted lines correspond respectively to the times and crustal thicknesses reached when 99 % of the LMO has crystallized.

more than 30 km depth and cool down at rates $\sim 10\,\mathrm{K\,Myr^{-1}}$ if considering the shortest solidification timescale, or $<1\,\mathrm{K\,Myr^{-1}}$ for the "longest scenario". These cooling rates are compatible with estimates of McCallum et al. (1996).

Sample 60025 has been dated at 4.51 Gyr using the U-Pb method and the plagioclase fraction by Hanan et al. (1987). A later study by Borg et al. (2011) reported an age of 4.360 Gyr using the U-Pb and Sm-Nd methods. However, as argued by Borg et al. (2023), the age reported by Hanan et al. (1987) can be questioned as it assumed that the initial Pb isotope composition of the Moon was identical to that of the Canyon Diablo iron meteorite, commonly used to represent the starting composition of the Solar System. There are many reasons to think that the Pb isotope composition of the Moon did not result from a single stage process and that the Moon precursors must have initially evolved with a U/Pb higher than that of Canyon Diablo. A multistage evolution would certainly modify the age calculated by Hanan et al. (1987). Our modeling results are indeed not consistent with the age of Hanan et al. (1987) and are more consistent with an age of 4.360 $\pm$0.003 Gyr for the last stages of the LMO crystallization (Borg et al., 2011).

Our model depicted in fig. 2.5 indicate that 99% of crystallization for a whole magma ocean (depth extending to 1300 km) is reached after 40 to 200 Myr, depending on the crustal thickness (34-45 km) and thermal conductivity. This means that the age of the Moon formation would have to be older than 4400-4560 Myr. This inference is at odds with the conclusions of Borg et al. (2023) who argued that the clustering of age for lunar rocks between 4.33-4.360 Gyr was a strong indication that the lunar magma ocean had cooled rapidly and that the Moon forming impact should have taken place at 4.360 Gyr. Our study suggests that an alternative interpretation of the chronological record for lunar rocks is necessary. First, the clustering of ages is indeed around 4.360 Gyr but, based on the data compiled by Borg et al. (2023) and including all uncertainties stemming from different dating methods, we estimate that the range of possible ages is 4297 to 4402 Myr suggesting that the duration of LMO crystallization could actually be longer than what is argued in that study. Second, apart from the age of mare basalts based on the ^{146}Sm-^{142}Nd chronometer, all the ages correspond to rocks formed at a late stage of LMO crystallization (>80%) or simply post-date LMO crystallization (KREEP, FAN, Mg- and alkali suites). Thus, the most problematic age is the ^{142}Nd model age of lunar mare basalts because the mare basalts are generally thought to originate from the melting of the first cumulates of olivine and pyroxene, that should have the oldest age of LMO crystallization (Borg et al., 2019). Looking more closely at this dataset (as compiled in Borg et al., 2019), several questions arise: in their fig. 6, if one considers only the mare basalts, a dichotomy appears between the low Ti-basalts and the high Ti-basalts, with the high-Ti basalts characterized by high Sm/Nd ratios that strongly constrain the ^{142}Nd age. Four

of the low-Ti basalts plot in the field of high Ti-basalts. However, by looking at their actual Ti contents, all of these samples are characterized by Ti contents greater than 4 wt% and cannot represent melts derived from an olivine + orthopyroxene cumulates, as is commonly thought for low-Ti basalts. They rather represent intermediate Ti basalts. As argued by Shearer (2006) the intermediate Ti basalts with 4 wt% TiO_2 require a Ti-rich phase in their sources derived from the late stage Ti-rich cumulates. Thus, one cannot consider that these rocks formed early during LMO crystallization, similarly to true low-Ti basalts. Consequently, it is not surprising that their apparent ages are very similar to those of more differentiated rocks such as anorthosites, or KREEP rocks. If one reexamines the ^{146}Sm-^{142}Nd isochron in light of these considerations, it becomes obvious that the only rocks representative of the early stage of LMO crystallization are the low-Ti mare basalts with TiO_2 <2wt%. This is represented by the rocks that have a nearly chondritic Sm/Nd source ratio and are as expected to be mildly fractionated (in incompatible elements) from a bulk Silicate Moon source. From these rocks, it becomes very difficult to extract an isochron age because there is little spread in their ^{147}Sm/^{144}Nd ratios. To the very least, their variable Ti contents could still be used to argue that the residual ^{142}Nd/^{144}Nd versus ^{147}Sm/^{144}Nd source trend represents a mixing line. These considerations strongly relax the argument that the LMO life span was extremely short and that requires that the Moon formation only shortly precedes the time of late LMO crystallization.

Third, there are new observational evidence for zircons that have crystallized at a time that precedes the late stage crystallization of the magma ocean (Zhang et al., 2021a), yielding an age of 4460 ± 31 Myr. This age was confirmed by a closer examination of the same sample using an atom probe that demonstrated that there was no clustering of radiogenic Pb (Greer et al., 2023) that would have resulted from a disturbance of radiogenic lead distribution. Thus, these observations suggest that the age of the Moon is at least 4460 Ma, which is well before the age of FAN and Mg-suite samples reported above, and consistent with our estimated age range for the Moon, based on our model.

Last, the studies of Jacobson et al. (2014) and Woo et al. (2024) have shown that the late accretion to the Earth that post-dates the Moon forming impact, indicated by highly siderophile element (HSE) enrichment in the bulk Silicate Earth, is not compatible with a late age for the formation of the Moon, as argued by Borg et al. (2023). Incidentally, these ages are also in agreement with the recent Rb-Sr age determination of the Moon (Yobregat et al., 2024), showing that the Moon-forming impact should have taken place no later than 79 Myr after the beginning of the Solar System.

2.6 Conclusion

We study the thermal evolution of the lunar magma ocean (LMO) using a physically robust 1D model. Our model is based on the sequential crystallization of olivine-pyroxene cumulates and a floating anorthositic crust, while taking into account conductive heat fluxes through the crust and from the cumulates, latent heat released by crystallization and radiogenic heat production. The first stage of crystallization is very fast: in 275 yr, 80 % of the LMO is crystallized. The second stage is slowed down by the formation of the buoyant crust with a low thermal diffusivity. For our reference case, the total LMO solidification time is 166 Myr. This solidification time depends on the crust conductivity and on the parameters of the phase diagram: the initial content in anorthite component C_0, which controls the final crust thickness, and the eutectic composition C_{E}, which affects the LMO thickness at the initiation of anorthosite crust growth. Considering these parameters variability, the LMO solidification time ranges from 45 Myr to 250 Myr and is long-lived.

The occurrence of an overturn during the second stage of LMO evolution may reduce this solidification time it if short-lived (i.e. less than ~ 5 Myr), or extend it if long-lived. Ferroan anorthosite sample 60025 has been consistently dated at 4360 Myr by different radiometric systems. Considering that this sample derives from more than 99% of LMO crystallization, as suggested from its Ca and Mg isotopic composition, we estimate that the Moon formed between 4400 Myr and 4560 Myr.

Acknowledgments

We thank two anonymous reviewers for their pertinent and useful comments, which helped improve our manuscript. This project has received funding from the European Research Council (ERC) under the European Union's Horizon 2020 research and innovation programme (grant agreement No. 101001689). CM acknowledges support of the Institut Universitaire de France.

2.7 Appendix A: Numerical solution

To obtain the flux at the base of the crust and at the top of cumulates, we need to solve the diffusion equation in the two layers:

$$\frac{\partial T_{\mathrm{i}}(t,r)}{\partial t} = \frac{\kappa_{\mathrm{i}}}{r^2}\frac{\partial}{\partial r}\left(r^2\frac{\partial T_{\mathrm{i}}(t,r)}{\partial r}\right) + \frac{h_{\mathrm{i}}(r,t)e^{-\lambda t}}{\rho c_{\mathrm{p}}}, \tag{2.29}$$

where subscript i stands for crust or cumulates. To deal with the growing thickness of the layer, we use a front-fixing method. This method consists in rescaling the radial coordinate r into a dimensionless radial coordinate $y \in [1, 2]$:

$$y = \frac{r - R^-}{R^+ - R^-} + 1, \tag{2.30}$$

where R^+ is the radius at the top and R^- the radius at the bottom of the layer. For the crust $R^+ = R_{\rm M}$ and $R^- = R_{\rm cr}(t)$, for the cumulates $R^+ = R_{\rm cu}(t)$ and $R^- = R_{\rm co}$. We also define the dimensionless temperature $\tilde{T}$ using:

$$\tilde{T} = \frac{T - T^+}{T^- - T^+} \in [0, 1], \tag{2.31}$$

where T^+ and T^- the temperatures at the top and bottom of the spherical shell, with $T^- > T^+$. Introducing eq. (2.30) and eq. (2.31) into eq. (2.29) gives, in the case of the crust:

$$\frac{\partial \tilde{T}}{\partial t} = -\frac{\partial \tilde{T}}{\partial y}\frac{\partial R^-}{\partial t}\left(\frac{y-2}{R^+ - R^-}\right) + \frac{\kappa}{r^2(R^+ - R^-(t))^2}\frac{\partial}{\partial y}\left(r^2\frac{\partial \tilde{T}}{\partial y}\right) + \frac{h_{\rm i}(y,t)e^{-\lambda t}}{\rho c_{\rm p}}, \tag{2.32}$$

A similar equation is also obtained for the cumulate layer. The change in variable introduces an advection term related to the growth rate of the solid layer. Similarly, we follow the evolution of the radial distribution in heat production in the spherical shell using:

$$\frac{\partial h_i(y,t)}{\partial t} = -u(y,t)\frac{\partial h_i(y,t)}{\partial y}, \tag{2.33}$$

where subscript i stands for crust or cumulates, $u_{\rm cr} = \dfrac{{\rm d}R^-}{{\rm d}t}\dfrac{y-2}{R^+ - R^-(t)}$ and $u_{\rm cu} = -\dfrac{{\rm d}R^+}{{\rm d}t}\dfrac{y-1}{R^+(t) - R^-}$. These equations are solved using a fully implicit time scheme and a first-order finite-volume scheme on a regular grid.

The thermal evolution code developed and used for this study is available in open source at https://github.com/LineColin/NEMMO.git.

2.8 Appendix B: Analytical solutions

An analytical approximate relation between the evolution of the radius at the base of the crust and the time can be found for the second stage when considering several simplifications to the model. Considering no radiogenic heating and no heat flux from the

cumulates, eq. (2.23) in Stage 2 becomes:

$$\frac{\mathrm{d}R_{\mathrm{cr}}}{\mathrm{d}t} = \frac{C_{\mathrm{E}}}{\rho L} k_{\mathrm{cr}} \frac{\mathrm{d}T}{\mathrm{d}r} \,. \tag{2.34}$$

Considering a steady-state in the crust, the solution to the diffusion equation is:

$$T(r) = -\frac{A}{r} + B \tag{2.35}$$

where A and B are constant. With $T(r = R_{\mathrm{M}}) = T_s$, where T_{s} is constant, and $T(r = R_{\mathrm{cr}}) = T_{\mathrm{E}}$, we have $A = \Delta T \dfrac{R_{\mathrm{M}} R_{\mathrm{cr}}}{R_{\mathrm{M}} - R_{\mathrm{cr}}}$ and $B = \dfrac{A}{R_{\mathrm{M}}} + T_{\mathrm{s}}$ with $\Delta T = T_{\mathrm{s}} - T_{\mathrm{E}}$. The temperature gradient at the base of the crust can be expressed as:

$$\frac{\mathrm{d}T(r)}{\mathrm{d}r} = \Delta T \frac{R_{\mathrm{M}} R_{\mathrm{cr}}}{R_{\mathrm{M}} - R_{\mathrm{cr}}} \frac{1}{r^2}\bigg|_{r=R_{\mathrm{cr}}} , \tag{2.36}$$

Considering the following initial condition, at $t = 0$, $R_{\mathrm{cr}} = R_{\mathrm{M}}$ and introducing eq. (2.36) into eq. (2.34) and integrating, we obtain:

$$t = -\frac{\rho L}{R_{\mathrm{M}} k_{\mathrm{cr}} \Delta T} \frac{1}{C_{\mathrm{E}}} \left[\frac{R_{\mathrm{M}} R_{\mathrm{cr}}^2(t)}{2} - \frac{R_{\mathrm{cr}}^3(t)}{3} - \frac{R_{\mathrm{M}}^3}{6} \right], \tag{2.37}$$

$$\Rightarrow \tau_{\mathrm{sol}} = -\frac{\rho L}{R_{\mathrm{M}} k_{\mathrm{cr}} \Delta T} \frac{1}{C_{\mathrm{E}}} \left[\frac{R_{\mathrm{M}} R_{\mathrm{cr,\,f}}^2}{2} - \frac{R_{\mathrm{cr,\,f}}^3}{3} - \frac{R_{\mathrm{M}}^3}{6} \right]. \tag{2.38}$$

Chapter 3

Numerical methods to study convection inside the cumulates

Dans le chapitre précédent, nous avons présenté un modèle pour l'évolution thermique de l'océan de magma lunaire. Il permet notamment d'estimer le temps de solidification de cet océan de magma, en fonction de la composition initiale en composant anorthite, donc de l'épaisseur finale de la croûte, de la composition eutectique et de la conductivité thermique de la croûte. Bien que ce modèle soit simple, il permet d'isoler précisément l'effet des différents paramètres sur le temps de solidification total de l'océan de magma lunaire. Nous montrons en particulier que ce temps de solidification est long, de l'ordre de plus d'une centaine de millions d'années. Plusieurs études suggèrent qu'à la fin de la cristallisation de l'océan de magma, la formation de phases minérales plus denses en haut des cumulats peut entraîner un retournement de ces derniers par une destabilisation de densité. Ce retournement pourrait être une explication de l'asymétrie dans l'épaisseur crustale. Cependant, ces modèles se basent sur une solidification rapide de l'océan de magma lunaire, de l'ordre de quelque dizaines de millions d'annés. Dans le cas où l'océan de magma cristallise sur des échelles de temps plus longues, il est possible que des instabilités thermiques se développent avant la cristallisation des phases denses. Nous proposons d'étudier le développement de ces instabilités thermiques dans les cumulats en prenant en compte une condition aux limites perméable à l'interface entre les cumulats et l'océan de magma lunaire, qui est en cours de cristallisation. C'est-à-dire qu'un échange de matière par cristallisation et/ou fusion à cette interface est possible.

Ce chapitre présente les méthodes numériques employées pour étudier la convection dans les cumulats. Nous combinons une analyse de stabilité linéaire, qui fournit les taux de croissance et les modes préférentiels des instabilités, et des simulations numériques directes, qui décrivent l'évolution temporelle et spatiale de la convection. L'objectif est de

valider la cohérence entre ces deux approches dans un cadre simplifié. Nous considérons un profil initial de température conductif, une gravité uniforme et des conditions aux limites thermiques fixes. La difficulté principale réside dans la condition de changement de phase à l'interface entre les cumulats et l'océan de magma. Enfin, nous explorons l'effet de différents autres paramètres sur la dynamique convective dans les cumulats, en particulier l'épaisseur de la coquille sphérique, l'influence d'une gravité non uniforme et la forme du profil initial de température.

3.1 Convection equations for the cumulates

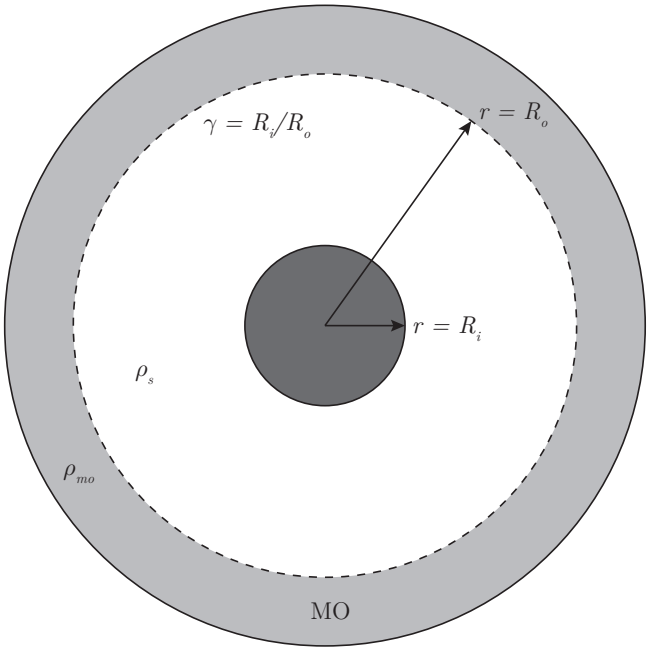

Figure 3.1: Schematic representation of the problem. The core is shown in dark gray, the cumulates in white and the magma ocean in light gray. R_i corresponds to the inner radius of the cumulates, R_o to the outer radius, γ to the aspect ratio, ρ_s to the density of the solid cumulates and ρ_{mo} to the density of the magma ocean.

3.1.1 Conservation equations

Solid-state convection is examined within a dimensionless spherical shell of inner radius R_i and outer radius R_o, with an aspect ratio $\gamma = \dfrac{R_i}{R_o} = 0.2$, and thickness $H = R_o - R_i = 1$. The values of the two dimensionless radius R_i and R_o are calculated according to γ. The solid cumulates have density ρ_s, and the density contrast between the solid and liquid layers is expressed as $\Delta\rho = \rho_s - \rho_{mo}$, with $\rho_s > \rho_{mo}$ (fig. 3.1). Gravitational acceleration is considered uniform, $g(r) = -g_0\mathbf{e_r}$, where g_0 is its intensity and $\mathbf{e_r}$ is the radial unit vector. The cumulates are modeled as an incompressible Newtonian fluid with constant viscosity η. We adopt the infinite Prandtl number approximation, which is appropriate for the cumulates and implies negligible inertial effects. In the Boussinesq approximation, density variations are considered negligible, except in the buoyancy term. We use the dimensionless temperature $\Theta = \dfrac{T - T_o}{\Delta T}$, with $\Delta T = T_i - T_o$, the initial temperature difference. Using the diffusive time scale $t_{\text{diff}} = \dfrac{H^2}{\kappa}$, with κ the thermal diffusivity, the dimensionless mass, momentum, and energy conservation equations are:

$$\boldsymbol{\nabla}\cdot\boldsymbol{u} = 0, \tag{3.1}$$

$$0 = -\boldsymbol{\nabla}p + \mathcal{R}a\Theta\mathbf{e_r} + \boldsymbol{\nabla^2}\boldsymbol{u}, \tag{3.2}$$

$$\frac{\partial\Theta}{\partial t} + \boldsymbol{u}\cdot\boldsymbol{\nabla}\Theta = \boldsymbol{\nabla}^2 T. \tag{3.3}$$

$\mathcal{R}a$ is the Rayleigh number:

$$\mathcal{R}a = \frac{\alpha\rho_s g_0 \Delta T H^3}{\kappa\eta}, \tag{3.4}$$

with α the thermal expansion coefficient.

3.1.2 Boundary and initial conditions

Thermal boundary conditions

For simplicity, the temperature at the top and bottom of the solid layer is assumed to be constant. The thermal boundary conditions in dimensionless form are:

$$T(r = R_o) = 0 \tag{3.5}$$

$$T(r = R_i) = 1 \tag{3.6}$$

This assumption is made in this chapter, but in the following chapter (Chapitre 4) we take into account the thermal evolution of the core, which modifies the thermal boundary condition for $r = Ri$.

Mechanical boundary conditions

Traditionally, convection studies assume a non-penetrative boundary condition at the horizontal boundaries between the solid and liquid. However, the present study accounts for possible material exchange through melting and crystallization at the interface between the cumulates and the Lunar Magma Ocean (LMO), as these layers are assumed to be in phase equilibrium at the interface. Our study is based on the work of Deguen (2013), Labrosse et al. (2018), Morison et al. (2019), and Morison et al. (2024).

The phase change condition is characterized by the competition between the time needed to build a viscous topography and the time needed to erase this topography. Material arriving at a horizontal boundary via convection movements forms a topography, whose height is limited by the weight that viscous forces can support. The timescale τ_η is the time needed to build a viscous topography h, and it corresponds to the viscous relaxation timescale:

$$\tau_\eta = \frac{\eta}{|\Delta\rho| g H}. \tag{3.7}$$

Its development occurs on a timescale similar to the post-glacial rebound on Earth (Turcotte et al., 2002). By assuming that the dynamic pressure on the liquid side can be neglected as its dynamic is fast compared to the solid side and its time average value is null, the normal stress continuity is:

$$2\eta \frac{\partial u_r}{\partial r}(h_s) - p(h_s) + \Delta\rho g h = 0, \tag{3.8}$$

with $\frac{\partial u_r}{\partial r}(h_s)$ the strain rate and $p(h_s)$ the dynamic pressure on the solid side of the boundary. The topography of the solid h_s is formed by the velocity of the solid u_r and the freezing front velocity V_r. The heat flux from the solid is neglected since it is small compared to the one transported by the liquid $\mathbf{q}_l$, the conservation energy is given by the Stephan's law:

$$\rho_s L_h V_r = \mathbf{q}_l \cdot \hat{\mathbf{r}}, \tag{3.9}$$

with L_h the latent heat of crystallization. To estimate the heat flux in the liquid, we use the parametrization introduced by Deguen et al. (2013):

$$\mathbf{q}_l \cdot \hat{\mathbf{r}} \sim \rho_l C_{p,l} u_{mo} \delta T, \tag{3.10}$$

where u_{mo} is the fluid velocity in the magma ocean and δT the temperature difference relative to the average temperature profile in the liquid due to the topography. Convection in the magma ocean should be vigorous, so we assume that the average temperature profile is isentropic, this lead to:

$$\delta T = \left(\frac{\partial T}{\partial P}\Big|_S - \frac{\partial T_l}{\partial P} \right) \rho_l g h. \tag{3.11}$$

$\frac{\partial T}{\partial P}|_S$ is the addiabatic temperature gradient and $\frac{\partial T_l}{\partial P}$ the Clapeyron slope. The expression for the freezing velocity V_r is obtained by combining eq. (3.9), eq. (3.10) and eq. (3.11):

$$V_r = -\frac{h}{\tau_\phi}, \tag{3.12}$$

with τ_ϕ the phase change time scale. This timescale correspond to the time needed to transport latent heat from the crystallization front to the melting front. It is expressed as:

$$\tau_\phi = \frac{\rho L_h}{(\rho - \Delta\rho)^2 C_{p,l} \left(\frac{\partial T_l}{\partial P} - \frac{\partial T}{\partial P}\Big|_S \right) g u_{mo}}. \tag{3.13}$$

According to Labrosse et al. (2018) and as justified by Morison et al. (2024), the viscous time scale τ_η is much shorter than the time scale associated with the evolution of the

topography, which can be considered quasi-static, so that $V_r = -u_r$, and the topography can be express as $h = u_r \tau_\phi$. The competition between τ_ϕ and τ_η allows us to introduce Φ, a dimensionless number that quantifies the exchange between solid and liquid:

$$\Phi = \frac{\tau_\phi}{\tau_\eta}. \tag{3.14}$$

Using the dimensionless number Φ (eq. 3.14), the continuity of the normal stress at the top of the spherical shell can be written in dimensionless form:

$$\Phi u_r + 2\,\frac{\partial u_r}{\partial r} - p = 0. \tag{3.15}$$

The radial velocity at this boundary may be non-zero if the melting/crystallization time τ_ϕ is shorter than τ_η. In the limit $\Phi \to 0$, the boundary condition reduces to a balance between the pressure and viscous normal stress, without constraining u_r, the boundary is therefore permeable (or penetrative). Conversely, as $\Phi \to \infty$, the condition enforces $u_r \to 0$, corresponding to an impermeable boundary (or non-penetrative).

Free-slip conditions are applied to the boundaries of the solid layer, corresponding to null shear stress in the tangential directions, in dimensionless form:

$$\tau_{r\theta} = r\,\frac{\partial}{\partial r}\left(\frac{u_\theta}{r}\right) + \frac{1}{r}\,\frac{\partial u_r}{\partial \theta} = 0, \tag{3.16}$$

$$\tau_{r\phi} = r\,\frac{\partial}{\partial r}\left(\frac{u_\phi}{r}\right) + \frac{1}{r\sin\theta}\,\frac{\partial u_r}{\partial \phi} = 0. \tag{3.17}$$

At the base of the spherical shell, we impose free-slip (eqs. 3.16 and 3.17) and an impermeable (or non-penetrative) boundary condition:

$$u_r(r = R_i) = 0. \tag{3.18}$$

Initial conditions

The initial temperature profile is defined as the steady-state solution of the heat conduction equation:

$$\nabla^2 T = 0. \tag{3.19}$$

Using the boundary condition described in eqs. (3.5) and (3.6), the initial temperature profile is defined as

$$T(r) = \frac{(R_i - \frac{R_i R_o}{r})}{(R_i - R_o)}. \tag{3.20}$$

For the direct numerical simulation, we introduce a small-amplitude random thermal perturbation into the temperature field to start convection. This initial noise, which has an amplitude A, is crucial in determining when the overturn starts. We adopt $A = 10^{-3}$, which is commonly used in the solid-state convection model.

3.1.3 Parameters

The problem can be characterized by two parameters: the Rayleigh number $\mathcal{R}a$ (eq. 3.4) and the phase change number Φ (eq. 3.14). The Rayleigh number corresponds to the competition between buoyancy and diffusivity. A high value of $\mathcal{R}a$ promotes convection in the cumulates. Convection can be established in the cumulates if the Rayleigh number is higher than the critical Rayleigh number $\mathcal{R}a_c$. In this chapter, we explore the range of $\mathcal{R}a \in [10^2, 10^8]$. The phase change number characterizes the permeability of the boundary between the magma ocean and the solid. If $\Phi \to 0$, the boundary is considered permeable, meaning that exchange between the cumulates and the magma ocean is straightforward. In the other case, if $\Phi \to \infty$, the boundary is impermeable and there is no exchange between the cumulates and the magma ocean, as commonly used in models mantle convection. For this chapter, we explore a large range of phase change number values, from $\Phi = 10^{-2}$ to the non-penetrative condition $\Phi \to \infty$.

3.2 Methodology

3.2.1 Linear stability analysis

We perform a linear stability analysis (LSA) to determine whether thermal convection can develop within the cumulates and, if so, to characterize the most unstable mode. The principle of this method is to consider an infinitesimal perturbation superimposed on a steady, motionless conductive background state. The sum of these perturbations with the background are assumed to satisfy the conservation equations eqs. (3.1) to (3.3) and the boundary conditions. Due to their small amplitude, nonlinear terms in the equations can be neglected. In the infinite Prandtl number approximation, the only nonlinear term in the conservation equation is the advective term $\boldsymbol{u} \cdot \boldsymbol{\nabla} T$ in the energy conservation (eq. 3.3), which is thus omitted in the linearized formulation.

The perturbations result from the superposition of fluctuations of all possible wavelengths and directions, namely in the radial direction r, latitude ϕ and longitude θ, and vary with time. These perturbations can be represented as a sum of spherical harmonics $Y_l^m(\theta, \phi)$, where $l \in \mathbb{N}$ denotes the spherical harmonic degree and $m \in [-l, l]$ the azimuthal order, whith a radial dependence. The temperature, velocity, and pressure

fields are then expressed as the sum of a stationary conductive background and a time-dependent perturbation. For instance, the temperature field can be written as:

$$\Theta(r,\theta,\phi,t) = \bar{\Theta}(r) + \tilde{\Theta}(r,\theta,\phi,t), \tag{3.21}$$

where the perturbation term is expanded as:

$$\tilde{\Theta}(r,\theta,\phi,t) = \sum_{l=0}^{\infty}\sum_{m=-l}^{l} \tilde{\Theta}_l^m(r) Y_l^m(\theta,\phi) e^{\sigma_l t}. \tag{3.22}$$

The radial dependence of the perturbation is discretized using a Chebyshev polynomial basis. The system can be written as a generalized eigenvalue problem using differential matrices. The growth rate σ_l is the eigenvalue of the problem. The most unstable mode corresponds to the maximum value of $\Re(\sigma_l)$, and its associated value l gives the preferred mode of convection. As shown by Morison et al. (2024), the problem is laterally degenerate, and the eigenvalues do not depend on m, so we focus on the dependence on l. We do not reproduce the full demonstration of this method here, but a detailed analysis is provided in Deguen (2013), Labrosse et al. (2018), Morison et al. (2019), and Morison et al. (2024).

In this study, we use the numerical tool `StablinRB` developed by Morison et al. (2024), to assess the stability of the conductive state in the problem. The results provide insights into the onset of convection and the dominant convective mode.

3.2.2 Direct numerical simulations

The LSA is useful for exploring a wide range of parameters values and provides information about the growth rate and the preferred convection mode, but it can not provide information about the temporal and spatial evolution of convection. This is why we perform direct numerical simulations (DNS) to have access to the temporal and spatial evolution of convection for a given value of the Rayleigh number and phase change number.

To perform these DNS, we use the software `Dedalus`. It is a parallelized open source platform designed to solve partial differential equations using spectral methods (Burns et al., 2020). The aim is to solve the partial differential equations (PDEs) described previously (eqs. 3.1, 3.2 and 3.3) by taking into account the phase change boundary condition (eq. 3.15) at the top of the spherical shell. This requires solving the PDEs numerically, in particular by discretizing the variables. The software `Dedalus` is based on spectral methods. The solutions are developed on an orthogonal basis (Chebychev polynomial and spherical harmonics in the spherical case). The aim is to combine high precision with

flexibility in terms of equations, domain, and parallelism. This software is precise and flexible for simple geometry. DNS provides access to the temporal and spatial evolution of temperature, velocity, and pressure fields. This information is used to calculate the quantities used to study convection at different points on the sphere. In addition, as the model uses spectral methods to resolve the equation system, we can deduce the precise convection mode.

3.3 Comparison between the two numerical methods

We combine linear stability analysis with direct numerical simulations, as the parameter space accessible to direct numerical simulations is inherently limited. Linear stability analysis expands our ability to study regimes that are inaccessible with direct numerical simulations.

3.3.1 Results from LSA

In this section, we present the results obtained from the LSA. As explained earlier in this chapter, with the LSA, we can obtain the growth rate of all modes, for a large range of parameters. We assume that the highest growth rate σ_{LSA} corresponds to the preferential mode of convection l.

In Morison et al. (2024), the critical Rayleigh number $\mathcal{R}a_c$ for $\gamma = 0.2$ and penetrative condition only at the top is $\mathcal{R}a_c = 73$ and $\mathcal{R}a_c = 1058$ for non-penetrative boundary conditions. We work with a value of the Rayleigh number $\mathcal{R}a$ higher than the critical Rayleigh number $\mathcal{R}a_c$ to study the effect of an increase in the Rayleigh number. We systematically vary the Rayleigh number and the phase change number. An increase in the Rayleigh number leads to an increase in the growth rate (fig. 3.2). Convection is facilitated by an increase in buoyancy, which is correlated with an increase in the Rayleigh number. As the phase change number increases, the growth rate decreases. The presence of a penetrative boundary condition at the top of the spherical shell promotes the development of convection by increasing the growth rate (Morison et al., 2019; Morison et al., 2024). The preferential mode of convection is mostly influenced by the value of the phase change number. For a low value of the phase change number, the preferential mode of convection is kept at $l = 1$. In fig. 3.2b, by increasing the phase change number, we observe a transition at $\Phi \sim 10$ where the mode of convection changes from $l = 1$ to $l = 2$.

Figure 3.3 illustrates the temperature perturbation and the streamlines of the fastest-growing mode in the equatorial plane ($\theta = \pi/2$) for the extreme cases, corresponding to a low ($\mathcal{R}a = 10^4$) and high ($\mathcal{R}a = 10^8$) value of Rayleigh number and penetrative

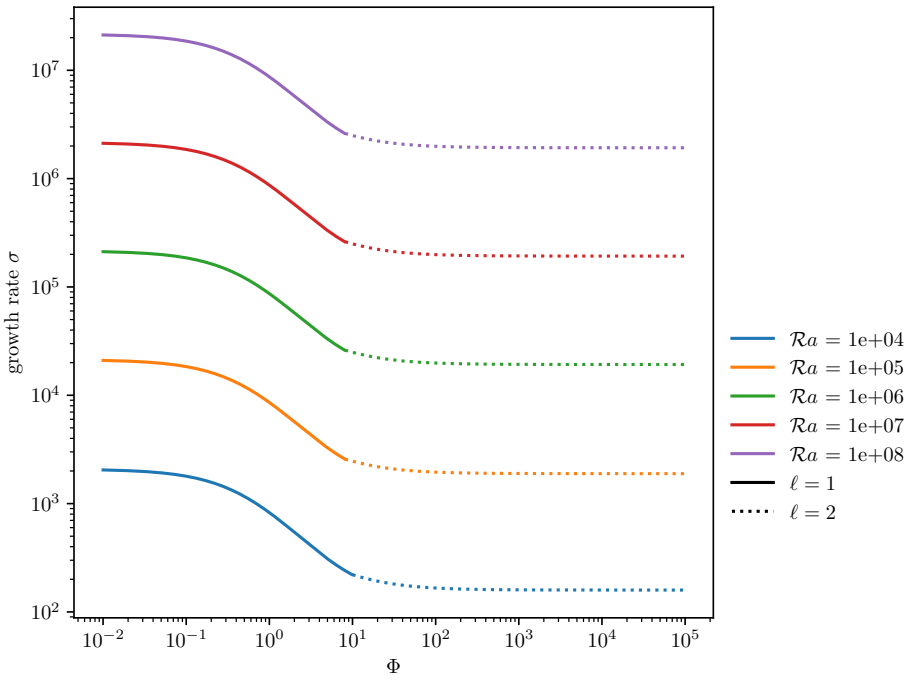

Figure 3.2: Growth rate σ_{LSA} as function of Φ for different values of Rayleigh number $\mathcal{R}a$. The solid lines correspond to case where $\ell = 1$ and the dotted lines to $\ell = 2$.

($\Phi = 10^{-2}$) and non-penetrative ($\Phi \to \infty$) boundary conditions. In the case $\Phi = 10^{-2}$, streamlines deviate around the core, and the dominant mode of instability corresponds to the spherical harmonic degree $l = 1$ for both tested Rayleigh numbers. In contrast, when $\Phi \to \infty$, the flow exhibits a degree $l = 2$ pattern, indicating a lower value of the growth rate of the degree-one mode. On fig. 3.3, we observe that for a penetrative boundary condition, the streamlines are open while for a non-penetrative condition, the streamlines are closed. This behavior is linked to the non-penetrative boundary condition imposed at the outer surface of the spherical shell. There is no effect of the Rayleigh number on the temperature perturbation and the streamline. With penetrative boundary conditions, even at Rayleigh numbers two to six orders of magnitude above the critical Rayleigh number, the degree-one harmonic remains dominant in the spherical shell, indicating that boundary permeability plays a crucial role in preserving large-scale convective structures.

3.3.2 Results from DNS

To present the results obtained from the DNS, we selected a reference case defined by a Rayleigh number $\mathcal{R}a = 10^4$ and a phase change number $\Phi = 6$. With DNS, it is not possible to explore the entire range of parameters. It is difficult to increase the value of $\mathcal{R}a$ while keeping the values of Φ low. The reference case corresponds to the highest Rayleigh number for which such a low value of Φ can be reached. Therefore, the case

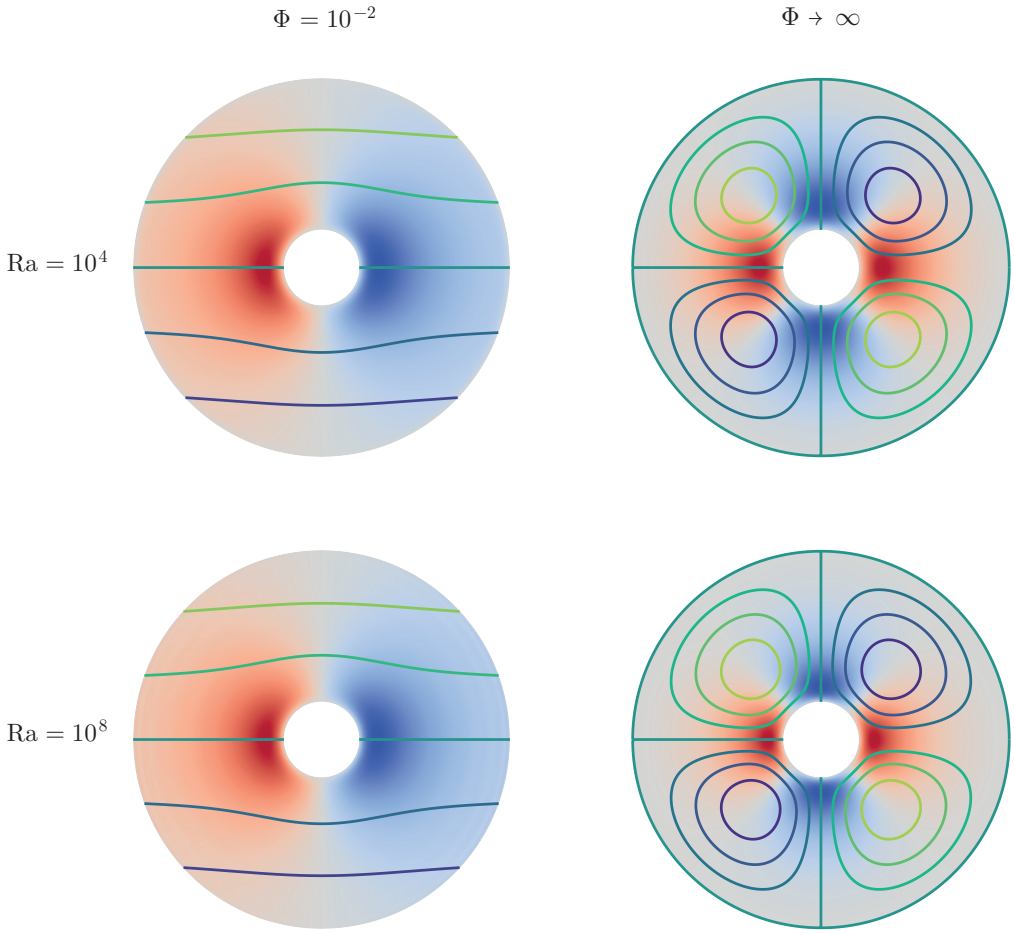

Figure 3.3: Temperature perturbation and streamlines of the most unstable mode for extreme cases: $\mathcal{R}a = 10^4$ and $\mathcal{R}a = 10^8$ with penetrative boundary condition, $\Phi = 10^{-2}$ and non-penetrative condition, $\Phi \to \infty$.

($\mathcal{R}a = 10^4,\ \Phi = 6$) is chosen as the reference case. The total flux is defined as the sum of the convective flux and the conductive flux:

$$f_r = -\frac{\partial T}{\partial r} + T u_r. \tag{3.23}$$

We study the temporal evolution of the dimensionless heat flux at the outer boundary of the spherical shell ($r = R_o$) (fig. 3.4a), as well as the evolution of the mean temperature within the shell (fig. 3.4b). The heat flux is initially constant, then rapidly increases until it reaches a maximum value $f_{\max}$ at time $t_{\max}$ (red star in fig. 3.4a). The time when the

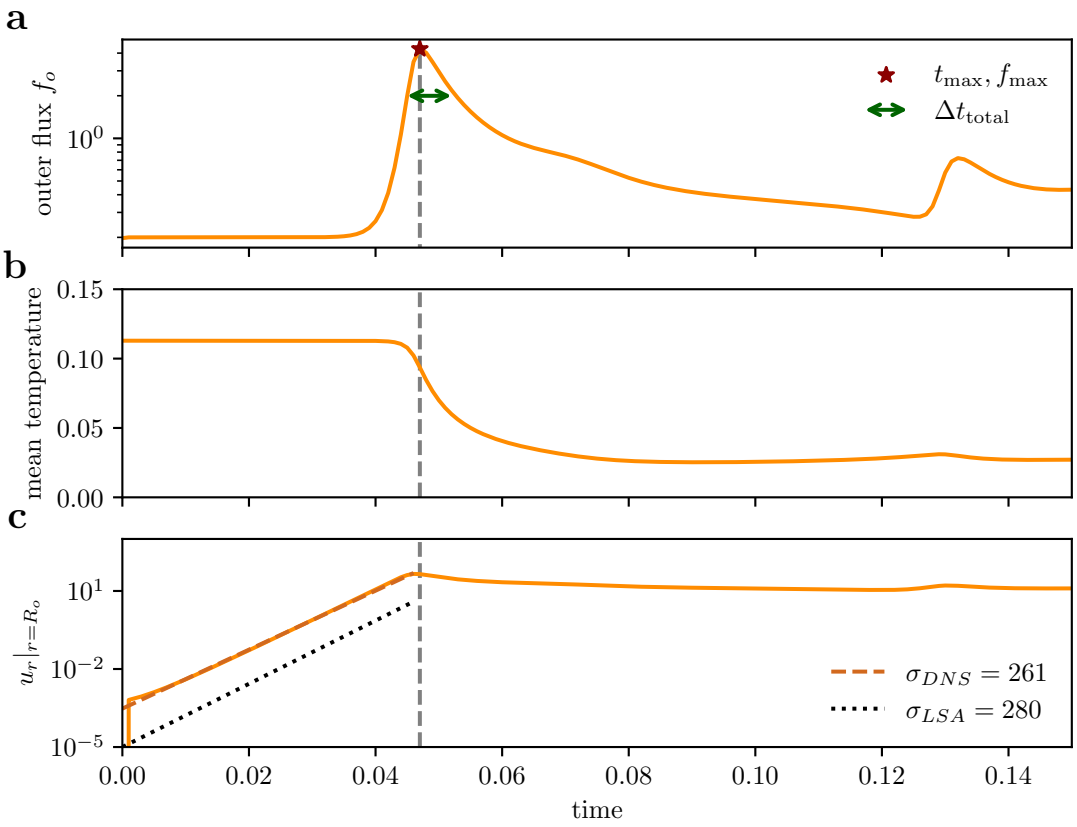

Figure 3.4: **a**- Temporal evolution of the outer flux f_o, the red star corresponds to the maximum flux and the green arrow to duration of the overturn Δt_{total}. **b**- Temporal evolution of the mean temperature. **c**- Temporal evolution of the RMS of the radial velocity at the outer radius ($u_r(r = R_o)$), with the growth rate of the DNS σ_{DNS} in dashed dark-orange line and LSA σ_{LSA} in dotted black line.

flux starts to grow depends on the initial amplitude noise A. Convection increases rapidly, and the duration of the peak is defined by Δt_{total}. It is defined as the duration between the time when the flux reaches the average of min and max values, $f_{mid} = (f_{\max} + f_{\min})/2$ when it grows and the same value when it decreases. Following the maximum, the flux

gradually decreases, reaches a second, less intense peak, and stabilizes. Convection is sustained because the basal temperature is kept constant, ensuring a continuous supply of thermal buoyancy that maintains the convective motions. The mean temperature begins to decrease as convection starts, and it decreases more rapidly during the period when the heat flux reaches its maximum. Afterwards, it stabilizes, with a small peak occurring before the secondary maximum of the heat flux.

In addition, we study the time evolution of the RMS of the radial velocity at $r = R_o$ between t_0 and $t_{\max}$ to obtain the growth rate of convection (fig. 3.4c). The growth rate is computed as the slope over the linear phase of the instability, from $t = 0$ to $t = t_{\max}$. A series of linear regressions is performed over multiple segments within this interval, and the average slope is taken as the DNS-based growth rate (fig. 3.5).

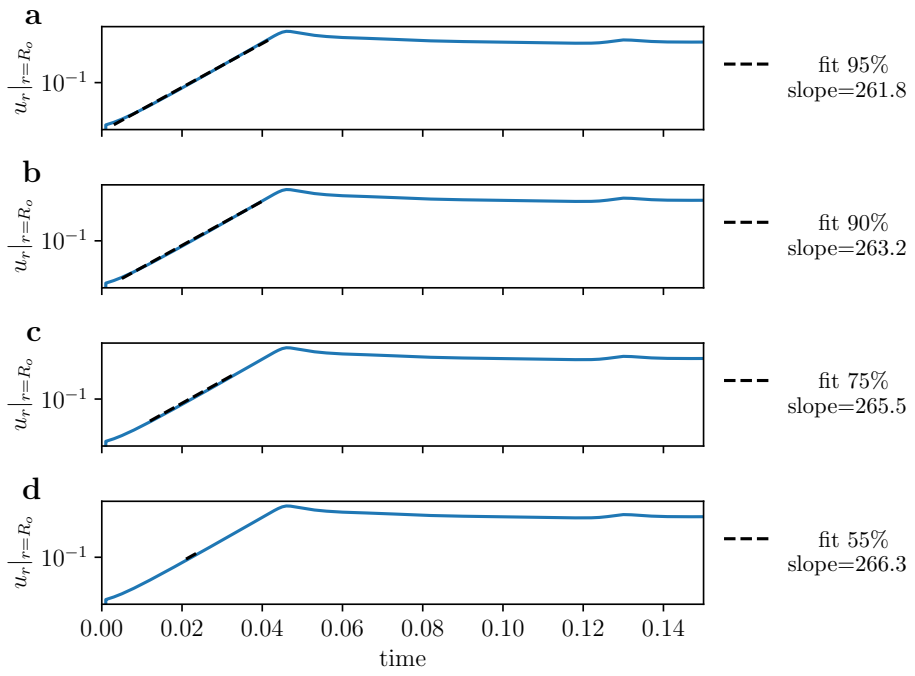

Figure 3.5: Temporal evolution of the RMS of the radial velocity at $r = R_o$ for the reference case $\mathcal{R}a = 10^4$, $\Phi = 6$. The dashed lines represent the slope calculated taking different percentage, from 90% of the slope in orange to 10% of the slope in purple, of the exponential part of the curve between t_0 and $t_{\max}$. The black line corresponds to the middle of the curve.

Since `Dedalus` is a spectral code, the temperature field can be decomposed into its spectral components. The resulting spectrum represents the amplitude associated with each spherical harmonic degree l. At t_0, the spectral coefficients are randomly distributed (fig. 3.6a). At $t = t_{\max}$, the dominant mode corresponds to the spherical harmonic degree $l = 1$. Higher-order coefficients are significantly smaller in amplitude, confirming the dominance of the $l = 1$ mode. We note an increase in the coefficient value for $l = 31$,

which may be related to the initial noise. Indeed, for this same harmonic, the coefficient value is higher. This elevated value for $l = 31$ persists until the end of the simulation at t_{end}, but it is still lower than the amplitude of $l = 1$.

Figure 3.7 provides a Mollweide projection of the outer surface heat flux at $t = t_{\text{max}}$. The spatial pattern of the flux is consistent with the spectral analysis, showing a large-scale structure dominated by degree $l = 1$, as expected by the spectral analysis.

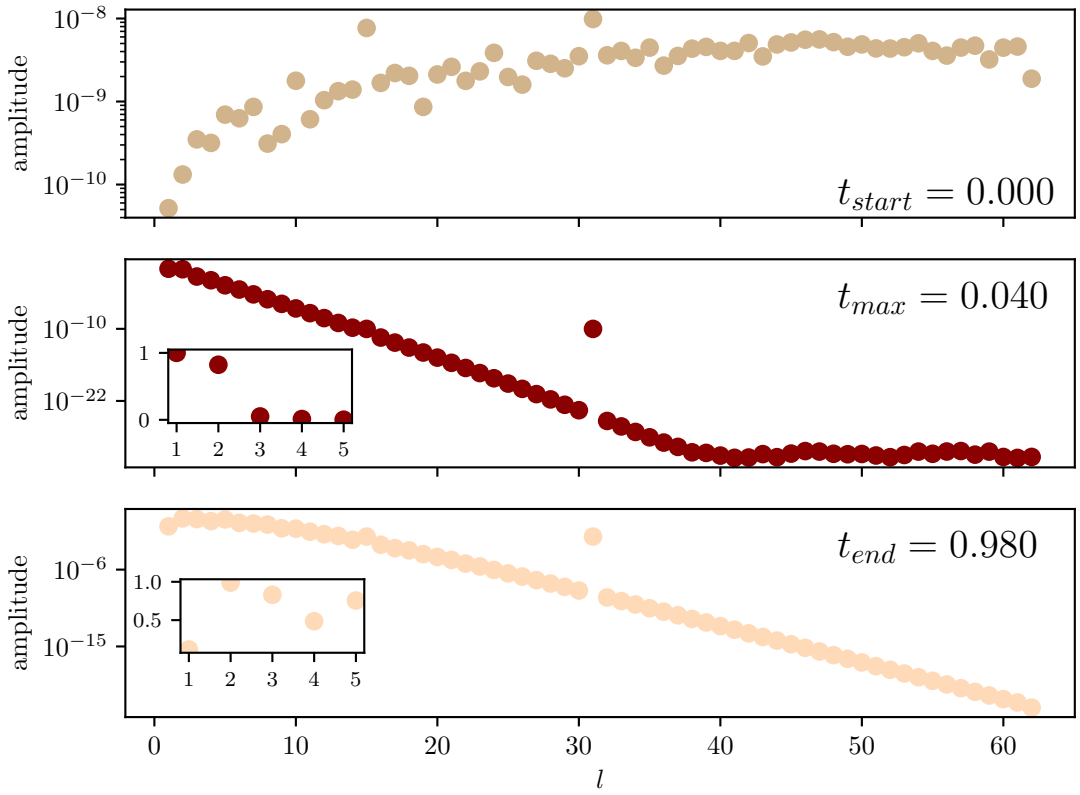

Figure 3.6: Spectral amplitude of the temperature field as a function of the spherical harmonic degree l at **a** the initial time t_0, **b** the maximum time t_{max} and **c** the final time corresponding to the end of the simulation t_{end}. The inset corresponds to the amplitude for the first 5 degrees of spherical harmonics. On **b** and **c** the amplitude is normalized by the maximum of the amplitude at t_{max}.

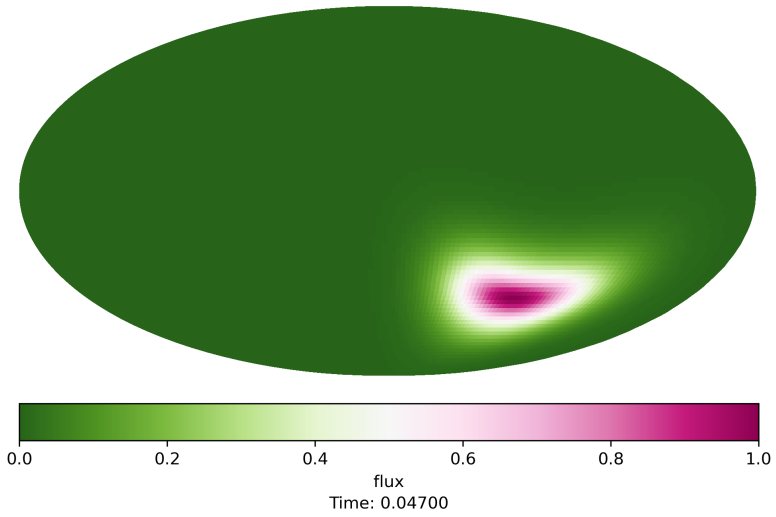

Figure 3.7: Mollweide representation of the surface heat flux at $t_{\max} = 0.047$, normalized by is maximum. The full video is availlaible at https://youtu.be/ipdkyJ8jSQg.

3.3.3 Comparison: LSA vs DNS

To assess the agreement between LSA and DNS, we focus on the only two quantities that can be directly compared: the instability growth rate, denoted σ, and the dominant mode of convection, characterized by the spherical harmonic of degree l. As shown in fig. 3.8, the growth rate computed from the DNS closely matches the value predicted by LSA.

This comparison provides a valuable validation step for the DNS framework. LSA, although limited to infinitesimal perturbations and linear dynamics, allows rapid exploration of a wide range of parameters. In contrast, DNS captures the full nonlinear evolution of convection, both in space and time, but is computationally limited, particularly when dealing with high Rayleigh numbers. The presence of the phase change boundary condition reduces the range of accessible parameters through the DNS.

Given the good agreement between the LSA and the DNS, and the growth rate that can be scaled by $\mathcal{R}a$ (dotted line on fig. 3.8b), the DNS results can be extrapolated to more extreme regimes, in particular for lower values of Φ and higher values of $\mathcal{R}a$. This extrapolation is examined in more detail in the following chapter (Chapter 4).

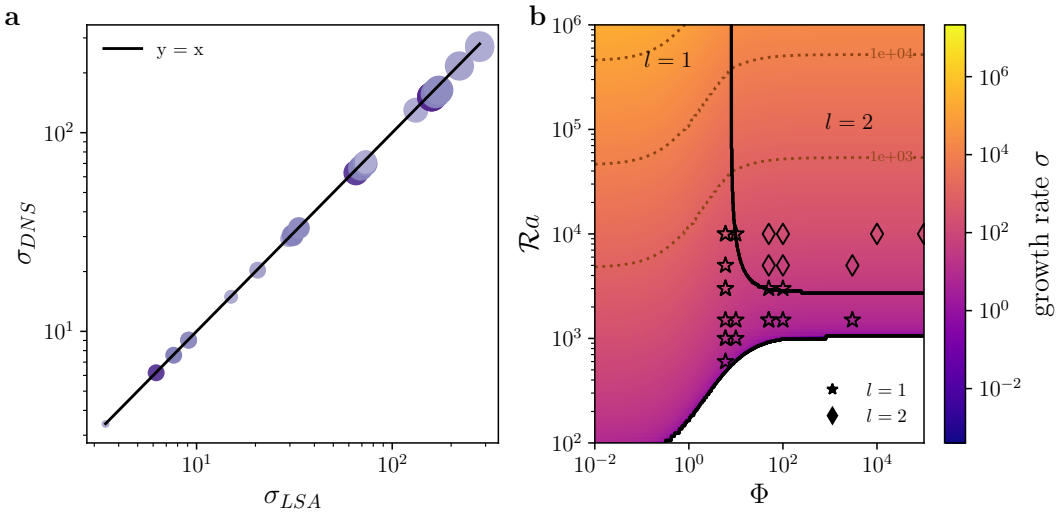

Figure 3.8: **a**- Growth rate of the convective instability obtained from DNS as a function of that predicted by LSA, for various values of $\mathcal{R}a$ and Φ (see table 3.2). Marker size scales with $\mathcal{R}a$, while color indicates Φ, with darker shades corresponding to higher values. The black line represents the $y = x$ reference. **b**- Map of growth rate values as a function of $\mathcal{R}a$ and Φ. Symbols represent DNS results, each symbol type corresponding to a different convection mode. Black solid lines indicate the boundaries where transitions between convection modes occur as predicted by LSA. Gray dashed lines corresponds to growth rate contour lines.

3.3.4 Effect of $\mathcal{R}a$ and Φ

In this section, we investigate the influence of two dimensionless numbers, the Rayleigh number and the phase change number, for a given initial temperature profile (eq. 3.20) and aspect ratio $\gamma = 0.2$. Both dimensionless numbers are unconstrained, as they depend on the properties of the solid shell and on the dynamic of the overlying magma ocean. With linear stability, we study the influence of these two dimensionless numbers on the growth rate and preferred mode of convection. As explained in section 3.3.1, the increase of the value of the Rayleigh number and the decrease of the phase change number favor the establishment of convection in the spherical shell. The low values of Φ favor a convection mode corresponding to a spherical harmonic of degree-one (fig. 3.8).

With DNS, we study how these two dimensionless numbers affect the outer flux f_o (fig. 3.9). At constant $\mathcal{R}a$, increasing the phase change number to a non-penetrative boundary condition $\Phi \to \infty$ delays the onset of convection and reduces the peak surface flux. Conversely, for a fixed $\Phi = 6$, decreasing $\mathcal{R}a$ (green line on fig. 3.9) results in an later onset of convection and a lower peak flux. More generally, increasing $\mathcal{R}a$ or decreasing Φ leads to earlier and more vigorous convection, characterized by a stronger maximum surface flux. Furthermore, a thinner peak width indicates that most of the energy stored

in the spherical shell is released over a shorter timescale.

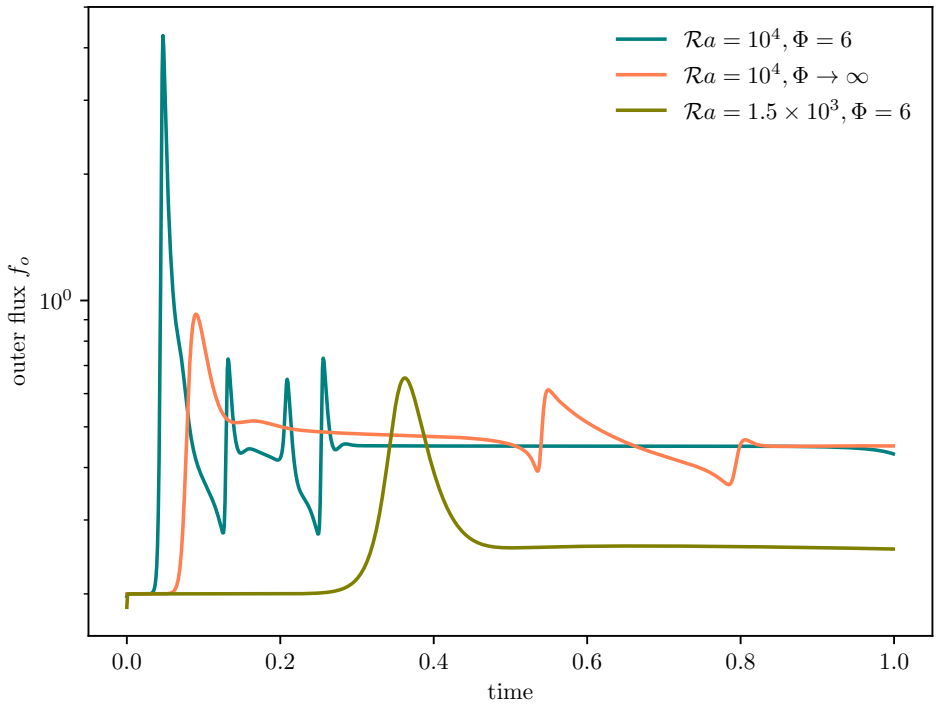

Figure 3.9: Dimensionless temporal evolution of the outer flux f_o for $\mathcal{R}a = 10^4$, $\Phi = 6$ (blue line), $\mathcal{R}a = 10^4$, $\Phi \to \infty$ (orange line) and $\mathcal{R}a = 1.5 \times 10^3$, $\Phi = 6$ (green line).

3.4 Effect of other parameters

The previous section (section 3.3) of this chapter is focused on a simplified case to compare the LSA and DNS. This case corresponds to a conductive initial temperature profile (eq. 3.20), a spherical shell with an aspect ratio $\gamma = 0.2$, a uniform gravity acceleration, and fixed thermal boundary conditions (eqs. 3.6 and 3.5). The aim of this section is to study the effect of other parameters on the convection. Particularly, we study the effect of the shell thikness (by varying the aspect ratio γ), a radially-dependent gravity acceleration, and the initial temperature profile.

3.4.1 Effect of the aspect ratio γ

In the study by Morison et al. (2024), the authors investigate the influence of the aspect ratio on the critical Rayleigh number $\mathcal{R}a_c$ (table 3.1) and on the prefered mode of the instabilities as a function of the value of Φ. We also propose to examine the influence of

the aspect ratio on convection, growth rate and mode of convection, through both LSA and DNS, using an initially conductive temperature profile, and a uniform gravity, by systematically varying $\mathcal{R}a$ and Φ.

As in section 3.3.3, we first compare the results from LSA with those from the DNS. We vary the aspect ratio of the spherical shell such that $\gamma \in [0.2, 0.6]$ (fig. 3.10). In the case $\gamma = 0.4$, the agreement between LSA and DNS remains robust (fig. 3.10a). The preferred convective mode is influenced by the phase change number: a transition is observed from a mode $l = 1$ to $l = 2$ for $\Phi = 5$, and then to $l = 3$ for $\Phi = 10$. Compared to previous configurations, the reduced shell thickness causes this transition toward shorter wavelengths to occur at slightly lower values of Φ (fig. 3.10c). A thinner shell makes the value of l to increase.

Table 3.1: Values of the critical Rayleigh number $\mathcal{R}a_c$ and associated wavelength l as function of the phase change number Φ and the aspect ratio γ from Morison et al. (2024).

γ \ Φ	**6**	**100**
0.2	$\mathcal{R}a_c$ =481, $l = 1$	$\mathcal{R}a_c$ =985, $l = 1$
0.4	$\mathcal{R}a_c$ =364, $l = 1$	$\mathcal{R}a_c$ =709, $l = 2$
0.6	$\mathcal{R}a_c$ =317, $l = 3$	$\mathcal{R}a_c$ =632, $l = 4$

For the DNS, we use a Rayleigh number $\mathcal{R}a = 1500$, which is higher than the critical value for the onset of convection (table 3.1). The simulations are performed for two values of the parameter Φ ($\Phi = 6$ and $\Phi = 100$). For the lower value of Φ, the growth rate is larger than for the higher one (fig. 3.11). This behavior is consistent with the fact that a lower Φ corresponds to more penetrative thermal boundary conditions at the top of the spherical shell, which promotes the onset of convection. For both explored values of Φ, the growth rate increases as the shell becomes thinner (*i.e.:* for higher values of γ). Convection therefore starts earlier in thinner shells (fig. 3.11). As shown by Morison et al. (2024), the critical Rayleigh number increases with shell thickness for values of $\Phi \gtrsim 10$. Consequently, for the chosen $\mathcal{R}a = 1500$, the case with $\gamma = 0.2$ is closer to the critical threshold than the case with $\gamma = 0.6$, which explains why the growth rate is smaller for thicker shells (table 3.1). In addition, a higher aspect ($\gamma \to 1$) ratio reduces the curvature of the spherical shell, which further facilitates the development of convection.

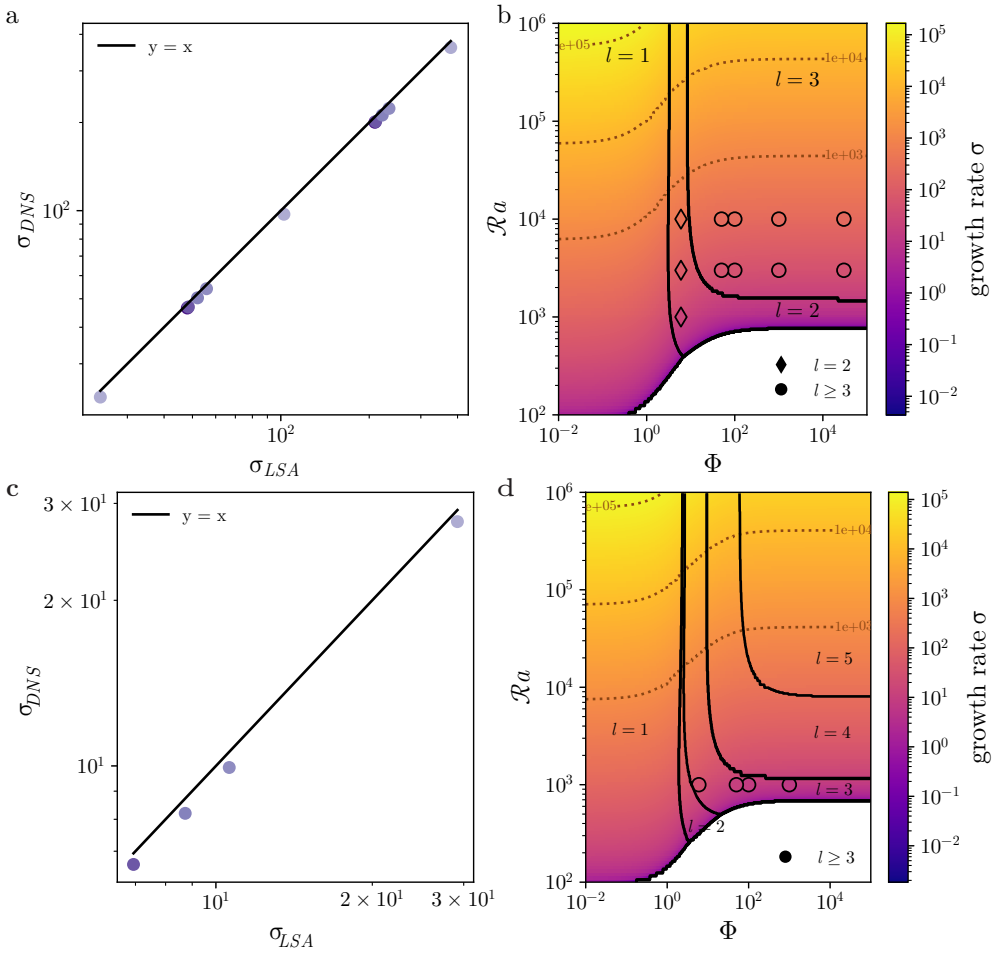

Figure 3.10: **a-c** Growth rate of the convective instability as obtained from DNS as a function of the growth rate obtained with LSA for different $\mathcal{R}a$ and Φ for an aspect ratio $\gamma = 0.4$ on the panel a and $\gamma = 0.6$ on the panel **c**. The size of the points is proportional to the value of $\mathcal{R}a$, the color corresponds to the value of Φ, a darker color corresponding to the highest Φ values. The black line correspond to the $y = x$ line. **b-d** Map of growth rate values as a function of $\mathcal{R}a$ and Φ. Symbols represent numerical simulation results, each symbol type corresponding to a different convection mode. Black solid lines indicate the boundaries where transitions between convection modes occur as predicted by LSA. Gray dashed lines corresponds to growth rate contour lines.

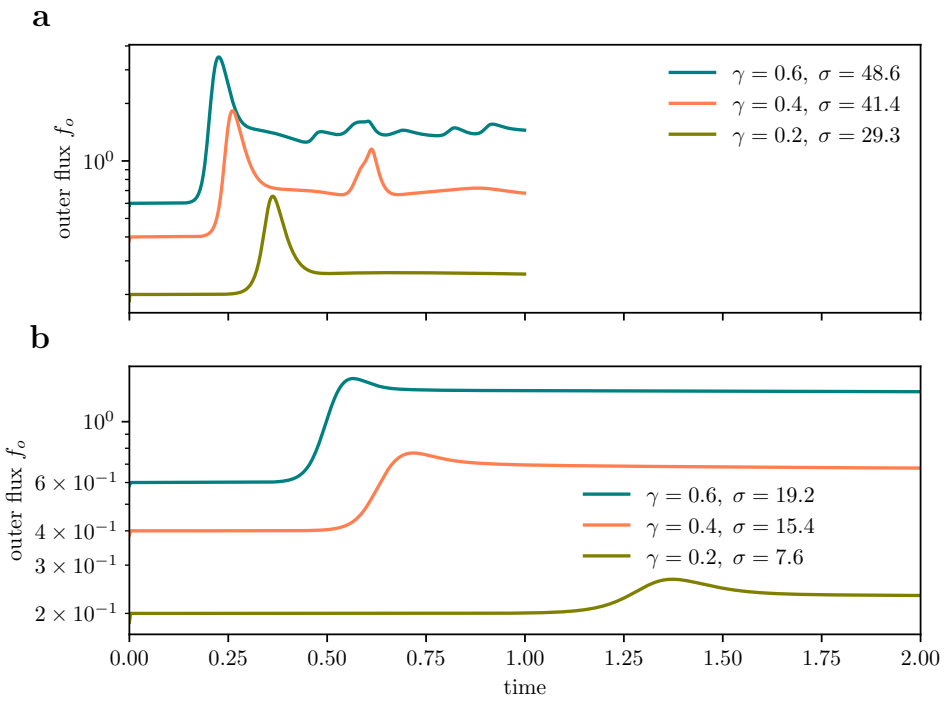

Figure 3.11: Temporal evolution of the dimensionless mean outer flux for $\mathcal{R}a = 1500$ and **a**- $\Phi = 6$ and **b**- $\Phi = 100$ for different aspect ration $\gamma = 0.6$ in blue line, $\gamma = 0.4$ in orange line and $\gamma = 0.2$ in green line.

3.4.2 Radius dependent gravity acceleration

This section investigates the influence of spatially varying gravitational acceleration on thermal convection by comparing two configurations: one with a uniform gravity field, as considered in previous sections, and another in which gravity increases linearly with radius. In this latter case, the gravitational acceleration is defined as

$$g(r) = -g_0 \frac{r}{R_o} \mathbf{e_r}, \tag{3.24}$$

where g_0 is the reference gravity at R_o and $\mathbf{e_r}$ is the radial unit vector. The dimensionless governing equations are modified accordingly. The continuity and energy equations remain unchanged, while the buoyancy term in the momentum equation now depends explicitly on the radial coordinate:

$$\boldsymbol{\nabla} \cdot \boldsymbol{u} = 0, \tag{3.25}$$

$$0 = -\boldsymbol{\nabla} p + \mathcal{R}aT \frac{r}{R_o} \mathbf{e_r} + \boldsymbol{\nabla^2 u}, \tag{3.26}$$

$$\frac{\partial T}{\partial t} + \boldsymbol{u} \cdot \boldsymbol{\nabla} T = \boldsymbol{\nabla}^2 T. \tag{3.27}$$

For the rest of this section, we consider the initial temperature profile described in eq. (3.20) and an aspect ratio $\gamma = 0.2$. We have modified the linear stability analysis code (`StablinRB`) to take into account a gravity varying linearly with radius. To quantify the impact of this radial gravity profile, we perform a LSA at fixed Rayleigh number while systematically varying the phase change parameter Φ. The results show that, for a given Φ, the onset of convection is slightly delayed when gravity increases with radius: growth rates are lower compared to the uniform gravity case (blue vs. orange line in fig. 3.12a). Consequently, a uniform gravitational field facilitates the development of convective instabilities. In addition, when gravity varies linearly with radius, the transition from the dominant spherical harmonic mode $l = 1$ to $l = 2$ occurs at slightly higher values of Φ (fig. 3.12b). This indicates that the radial dependence of gravity has a stabilizing effect on the lowest degree modes.

To further assess the dynamical impact of non-uniform gravity, we perform DNS at $\mathcal{R}a = 10^4$ and $\Phi = 6$, incorporating the same radial gravity profile. The mean surface heat flux is then used to characterize the vigor of convection. As shown in fig. 3.12c, convection sets in earlier and the surface heat flux is slightly higher in the case of uniform gravity (blue line) compared to the case with linearly increasing gravity (orange line). This reduction in convective efficiency is attributed to the fact that buoyancy forces are weaker near the inner boundary in the non-uniform case, where radial distance, and thus gravity, are smaller. This radius dependent gravity acceleration reduces the driving force for convective motions at depth, thereby delaying the onset and slightly weakening the overall heat transport.

3.4.3 Effect of the temperature profile

In the lunar context, the temperature distribution within the solidifying mantle is more curved than the conductive temperature profile (fig. 2.3 in Chapter 2). This temperature profile is typically derived analytically from the phase diagram and exhibits a sharp variation near the top of the mantle, over a relatively thin region. To capture this behavior while maintaining an analytical formulation, we approximate the temperature profile using a parabolic function defined as:

$$T(r) = \begin{cases} 1 & \text{if } R_i \leq r \leq (R_o - d), \\ -\dfrac{1}{d^2}(r - R_o + d)^2 + 1 & \text{if } (R_o - d) < r \leq R_o, \end{cases} \tag{3.28}$$

where the parameter d sets the thickness of the layer in which the temperature follows a parabolic profile (fig. 3.13). This parameterization allows us to systematically explore how the thickness of the region over which temperature varies affects convection. A

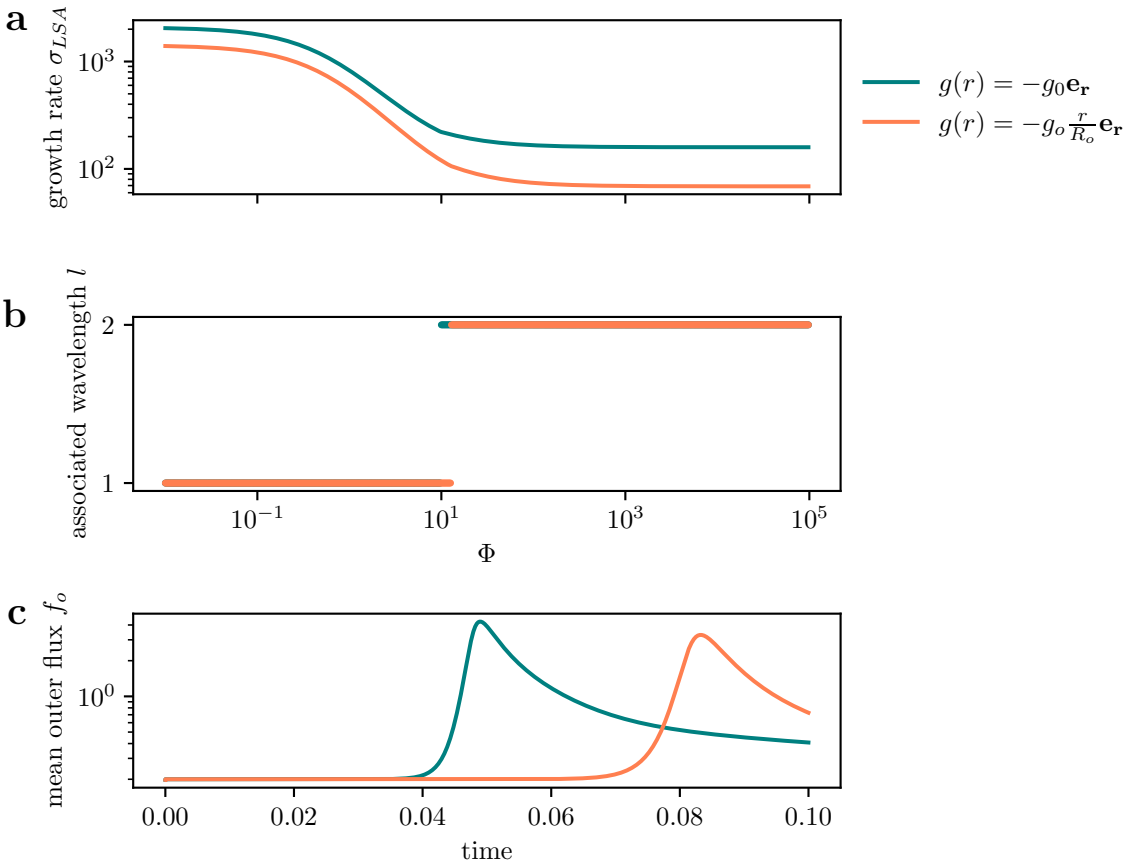

Figure 3.12: **a**- Growth rate and **b**-associated wavelength (LSA) as function of phase change number Φ for $\mathcal{R}a = 10^4$ with a uniform gravity acceleration, in blue line, and for a radius dependent gravity acceleration, in orange line. **c**- Temporal evolution of the dimensionless mean outer flux (DNS) for $\mathcal{R}a = 10^4$ and $\Phi = 6$ for a uniform gravity acceleration, in blue line, and for a radius dependent gravity acceleration, in orange line. The LSA and DNS are perfomed with a conductive initial temperature profile (eq. 3.20) and $\gamma = 0.2$. For the DNS the initial amplitude noise is $A = 10^{-3}$.

value of $d = R_o - R_i$ (corresponding to $d = H$, see section 3.1.1) corresponds to a temperature variation extending over the entire domain (blue line on fig. 3.13). This temperature profile is not a solution of the stationary diffusion equation (eq. 3.19), therefore, we use the "frozen-time" approach, in which we neglect the diffusive evolution of the reference temperature profile. This definition leads to an effective Rayleigh number, $\mathcal{R}a_E$, associated with the region where the temperature variation is effective:

$$\mathcal{R}a_E = \frac{\alpha\rho g\Delta T d^3}{\kappa\mu}, \tag{3.29}$$

which increases with d^3.

To isolate the effect of the curvature of the temperature profile on the dynamics, we

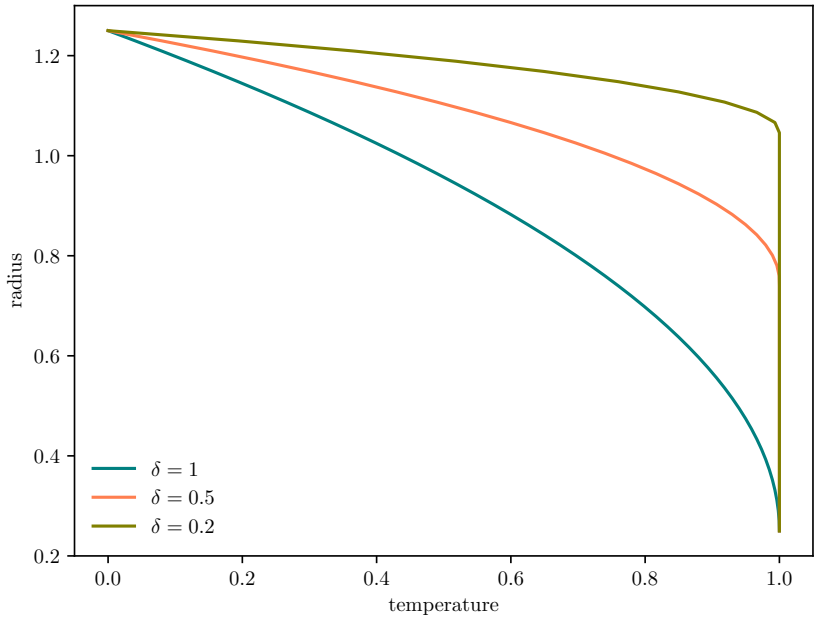

Figure 3.13: Dimensionless temperature profile according to eq. (3.28) as function of the dimensionless radius for dimensionless $\delta = 1$ in blue line, $\delta = 0.5$ in orange line and $\delta = 0.2$ in green line.

conducted simulations with fixed temperature boundary conditions, a uniform gravitational acceleration, a constant aspect ratio $\gamma = 0.2$, and dimensionless thickness δ. By varying δ, we assess the effect of the curvature of the temperature profile on the onset and characteristics of convection in the spherical shell. This approach enables us to evaluate how the localization of thermal buoyancy affects the convective behavior. Using LSA, we examine how the critical Rayleigh number $\mathcal{R}a_c$ evolves as a function of the thickness δ of the domain over which the temperature variation is effective (see fig. 3.14). The critical Rayleigh number corresponds to the minimum value of the Rayleigh number for which convection can develop in the spherical shell. We observe that $\mathcal{R}a_c$ decreases as δ increases. When $\delta \to 1$, $\mathcal{R}a_c$ approaches a lower limit. For values of δ close to 1, the temperature variation is effective throughout the entire shell. As the value of Φ increases, the critical Rayleigh number $\mathcal{R}a_c$ also becomes larger. This behavior is physically consistent, since a higher Φ corresponds to a non-penetrative boundary condition at the top of the cumulate (fig. 3.14a). In this case, it becomes more difficult for convection to develop, and a higher $\mathcal{R}a$ is therefore required to trigger the instability. The representation of $\mathcal{R}a_c\delta^3$ (fig. 3.14b) shows the opposite trend, *i.e.*, it increases with δ. Plotting $\mathcal{R}a_c\delta^3$ aims to test the influence of the effective temperature variation over the thickness δ on the onset of convection. If $\mathcal{R}a_c\delta^3$ is independent of δ, then only the temperature variation in

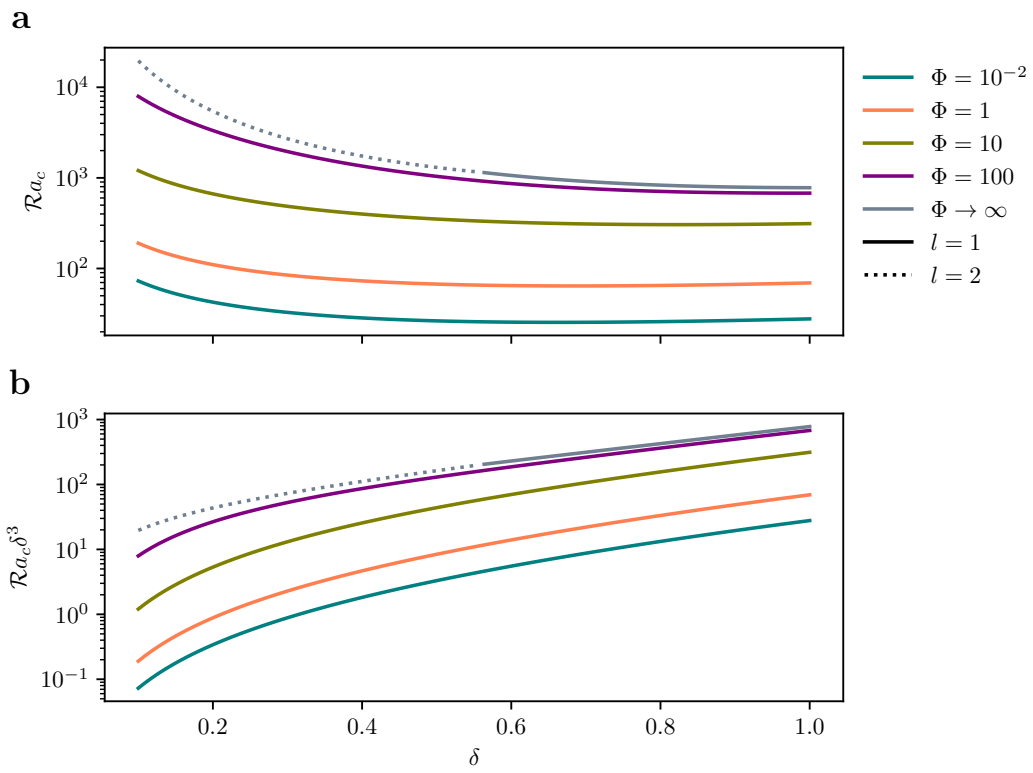

Figure 3.14: **a**- Evolution of the critical Rayleigh number $\mathcal{R}a_c$ and **b**- $\mathcal{R}a_c d^3$ as function of δ, the dimensionless proportion of the domain where the variation of temperature is effective for $\Phi = 10^{-2}$ in blue line, $\Phi = 1$ in orange line, $\Phi = 10$ in green line, $\Phi = 100$ in purple line, and $\Phi \to \infty$ in gray line. The solide lines correspond to $l = 1$ and the dotted line to $l = 2$.

the thickness δ influences the onset of convection. As shown in fig. 3.14b, this is not the case, even if the source of buoyancy is located in δ, because the deformation affects the entire shell, not just the layer of thickness δ. The onset of convection does not depend only on the thickness over which the temperature varies, but also takes into account a global mode, as it developps on the entire shell (with $\gamma = 0.2$).

A preferential convection mode with degree $l = 2$ is observed only in the limit where $\Phi \to \infty$ (fig. 3.14), particularly for small values of δ, that is, when the temperature variation occurs over a thin layer ($d < 0.56$). In all other cases, the dominant convective mode remains $l = 1$. When the temperature gradient is confined to a thin region and non-penetrative boundary condition is imposed, the system is more resistant to deformation. Under these conditions, convection is less efficient at developing large-scale flow (low-l modes) and instead favors smaller-scale structures corresponding to higher spherical harmonic degrees. This trend suggests that both the thickness of the layer where the temperature variation is effective and the permeability contrast play a key role in determining the spatial pattern of convection.

We now investigate the evolution of the growth rate σ_{LSA} as a function of δ, for fixed values of $\mathcal{R}a = 1500$ and $\mathcal{R}a = 10^7$, while varying $\Phi \in [10^{-2}, \infty[$ (fig. 3.15). This analysis complements the critical Rayleigh number trends discussed previously and provides insight into the temporal development of instabilities within the parameter ranges detailed above (see section 3.3). For $\mathcal{R}a = 1500$ and $\Phi = 10^{-2}$ or $\Phi = 1$, the growth rate increases slightly with δ, reaches a maximum around $d \sim 0.2$, and then gradually decreases. For the same Rayleigh number but with higher values of Φ ($\Phi = 10$, 100, and $\Phi \to \infty$), the growth rate increases and reaches a plateau. In particular, for $\Phi = 100$ and $\Phi \to \infty$, the growth rate becomes negative for $d < 0.38$ and $d < 0.45$, respectively, indicating that convection cannot develop in these cases.

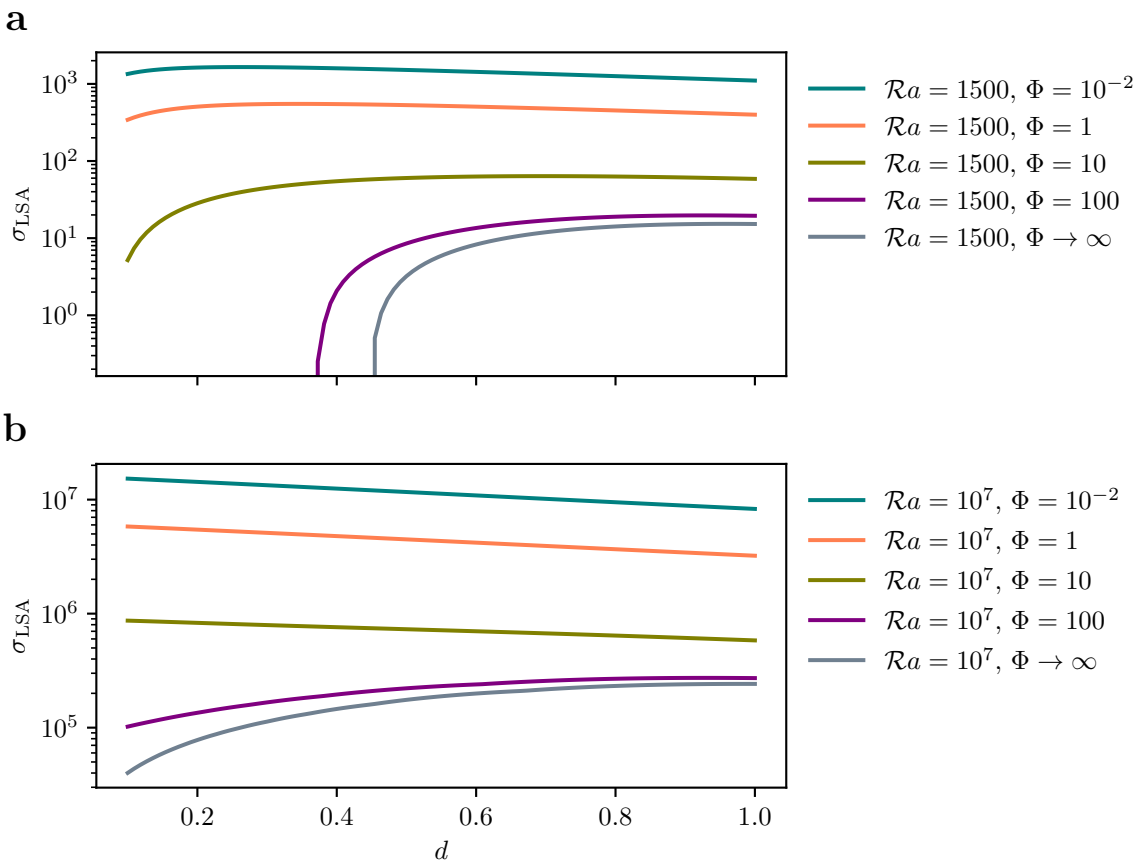

Figure 3.15: Evolution of the growth rate σ_{LSA} as function of δ the proportion of the domain where the variation of temperature is effective for $\Phi = 10^{-2}$ in blue line, $\Phi = 1$ in orange line, $\Phi = 10$ in green line, $\Phi = 100$ in purple line, and $\Phi \to \infty$ in gray line for $\gamma = 0.2$. **a** correspond to $\mathcal{R}a = 1500$ and **b** to $\mathcal{R}a = 10^7$.

For higher Rayleigh numbers (*i.e.*, $\mathcal{R}a = 10^7$), the behavior differs depending on the boundary condition: for permeable boundary conditions ($\Phi = 10^{-2}$, $\Phi = 1$ and $\Phi = 10$), the growth rate decreases slightly with δ (fig. 3.15a). On the contrary, while

for impermeable conditions ($\Phi = 100$ and $\Phi \to \infty$), the growth rate increases with δ (fig. 3.15b).

When the temperature gradient is restricted to a thinner region of the spherical shell (*i.e.*, for small δ), the effective Rayleigh number is reduced, which tends to delay the onset of convection, as observed in fig. 3.14. However, when a phase change boundary condition is imposed at the top of the spherical shell, this trend may reverse: the growth rate tends to decrease with δ. In particular, for high Rayleigh values, in the case of an impermeable condition ($\Phi = 100$ and $\Phi \to \infty$), the establishment of convection is mainly controlled by the thickness over which the temperature variation is effective. This is why the growth rate increases with δ, and larger l are observed at low δ. In this case, the phase change boundary condition alters the force balance near the boundary, reducing viscous dissipation and facilitating vertical motion. This allows convection to develop more easily, even when the unstable layer is thin. The maximum observed in the growth rate therefore results from the combined effect of increased buoyancy with increasing δ and improve the efficiency of convective transport enabled by the permeable interface at small to moderate δ.

It is not possible to compare the results of LSA with DNS in this section due to the diffusivity of the temperature profile. Indeed, at low Rayleigh numbers such as $\mathcal{R}a = 1500$, the growth rate is slow (fig. 3.15a). During this initial phase, the initial temperature profile has enough time to diffuse throughout the shell before convection begins. As a result, the temperature profile is no longer representative of the unstable base state configuration assumed in LSA (see Chapter 4).

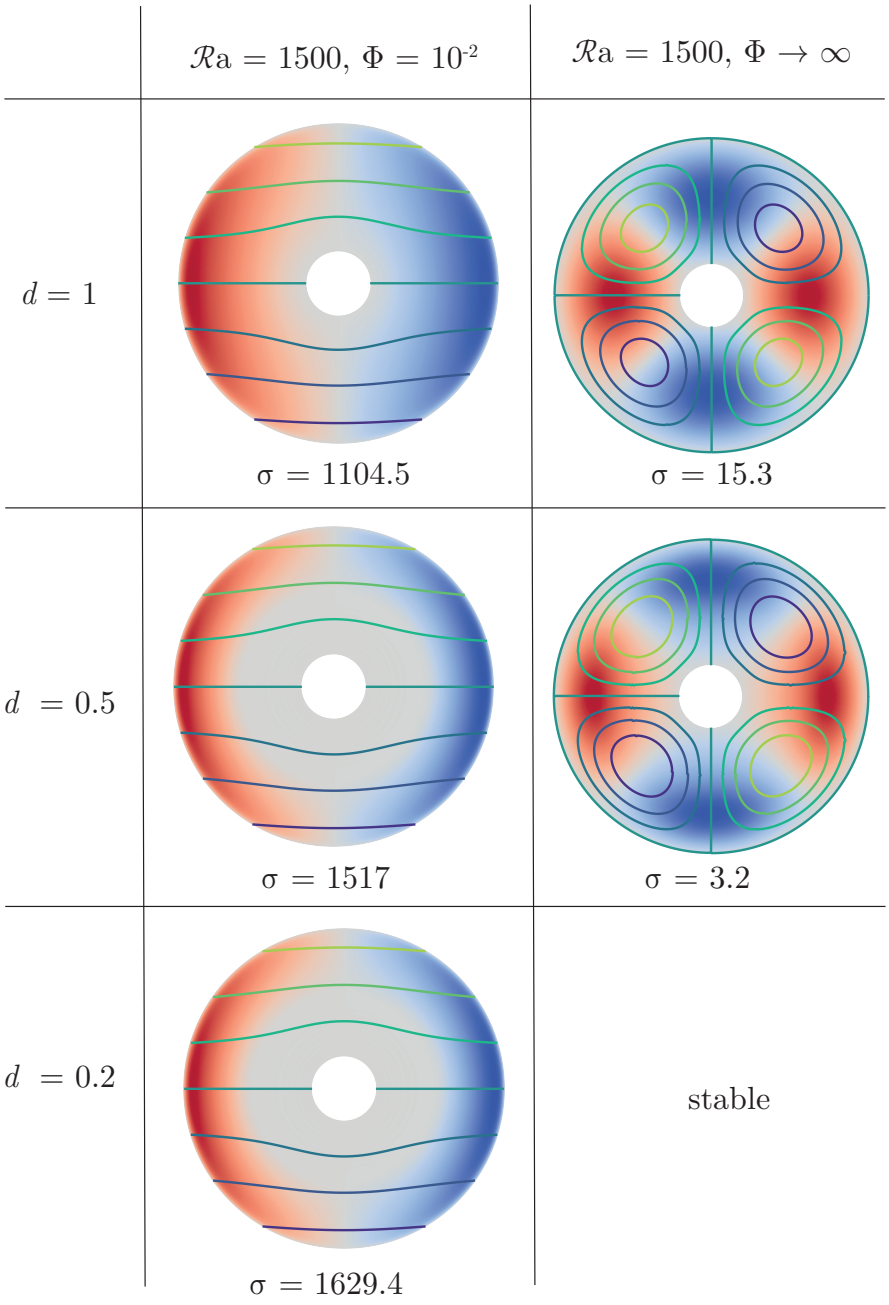

Figure 3.16: Temperature perturbation and streamlines of the most unstable mode for different values of $\mathcal{R}a$ and Φ depending of the thickness of effective temperature δ.

3.5 Conclusions

This chapter presents the two methods used in the following sections to investigate the overturn of lunar cumulates: linear stability analysis and direct numerical simulations. The comparison between these two approaches demonstrates the consistency of the results and provides validation for the direct numerical simulations, particularly since phase

change has not previously been incorporated into such simulations (previously explored only in a 2D spherical annulus geometry Morison, 2019). Additionally, I investigate how different parameters influence convection in lunar cumulates:

1. The aspect ratio (γ) controls the preferred mode of convection. In thin spherical shells (i.e., higher γ), the dominant convection mode shifts toward higher spherical harmonic degrees compared to cases with lower γ values.

2. Accounting for a gravitational acceleration that varies linearly with radius reduces the growth rate, thereby delaying the onset of convection.

3. Finally, I examine the influence of the curvature of the temperature profile. The results show that when temperature variations are confined to a thin thermal boundary layer, the onset of convection is delayed. However, this stabilizing effect can be partially compensated by the presence of phase change at the interface between the cumulates and the magma ocean.

Parameters for DNS

Table 3.2: List of DNS and parameters used. $\mathcal{R}a$ Rayleigh number, Φ phase change number, γ aspect ratio, safety for CFL, $\mathrm{dt}_{\mathrm{initial}}$ the initial time step for the simulation and also corresponds to the maximum value of time step allowed, N_ϕ resolusion in the N_θ N_r radial resolution.

	$\mathcal{R}$a	Φ	γ	safety	$\mathrm{dt}_{\mathrm{initial}}$	N_ϕ	N_θ	N_r	cadence	threshold	max_change	min_change	initial_noise	gravity	BC
1	10^4	6	0.2	2	10^{-5}	96	64	128	1	0.1	1.5	0.5	10^{-3}	cst	fixed temperature
2	10^4	6	0.2	2	10^{-5}	64	32	96	1	0.1	1.5	0.5	10^{-3}	cst	fixed temperature
3	10^4	10	0.2	2	10^{-5}	96	64	128	1	0.1	1.5	0.5	10^{-3}	cst	fixed temperature
4	10^4	50	0.2	2	10^{-5}	32	16	64	1	0.1	1.5	0.5	10^{-3}	cst	fixed temperature
5	10^4	100	0.2	2	10^{-5}	32	16	64	1	0.1	1.5	0.5	10^{-3}	cst	fixed temperature
6	10^4	10^4	0.2	2	10^{-5}	32	16	64	1	0.1	1.5	0.5	10^{-3}	cst	fixed temperature
7	10^4	30000	0.2	2	10^{-5}	32	16	64	1	0.1	1.5	0.5	10^{-3}	cst	fixed temperature
8	10^4	∞	0.2	2	10^{-5}	64	32	64	1	0.1	1.5	0.5	10^{-3}	cst	fixed temperature
9	5×10^3	6	0.2	2	10^{-5}	32	16	64	1	0.1	1.5	0.5	10^{-3}	cst	fixed temperature
10	5×10^3	50	0.2	2	10^{-5}	32	16	64	1	0.1	1.5	0.5	10^{-3}	cst	fixed temperature
11	5×10^3	100	0.2	2	10^{-5}	32	16	64	1	0.1	1.5	0.5	10^{-3}	cst	fixed temperature
12	5×10^3	3000	0.2	2	10^{-5}	32	16	64	1	0.1	1.5	0.5	10^{-3}	cst	fixed temperature
13	3×10^3	6	0.2	2	10^{-5}	32	16	64	1	0.1	1.5	0.5	10^{-3}	cst	fixed temperature
14	3×10^3	50	0.2	2	10^{-5}	32	16	64	1	0.1	1.5	0.5	10^{-3}	cst	fixed temperature
15	3×10^3	100	0.2	2	10^{-5}	32	16	64	1	0.1	1.5	0.5	10^{-3}	cst	fixed temperature
16	1.5×10^3	6	0.2	2	10^{-5}	32	16	64	1	0.1	1.5	0.5	10^{-3}	cst	fixed temperature
17	1.5×10^3	10	0.2	2	10^{-5}	32	16	64	1	0.1	1.5	0.5	10^{-3}	cst	fixed temperature
18	1.5×10^3	50	0.2	2	10^{-5}	32	16	64	1	0.1	1.5	0.5	10^{-3}	cst	fixed temperature
19	1.5×10^3	100	0.2	2	10^{-5}	32	16	64	1	0.1	1.5	0.5	10^{-3}	cst	fixed temperature
20	1.5×10^3	6	0.2	2	10^{-5}	32	16	64	1	0.1	1.5	0.5	10^{-3}	cst	fixed temperature
21	1.5×10^3	10	0.2	2	10^{-5}	32	16	64	1	0.1	1.5	0.5	10^{-3}	cst	fixed temperature
22	6×10^2	6	0.2	2	10^{-5}	32	16	64	1	0.1	1.5	0.5	10^{-3}	cst	fixed temperature
23	10^4	6	0.2	2	10^{-5}	64	32	96	1	0.1	1.5	0.5	10^{-3}	r	fixed temperature
24	10^4	6	0.4	2	10^{-5}	32	16	64	1	0.1	1.5	0.5	10^{-3}	cst	fixed temperature
25	10^4	50	0.4	2	10^{-5}	32	16	64	1	0.1	1.5	0.5	10^{-3}	cst	fixed temperature
26	10^4	100	0.4	2	10^{-5}	32	16	64	1	0.1	1.5	0.5	10^{-3}	cst	fixed temperature
27	10^4	1000	0.4	2	10^{-5}	32	16	64	1	0.1	1.5	0.5	10^{-3}	cst	fixed temperature
28	10^4	30000	0.4	2	10^{-5}	32	16	64	1	0.1	1.5	0.5	10^{-3}	cst	fixed temperature
29	3×10^3	6	0.4	0.5	10^{-5}	32	16	64	1	0.1	1.5	0.5	10^{-3}	cst	fixed temperature
30	3×10^3	50	0.4	0.5	10^{-5}	32	16	64	1	0.1	1.5	0.5	10^{-3}	cst	fixed temperature
31	3×10^3	100	0.4	0.5	10^{-5}	32	16	64	1	0.1	1.5	0.5	10^{-3}	cst	fixed temperature
32	3×10^3	1000	0.4	0.5	10^{-5}	32	16	64	1	0.1	1.5	0.5	10^{-3}	cst	fixed temperature
33	3×10^3	100	0.4	0.5	10^{-5}	32	16	64	1	0.1	1.5	0.5	10^{-3}	cst	fixed temperature
34	3×10^3	30000	0.4	0.5	10^{-5}	32	16	64	1	0.1	1.5	0.5	10^{-3}	cst	fixed temperature
35	1.5×10^3	6	0.4	0.5	10^{-5}	32	16	64	1	0.1	1.5	0.5	10^{-3}	cst	fixed temperature
36	1.5×10^3	100	0.4	0.5	10^{-5}	32	16	64	1	0.1	1.5	0.5	10^{-3}	cst	fixed temperature
37	1.5×10^3	6	0.6	0.5	10^{-5}	32	16	64	1	0.1	1.5	0.5	10^{-3}	cst	fixed temperature
38	3×10^3	100	0.6	0.5	10^{-5}	32	16	64	1	0.1	1.5	0.5	10^{-3}	cst	fixed temperature
39	$\times 10^3$	6	0.6	0.2	10^{-5}	32	16	64	1	0.1	1.5	0.5	10^{-3}	cst	fixed temperature
40	$\times 10^3$	50	0.6	0.2	10^{-5}	32	16	64	1	0.1	1.5	0.5	10^{-3}	cst	fixed temperature
41	$\times 10^3$	100	0.6	0.2	10^{-5}	32	16	64	1	0.1	1.5	0.5	10^{-3}	cst	fixed temperature
42	$\times 10^3$	1000	0.6	0.2	10^{-5}	32	16	64	1	0.1	1.5	0.5	10^{-3}	cst	fixed temperature

Chapter 4

Duration of the lunar overturn during magma ocean crystallization

Dans ce chapitre nous appliquons les méthodes dévelopées dans le chapitre précédent au cas de la Lune spécifiquement. Nous étudions le retournements des cumulats lunaires, en prenant comme état initial, l'évolution thermique de l'océan de magma lunaire. Nous nous plaçons au tout début de la seconde étape de cristallisation, au moment où la croûte commence à se former. Nous considérons un refroidissement séculaire et homogène du noyau, et nous tenons compte du changement de phase à l'interface cumulats/océan de magma. Nous montrons que le retournement peut se mettre en place bien avant la fin de la solidification de l'océan de magma lunaire, et qu'il se développe selon une harmonique sphérique de degré un. La durée de ce retournement est comprise entre quelques milions d'années à plusieurs dizaines de millions d'années. Ce retournement pourrait affecter la croissance et la stabilisation de la croûte si l'interface supérieure est suffisamment perméable et si le nombre de Rayleigh n'est pas trop élevé. Compte tenu de l'évolution thermique du noyau, ce renversement précoce pourrait générer une dynamo lunaire précoce. Ce chapitre a fait l'objet d'un article soumis dans le revue Earth and Planetary Science Letters.

abstract

The Moon presents a striking asymmetry between the nearside, which concentrates the lunar mare and shows a thin crust, and the farside, composed of thick anorthosite terranes. One proposed explanation for this asymmetry is a mantle overturn, driven by the instability of a dense, ilmenite-rich layer at the top of cumulates near the end of lunar magma ocean solidification. However, thermal instabilities may arise before the crystallization of this dense layer. In particular, material exchange by melting and crystallization at the magma ocean-cumulates boundary facilitates flow through the boundary and hence the onset of convection in the cumulates. Accounting for this flow-through interface, we investigate the onset and duration of a thermal overturn using linear stability analysis and direct numerical simulations. Our results show that a thermal overturn can initiate well before the end of magma ocean solidification, lasting from ten thousand years to tens of millions of years. The dominant convective mode corresponds to a spherical harmonic degree-one and could affect crustal growth and stabilization if the top interface is sufficiently flow-through and the Rayleigh number not too large. Taking into account the thermal evolution of the core, this early overturn could generate an early lunar dynamo.

4.1 Introduction

The giant impact hypothesis has emerged as the predominant model for the formation of the Moon. According to this hypothesis, the Moon was formed as a result of a massive collision between the proto-Earth and a planetary embryo. This highly energetic impact released enough energy to induce a fully molten Moon (Pritchard et al., 2000; Canup, 2012; Ćuk et al., 2012; Nakajima et al., 2014). Unlike the Earth, the Moon has retained a record of the early cooling and crystallization processes that followed the Lunar Magma Ocean (LMO) stage in its crustal structure. The lunar crust that forms the highlands is indeed primitive in age (Borg et al., 2023). A striking feature of the lunar crust, partly revealed by the GRAIL gravity survey, is the degree-one variation in its structure. The near side is significantly lower in topography than the far side. This degree-one variation in topography is attributed to a variation in crustal thickness, with a crust that is significantly thinner on the near side (20 km to 30 km), than on the far side (50 km to 60 km) (Wieczorek et al., 2013).

Several hypotheses have been proposed to explain this asymmetric structure of the crust. They include the influence of the position of the Moon relative to the Earth in its magma ocean stage, which could have generated a differential heating and a thinner crust on the near side (Roy et al., 2014), the secondary destabilization of a basal layer enriched in heat producing elements (Zhong et al., 2000a), the non-uniform distribution

of heat-producing elements in the lunar interior (Laneuville et al., 2013) and the unstable growth of a stagnant lid on top of a partially molten mantle (Watson et al., 2022b).

In the classical scenario of LMO crystallization, dense minerals such as olivine and pyroxene sink to the base of the mantle, forming cumulates. The lunar crust forms in a second stage, by flotation of buoyant plagioclase minerals, when anorthite begins to crystallize after $\sim 70 - 80\%$ of LMO solidification (Wood, 1970; Elkins-Tanton et al., 2011; Colin et al., 2024). Within this scenario, one proposed mechanism to account for the degree-one variation in lunar crustal structure is a mantle overturn driven by the crystallization of very dense ilmenite-bearing cumulates (IBC) in the final stage of LMO crystallization (Parmentier et al., 2002; Elkins-Tanton et al., 2002; Maurice et al., 2017; Boukaré et al., 2018). But models proposed for such a compositional overturn do not support the occurrence of a degree-one pattern (Maurice et al., 2024).

However, recent investigations by Boukaré et al. (2018) and Maurice et al. (2024) show that thermal instabilities can develop prior to ilmenite crystallization, thus before the end of LMO crystallization. The rapid (< 1000 yrs) first stage of LMO crystallization results indeed in an unstable temperature profile in the cumulates (Colin et al., 2024; Maurice et al., 2024). The second stage of LMO crystallization, involving the growth of an insulating anorthosite flotation crust, lasts in fact much longer, with crystallization timescales of at least 45 Myr and possibly reaching 200 Myr (Maurice et al., 2020; Colin et al., 2024). This long crystallization time could allow convection to develop before complete LMO solidification. In particular, Morison et al. (2019) demonstrated that material exchange between the cumulates and the LMO, related by phase equilibrium, hastens the onset of convection and favors the development of an instability in the form of a spherical harmonic of degree-one. However, Morison et al. (2019) only constrained the timescale for the onset of the overturn, not its duration. If a thermal overturn with a degree-one structure occurs before the end of LMO solidification, it could strongly influence the growth of the crust by releasing the excess heat stored in mantle cumulates into one hemisphere. In addition, the enhanced mantle cooling associated with this overturn could produce a sufficiently large heat flux at the lunar core-cumulates boundary to initiate an early dynamo, which could provide an explanation for the observations from paleomagnetic measurements of an early lunar dynamo (Cournède et al., 2012; Weiss et al., 2014; Nichols et al., 2021; Jung et al., 2024).

Here, we use linear stability analysis and three-dimensional spherical shell simulations to study the onset and duration of this lunar thermal overturn. We use the initial temperature profile in the cumulates given by the model of Colin et al. (2024) at the end of the first stage of LMO solidification and consider an exchange of material between the lunar cumulates and the LMO by introducing a phase-change boundary condition

(Deguen, 2013; Labrosse et al., 2018; Agrusta et al., 2019; Morison et al., 2019; Morison et al., 2024). We also model core cooling to evaluate whether this thermal overturn could trigger an early lunar dynamo and when.

4.2 Model

4.2.1 Thermal context

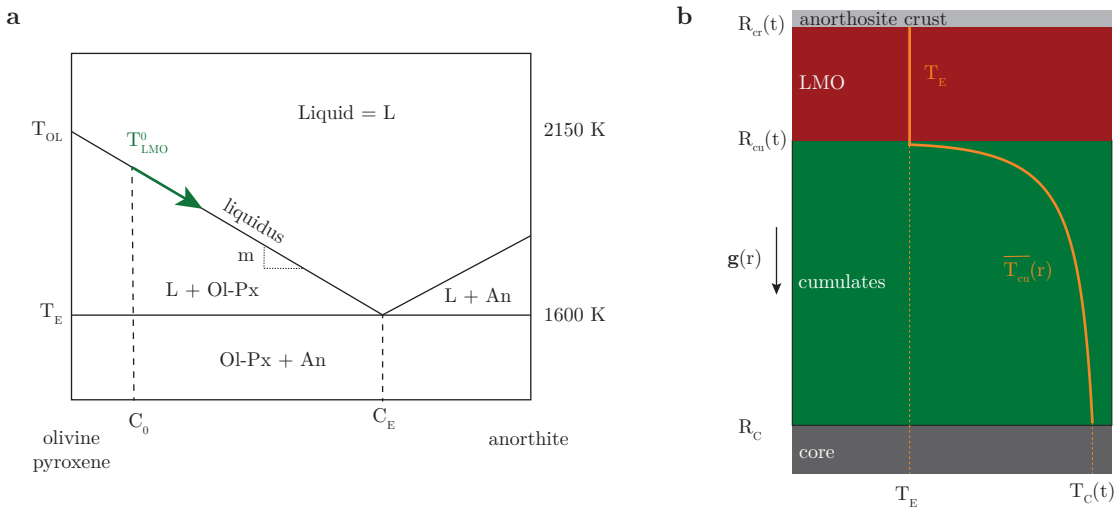

Figure 4.1: a) Simplified olivine-pyroxene anorthite phase diagram adapted from O'Driscoll et al. (2010), with T_{E} and C_{E}, the eutectic temperature and composition, m the liquidus slope and T^0_{LMO} and C_0 the initial temperature and composition of the LMO. b) Schematic of the structure of the Moon during LMO crystallization. The core is shown in dark gray, olivine-pyroxene cumulates in green, the LMO in red, and the crust in light gray. The initial temperature profile $\overline{T_{\mathrm{cu}}}(r)$ is in orange.

Solid-state convection in the lunar mantle is investigated in the context of LMO crystallization. The LMO solidification scenario considers that the primary crust forms by aggregation of buoyant anorthite minerals floating on the surface, while cumulates form by sedimentation of olivine and pyroxene crystals. We use the LMO solidification model of Colin et al. (2024), which is based on a simple binary eutectic phase diagram with two components: anorthite and olivine-pyroxene (fig. 4.1a). LMO solidification occurs in two stages. In the first stage, only olivine and pyroxene crystallize, forming cumulates. The liquidus temperature T_{liq} is assumed to vary linearly with the mass fraction in anorthite component $C(t)$:

$$T_{\mathrm{liq}} = T_{\mathrm{OL}} - mC(t), \tag{4.1}$$

with $T_{\rm OL}$ the liquidus temperature of the olivine-pyroxene component, and $m = \dfrac{T_{\rm OL} - T_{\rm E}}{C_{\rm E}}$ the liquidus slope, with $T_{\rm E}$ and $C_{\rm E}$, the eutectic temperature and composition. Mass conservation gives a relation between the initial composition in anorthite component C_0, the LMO composition $C(t)$, and the radius of cumulates $R_{\rm cu}(t)$:

$$\left(R_{\rm M}^3 - R_{\rm C}^3\right) C_0 = \left(R_{\rm M}^3 - R_{\rm cu}^3(t)\right) C(t) \tag{4.2}$$

with $R_{\rm M}$ the radius of the Moon and $R_{\rm C}$ the radius of the core. At the end of the first stage, $C(t) = C_{\rm E}$ and $(C_{\rm E} - C_0)/C_{\rm E}$ correspond to the fraction of LMO crystallized at that time. The first stage is very fast: in $\sim 300\,$yr, 80% of the LMO has crystallized. The first stage being too short for diffusion to proceed, the temperature profile in the cumulates is obtained by combining eq. (4.1) and eq. (4.2):

$$T_{\rm cu}(r) = T_{\rm OL} - mC_0 \frac{R_{\rm M}^3 - R_{\rm C}^3}{R_{\rm M}^3 - r^3} \quad \text{for} \quad R_{\rm C} \leq r \leq R_{\rm cu}. \tag{4.3}$$

The temperature gradient at the end of the first stage is super-isentropic and thus prone to instability and overturn (fig. 4.1b). The timescale for the onset of cumulate instability/overturn may be short, but is likely longer than this first stage of solidification (Morison et al., 2019). However, Morison et al. (2019) investigated the onset of instability/overturn using a temperature profile based on a generic pressure- and composition-dependent phase diagram that did not include the eutectic included here, which is necessary to the crystallization of an anorthositic crust. When the eutectic is reached in the LMO, anorthite starts to crystallize (fig. 4.1a) and floats, forming a conductive and insulating lid, which makes the remaining $\sim 20\%$ of the LMO crystallize in 45 to 200 Myr (Colin et al., 2024). Our goal is to evaluate whether a thermal overturn of the cumulates may then occur before the end of the second stage.

4.2.2 Convection equations in the cumulates

We investigate solid-state convection within the cumulates, which are bounded above by the liquid LMO, with temperature T_E and density $\rho_{\rm mo}$, and underneath by the core of temperature $T_{\rm co}(t)$. The cumulates form a spherical shell of inner radius $R_{\rm C}$ and outer radius $R_{\rm cu}$ with density $\rho_{\rm cu}$. We note $\Delta\rho = \rho_{\rm cu} - \rho_{\rm mo}$, with $\rho_{\rm cu} > \rho_{\rm mo}$. During LMO crystalization, heat-producing elements are retained within the liquid phase; thus, we neglect internal heating in the cumulates. We assume that the cumulate layer behaves as a Newtonian fluid with constant viscosity $\eta_{\rm cu}$ independent of temperature and pressure. This assumption is justified by the relatively small temperature variation $T_{\rm co} - T_{\rm E} = 550\,$K within the cumulates, the temperature at the upper boundary being that of melting.

Gravity varies linearly with radius r following $\mathbf{g} = -g_0 \frac{r}{R_{\rm cu}} \mathbf{e_r}$, where $\mathbf{e_r}$ is the unit vector in the radial direction and g_0 the gravity acceleration at the top of the cumulates. We adopt the infinite–Prandtl–number approximation, appropriate for mantle materials, implying negligible inertial effects. Under the Boussinesq approximation, density variations are considered negligible except in the buoyancy term. The density evolves with temperature following:

$$\rho = \rho_{\rm E} \left(1 - \alpha \left(T - T_{\rm E}\right)\right), \tag{4.4}$$

where $\rho_{\rm E}$ and $T_{\rm E}$ are the reference density and temperature, respectively, chosen at the eutectic point, and α is the thermal expansion coefficient which is considered constant. With these assumptions, the equations for the conservation of mass, momentum, and energy write:

$$\boldsymbol{\nabla} \cdot \boldsymbol{u} = 0, \tag{4.5}$$

$$0 = -\boldsymbol{\nabla} p + \rho_0 \alpha (T - T_{\rm E}) g_0 \frac{r}{R_{\rm cu}} \mathbf{e_r} + \eta_{\rm cu} \boldsymbol{\nabla^2} \boldsymbol{u}, \tag{4.6}$$

$$\frac{\partial T}{\partial t} + \boldsymbol{u} \cdot \boldsymbol{\nabla} T = \kappa \boldsymbol{\nabla}^2 T, \tag{4.7}$$

with $\boldsymbol{u}$ the flow velocity, T the temperature, and p the dynamic pressure. Using the lengthscale $H = R_{\rm cu} - R_{\rm C}$, the diffusive time scale $t_{\rm diff} = \dfrac{H^2}{\kappa}$, and the initial temperature difference $\Delta T = T_{\rm LMO^0} - T_E$, with $T_{\rm LMO^0}$ the initial temperature in the LMO, as the temperature scale, the conservation equations can be made dimensionless as follow:

$$\boldsymbol{\nabla} \cdot \boldsymbol{u} = 0, \tag{4.8}$$

$$0 = -\boldsymbol{\nabla} p + \mathcal{R}a \frac{H}{R_{\rm cu}} \Theta r \mathbf{e_r} + \boldsymbol{\nabla^2} \boldsymbol{u}, \tag{4.9}$$

$$\frac{\partial \Theta}{\partial t} + \boldsymbol{u} \cdot \boldsymbol{\nabla} \Theta = \boldsymbol{\nabla}^2 \Theta, \tag{4.10}$$

with $\Theta = \dfrac{T - T_{\rm E}}{\Delta T}$ and using the same symbols for velocity and pressure as for the dimensional equations, for the sake of simplicity. The Rayleigh number is defined as $\mathcal{R}a = \dfrac{\alpha \rho_{\rm E} g_0 \Delta T H^3}{\kappa \eta_{\rm cu}}$.

4.2.3 Boundary conditions

Thermal Boundary conditions

At the upper boundary of the cumulate layer, the material is in contact with the LMO, which is maintained at the constant eutectic temperature T_E:

$$T(r = R_{\mathrm{cu}}) = T_E. \tag{4.11}$$

At the base of the cumulate layer, the material is in contact with the core, which is assumed well mixed and at a uniform temperature T_{co}. We allow for core cooling and solve the following energy balance equation:

$$\rho_{\mathrm{co}} c_{p,co} \frac{4}{3} \pi R_{\mathrm{C}}^3 \frac{\mathrm{d}T_{\mathrm{co}}}{\mathrm{d}t} = -4\pi R_{\mathrm{C}}^2 q_{\mathrm{co}}, \tag{4.12}$$

with ρ_{co}, $c_{p,co}$ the density and specific heat capacity of the core, respectively. The heat flux q_{co} extracted from the core is given by Fourier's law:

$$q_{\mathrm{co}} = -k_{\mathrm{cu}} \frac{\partial T}{\partial r}\bigg|_{r=R_{\mathrm{C}}}, \tag{4.13}$$

with k_{cu} the thermal conductivity of the cumulates.

In dimensionless form, the temperature boundary conditions are:

$$\Theta = 0, \text{ at the top,} \tag{4.14}$$

$$\frac{\partial \Theta}{\partial t} = \frac{3H}{R_{\mathrm{C}}} \frac{\partial \Theta}{\partial r}, \text{ at the bottom.} \tag{4.15}$$

Mechanical boundary conditions

The interface between the LMO and the cumulates is assumed to be in phase equilibrium, which imposes a specific mechanical boundary condition. The stress associated to convective flows in the solid generates a dynamic topography at horizontal boundaries, whose height is limited by the weight that viscous forces can support. Its development occurs on a timescale

$$\tau_\eta = \frac{\eta_{\mathrm{cu}}}{|\Delta\rho| g H}, \tag{4.16}$$

similar to the post-glacial rebound timescale on Earth (e.g. Turcotte et al., 2002). In the thermal evolution model, we assumed that the temperature within the LMO is constant and does not vary with pressure (Colin et al., 2024). In reality, the eutectic tempera-

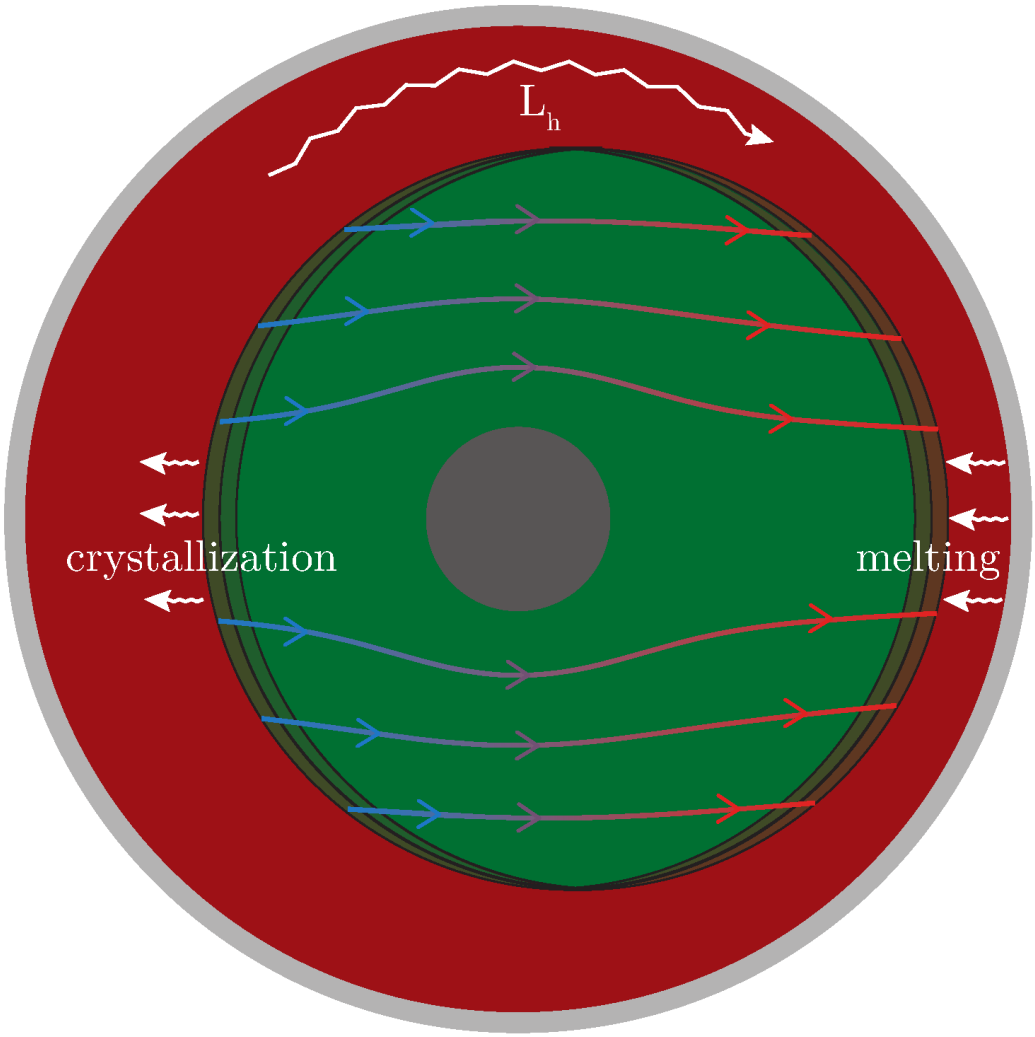

Figure 4.2: Schematic of the structure of the Moon during the crystallization of the lunar magma ocean (LMO), with exaggerated dynamic topography at the mantle-LMO boundary. The core is shown in dark gray, the olivine-pyroxene cumulates in green, the LMO in red and the crust in light gray. The white arrows correspond to the latent heat released by crystallization in topographic lows, transported by convection in the LMO and used for melting on topographic highs. The red-blue arrows represent the flow lines inside the cumulates.

ture increases with pressure by ∼100 K per 1 GPa (Presnall et al., 1978; Latypov et al., 2020). The energy released by LMO cooling along the eutectic as pressure decreases is much smaller than latent heat released by crystallization, justifying this assumption of a constant eutectic temperature. However, the dynamical effect of this variation may be important. For a positive topography relative to the mean interface, the melting temperature is lower, while a negative topography results in a higher melting temperature at the interface (see fig. 1 in Labrosse et al., 2018). This results in lateral temperature variations in the liquid above the interface which trigger convection in this layer. Convection in the LMO acts against these lateral variations, and tends to erase the topography by melting and crystallization, over a timescale τ_ϕ, the phase change timescale. This timescale corresponds to the time needed to transport latent heat in the magma ocean, from freezing areas, where it is released, to melting areas, where it is consumed (Deguen, 2013; Labrosse et al., 2018). It can be expressed as follows:

$$\tau_\phi = \frac{\rho_s L_h}{\left(\rho_s - \Delta\rho\right)^2 c_{p,l} g \left(\dfrac{\partial T_E}{\partial P} - \dfrac{\partial T_{\mathrm{ad}}}{\partial P}\right) u_{\mathrm{LMO}}}, \tag{4.17}$$

with uLMO the velocity scale in the LMO, $\dfrac{\partial T_{\mathrm{ad}}}{\partial P}$ the adiabatic gradient, $\dfrac{\partial T_E}{\partial P}$ the variation of the eutectic temperature with pressure and $c_{p,l}$ the heat capacity of the LMO. A detailed explanation is given in Deguen (2013), Labrosse et al. (2018), Agrusta et al. (2019), Morison et al. (2019), and Morison et al. (2024).

Writing the continuity of normal stress across the phase-change boundary, the mechanical boundary condition is given by (Deguen, 2013; Labrosse et al., 2018; Morison et al., 2019):

$$\Delta\rho g \tau_\phi u_r + 2\eta_{\mathrm{cu}} \frac{\partial u_r}{\partial r} - p = 0. \tag{4.18}$$

In dimensionless form, eq. (4.18) becomes:

$$\Phi u_r + 2\frac{\partial u_r}{\partial r} - p = 0, \tag{4.19}$$

with

$$\Phi = \frac{\tau_\phi}{\tau_\eta}, \tag{4.20}$$

a dimensionless number that quantifies the exchange between solid and liquid at the boundary. Equation (4.19) implies that u_r tends to zero at the boundary as $\Phi \to \infty$. This is the classical no-penetration or impermeable boundary condition. In the other end-member situation, as $\Phi \to 0$, the radial velocity, u_r is not required to be null at the boundary, which is therefore flow-through. In that case, exchange of material is

straightforward between the magma ocean and the crystallization layer. Owing to the small viscosity of both the magma and the liquid core, free-slip conditions are applied to both boundaries of the solid layer, corresponding to null shear stress in the tangential directions:

$$\tau_{r\theta} = 0 \Rightarrow r \frac{\partial}{\partial r}\left(\frac{u_\theta}{r}\right) + \frac{1}{r}\frac{\partial u_r}{\partial \theta} = 0, \tag{4.21}$$

$$\tau_{r\phi} = 0 \Rightarrow r \frac{\partial}{\partial r}\left(\frac{u_\phi}{r}\right) + \frac{1}{r\sin\theta}\frac{\partial u_r}{\partial \phi} = 0. \tag{4.22}$$

At the base of the cumulates ($r = R_C$), phase change is not allowed, as the core and the cumulates are not related by a phase equilibrium. In absence of a phase-change flux, the boundary condition is non-penetrative which implies:

$$u_r(r = R_C) = 0. \tag{4.23}$$

4.2.4 Initial conditions

We adopt as initial temperature profile the one resulting from the first stage of LMO crystallization (eq. 4.3). To initiate convection, we add a small-amplitude random thermal perturbation to the temperature field, without imposing any specific spherical harmonic structure. This initial white noise is characterized by an amplitude A, and plays a key role in controlling the onset time of the overturn. The amplitude is set to $A = 10^{-3}$, corresponding to a temperature variation of about 1 K, which appears reasonable for the lunar mantle. The results show that varying the initial amplitude A only affects the onset time of the overturn (see Supplementary Materials, fig. S3).

4.2.5 Range of parameters

The least well known of the physical parameters entering the definition of the Rayleigh number is the viscosity. Assuming a reasonable range η_{cu} =10^{17} Pa s to 10^{21} Pa s, we obtain a range of $\mathcal{R}a = 10^5$ to 10^8 for the Rayleigh number.

The phase change number Φ, which controls the efficiency of flow-through at the interface between the cumulates and the LMO, ranges from 10^{-4} to 10, according to eq. (4.20) and table S1 (in Supplementary Materials). This variability reflects the combined influence of the viscosity of cumulates η_{cu}, the variation of the eutectic temperature with pressure, and the dynamics of the LMO. The velocity inside the LMO, u_{LMO}, based on the heat flux through the flotation crust given by our thermal evolution model, is estimated to be on the order of 10^{-3} m s^{-1} to 10^{-2} m s^{-1} (eq.(26) in Solomatov, 2015) which is used in the estimation of Φ. Based on previous studies, such low values of Φ suggest that the boundary is predominantly flow-through.

4.3 Numerical methods

4.3.1 Linear stability analysis

The linear stability analysis (LSA) follows the approach of Morison et al. (2019) and Morison et al. (2024), and makes use of the numerical tool `StablinRB`. In this framework, we consider a steady background temperature profile and study the growth of infinitesimal perturbations to this state. The perturbations are expanded on spherical harmonics $Y_l^m(\theta, \phi)$ for the angular dependence and on Chebyshev polynomials for the radial dependence. The problem is then discretized radially using a Chebyshev collocation method and formulated as a generalized eigenvalue problem, whose eigenvalues σ_{LSA} represent the growth rates of the perturbations. The most unstable convective mode corresponds to the spherical harmonic degree l associated with the largest growth rate σ_{LSA}. As explained in Morison et al. (2024), the problem is degenerate with respect to the order m of the spherical harmonics and only depends on its degree l.

4.3.2 Direct numerical simulations

To solve the system of equations presented in section 4.2.2, we perform direct numerical simulations (DNS) using the `Dedalus` code (Burns et al., 2020). `Dedalus` is an open-source, parallel spectral solver designed for partial differential equations in general geometries. In this study, it is employed to simulate thermal convection with phase-change boundary conditions at the upper surface. The DNS approach yields the full spatio-temporal evolution of the temperature, velocity, and pressure fields, enabling the computation of convective flux and the characterization of dominant modes through spherical harmonic spectral analysis. This method allows us to follow the complete dynamical evolution of the system, from the initial temperature profile. In numerical simulations, we use dimensionless values for the cumulate and core radius, noted R_o and R_i respectively and computed as a function of the aspect ratio $\gamma = \dfrac{R_\mathrm{C}}{R_\mathrm{cu}} = \frac{R_i}{R_o}$ (see Supplementary Materials table S1).

4.4 Results

4.4.1 Study of a reference case

The range of parameters estimated for the lunar cumulates, as discussed in section 4.2.5, cannot be explored entirely by DNS, due to numerical limitations. In practice, we only get solutions for low values of $\mathcal{R}a$ and large values of Φ. The most extreme choice of

parameters, which we use as reference case in the following, corresponds to $\mathcal{R}a = 10^4$ and $\Phi = 6$. It is possible to run cases with a larger Rayleigh number only for larger values of Φ, for which the boundary condition is non-penetrative. The reference case is, among all runs we could complete, the one with the highest value of $\mathcal{R}a$ for $\Phi < 10$.

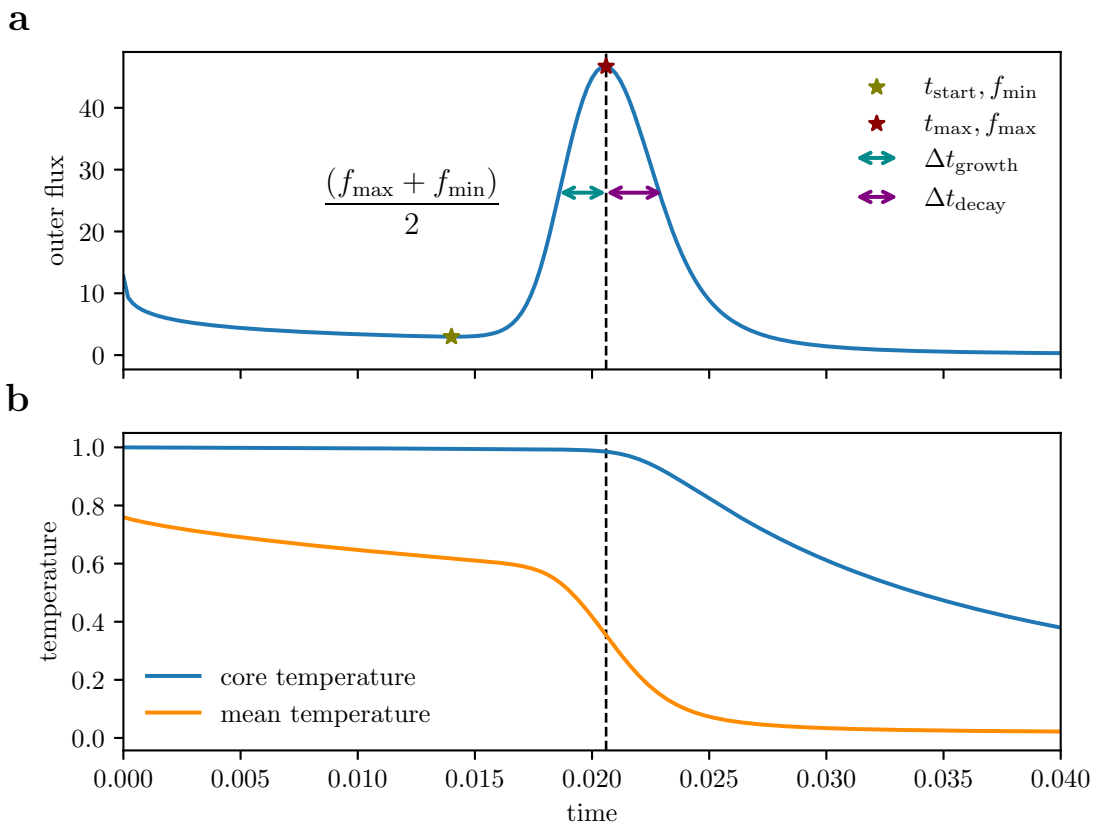

Figure 4.3: a) Temporal evolution of the average dimensionless heat flux at the top of the cumulates for $\mathcal{R}a = 10^4$ and $\Phi = 6$. The green and red stars correspond to the local minimum and maximum fluxes f_{min} and f_{max} respectively, occurring at t_{start}, defined as the onset time of the overturn and t_{max}. The blue and purple arrows correspond respectively to Δt_{growth} and Δt_{decay}. b) Temporal evolution of the dimensionless core temperature in blue and mean temperature inside the cumulates in orange. The vertical dashed line correspond to t_{max}.

The dimensionless heat flux at the top of the cumulate layer, f_o, evolves with time, reaching a peak value f_{max} at time t_{max} (fig. 4.3a). Prior to this maximum, the outer flux first slightly decreases, it reaches a local minimum noted f_{min} at t_{start}, before increasing significantly up to f_{max} as the overturn proceeds. We define the growth time, Δt_{growth}, as the duration between the time when the flux reaches the average of min and max values, $f_{mid} = (f_{max} + f_{min})/2$, and t_{max}. After reaching f_{max}, the flux decreases rapidly. The decay time, Δt_{decay}, is defined as the interval between t_{max} and the time when the flux falls

back to f_{mid} during the downward phase. We define the total duration of the overturn as $\Delta t_{\text{total}} = \Delta t_{growth} + \Delta t_{decay}$. These different times are used to quantify the duration of the overturn.

Initially, the core temperature remains nearly constant (fig. 4.3b); it starts to decrease at time $t_{\max}$, indicated by the vertical dashed line on fig. 4.3, coinciding with the peak of the outer flux. Meanwhile, the mean temperature $\overline{T}(t)$ decreases towards zero, and exhibits a rapid decay over the duration of the overturn Δt_{total}. The temporal evolution of the mean and core temperatures is an indicator of the thermal transfer during the overturn of the spherical shell. The decrease in core temperature at $t_{\max}$, coincides with the decrease of the convection and marks the transition where the overturn decays.

4.4.2 Effects of $\mathcal{R}a$ and Φ

In this section, we study the effects of the two dimensionless numbers that characterize our problem: the Rayleigh number $\mathcal{R}a$ and the phase change number Φ. We investigate the time evolution of the surface heat flux for a series of calculations exploring solid-state convection in the cumulates topped by the LMO, while accounting for core cooling (fig. 4.4).

We systematically vary the Rayleigh number $\mathcal{R}a$ and the phase change number Φ. The reference case ($\mathcal{R}a = 10^4$, $\Phi = 6$, orange line in fig. 4.4) exhibits a rapid onset of convection followed by a brief but intense overturn phase. When $\Phi \to \infty$ with the same Rayleigh number (green line in fig. 4.4), the onset of convection is delayed, the overturn lasts longer and the surface heat flux is significantly reduced, consistent with the suppression of matter exchange at the boundary with the LMO.

Lowering the Rayleigh number to $\mathcal{R}a = 3\times10^3$ while keeping $\Phi = 6$ (red line in fig. 4.4) also delays the onset of convection compared to the reference case, though it precedes the non-penetrative case. The overturn is prolonged, and the flux remains weaker than for $\mathcal{R}a = 10^4$.

A similar trend is observed when comparing the cases with $\mathcal{R}a = 10^5$ (blue line in fig. 4.4) and 10^4 for a phase change number $\Phi \to \infty$: a lower Rayleigh number results in a delayed onset of the overturn and a reduced heat flux, while the overturn extends over a longer period. These results demonstrate that both the vigor and temporal characteristics of convection are sensitive to the boundary permeability and thermal buoyancy. A decrease in the Rayleigh number and an increase in the phase change number Φ both tend to delay the onset of the overturn, prolong its duration, and reduce its intensity.

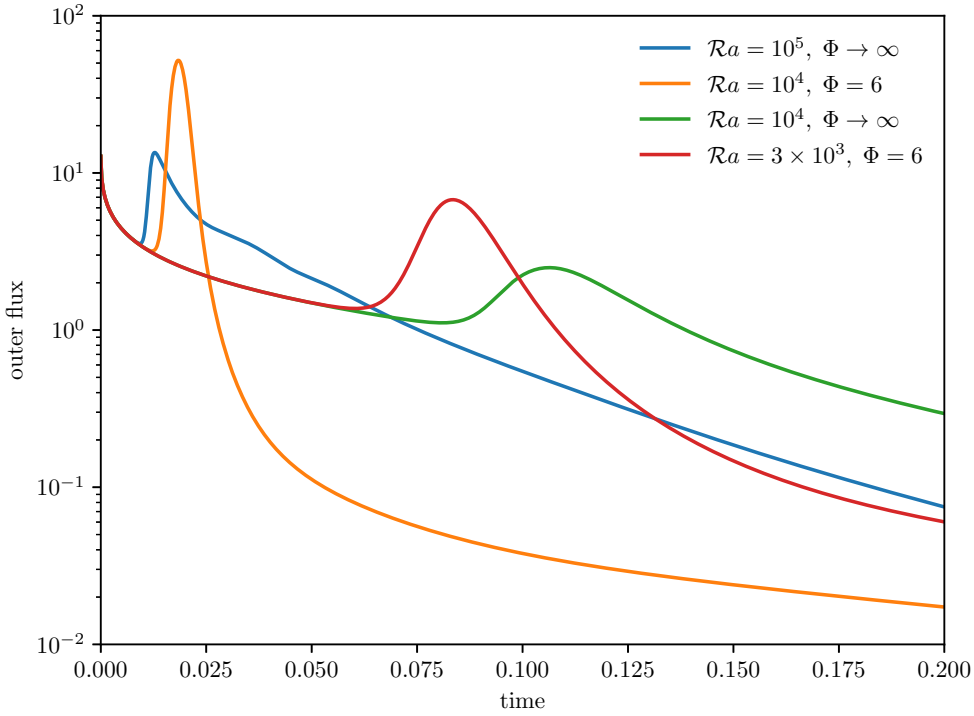

Figure 4.4: Dimenisonless temporal evolution of the heat flux at the top of the cumulates for different cases: $\mathcal{R}a = 10^5, \Phi \to \infty$ in blue line, $\mathcal{R}a = 10^4, \Phi = 6$ in orange line, $\mathcal{R}a = 10^4, \Phi \to \infty$ in green line and $\mathcal{R}a = 3 \times 10^3, \Phi = 6$ in red line.

As Φ increases, the dominant convective mode transitions to higher-order structures (fig. 4.5). For $\Phi = 6$, the convective pattern is dominated by a mode with spherical harmonics of degree $l = 1$, with a single plume confined to one hemisphere, for all values of $\mathcal{R}a$ used in DNS. However, in the $\Phi \to \infty$ limit, the convective mode shifts to $l = 2$ for $\mathcal{R}a = 10^4$ and a combination of different modes for $\mathcal{R}a = 10^5$, dominated by a degree two. A clear signature of this behavior is observed in the distribution of the surface flux along the cross–section (red ligne in fig. 4.5). For the two cases where $\Phi = 6$, the flux is concentrated within a single hemisphere and vanishes elsewhere, consistent with a dominant spherical harmonics of degree $l = 1$. The increase in the Rayleigh value shows a sharper transition between the hemisphere with null flux and the hemisphere with maximum flux and a larger peak value. As the $\mathcal{R}a$ number increases, deformation and convective circulation are indeed facilitated. Lower values of Φ favor convective patterns of longer wavelengths, as shown by the linear stability analysis of Morison et al. (2024). In contrast, in the limit $\Phi \to \infty$, corresponding to the classic non-penetrative case, the dominant convective mode shifts to higher spherical harmonics.

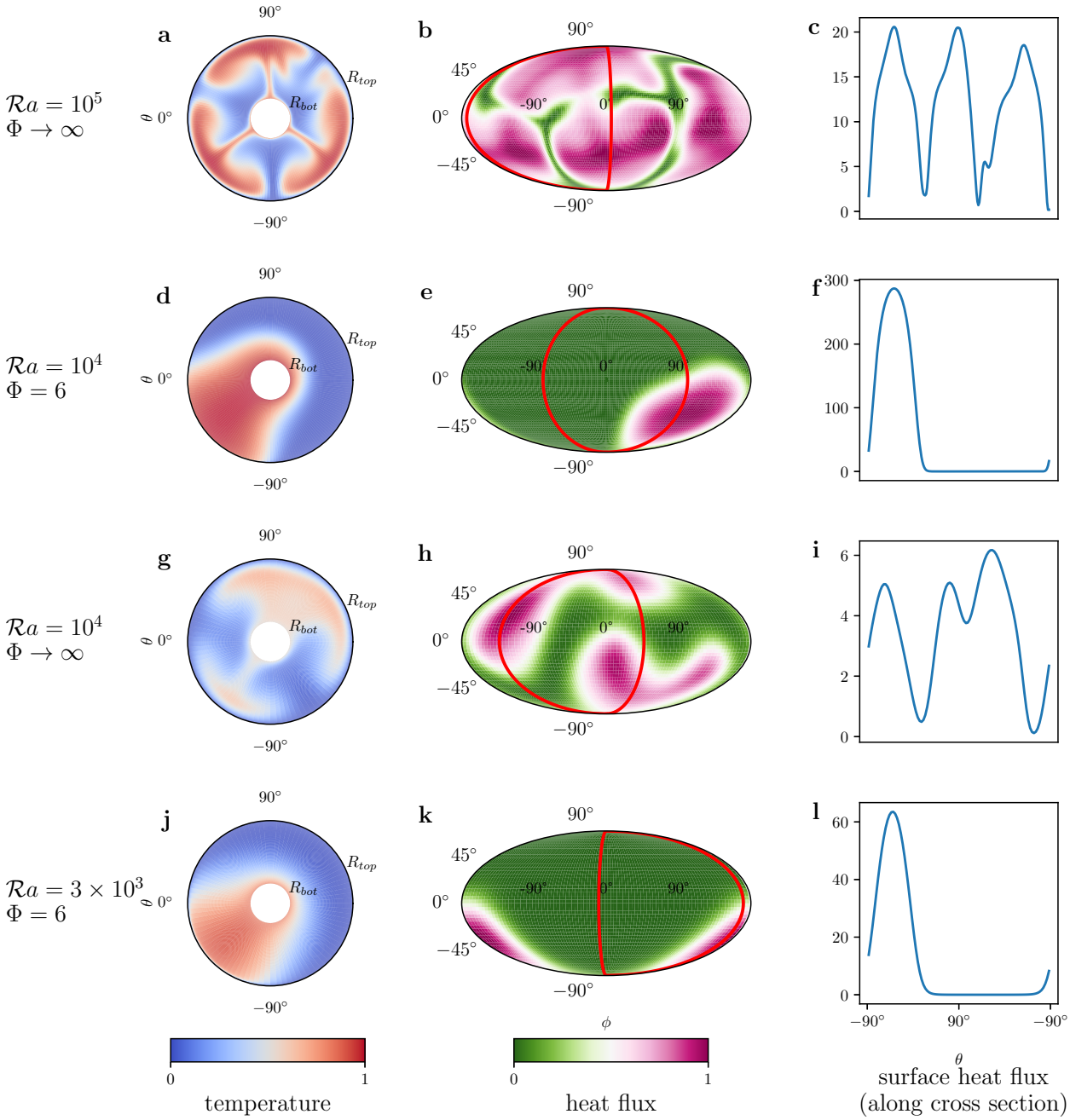

Figure 4.5: Snapshots from numerical simulations for the cases presented on fig. 4.4- $\mathcal{R}a = 10^5$ and $\Phi \to \infty$ (a, b, c), $\mathcal{R}a = 10^4$ and $\Phi = 6$ (d, e, f), $\mathcal{R}a = 10^4$ and $\Phi \to \infty$ (g, h, i) and $\mathcal{R}a = 3 \times 10^3$ and $\Phi = 6$ (j, k, l)- at $t_{\max}$ for each case, showing the temperature field in a cross section (a, d, g, j), surface heat flux at the top of the cumulates (b, e, h, k, Mollweide projection), and the surface heat flux along the cross section going through the poles and the maximum in surface heat flux and represented by the red lines on the middle plots (c, f, i, l). Both the temperature and flux fields have been renormalized to their extremal values to keep the same colorbar for all cases. The actual flux values are visible on panels c, f, i, l.

4.4.3 Comparison with linear stability analysis

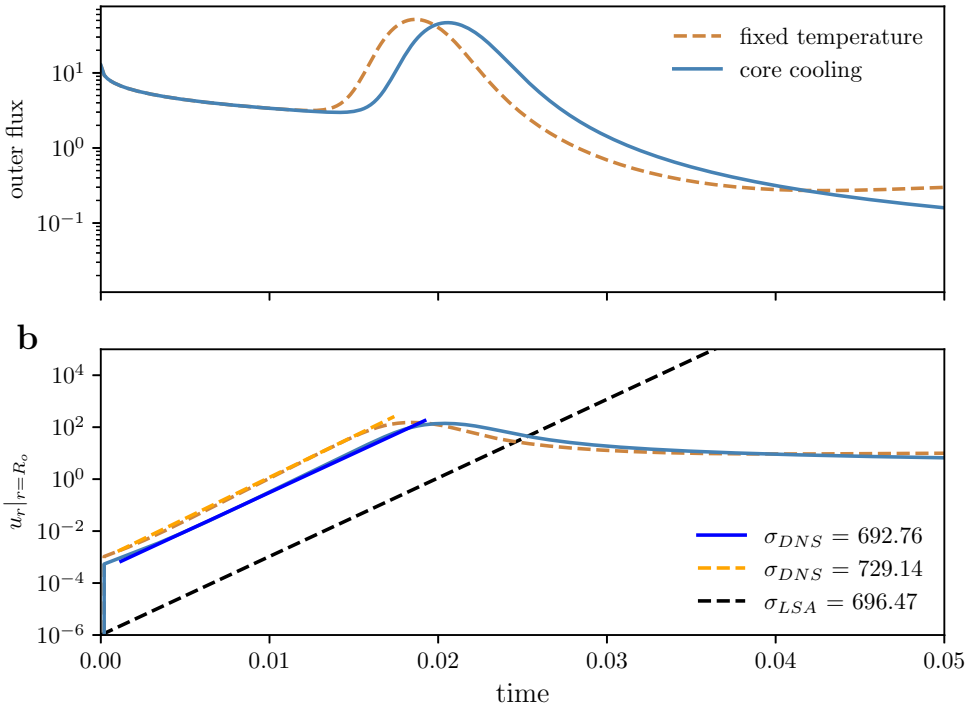

Figure 4.6: a) Dimensionless temporal evolution of the outer heat flux for a fixed temperature at the base of the cumulates (dashed orange line), and when accounting for core cooling (solid blue line) for $\mathcal{R}a = 10^4$ and $\Phi = 6$. b) Dimensionless temporal evolution of the radial velocity at the top of the cumulates; the slope of the curve corresponds to the growth rate σ of the convective instability for the same conditions as in a). The black dashed line corresponds to the growth rate obtained from linear stability analysis.

The range of parameter values accessible through DNS is limited. To complement these simulations, a LSA provides a useful approach to investigate convection, giving access to the growth rate σ_{LSA} of the overturning instability (or, equivalently, the instability growth time $\mathcal{T}_{LSA} = 1/\sigma_{LSA}$), and the associated convection mode, as measured by its spherical harmonics degree l. The objective is to compare the growth rates obtained from LSA and DNS.

To estimate the growth rate of the convective perturbation from DNS, we fit the time evolution of the RMS of the radial velocity at R_o by an exponential function of time between t_0 and $t_{\max}$ (see Supplementary Materials Section S2). Unlike previous studies (Morison et al., 2019; Morison et al., 2024), we consider a gravitational acceleration that varies linearly with the radius. For the sake of simplicity, the LSA assumes a fixed temperature boundary condition at the base of the cumulates. When applying this boundary

condition to DNS calculations, which implies that the core temperature remains constant, convection is maintained after the initial overturning instability and the surface heat flux reaches a constant (dashed orange line in fig. 4.6a). When core cooling is taken into account, the surface heat flux progressively decreases after the overturn as convection ceases (solid blue line in fig. 4.6). The growth rates obtained from DNS (blue line and orange dashed line in fig. 4.6b) for the two different boundary conditions, and from LSA (black dashed line in fig. 4.6b) are very similar. The effect of the evolving boundary condition at R_i appears to be negligible for the onset of the overturn. The growth rate predicted by LSA is sligthly lower than that observed in DNS for a fixed temperature at $r = R_i$.

A systematic comparison of the growth rates obtained from LSA and from DNS, shows a good agreement between the two approaches for $\mathcal{R}a \in [500, 10^5]$ and $\Phi \in [0.1, \infty[$ (see fig. 4.7a, where larger $\mathcal{R}a$ correspond to larger symbols and the color scale stands for variation in Φ). The agreement between the two approaches is very good for large values of the growth rate, *i.e.* for low values of Φ and high values of the Rayleigh number $\mathcal{R}a$. Discrepancies between the two approaches are more pronounced for smaller growth rates, *i.e.* at lower $\mathcal{R}a$ and higher Φ, because the temperature profile whose stability is computed is fixed in the LSA whereas it evolves by diffusion in the DNS, which makes the region where the temperature gradient is important wider (see Supplementary Materials Section S3). For a given Rayleigh number, higher values of Φ lead to delayed onset of convection (as shown in section 4.4.2), allowing more time for thermal diffusion to modify the temperature profile before convection sets in. The same effect is observed when the Rayleigh number is decreased. The consistency between the results from DNS and linear stability calculations at high $\mathcal{R}a$ and low Φ, which is the expected regime for the lunar cumulates, confirms the predictive capability of the linear stability approach in capturing the early-stage system dynamics to access growth rates over a range of values that are inaccessible with DNS (fig. 4.7b). In LSA, the growth rate corresponds to the spherical harmonic mode with the fastest amplification. This provides information not only on the growth rate but also on the dominant convective mode (symbols in fig. 4.7b). For values of $\Phi \leq 14$, the preferred mode of convection is of degree $l = 1$ in both methods. As Φ increases, a transition occurs from $l = 1$ to $l = 2$ modes. In the region where the preferred mode is $l = 2$ for LSA, for DNS, both modes, $l = 2$ and $l = 3$, coexist, with a preference for $l = 3$ (see Supplementary Materials fig. S4 and fig. S5). A second transition to $l = 3$ occurs when entering the region defined by $\mathcal{R}a \gtrsim 1.3 \times 10^4$ and $\Phi \gtrsim 44$, and the preferred convection mode is $l = 3$ for the DNS. The evolution with Φ is expected from previous studies on the effect of the phase change boundary condition on convection (Deguen, 2013; Labrosse et al., 2018; Agrusta et al., 2019; Morison et al., 2019; Morison et al., 2024): increasing Φ makes the system evolves towards the classical

no-penetration boundary condition, which leads to smaller scale modes of convection. Increasing the Rayleigh number beyond its critical value makes the forcing increase and widens the range of unstable modes. We find that, for large values of Φ, the degree of the fastest growing mode increases with the Rayleigh number, *i.e.* makes the preferred scale of the flow decrease. On the other hand, the degree-one mode is the fastest growing one for all values of $\mathcal{R}a$ for $\Phi \leq 14$.

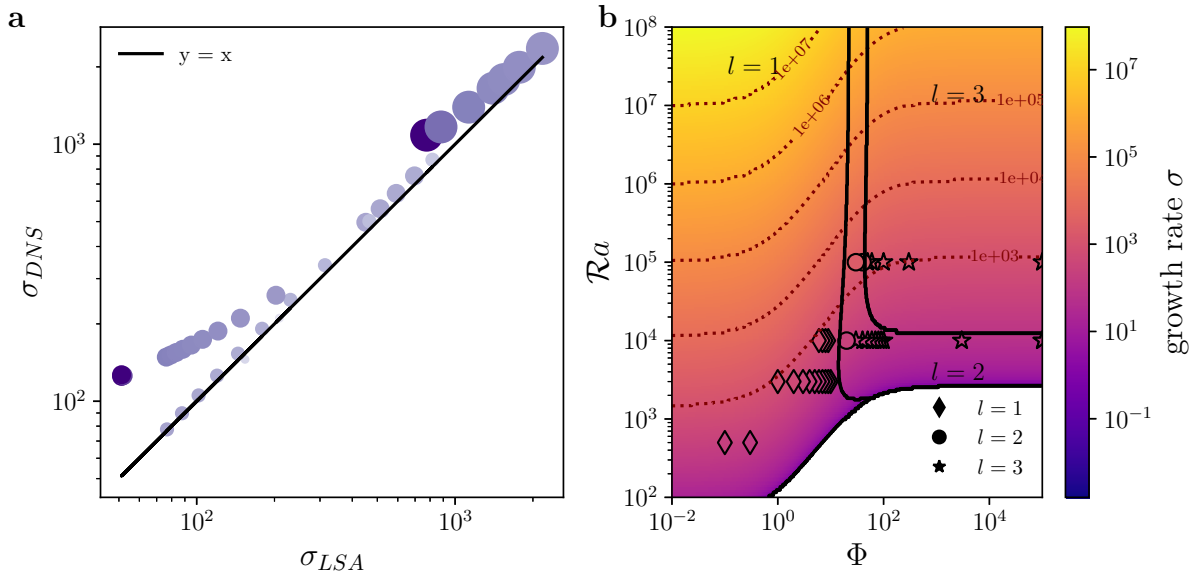

Figure 4.7: a) Growth rate of the convective instability as obtained from DNS as a function of the growth rate obtained with LSA for different $\mathcal{R}a$ and Φ. The dot size is proportional to the value of $\mathcal{R}a$ while a darker color corresponds to a higher Φ value. The black line represents $y = x$. b) Map of the growth rate as a function of $\mathcal{R}a$ and Φ, white standing for negative values, *i.e.* stable cases. Symbols represent numerical simulation results, each symbol type corresponding to a different convection mode. The symbol color corresponds to the growth rate value obtained from DNS, where the color scale is the same as for the LSA (see colorbar). Black solid lines indicate the boundaries where transitions between convection modes occur as predicted by LSA. Gray dashed lines correspond to growth rate contour lines.

4.4.4 Extrapolation of the data

Numerical simulations provide insight into the temporal evolution of the overturn, from its onset to its fading out, but are constrained in the range of parameters that can be explored. In contrast, LSA allows for the investigation of a broader parameter space but gives insight only on the onset of the overturning instability. Figure 4.7 shows that the isocontours of the growth rate appear to vary linearly with $\mathcal{R}a$ and follow a sigmoid-like curve as a function of Φ. Based on this observation, we propose to represent the instability

growth time $\mathcal{T}$, scaled by the Rayleigh number $\mathcal{R}a$. This is done on fig. 4.8 which shows $\mathcal{T}\mathcal{R}a = \mathcal{R}a/\sigma$ as function of Φ for all values of $\mathcal{R}a$ investigated, using either the DNS or LSA approach. The other time-scales obtained using DNS, as defined in section 4.4.1 and fig. 4.3, are also plotted. The growth rate indeed varies linearly with $\mathcal{R}a$ since all the curves of $\mathcal{T}_{LSA}\mathcal{R}a$ obtained from the LSA collapse into a master curve for $\mathcal{R}a$ between 10^4 and 10^8 (Figure 4.8). The same applies also to the various time-scales obtained from the DNS results, the onset time of the overturn, t_{start} (fig. 4.8a), and the half-times Δt_{growth} and Δt_{decay} (fig. 4.8b). Moreover, the master curves for the various time scales all have a sigmoid shape. We can fit the instability time from the DNS, $\mathcal{T}_{DNS}$ with the instability time from LSA $\mathcal{T}_{\text{LSA}}$:

$$\mathcal{T}_{\text{DNS}}\mathcal{R}a = f(\Phi) = (\mathcal{T}_{\text{LSA}}\mathcal{R}a)_{min} + \frac{(\mathcal{T}_{\text{LSA}}\mathcal{R}a)_{max} - (\mathcal{T}_{\text{LSA}}\mathcal{R}a)_{min}}{1 + \exp[-k(\log_{10}(\Phi) - \log_{10}(\Phi_0))]}, \tag{4.24}$$

where $(\mathcal{T}_{\text{LSA}}\mathcal{R}a)_{\text{min}}$ and $(\mathcal{T}_{\text{LSA}}\mathcal{R}a)_{\text{max}}$ are the asymptotic limits for $\Phi \to 0$ and $\Phi \to \infty$, respectively, k is the slope parameter, and Φ_0 is the value of Φ at the inflection point (*i.e.*, the midpoint of the transition, all of the value are given in table S2 in Supplementary Materials). Moreover, the maximum time t_{max}, the onset time t_{start}, as well as the half-growth Δt_{growth} and half-decay times Δt_{decay}, vary linearly with the instability growth time $\mathcal{T}_{\text{DNS}}$ (fig. 4.8c). Using the scaling laws and the expression of the growth rate given in eq. (4.24) these linear relationships enable us to use the linear stability results to obtain the values of the various timescales in a broader range of Rayleigh number $\mathcal{R}a$ and phase change number Φ than is accessible using DNS, particularly for low values of Φ.

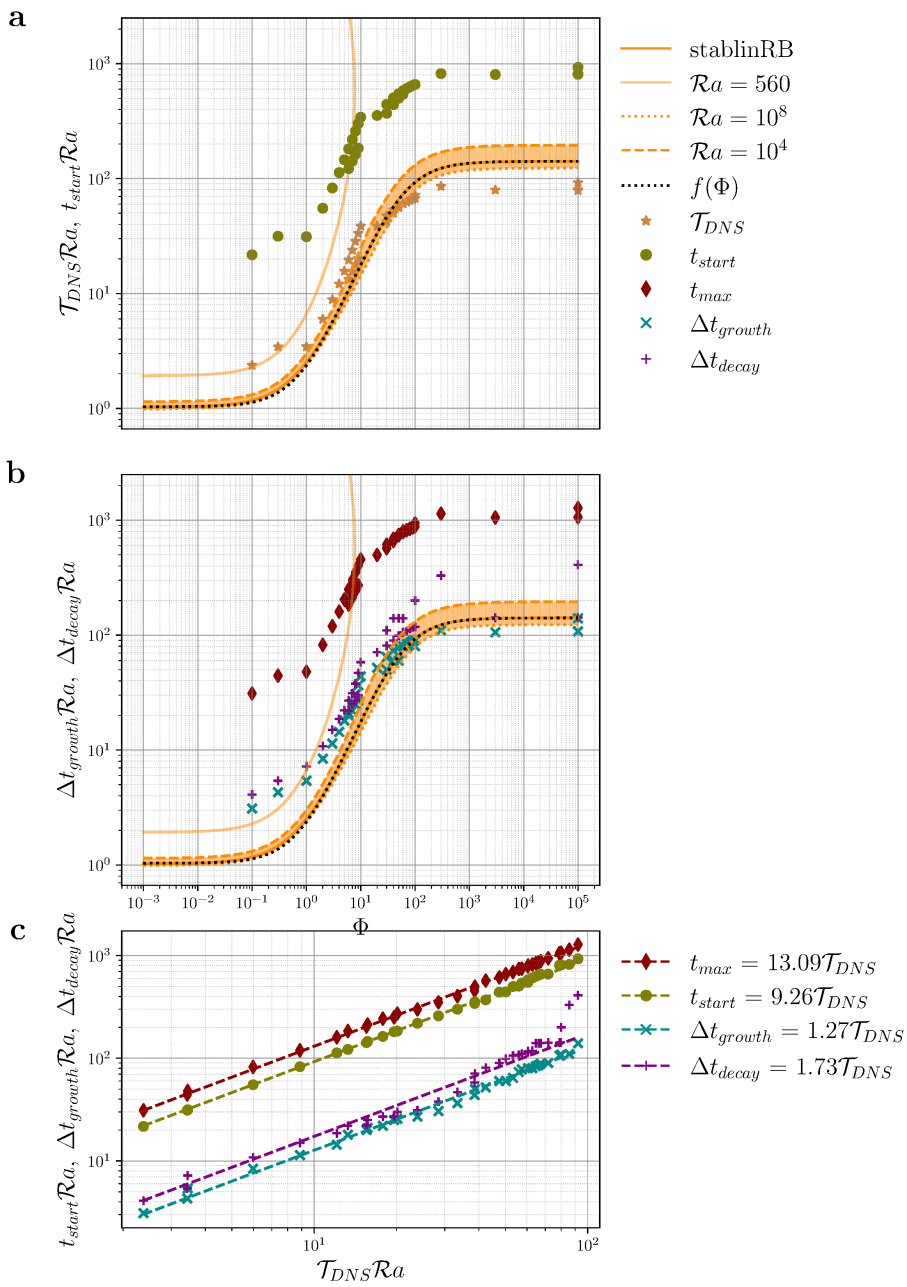

Figure 4.8: a) Variation of the destabilization timescale $\mathcal{T}$ obtained from LSA, multiplied by the Rayleigh number $\mathcal{R}a$: the black dotted line shows the sigmoid-like scaling fit $f(\Phi)$, the associated error is shown in light orange, bounded by the two orange dotted lines. The light orange curve corresponds to the linear stability result for $\mathcal{R}a = 560$. This curve diverges as $\Phi > 3$, indicating the absence of overturn beyond these values. The orange stars show the destabilisation time from DNS, while the green dots represent the onset times t_{start}, both multiplied by $\mathcal{R}a$. b) Same as a), but showing the maximum time t_{max} (red diamonds), the half-growth time Δt_{growth} (purple crosses), and the half-decay time Δt_{decay} (blue crosses), all multiplied by $\mathcal{R}a$. c) Scaling laws of the various timescales obtained from DNS, multiplied by $\mathcal{R}a$, as a function of the destabilization timescale $\mathcal{T}$.

4.4.5 Application in the context of the LMO solidification

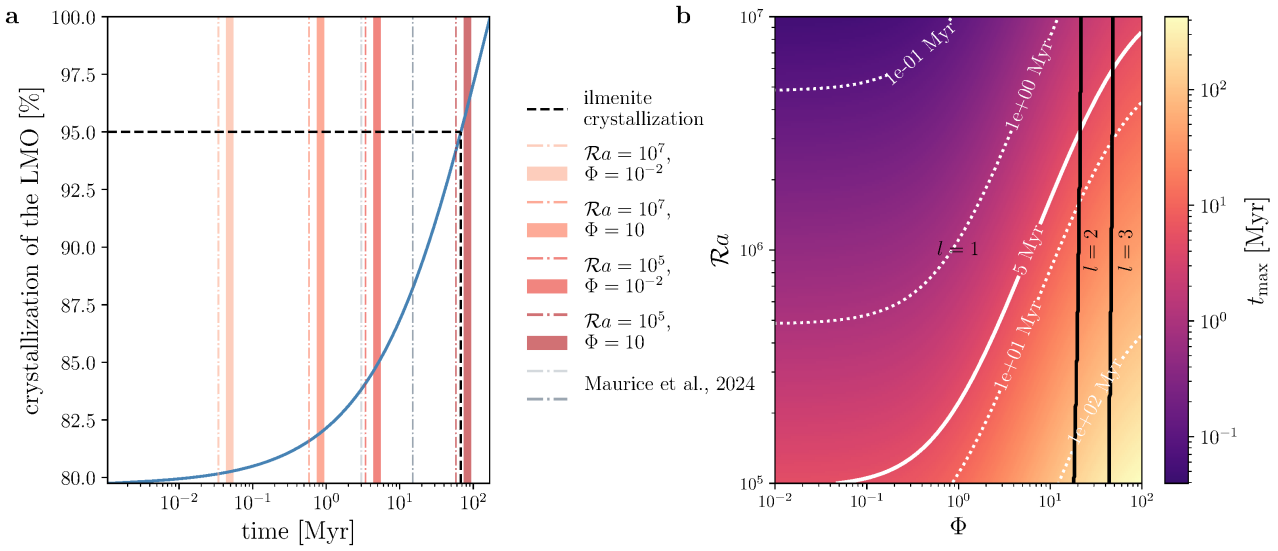

Figure 4.9: a) Temporal evolution of the percentage of LMO crystallization from Colin et al. (2024) (blue line). The black dashed horizontal line indicates the onset of ilmenite crystallization at 95% solidification. The vertical dot-dashed lines correspond to the onset time of the overturn for our study (red) and the vertical stripes represent the duration of the overturn Δt_{total} centered on the maximum time t_{max} for four sets of parameters: ($\mathcal{R}a = 10^7$, $\Phi = 10^{-2}$), ($\mathcal{R}a = 10^7$, $\Phi = 10$), ($\mathcal{R}a = 10^5$, $\Phi = 10^{-2}$) and ($\mathcal{R}a = 10^5$, $\Phi = 10$). The gray dot-dashed lines correspond to the onset of thermal instabilities from Maurice et al. (2024). b) Map of the maximum time of the overturn t_{max} as function of $\mathcal{R}a$ and Φ. Black solid lines indicate the boundaries where transitions between convection mode occur as predicted by LSA. white dotted lines correspond to the maximum time contour lines, and the white solid line corresponds to $t_{\text{max}} = 5\,\text{Myr}$.

Using the growth rate from LSA, we extrapolate the results of DNS and we estimate the onset time, the maximum time and duration of the mantle overturn for Rayleigh numbers $\mathcal{R}a$ and phase change number Φ within the range expected for lunar cumulates (fig. 4.8 and eq. 4.24). These estimates can be placed in the context of LMO solidification, based on the reference scenario of Colin et al. (2024), with a final crustal thickness of 44 km (corresponding to an initial content in anorthite component of $C_0 = 0.075$), 80% of crystallization at the end of the first stage (corresponding to an eutectic composition of $C_{\text{E}} = 0.37$), and a thermal conductivity of k_{c} =2 $\text{W m}^{-1}\,\text{K}^{-1}$ (fig. 4.9a). In this scenario, the total solidification time is 170 Myr, with ilmenite crystallizing at 95% of solidification, around 70 Myr. The range of parameters explored covers $\mathcal{R}a = 10^5$ to 10^7 and $\Phi = 10^{-2}$ to 10 for lunar cumulates. The shortest overturn time corresponds to $\mathcal{R}a = 10^7$ and $\Phi = 10^{-2}$, and the longest to $\mathcal{R}a = 10^5$ and $\Phi = 10$. In the latter case, the overturn

starts slightly before the onset of ilmenite crystallization and lasts for several tens of millions of years (fig. 4.9a). The time at which the overturn reaches its maximum flux, $t_{\max}$, ranges from 4×10^{-2} Myr to 4×10^{2} Myr over an extended range of Φ values (tested up to 100, beyond the expected lunar range). The higher the values of $\mathcal{R}a$, the earlier the maximum peak occurs. An increase in Φ delays $t_{\max}$ and promotes higher degree overturn modes. For $\Phi \leq 14$, the preferred spherical harmonic is degree-one (fig. 4.9b). For comparison, ilmenite begins to crystallize at ∼70 Myr in the reference LMO scenario. The thermal overturn is thus likely to occur before ilmenite crystallization as only low values of $\mathcal{R}a \leq 4 \times 10^{5}$ are such that the maximum of the overturn flux occurs as the same time or after the appearance of ilmenite.

4.5 Discussion

4.5.1 Implications of a thermal overturn

Combining the results from DNS and LSA, we estimate the duration of the overturn accounting for a phase change at the interface between the LMO and the cumulates. A major source of uncertainty in this estimate lies in the values of $\mathcal{R}a$ and Φ as both are sensitive to the viscosity of the cumulates and the dynamics of the LMO, which are poorly constrained. Moreover, Φ may vary with time, as it is influenced by the changing dynamics of the LMO during its crystallization. Given the likely range of values for $\mathcal{R}a$ and Φ for the lunar cumulates (see section 4.2.5), the overturn is likely to occur early in the second stage of crystallization and to be rapid compared to the total solidification time of the LMO. In particular, the time for the maximum heat flux at the top of the cumulates does not exceed 100 Myr, and the overturn should develop in a degree-one as $\Phi < 14$.

In terms of timescales, our results are consistent with those of Boukaré et al. (2018) and Maurice et al. (2024). In particular, Maurice et al. (2024, tab. A1) found that thermal instabilities develop after 3 Myr to 15 Myr for $\mathcal{R}a = 7.4 \times 10^{6}$ (gray dash-dotted lines on fig. 4.9a), which is comparable to our predicted onset time ($t_{\text{start}} = 6.5$ Myr), for the same initial noise amplitude (personal communication). However, a direct comparison between the two models remains difficult. The model of Maurice et al. (2024) is significantly more complex, accounting for a variable viscosity, a dense upper ilmenite layer, and other physical processes, and it employs a 2-D cylindrical geometry. In contrast, our study uses a more idealized physical setup, which allows us to isolate the influence of the Rayleigh number on the development of thermal instabilities and to include the effect of phase change coupling with the LMO in a 3D spherical shell geometry. A larger noise amplitude leads to an earlier growth of instabilities and thus to an earlier onset of convection.

Conversely, reducing the noise amplitude delays the development of convective motions (see Supplementary Materials Section S4 and fig. S3). Incorporating a phase change at the LMO-cumulates interface tends to promote the onset of the overturn, thereby reducing its initiation time; it also favors the development of a degree-one convective mode. On the contrary, in models considering a solidified or partially molten mantle, the overturn generally develops at smaller wavelengths. Parmentier et al. (2002) show that a degree-one compositional overturn can develop only if the dense layer is sufficiently thick and if the viscosity contrast between the IBC and the underlying mantle exceeds four orders of magnitude. According to our results, such a scenario is not necessary because, from a thermal perspective, if the mass exchange between the cumulates and the LMO is efficient ($\Phi \leq 14$), a degree-one overturn can arise as early as the beginning of the second crystallization stage. Furthermore, even though the initial thermal overturn may be short-lived, it can influence the initial conditions for subsequent instabilities. As it favors a dominant degree-one perturbation in the system, even though a compositional overturn does not intrinsically favor degree-one modes.

The total amount of thermal energy released to the LMO by the overturn can be computed analytically using the solution of Colin et al. (2024) and is equal to 1.8×10^{28} J (Note the typographic error in Colin et al., 2024, where a value of 1.8×10^{18} J was given). However, the duration of this release, and therefore the associated peak heat flux during the overturn, depends on the values of $\mathcal{R}a$ and Φ. Figure 4.4 shows that the peak heat flux value increases with the Rayleigh number and as $\Phi \to 0$. According to Colin et al. (2024), if the released flux is below 10^{14} W and spread over more than 5 Myr (white line in fig. 4.9b), it may lead to a prolonged crystallization timescale. Conversely, if the flux exceeds this threshold and is released over a shorter period, the crystallization time is reduced because all the heat stored in the cumulates is released while the heat flow out of the LMO is still very large. In the extreme case, the flux can be large enough to melt the initially thin crust at the beginning of the second stage. While the basal heat flux evolution considered in Colin et al. (2024) is a decreasing exponential function of time that is spatially uniform and therefore different from the evolution obtained here, it is likely that if it occurs over a timescale that is similar, though shorter, than the crust crystallization timescale, *i.e.* if it occurs within 1 Myr to 200 Myr, it can influence its growth. With these considerations, our results suggest that for parameters $\mathcal{R}a$ and Φ in the region below the $t_{max} = 1$Myr contour line, *i.e.* roughly $\mathcal{R}a \leq 10^7$ and $\Phi \leq 14$, the overturn can influence crustal growth (fig. 4.9b). The heat flux is then released over a limited area in a single hemisphere. This could lead to a differential heat flux that may be imprinted on the lunar crust (Bouffard et al., 2025) and lead to an asymmetric crust. If the flux is sufficiently high, as our results suggest, it may even induce partial melting

of a localized region of the crust.

4.5.2 Lunar dynamo

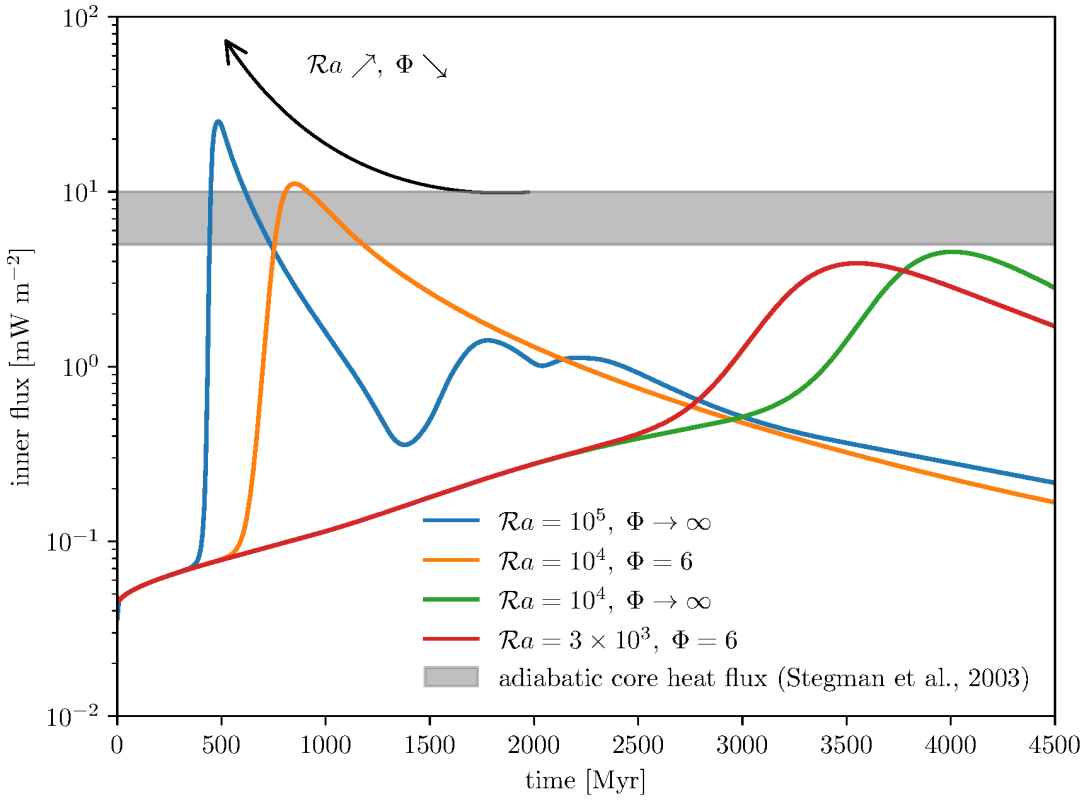

Figure 4.10: Dimensional temporal evolution of the flux at the core-mantle boundary for $Ra = 10^5, \Phi \to \infty$ in blue, $Ra = 10^4, \Phi = 6$ in orange, $Ra = 10^4, \Phi \to \infty$ in green and $Ra = 3 \times 10^3, \Phi = 6$ in red. The gray box corresponds to the adiabatic core flux estimated by Stegman et al. (2003b).

One plausible hypothesis for the generation of the lunar magnetic field is a thermally driven core dynamo (Stegman et al., 2003b). For this mechanism to operate, the heat flux at the base of the cumulates must exceed the heat flux down the core adiabat. To evaluate this basal heat flux, we use the non-dimensional heat flux at the core-cumulates boundary. The resulting flux is expressed in dimensional units (W m^{-2}) by multiplying the dimensionless flux by $k\Delta T/H$. To study the effets of $\mathcal{R}a$ and Φ, we use the same cases as presented in section 4.4.2.

For ($\mathcal{R}a = 10^4$, $\Phi \to \infty$) and ($\mathcal{R}a = 3 \times 10^3$, $\Phi = 6$), the basal flux remains below the isentropic range. But, for the reference case ($\mathcal{R}a = 10^4$, $\Phi = 6$), and for ($\mathcal{R}a = 10^5$, $\Phi \to \infty$), the basal flux exceeds the range estimated for the isentropic heat flow.

Compared to the reference case ($\mathcal{R}a = 10^4$ and $\Phi = 6$), a decrease in the Rayleigh number results in a lower peak basal flux and delays its onset. Similarly, increasing Φ at fixed Rayleigh number also reduces the flux magnitude and shifts the peak to later times. Thus, a thermally driven core dynamo could be sustained during the thermal overturn, if the Rayleigh number of the cumulates layer is sufficiently large and the phase change number sufficiently low

However, it is noteworthy that the timing of the flux peak spans from approximately 500 Myr to more than 800 Myr in the cases presented on fig. 4.10, hence after the end of LMO solidification. These cases are thus not satisfactory, but they correspond to parameter regimes with low $\mathcal{R}a$ and high Φ relative to estimates for the lunar cumulates. Increasing $\mathcal{R}a$ and decreasing Φ shifts the flux peak to earlier times, as shown in section 4.4.4 for the outer flux. We use the same method as in section 4.4.4 and the same expression for the sigmoid function (eq. 4.24) to extrapolate the time at which the heat flux at the base of the cumulates reaches its maximum value, $t_{\mathrm{max,i}}$. We obtain a scaling law between $t_{\mathrm{max,i}}$ and $\mathcal{T}_{DNS} = 1/\sigma_{DNS}$ (see Supplementary Materials fig. S6):

$$t_{\mathrm{max,i}} = 13.84\mathcal{T}_{DNS}. \tag{4.25}$$

The peak of the basal heat flux occurs thus slightly after the peak in the surface heat flux, as represented on fig. 4.10 and table S2 (in Supplementary Materials). For the highest values of $\mathcal{R}a$ and the lowest values of Φ consistent with the lunar cumulates, this dynamo would have set up too early to be recorded in lunar rocks as the crust is then too thin (Colin et al., 2024). However, using the fact that $t_{max,i}$ is close to t_{max}, which is represented on fig. 4.10, we can identify the region in the parameter space giving $t_{max,i} > 1$ Myr as the one below the $t_{max} = 1$ Myr contour line. Therefore for values of $\Phi \in [10^{-1}, 14]$ and $Ra \lesssim 10^7$, the maximum flux is reached within a timescale such that this lunar dynamo could have been recorded in the crust. Paleomagnetic measurements on Apollo samples have shown that an early dynamo likely operated between at least 4.25 and 3.56 Gyr (Tikoo et al., 2017). A thermal overturn could have triggered its onset during LMO crystallization. The persistence or revival of the dynamo after LMO solidification would however be explained by another mechanism, such as a persistent mantle convection sustained by compositional instabilities or internal heating, or by other mechanisms, such as mechanical stirring from large impacts (Le Bars et al., 2011) or precession (Dwyer et al., 2011).

4.6 Conclusion

In this study, we investigated the conditions under which a thermal overturn may arise during the solidification of the LMO. Through the combined use of 3D direct numerical

simulations, and linear stability analysis on the convection equations, we derived scaling laws that predict both the onset and duration of a purely thermal overturn as a function of key control parameters. Extrapolation of the linear stability results using a sigmoidal scaling law allows us to estimate overturn durations in regimes relevant to the Moon, which remain inaccessible to direct numerical modeling. Our results show that a rapid mantle overturn can occur early in the second stage of LMO crystallization (after 70-80% solidification). In particular, for Rayleigh numbers, $\mathcal{R}a < 10^7$, and in the presence of a phase-change boundary, $\Phi < 14$, the thermal overturn is dominated by a degree-one mode and its characteristic timescale is such that is able to both influence crustal growth and cause and early lunar dynamo that could be recorded in the early crust. Thus, for this range of Rayleigh and phase change numbers, this mechanism provides a plausible dynamical mechanism for the observed lunar crustal thickness asymmetry.

Acknowledgments

This project has received funding from the European Research Council (ERC) under the European Union's Horizon 2020 research and innovation programme (grant agreement No. 101001689). CM acknowledges support of the Institut Universitaire de France.

Supplementary Materials

S1 Table of parameters

table S1 represents the list of the symbols used and their values.

Symbol	Description	Value	References
Fixed parameters			
R_{M}	radius of the Moon	1737 km	
R_{C}	radius of the core	390 km	
R_{cu}	radius of the cumulates	1612 km	
T_{OL}	liquidus temperature for the ol-px component	2150 K	O'Driscoll et al. (2010)
T_{E}	eutectic temperature	1600 K	O'Driscoll et al. (2010)
m	liquidus slope	$\frac{T_{\mathrm{OL}} - T_{\mathrm{E}}}{C_{\mathrm{E}}}$	
g_0	surface gravity	$1.62\,\mathrm{m\,s^{-2}}$	
ρ_{cu}	density of cumulates	$3.3 \times 10^3\,\mathrm{kg\,m^{-3}}$	
ρ_{mo}	LMO density	$2.8 \times 10^3\,\mathrm{kg\,m^{-3}}$	
$\Delta\rho$	cumulates-LMO density contrast	$500\,\mathrm{kg\,m^{-3}}$	
c_p	heat capacity	$1 \times 10^3\,\mathrm{J\,kg^{-1}\,K^{-1}}$	
L_{h}	latent heat	$5 \times 10^5\,\mathrm{J\,kg^{-1}}$	
α	thermal expansion	$1 \times 10^{-5}\,\mathrm{K^{-1}}$	Maurice et al. (2020)
η_{mo}	LMO viscosity	1 Pa s	
u_{mo}	LMO velocity scale	$1\,\mathrm{m\,s^{-1}}$	
k_{cu}	conductivity of cumulates	$4\,\mathrm{W\,m^{-1}\,K^{-1}}$	Maurice et al. (2020)
$c_{p,\mathrm{co}}$	core heat capacity	$840\,\mathrm{J\,kg^{-1}\,K^{-1}}$	Maurice et al. (2020)
ρ_{co}	core density	$7.2 \times 10^3\,\mathrm{kg\,m^{-3}}$	
$\partial_r T$	temperature gradient	$1 \times 10^{-2}\,\mathrm{K\,m^{-1}}$	
Explored parameters			
η_{cu}	viscosity of cumulates	1×10^{17} Pa s – 1×10^{21} Pa s	
$\mathcal{R}a$	Rayleigh number	10^5-10^7	
Φ	phase change number	10^{-2}-∞	
Dimensionless parameters			
γ	aspect ratio	$R_{\mathrm{C}}/R_{\mathrm{M}} = 0.24$	
R_i	inner radius	$\gamma/(1-\gamma) = 0.31$	
R_o	outer radius	$1+\gamma/(1-\gamma) = 1.31$	

Table S1: List of the parameters and variables of the model.

S2 Calculation of the growth rate from the numerical simulations

To determine the growth rate from numerical simulations, we compute the slope of the logarithm of the square of the radial velocity at the outer boundary ($r = R_{\mathrm{cu}}$). However, as illustrated in fig. S1, the estimated slope—and thus the inferred growth rate—depends slightly on the portion of the curve selected for the fit. For instance, panel a) of fig. S1, which shows the slope computed over 95% of the curve, yields a higher growth rate than panel d), where the slope is evaluated over only 5% of the curve. To account for this variability, we systematically estimate the growth rate in all numerical simulations by averaging the slope over several intervals, ranging from 95% down to 60%, with a step size of 1%.

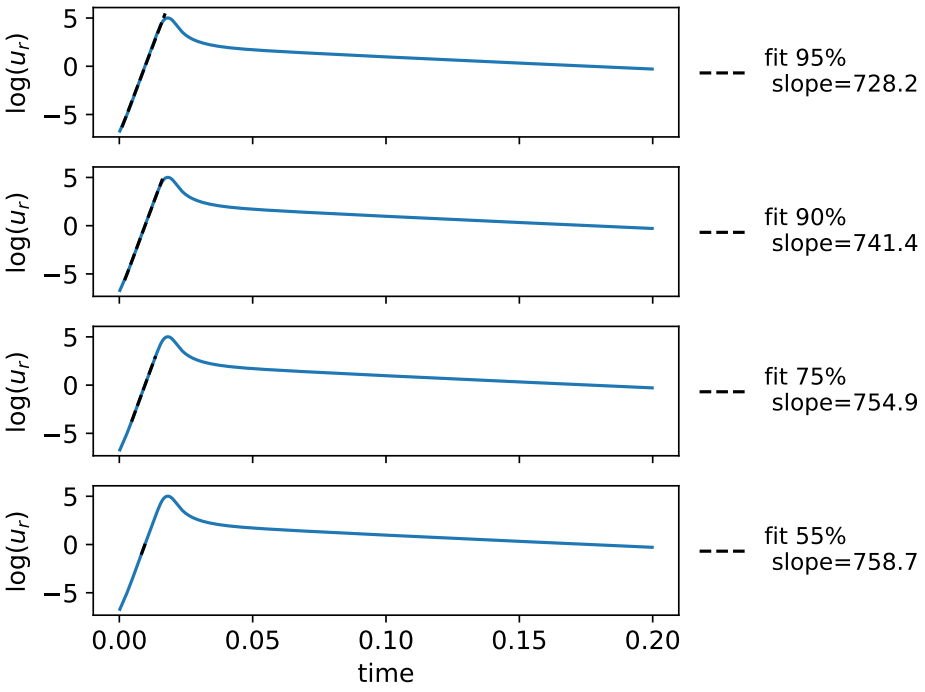

Figure S1: Temporal evolution of the logarithm of the radial velocity at $r = R_o$ for the reference case $\mathcal{R}a = 10^4$, $\Phi = 6$. a)-d) represent the slope calculated taking different percentage, from 95% to 5%, of the linear part of the curve.

S3 Effect of the temperature profile

As discussed in Section 3.3, the discrepancy between the growth rate obtained from numerical simulations (σ_s) and that predicted by linear stability analysis (σ_l) increases with the value of Φ, particularly at low Rayleigh numbers (fig. 7a). We attribute this discrepancy to the fact that the onset time τ of the overturn increases with the decrease of Ra and the increase of Φ. If τ becomes similar or even larger than the thermal diffusion time-scale for the initial temperature profile, the linear stability approach that we use, which assumes a time-independent profile, is not correct. As a result, thermal diffusion has a non-negligible effect in the numerical simulations before convection begins. This effect is illustrated in fig. S2. At the time convection initiates, t_{start}, the temperature profile in the reference case ($\mathcal{R}a = 10^4$, $\Phi = 6$) is only slightly less curved than the initial profile (blue and orange lines in fig. S2b). In contrast, when $\mathcal{R}a = 10^4$ and $\Phi \to \infty$, the temperature profile at t_{start} is significantly more straight than the initial one, indicating substantial diffusion has occurred since the initial state at t_0 (blue and orange lines in fig. S2c). This thermal diffusion prior to the onset of convection provides an explanation for the observed differences between σ_s and σ_l, particularly as Φ increases or Ra decreases.

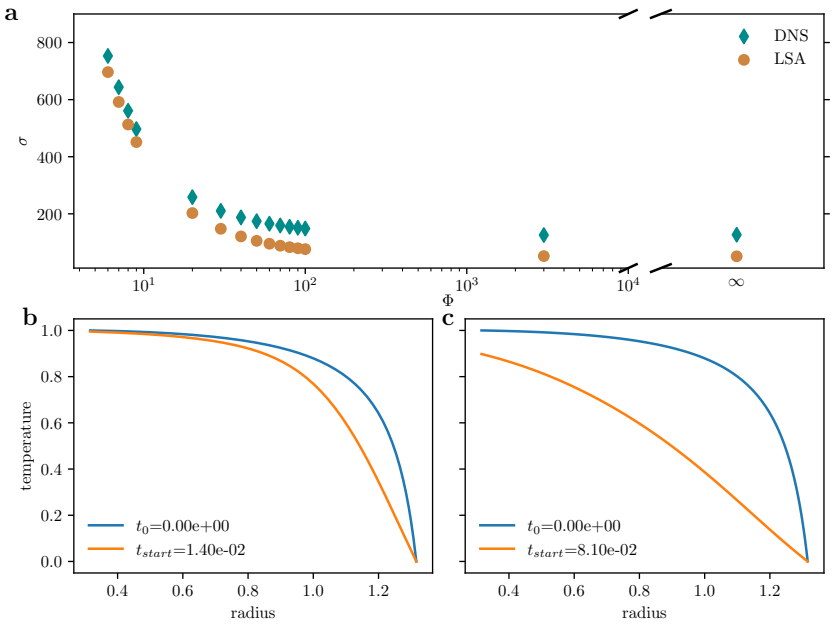

Figure S2: **a**- Comparison of the growth rate of the linear stability analysis, orange points, and numerical simulations, blue diamonds, for $Ra = 10^4$ and varying Φ. Evolution of the temperature profile $T(r)$ in the cumulates at t_0 (blue line) and t_{start} (orange line) for $Ra = 10^4$ and $\Phi = 6$ in **b** and $Ra = 10^4$ and $\Phi \to \infty$ in **c**.

S4 Effect of the initial noise

In our numerical models, the initial state includes a random perturbation representing small-scale thermal heterogeneities, characterized by an amplitude A. This initial noise plays a critical role in controlling the onset timing of the lunar mantle overturn. As illustrated in fig. S3, larger perturbation amplitudes facilitate the growth of instabilities and thus favor the onset of the overturn. Reducing the amplitude of the initial perturbation tends to delay the development of convective motions, leading to a later overturn.

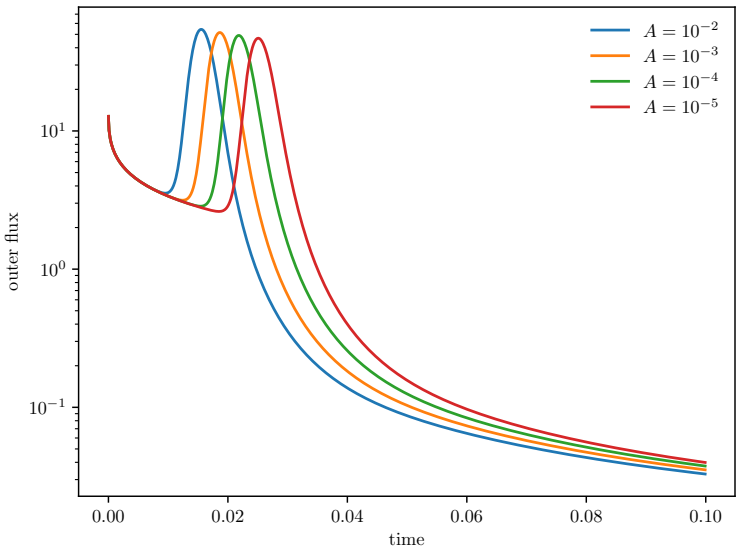

Figure S3: Comparison of the effect of the initial amplitude of the noise for the reference case, $\mathcal{R}a = 10^4$ and $\Phi = 6$. In blue line for an initial perturbation of amplitude $A = 10^{-2}$, in orange line for $A = 10^{-3}$, in green line for $A = 10^{-4}$ and in red line $A = 10^{-5}$.

S5 Mode of convection with DNS

To identify the preferred convective mode using DNS, we analyze the temperature spectra at t_0, t_{start}, t_{max} and t_{end} (see fig. S4). The preferred mode is determined by the spectral component with the highest amplitude at t_{start}.

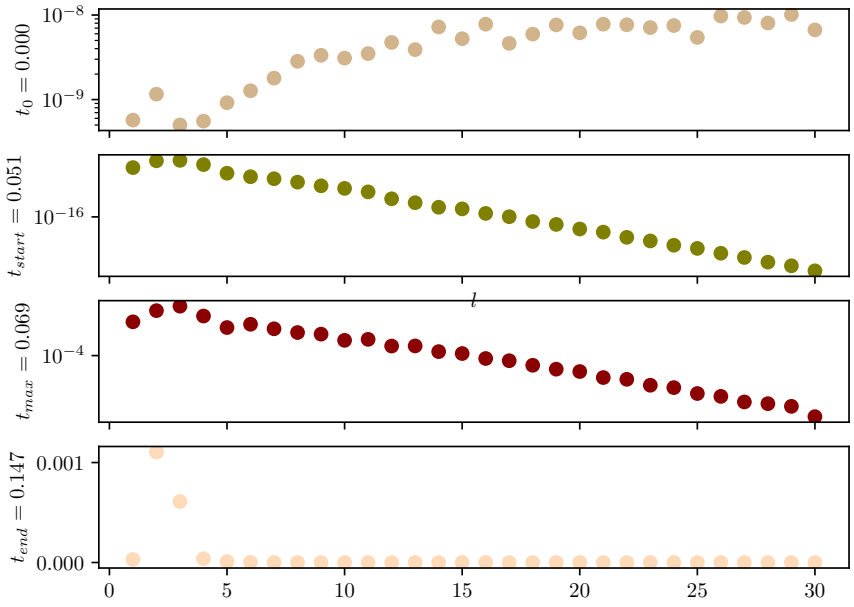

Figure S4: Spectra of the temperature field computed at different times of the simulation: $t = 0$, t_{start}, t_{max} and t_{end} for $(\mathcal{R}a = 10^4, \Phi = 40)$. Each curve shows the distribution of spectral amplitude as a function of the spherical harmonic degree l.

S6 Duration of the overturn

$\mathcal{R}a$	Φ	τ [Myr]	t_{start} [Myr]	Δt_{growth} [Myr]	Δt_{decay} [Myr]	Δt_{total} [Myr]	t_{end} [Myr]
1.0e+07	1.0e-02	0.004	0.034	0.005	0.006	0.011	0.045
1.0e+07	1.0e+01	0.063	0.583	0.080	0.109	0.189	0.772
1.0e+07	1.0e+05	0.502	4.647	0.637	0.868	1.506	6.153
1.0e+06	1.0e-02	0.037	0.343	0.047	0.064	0.111	0.454
1.0e+06	1.0e+01	0.630	5.834	0.800	1.090	1.890	7.725
1.0e+06	1.0e+05	5.018	46.471	6.373	8.682	15.055	61.527
1.0e+05	1.0e-02	0.370	3.428	0.470	0.640	1.111	4.538
1.0e+05	1.0e+01	6.301	58.343	8.002	10.900	18.902	77.245
1.0e+05	1.0e+05	50.185	464.712	63.735	86.820	150.555	615.267
1.0e+04	1.0e-02	3.702	34.279	4.701	6.404	11.106	45.385
1.0e+04	1.0e+01	63.006	583.433	80.017	109.000	189.017	772.451
1.0e+04	1.0e+05	501.849	4647.123	637.348	868.199	1505.547	6152.670

Table S2: Timescale of the duration of the overturn for different values of $\mathcal{R}a$ and Φ, using the scaling law (eq. 24 and fig. 8) from the extrapolation of datas for a fixed initial noise of $A = 10^{-3}$ in particular for t_{start} and t_{end}.

The growth rate varies linearly with $\mathcal{R}a$ since all the curves of $\mathcal{T}_{LSA}\mathcal{R}a$ obtained from the LSA merge into a master curve for $\mathcal{R}a$ between 10^4 and 10^7 (fig. 8). However, for $\mathcal{R}a = 10^4$ and $\Phi > 50$, the curve deviates from the sigmoid (fig. 8). It is this deviation

that induces errors in the calculation of the different times, in particular for $\mathcal{R}a$ and $\Phi \to \infty$. This is why the data presented in the table does not correspond to the DNS results.

S7 Lunar dynamo

In this section, we present the extrapolation of the DNS for the inner heat flux, corresponding to the heat flux at the base of the cumulates, fig. S5 and table S3. As with table S2, the results do not match the DNS results due to the error in estimating the growth rate using the sigmoid function.

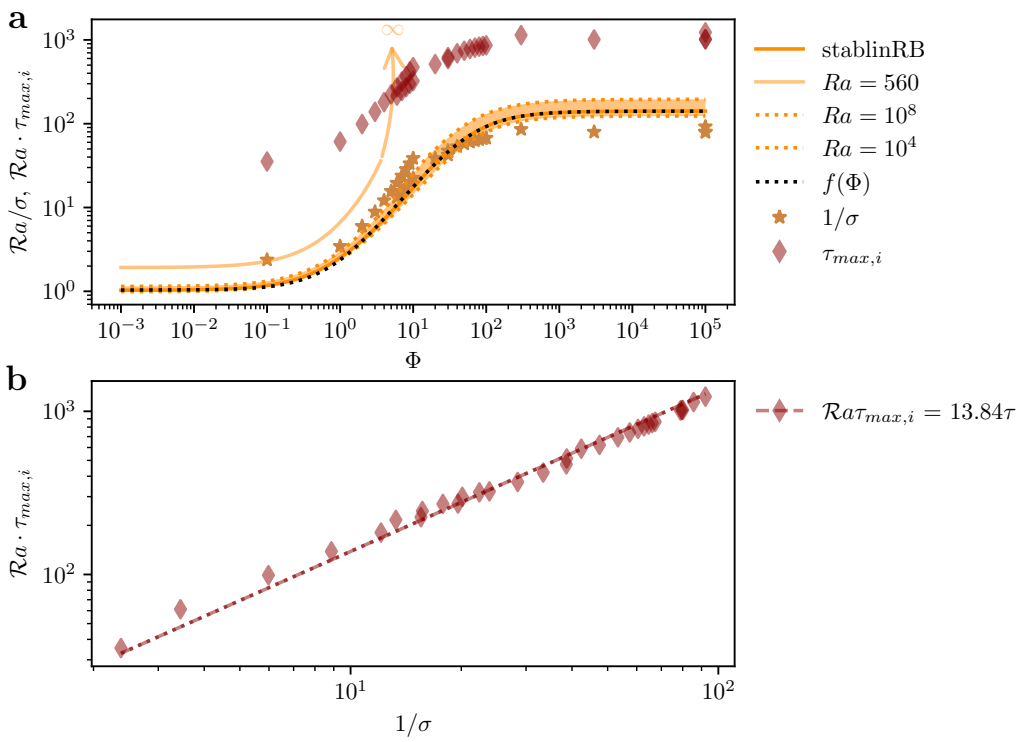

Figure S5: Variation of the dimensionless time of the maximum inner flux multiplied by $\mathcal{R}a$ as function of Φ, the instability growth time from linear stability analysis, orange line and from DNS, orange starts, and the maximum time $t_{\mathrm{max,i}}$ in green point.

$\mathcal{R}a$	Φ	$t_{\mathrm{max,i}}$ [Myr]
1.0e+07	1.0e-02	0.051
1.0e+07	1.0e+01	0.872
1.0e+07	1.0e+05	6.946
1.0e+06	1.0e-02	0.512
1.0e+06	1.0e+01	8.720
1.0e+06	1.0e+05	69.456
1.0e+05	1.0e-02	5.123
1.0e+05	1.0e+01	87.200
1.0e+05	1.0e+05	694.559
1.0e+04	1.0e-02	51.233
1.0e+04	1.0e+01	872.000
1.0e+04	1.0e+05	6945.592

Table S3: Time corresponding to the maximum of the inner flux $t_{\mathrm{max,i}}$, for different values of $\mathcal{R}a$ and Φ using

Chapter 5

Formation of an anorthositic crust on Mars

L'hypothèse de la possibilité de la formation d'une croûte primaire purement anorthositique sur Mars a longtemps été écartée. En effet, la taille plus importante de la planète et sa gravité plus élevée que celles de la Lune rendent la cristallisation de l'anorthite plus difficile. Cependant, les missions orbitales ont révélé la présence d'anorthite sur la surface martienne. Ces roches riches en anorthite pourraient provenir d'une différentiation magmatique dans des reservoirs crustaux, comme sur Terre, ou de la cristallisation d'un océan de magma, à l'instar de la Lune. Dans ce contexte, nous avons adapté le modèle d'évolution thermique initialement développé pour la Lune afin de l'appliquer à Mars. Cependant dans un océan de magma global martien, les cristaux d'olivine peuvent flotter à une certaine pression, créant une situation dans laquelle la couche de cumulats se forme entre un océan de magma basal et un océan de magma supérieur. Cette transition de flottabilité implique la cristallisation fractionnée et ainsi la formation d'anorthite, ce qui pourrait permettre la formation d'une croûte primaire anorthositique martienne. Nous modifions le modèle initialement développé pour l'évolution thermique de la Lune, en intégrant cette transition de flottabilité. Nous estimons les teneurs initiales en anorthite possibles en fonction de la transition de flottabilité, ainsi que l'épaisseur maximale de la croûte primaire martienne, qui est comprise entre 14 et 30 km. Le temps de formation de cette croûte est compris entre 5 et 35 millions d'années.

5.1 Introduction

The concept of magma ocean played a central role in understanding the early differentiation of planetary bodies, the Moon being the most studied example. A global lunar magma ocean, generated by the energy of a giant impact, crystallized to form an anorthositic flotation crust that accounts for nearly 80% of the present-day lunar surface (Pritchard et al., 2000; Ćuk et al., 2012; Canup, 2012; Nakajima et al., 2014; Warren et al., 1979). The low pressure range and dry magma ocean both favor plagioclase stability, and hence the formation of an anorthositic floatation crust (Wood et al., 1970). Geochemical and thermal models of a martian magma ocean indicate that higher pressures in the mantle and early sequestration of aluminum in garnet at depth may have reduced the amount of aluminum available for plagioclase crystallization and prevented the formation of a plagioclase-rich floating crust as on the Moon (Borg et al., 2003; Elkins-Tanton et al., 2010; Elkins-Tanton et al., 2005).

On Mars, stratigraphic and spectral analyses of pre-Noachian crustal outcrops suggest that some regions may be remnants of a primary crust with feldspathic compositions (Carter et al., 2013; Wray et al., 2013). The localisation of these anorthositic outcrops in impact basins suggests that these rocks may represent the primary crust of Mars (Phillips et al., 2022). These lithologies could reflect crystallization from a global magma ocean, or alternative processes, such as magmatism in crustal reservoirs (Carter et al., 2013). The interpretation is further complicated by the association of feldspar-rich signatures with secondary alteration products such as clay minerals (Wray et al., 2013). Orbital observations confirm that plagioclase occurrences on Mars span multiple lithologies, reflecting the complexity of its magmatic and crustal evolution (Rogers et al., 2022; Flahaut et al., 2023). While most detections are consistent with localized plutonic origins, the existence of a global anorthositicc floating crust similar to that of the Moon remains uncertain and cannot be completely ruled out (Carter et al., 2013).

However, given the high pressures in the martian mantle, the first olivine crystals to form may have accumulated at intermediate depths. Experimental studies suggest that olivine crystals can experience a buoyancy transition (Suzuki et al., 1998; Suzuki et al., 2003). The occurrence of such a transition implies that the magma ocean is divided into three layers : a basal magma ocean, a layer of olivine cumulates, and an upper magma ocean. Using the same phase diagram as for the Moon, if the pressure at the eutectic is below 1 GPa, anorthite crystallizes, enabling the formation of an anorthositic floatation crust (Walker et al., 1977).

Here, we explore this possibility by applying the lunar magma ocean (LMO) solidification model to Mars. The modification of our model incorporates the buoyancy transition of olivine and modifies the thermal evolution accordingly. This approach allows us to con-

strain the maximum thickness of a primary anorthositic crust on Mars and to estimate the timescales required for its solidification.

5.2 Modification of the model

5.2.1 Olivine density crossover

In this study, we aim to apply the solidification model developed for the LMO (Chapter 2) to the case of Mars, with the objective of constraining the maximum thickness of a pure anorthite primary crust and the time required for its formation. However, this model must be adapted to account for the specific characteristics of Mars. In particular, the higher size and higher gravity of Mars influence the stability and the appearance of anorthite in the crystallization sequence. The main parameters are the initial content in anorthite component C_0, and the eutectic composition C_{E}. According to the phase diagram, the solidification of the magma ocean is divided into two distinct stages. In the first stage, only olivine crystallizes and settles to the bottom. In the second stage, olivine continues to crystallize and settle, while anorthite crystals form the flotation crust. For example directly applying our LMO model to Mars, and using an initial content of anorthite component corresponding to a hydrated Moon-like composition $C_0 = 0.06$, and assuming that the first stage of crystallization reaches the eutectic when approximately 80% of the magma ocean is solidified, the resulting radius of the cumulates at the end of the first stage can be calculated from:

$$R_{\mathrm{cu,E}} = \left(R_{\mathrm{M}}^3 - 0.8(R_{\mathrm{M}}^3 - R_{\mathrm{co}}^3)\right)^{\frac{1}{3}}, \tag{5.1}$$

where R_{M} and R_{co} are the radii of Mars and at the core, respectively (table 5.1). In this case $R_{\mathrm{cu,E}}$ =2233 km (corresponding to $C_{\mathrm{E}} = 0.7$). With ρ and g the average density and gravity, the corresponding pressure at that depth, assuming $P(r) = \rho g(R_{\mathrm{M}} - r)$, is ∼14 GPa, which is too high to allow for anorthite to crystallize (Walker et al., 1977). At such high pressures, the aluminum-rich compound that forms is garnet. Hence, the phase diagram we use for the Moon may not directly apply to Mars because the range of pressures is too wide.

However, given the higher pressures range inside Mars than on the Moon, it is likely that the planet experienced a density crossover between olivine crystals and the liquid from which they crystallized, with olivine becoming less dense than the high-pressure liquid below (Agee et al., 1988). It has been proposed that a density crossover on Mars exists at a depth of approximately 600 km, corresponding to a pressure of 7.3 GPa, (Suzuki et al., 1998). Other studies report pressure values for this density crossover around 6.3

GPa (Suzuki et al., 2003), which can even drop to 3.9 GPa in some study (Lange et al., 1990). We denote the pressure corresponding to this transition in density as P_{C^*}. The occurrence of a density crossover leads to the formation of three distinct layers (fig. 5.1): an Upper Magma Ocean (UMO), the cumulates, and a Basal Magma Ocean (BMO), the latter potentially persisting today at the base of the martian mantle (Samuel et al., 2023; Khan et al., 2023). For simplicity, we treat the BMO and the core, as a single thermal reservoir denoted by the subscript C^*. To simplify our model, we assume that gravity and density in the mantle are uniform. The density crossover radius R_{C^*} can be defined by the relationship:

$$R_{C^*} = R_M - \frac{P_{C^*}}{\rho g}, \tag{5.2}$$

with P_{c^*} the pressure and R_{C^*} the radius at the top of the core-BMO system.

For our study, we examine a range of values for P_{C^*} between 3.5 and 7.5 GPa (table 5.1). In this context, the floating crust forms exclusively from the UMO by fractional crystallization with the sedimentation of olivine crystals. In the case of Mars, the phase diagram used is not the most relevant. Other aluminium-rich phases can crystallize at pressures higher than 1 GPa, such as garnet, which does not float (Borg et al., 2003). We therefore focus on the evolution of the UMO, located above the density crossover pressure P_{C^*}, and adapt the initial LMO model to include the effect of this transition. We will thus study the crystallization of UMO, and we will only track the evolution of the average temperature of the BMO, which will serve as our boundary condition. As for the Moon, the solidification of the UMO occurs in two stages. During the first stage, olivine crystals aggregate at the density crossover radius. During the second stage, there is simultaneous crystallization of olivine crystals, which continue to settle, and aluminium-rich minerals. If the pressure reached on the UMO at the end of the first stage is below 1 GPa, then anorthite crystallizes, and floating crust forms. But if, at the end of the first stage, the pressure is higher than 1 GPa in the UMO, then garnet forms instead of anorthite, and our model cannot be applied. Thus, we first need to constrain the conditions of applicability of our model in terms of model parameters.

5.2.2 Conservation of anorthite component in the UMO

As for the LMO, we use a phase diagram with an eutectic, which is composed of two end members: olivine (ol) and anorthite (an). The crystallization of the UMO is treated in two successive stages. During the first stage, mass conservation in the UMO yields the relation:

$$\left(R_M^3 - R_{C^*}^3\right) C_0 = \left(R_M^3 - R_{cu}^3(t)\right) C(t), \tag{5.3}$$

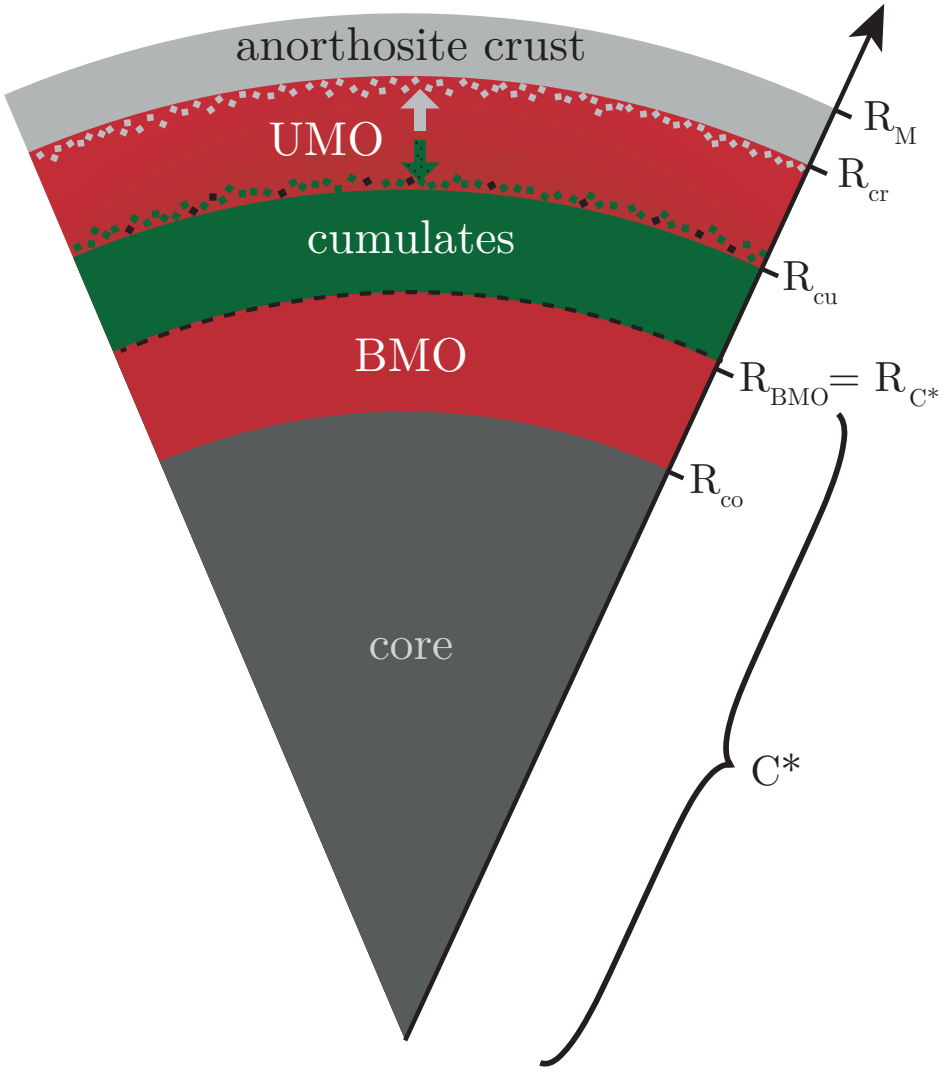

Figure 5.1: Schematic representation of the interior of Mars with a basal magma ocean during the second stage of crystallization. The core is shown in dark gray, the olivine cumulates in green, the BMO and UMO in red, and the conductive crust in light gray. The core-BMO system is denoted by C∗

Table 5.1: List of the parameters and variables of the model.

Symbol	Description	Value	References
Parameters			
R_{M}	Radius of Mars	3400 km	
R_{co}	Radius of the core	1700 km	
T_{OL}	Liquidus temperature for the olivine component	2150 K	O'Driscoll et al. (2010)
T_{E}	Eutectic temperature	1600 K	O'Driscoll et al. (2010)
m	Liquidus slope	$m = (T_{\mathrm{OL}} - T_{\mathrm{E}})/C_{\mathrm{E}}$	
h_0	Initial heat production	$23\,\mathrm{pW\,kg^{-1}}$	Taylor (1982)
	Initial uranium abundance	16 ppb	Taylor (1982)
	Initial thorium abundance	56 ppb	Taylor (1982)
	Initial potasium abundance	305 ppb	Taylor (1982)
λ	Effective radiogenic decay constant	$5.8 \times 10^{-10}\,\mathrm{Myr^{-1}}$	
D	Solid/liquid partition coefficient for HPEs	10^{-3}	Sun et al. (2017)
g	Gravity acceleration	$3.7\,\mathrm{m\,s^{-2}}$	
ρ	Density	$3.5 \times 10^3\,\mathrm{kg\,m^{-3}}$	
c_{p}	Heat capacity	$10^3\,\mathrm{J\,kg^{-1}\,K^{-1}}$	
L	Latent heat of crust	$5 \times 10^5\,\mathrm{J\,kg^{-1}}$	Weill et al. (1980)
σ	Stefan-Boltzman constant	$5.67 \times 10^{-8}\,\mathrm{J\,K^{-1}}$	
ε	Emissivity	1	
A	Albedo	0.12	
$T_{\odot}$	Sun surface temperature	5780 K	
$R_{\odot}$	Sun radius	700×10^3 km	
$D_{\odot}$	Mars-Sun distance	2.27×10^{11} km	
T_{∞}	Black body equilibrium temperature	7 K	
α	Thermal expansion coefficient	$10^{-5}\,\mathrm{K^{-1}}$	Maurice et al. (2020)
μ_{UMO}	Viscosity	1 Pa s	
k	Thermal conductivity of the UMO	$4\,\mathrm{W\,m^{-1}\,K^{-1}}$	
k_{cu}	Thermal conductivity of cumulates	$4\,\mathrm{W\,m^{-1}\,K^{-1}}$	Maurice et al. (2020)
k_{cr}	Thermal conductivity of the crust	$2\,\mathrm{W\,m^{-1}\,K^{-1}}$	Maurice et al. (2020)
β	Thermal boundary layer coefficient	1/3	Gastine et al. (2016)
γ	Scaling prefactor	0.07	Gastine et al. (2016)
$c_{\mathrm{p,\,co}}$	Heat capacity of the core	$840\,\mathrm{J\,kg^{-1}\,K^{-1}}$	Maurice et al. (2020)
ρ_{co}	Density of the core	$7.2 \times 10^3\,\mathrm{kg\,m^{-3}}$	
Explored parameters			
C_{E}	Eutectic composition	$\in [0.2, 0.7]$	
P_{C^*}	pressure of density crossover	$\in$ [3.5, 7.5] GPa	
R_{C^*}	Density crossover radius	$\in$ [2820.8, 3129.7] km	

where R_{cu} is the radius of the cumulates and $C(t)$ the mass fraction in anorthite component in the UMO. When the temperature inside the UMO reaches the eutectic temperature, the first stage ends, and the cumulate radius at the eutectic $R_{\mathrm{cu,\,E}}$ is given by:

$$R_{\mathrm{cu,\,E}} = \left[R_{\mathrm{M}}^3 - \frac{C_0}{C_{\mathrm{E}}} \left(R_{\mathrm{M}}^3 - R_{\mathrm{C}^*}^3 \right) \right]^{1/3}, \tag{5.4}$$

with C_{E} the eutectic composition.

However, anorthite can only crystallize at pressures lower than $P_{\max} = 1\,\mathrm{GPa}$, which imposes a minimum depth for the crystallization of anorthite and gives a constraint on the value of $R_{\mathrm{cu,E}}$. This condition is expressed as:

$$\rho g (R_{\mathrm{M}} - R_{\mathrm{cu,E}}) \leq P_{\max}. \tag{5.5}$$

For our model and the phase diagram to be applicable, the radius at the end of the first stage must thus reach:

$$R_{\mathrm{cu,\,E}} \geq R_{\mathrm{M}} - \frac{P_{\max}}{\rho g}. \tag{5.6}$$

Combining eq. (5.4) and eq. (5.6), we obtain an upper bound for the ratio $\dfrac{C_0}{C_{\mathrm{E}}}$ as function of the density crossover radius R_{C^*}:

$$\frac{C_0}{C_{\mathrm{E}}} \leq \frac{R_{\mathrm{M}}^3 - \left(R_{\mathrm{M}} - \dfrac{P_{\max}}{\rho g} \right)^3}{R_{\mathrm{M}}^3 - R_{\mathrm{C}^*}^3}, \tag{5.7}$$

In the second stage of crystallization, assuming all remaining anorthite crystallizes and contributes to crust formation, mass conservation gives:

$$\left(R_{\mathrm{M}}^3 - R_{\mathrm{cr,f}}^3 \right) = \left(R_{\mathrm{M}}^3 - R_{\mathrm{C}^*}^3 \right) C_0, \tag{5.8}$$

giving directly $R_{\mathrm{cr,f}}$, the final crust radius. We solve the conduction equations in the crust and the cumulates and apply an energy budget in the UMO.

5.2.3 Heat Producing Elements

As for the Moon, Heat Producing Elements (HPEs) are an important source of heat in the magma ocean. In the model, we consider that the HPEs are initially distributed homogenously between the UMO and the BMO. The silicate part is characterized by heat production per unit volume h_0. In the case of the core-BMO system, the volume of the core must be taken into account, which is considered to have no heat production. We

define h_{C^*} as the heat production per unit volume of the core-BMO system such that:

$$h_{C^*} = h_0 \frac{V_{BMO}}{V_{C^*}}, \tag{5.9}$$

where $V_{BMO} = \frac{4\pi}{3}(R_{C^*}^3 - R_{co}^3)$ is the volume of the BMO and $V_{C^*} = \frac{4\pi}{3}R_{co}^3$ is the total volume of the core-BMO system. Later, it is considered that this heat production contributes to the secular cooling of the core-BMO system (see section 2..2)

As explained in Chapter 2, we consider a partition coefficient D between the liquid and the solid in the UMO. Since HPEs are incompatible elements, they tend to remain in the liquid phase.

5.2.4 Stage 1

We consider the UMO as a spherical shell of outer radius R_M, and inner radius $R_{cu}(t)$ which starts from R_{C^*} and increases with time as the UMO cools down and solidifies. To follow the temporal evolution of the cumulate radius and the temperature inside the UMO we apply the same model as developed in Chapter 2 for the LMO. The heat lost by radiation into space at the surface Φ_{surf} is balanced by the sum of the latent heat released by crystallization of olivine cumulates Φ_{L_h}, the heat produced by radiogenic decay Φ_{HPE}, and secular cooling of the UMO Φ_{MO}:

$$\Phi_{surf} = \Phi_{L_h} + \Phi_{HPE} - \Phi_{MO}. \tag{5.10}$$

Given the short duration of the first crystallization stage, we neglect the contribution of the core-BMO system and thermal diffusion in the cumulates.

5.2.5 Stage 2

During the second stage of crystallization we solve the conduction equations in the crust and in the cumulates and the heat conservation equations in the UMO. The main difference between models for the Moon and Mars during that stage lies in the cooling of the core. For Mars, we consider the core and the BMO as a single entity with a heat production rate h_{C^*} and uniform temperature T_{C^*}. The conservation of heat in the combined core–BMO system governs the evolution of the temperature T_{C^*}:

$$\rho_{C^*} c_{p,C^*} \frac{4}{3}\pi R_{C^*}^3 \frac{dT_{C^*}}{dt} = -4\pi R_{C^*}^2 q_{C^*} + \frac{4}{3}\pi R_{C^*}^3 h_{C^*} e^{-\lambda t}, \tag{5.11}$$

where ρ_{C^*} is the density of the core–BMO system, c_{p,C^*} its specific heat capacity, and λ the radiogenic decay constant. As in the lunar case, the heat flux from the core–BMO

system q_{C^*} is obtained from the temperature gradient at the base of the cumulates. Equation (5.11) thus provides the thermal evolution of the core, which is used as the lower boundary condition for the cumulates.

To track the temporal evolution of the crustal radius $R_{cr}(t)$ and cumulates radius $R_{cu}(t)$ during the second stage of crystallization, we apply heat conservation in the UMO. The heat flux conducted through the crust, Φ_{cr}, is balanced by the sum of the diffusive heat flux from the cumulates, Φ_{cu}, the latent heat released by crystallization, Φ_{L_h}, and the radiogenic heating from heat-producing elements, Φ_{HPE} in the UMO:

$$\Phi_{cr} = \Phi_{cu} + \Phi_{L_h} + \Phi_{HPE}. \tag{5.12}$$

A detailed description of the two crystallization stages is provided in Chapter 2 of this manuscript.

5.3 Results

5.3.1 Maximum possible crustal thickness given R_{C^*} and C_E

For anorthite to crystallize rather than garnet once the eutectic composition is reached, the pressure at eutectic at the base of the UMO must be less than P_{max}. We have shown in section 5.2.1 that on Mars there likely exist a density crossover pressure, *i.e.*, a pressure at which the density of olivine is lower than that of the magma ocean. Equation (5.7) shows that the conditions for appearance of anorthite at the eutectic depends on this pressure of density crossover. We first investigate how variations of the eutectic composition C_E and of the pressure of density crossover P_{C^*} (and associated radius R_{C^*}) affect the condition of application of our phase diagram. The objective is to determine the maximum value of C_0, denoted $C_{0,max}$, that is possible to allow the crystallization of anorthite once the eutectic is reach. The maximum value $C_{0,max}$ is derived from these two parameters according to eq. (5.7):

$$C_{0,max} = \frac{R_M^3 - \left(R_M - \frac{P_{max}}{\rho g}\right)^3}{R_M^3 - R_{C^*}^3} C_E \tag{5.13}$$

For the explored parameter space, *i.e.*, for $P_{C^*} \in [3.5, 7.5]$ GPa and $C_E \in [0.2, 0.7]$, $C_{0,max}$ varies between 0.03 and 0.2 (gray dashed lines on fig. 5.2). As expected from eq. (5.13), $C_{0,max}$ increases with C_E. A higher eutectic composition delays the onset of the second crystallization stage, leading to a smaller pressure at the end of the first stage, and allowing for higher values of $C_{0,max}$. If the pressure at the density crossover is lower, $C_{0,max}$ can also lead to higher values. This occurs because the initial depth of the UMO is

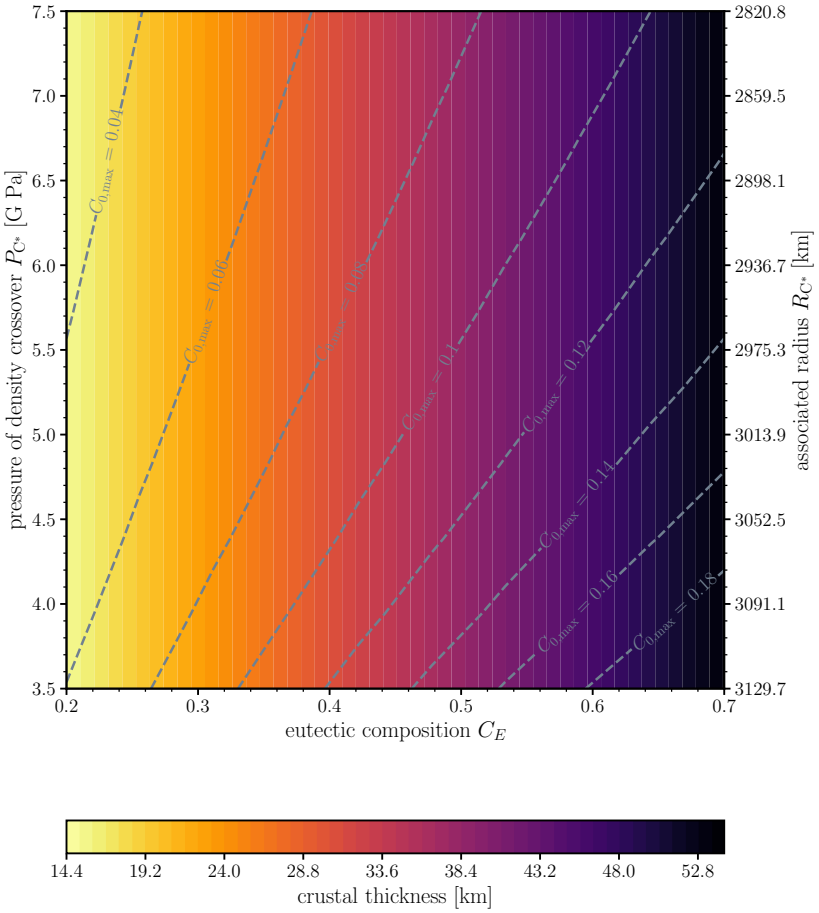

Figure 5.2: Maximum possible initial anorthite content C_0 and final crustal thickness as function of C_{E} and P_{C^*}, where we use $k_{\mathrm{crust}} = 2\,\mathrm{W\ m^{-1}\ K^{-1}}$. The colorbar corresponds to the maximum crustal thickness. The grey dashed lines correspond to isovalues of the maximum content in anorthite component, and hence, to the thickness of the crust according to eq. (5.8)

reduced, making the condition for anorthite crystallization below 1 GPa less restrictive. The maximum crust thickness is controlled by the eutectic composition rather than by the depth of the density crossover. Indeed, from eq. (5.8), the final crustal radius $R_{\mathrm{cr,f}}$ is given by:

$$R_{\mathrm{cr,f}} = \left(R_{\mathrm{M}}^3 - C_{0,\mathrm{max}}(R_{\mathrm{M}}^3 - R_{\mathrm{C}^*}^3)\right)^{\frac{1}{3}}, \tag{5.14}$$

and combining the expression of $C_{0,\mathrm{max}}$ from eq. (5.13) and the final crustal radius, eq. (5.14) yields:

$$R_{\mathrm{cr,f}} = \left(R_{\mathrm{M}}^3 - C_{\mathrm{E}}\left(R_{\mathrm{M}}^3 - \left(R_{\mathrm{M}} - \frac{P_{\mathrm{max}}}{\rho g}\right)^3\right)\right)^{\frac{1}{3}}, \tag{5.15}$$

which no longer depends on R_{C^*} and only depends on C_{E}. Therefore, R_{C^*} only influences

the initial content in anorthite component. Crustal thicknesses vary between 14.4 km and 53 km (see colorbar in fig. 5.2) and depend primarily on C_{E}. If the pressure at the base of the UMO reaches a value greater than $P_{\max}$ at the eutectic, garnet crystallizes instead of anorthite until the pressure at the base of the UMO reaches 1 GPa. This should have the effect of reducing the thickness of the crust. The values obtained in this section correspond to a maximum crust thickness.

5.3.2 Solidification time and crustal thickness for a hydrated Mars

The value of $C_{0,\max}$, the initial content in anorthite component is in fact limited as anorthite is less stable in presence of water (Lin et al., 2017). In this study, we thus adopt $C_0 = 0.06$, consistent with the value inferred for a hydrated Moon (Lin et al., 2017; Colin et al., 2024), as Mars was likely wet, at least initially (McSween Jr et al., 2001). According to the results presented in section 5.3.1, there remains a region of the parameter space where the phase diagram we consider is not applicable. This area, shown in gray in fig. 5.3, corresponds to cases where $C_{0,\max} < 0.06$ (fig. 5.2). In this zone, the pressure reached at the eutectic is greater than $P_{\max}$, so other phase form instead of anorthite, and do not float. Apart from this zone, the value $C_0 = 0.06$ is lower than the maximum possible value $C_{0,\max}$, which allows the formation of an anorthositic floatation crust. We therefore estimate, on the part of the phase diagram where our model applies, the thickness of the crust that can form on Mars and the time required for its formation. The final crustal thickness ranges from 14 km to 29.4 km. The solidification time of the primary flotation crust goes from 5 Myr to 35 Myr. The thickness of the crust increases as R_{C^*} decreases, in agreement with the conservation of anorthite component, (eq. (5.8)). A smaller R_{C^*} implies a thicker initial UMO, and therefore more anorthite available for crust formation. The timescale of crust solidification increases, for instance, with $C_{\mathrm{E}} = 0.4$, the solidification time nearly triples, when R_{C^*} varies from 3129.7 km to 2820.8 km. This increase in solidification time is related to an increase in the thickness of the crust, as well as to a larger UMO volume that must crystallize. For a fixed value of R_{C^*}, and thus a fixed final crustal thickness, the solidification time increases with C_{E}. This difference shows that the amount of UMO remaining at the beginning of the second stage affects the total solidification time (as shown in Chapter 2). By fixing the final crust thickness at 20 km, the solidification time decreases from ∼15 Myr to ∼10 Myr for values of C_{E} between 0.3 and 0.7. In the first case, 80% of the UMO has crystallized at the end of the first stage, while in the second case, 88% is crystallized. A thinner UMO at the onset of the second stage of crystallization leads to a shorter solidification time.

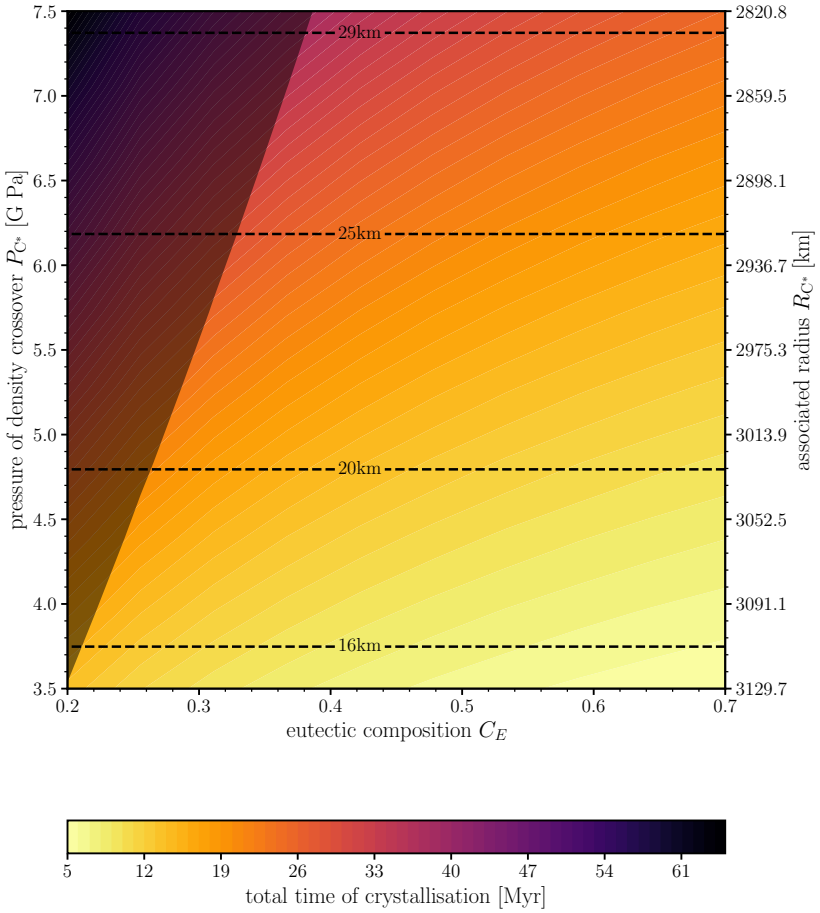

Figure 5.3: Total solidification time for the UMO (colorbar) and crustal thickness (black dashed lines) as function of C_{E} and the pressure density crossover P_{C^*}, using $C_0 = 0.06$ and $k_{\mathrm{crust}} = 2\mathrm{W\ m^{-1}\ K^{-1}}$. The colorbar corresponds to the solidification time. The black dashed lines correspond to the isovalues of the thickness of the crust as it depends of the value of R_{C^*}. The shaded area corresponds to the region of parameters space where our phase diagram does not apply for $C_0 = 0.06$.

5.4 Implications for Mars

The pressure reached at the eutectic must be less than $P_{\max}$ for anorthite to crystallize at this point, and for our phase diagram to be valid. Equation (5.7) can be used to determine an upper bound for C_0, noted $C_{0,\max}$ that satisfies the stability conditions for anorthite formation. Assuming a composition similar to that of a hydrated Moon ($C_0 = 0.06$, consistent with eq. (5.7)), the final crustal thickness is controlled by the radius R_{C^*}. A higher crossover pressure corresponds to a deeper UMO, which results in a thicker final crust (figs. 5.2 and 5.3, eq. (5.7)) and a longer solidification timescale. As for the Moon, the total solidification time of the flotation crust increases as C_{E} decreases, since a larger amount of latent heat must be removed through the floating lid due to higher depth at the beginning of the second stage of crystallization. Our model is simple and only allows

for the crystallization of anorthite without considering other phases. When the eutectic is reached at pressures above 1 GPa, other phases, than anorthite, that are denser crystallize, and the phase diagram we use is no longer available. In this case the cumulates continue to grow without the formation of a flotation crust. Furthermore, if the components that form anorthite go into other phases, this reduces the total amount of anorthite that can crystallize. This is equivalent to reducing the value of C_0 and therefore reducing the thickness of the crust that can form on Mars.

Considering a density crossover pressure between 3.5 GPa and 7.5 GPa, we show that $C_{0,\max}$ values can reach up to 0.2. Considering this extreme case, the crust thickness can reach up to 60 km in theory (fig. 5.2). Given the aluminum depletion of the martian magma ocean and the evidence for water in the martian mantle, such a high C_0 appears unlikely. Adopting a more realistic initial anorthite content, comparable to that used for a hydrated Moon ($C_0 = 0.06$; Lin et al. 2017), the maximum thickness of a primary anorthositic crust on Mars is ∼30 km, with a maximum formation timescale of about 35 Myr (fig. 5.3).

This maximum thickness, although smaller than that inferred for the Moon, is still significant and suggests that remnants of a buoyant anorthosite-rich primary crust could locally persist within the martian crust. However, a substantial fraction of this early crust was likely reprocessed during the subsequent evolution of Mars through large impacts, magmatism, and partial melting.

Isotopic measurements provide age constraints on martian meteorites, allowing estimates of the solidification timescale of the martian magma ocean. Debaille et al. (2007) performed isotopic analyses on shergottites and suggested that a global magma ocean state may have persisted for approximately 100 Myr. Other isotopic studies on shergottites indicate that large-scale silicate differentiation of Mars occurred about 60 Myr after the formation of the Solar System (Borg et al., 2016). More recent high-precision uranium-lead dating of zircons shows that the martian magma ocean had fully solidified in less than 20 Myr after Solar System formation (Bouvier et al., 2018). In addition, models for the formation of the primitive martian crust by melting of the deep mantle following a compositional overturn suggest crystallization times of the order of 30 Myr to 50 Myr (Elkins-Tanton et al., 2005). Taken together, these results indicate that the crystallization of the martian magma ocean was relatively rapid, likely completed within a few tens of millions of years after the accretion of Mars. In our model for the solidification of the UMO, the maximum crustal thickness forms within 35 Myr for a hydrated composition, which represents an upper bound and is in good agreement with both isotopic constraints and previous modeling studies.

The Insight mission revealed that the martian crust is layered, at least beneath the

InSight station (Knapmeyer-Endrun et al., 2021). However, analyses of seismic propagation times associated with located quakes on Mars do not indicate wave velocity ratios $\frac{V_p}{V_s}$ characteristic of anorthosite composition for these layers, at least at the regional scale around InSight (Drilleau et al., 2022). The martian highlands, which have a higher topography and potentially lower density (Baratoux et al., 2014; Goossens et al., 2017; Wieczorek et al., 2022), are the areas where anorthite outcrops have been detected (Wray et al., 2013; Carter et al., 2013). However, few marsquakes have occurred in these regions (Drilleau et al., 2022), which does not provide sufficient data to confirm or refute the presence of an anorthositic primary crust there.

5.5 A thermal overturn on Mars ?

In this section, we investigate the possibility of thermal instabilities occurring in martian cumulates before the end of the UMO solidification time. The application of our solidification model, previously developed for the Moon to Mars, shows that a thin primary floatation crust may have formed on Mars over tens of millions of years. We also hypothesize the existence of a BMO, meaning that a magma ocean is present both at the base and at the top of the cumulate layer. In this configuration, we can assume that a phase-change boundary condition applies at both the top and bottom of the cumulates. We use a linear stability analysis with a phase-change boundary condition to study the onset of the overturn in the cumulates (see Chapter 3). Several studies have suggested for instance that an overturn of the martian mantle may indeed have occurred (Elkins-Tanton et al., 2005; Plesa et al., 2022).

In our model, using $C_0 = 0.06$ and $C_\mathrm{E} = 0.3$, 80% of the UMO is crystallized at the end of the first stage, and we obtain a final crust thickness of 20 km, and a radius for the core–BMO system of $R_{\mathrm{C}^*} = 3030$ km. At the end of the first stage, the cumulate thickness is ∼300 km thick, leading to an aspect ratio of $\gamma = \frac{R_{\mathrm{C}^*}}{R_\mathrm{cu}} = 0.9$. The solidification timescale for this example is ∼20 Myr. The diffusion timescale $\mathcal{T} = \dfrac{H^2}{\kappa}$ in the cumulates is approximately $\mathcal{T} \sim 3.1$ Gyr, long compared to the total solidification time of the crust. Thus, the BMO should not crystallize much during the solidification of the UMO, making our estimate of γ reasonable for studying the onset of convection.

We perform a linear stability analysis (LSA) by systematically varying the Rayleigh number, $\mathcal{R}a \in [10^4, 10^7]$, and the phase change numbers at the top Φ^+ and bottom Φ^- of the cumulates. For simplicity, we assume $\Phi^+ = \Phi^-$ and denote this common value as Φ, with $\Phi \in [10^{-2}, 10^5]$. We are looking for the maximum growth rate σ_{LSA} that associated to the preferred convection mode l (fig. 5.4). As shown in the previous chapters, the growth rate σ_{LSA} decreases with the phase-change number Φ (fig. 5.4a). Non-penetrative

conditions ($\Phi \to \infty$) make the onset of convection more difficult. The growth rate also decreases while decreasing values of the Rayleigh number $\mathcal{R}a$. A too small Rayleigh number similarly prevents the development of convection. For the associated wavelength l, three regimes can be identified (fig. 5.4b). In the first one, for $\Phi < 2$, the preferred convective mode is $l = 1$, independent of both the Rayleigh number and the phase change number. Between $\Phi = 2$ and $\Phi = 400$, the preferred value of l increases with Φ, and the influence of $\mathcal{R}a$ becomes increasingly visible as Φ increases. As $\mathcal{R}a$ increases, the preferred wavelength of convection increases. A large Rayleigh number increases the value of $\mathcal{R}a$ increases the value of l. This effect also persists in the third regime ($\Phi > 400$), where l no longer varies with Φ but depends solely on $\mathcal{R}a$. The high spherical harmonic degree observed as Φ increases is due to the high value of the aspect ratio γ of the cumulates.

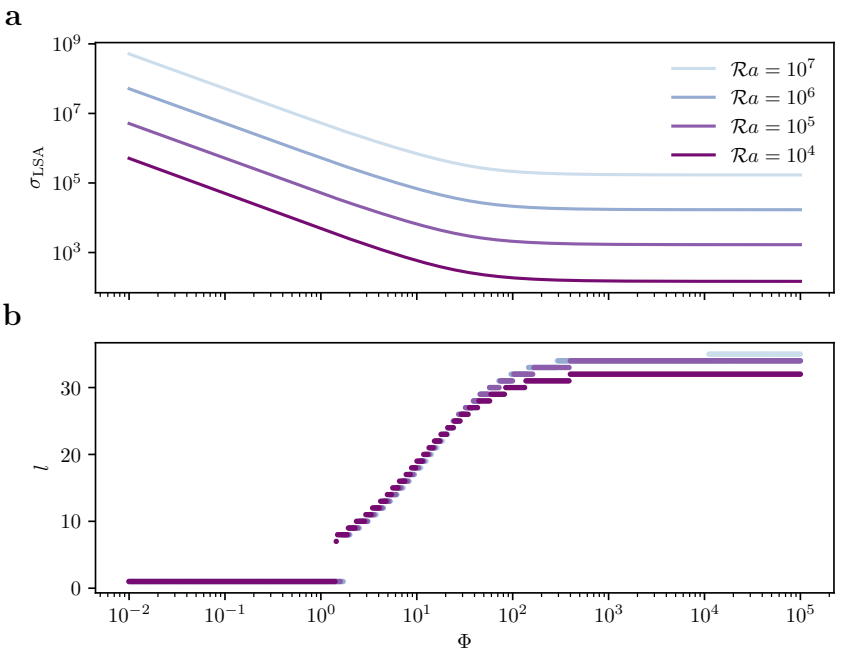

Figure 5.4: Linear stability analysis of the preferred convection mode or the dimensionless growth rate σ_{LSA} (a) of the cumulates and associated spherical harmonic degree l (b) as a function of Φ (assuming that $\Phi^+ = \Phi^-$) for different values of the Rayleigh number. $\mathcal{R}a = 10^7$ in pale blue line, $\mathcal{R}a = 10^6$ in blue line, $\mathcal{R}a = 10^5$ in pale purple line, and $\mathcal{R}a = 10^4$ in purple line.

The dimensional destabilization timescale is given by the relation $\tau = H^2/(\kappa\sigma)$ (fig. 5.5). The onset time for the instability and the associated characteristic wavelength depend on both the Rayleigh number and the phase change number. For a small phase change ($\Phi = 10^{-2}$), the onset time ranges from a few years at $\mathcal{R}a = 10^7$ to a few thousand years at $\mathcal{R}a = 10^4$ (fig. 5.5). The overturn develops well before the completion of UMO solidification and is dominated by a degree-one spherical harmonic, even in the case of a very

thin shell if the interface are permeable. As the phase change is at both of the interface of the cumulates, this corresponds to a translation mode described by Morison et al. (2024). This translation mode is represented on fig. 5.6a, where the streamlines are open at the top and the bottom of the cumulates compared to the case with impermeable boundary conditions (fig. 5.6b). In the scenario where the cumulates are larger, corresponding to a decrease in γ, the onset of convection would be facilitated and the preferred mode of convection would tend to lower values of l (see Chapter 3). In all of these configurations $(\mathcal{R}a, \Phi)$, the onset time of instability remains shorter than the solidification timescale. These results suggest that degree-one convection may develop within the martian cumulates before the complete solidification of the UMO in the case of an efficient phase change at both cumulate boundaries. To test this possibility, direct numerical simulations combined with linear stability analysis are needed to more accurately constrain the timescale and mode of convection at the onset of convection in the cumulates. Additionally, a more accurate estimate of the thickness of the cumulates should be provided, taking into account the thermal evolution of the BMO.

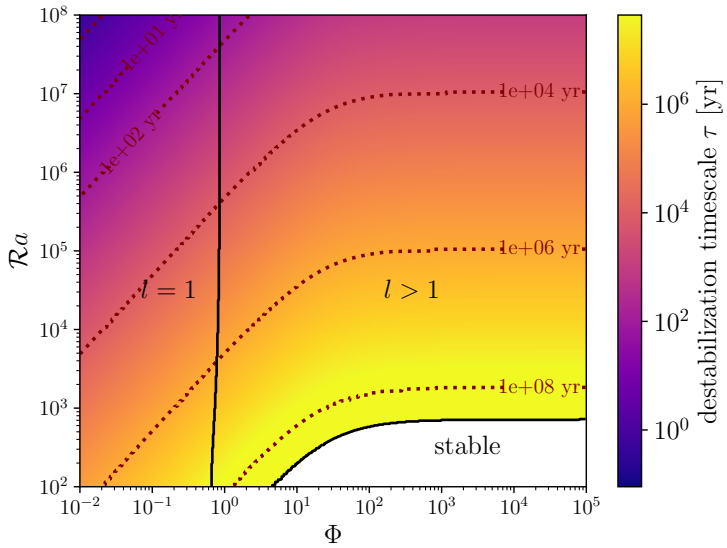

Figure 5.5: Dimensional timescale τ in years for the onset of convection as a function of $\mathcal{R}a$ and Φ. The black solid line corresponds to the transition between the mode $l = 1$ and the higer mode. The brown dotted lines correspond to isovalues of τ.

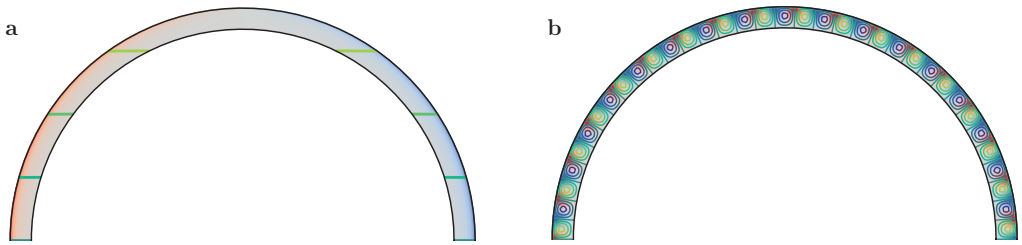

Figure 5.6: Temperature perturbation and streamlines for $\mathcal{R}a = 10^7$ and **a**- $\Phi = 10^{-2}$, and **b**- $\Phi \to \infty$.

5.6 Conclusion

In this chapter, we modify the original model of LMO solidification to study the possible formation of a buoyant anorthositic crust on Mars, and the time required for its formation. The pressure inside Mars is higher than that within the Moon. We consider the occurrence of a transition between olivine crystals and the melt at a given pressure in the Martian mantle. The presence of this density crossover in buoyancy implies that the initial magma ocean is divided into three parts: a basal magma ocean, the cumulate layer, and an upper magma ocean.

Here, we focus on the thermal evolution of the upper magma ocean, and use the same phase diagram we applied for the Moon. We determine an upper limit for the initial anorthite component for our model to be applicable, that depends on the pressure of density crossover. We then estimate the maximum thickness of the crust based on a Moon-like hydrated composition. For an initial composition C_0 corresponding to a hydrated planet, the resulting floating crust can have a minimum thickness of ∼15 km and a maximum thickness of ∼30 km, depending on the pressure of density crossover. The time required for such a crust to form varies between ∼ 5 Myr and 35 Myr. Furthermore, we investigate the possibility of a thermal overturn in the martian cumulates by considering phase changes at both the top and bottom of the cumulates. We show that, for small ($\Phi = 10^{-2}$) and identical phase change numbers at both boundaries, a mantle overturn can occur very rapidly, within a few years to a few thousand years, depending on the Rayleigh number, even in the case of a thin spherical shell. The dominant overturn mode corresponds to a spherical harmonic of degree one. On Mars, the topography shows a dichotomy between the south pole and the north pole. Degree-one convection in the martian cumulates during the solidification of the magma ocean may be one way to explain this dichotomy.

Chapter 6

Conclusion et perspectives

6.1 Conclusion

Dans l'introduction de ce manuscrit, plusieurs questions ont été soulevées : quel est le temps nécessaire à la solidification de l'océan de magma lunaire ? Quel est le temps caractéristique du développement d'une instabilité thermique ? Dans le cas d'un retournement des cumulats lunaires, quel est son temps d'initiation et sa durée ? Nous avons apporté des éléments de réponse à ces différentes questions.

Dans un premier temps, à partir d'un modèle simplifié et d'un diagramme de phase présentant un eutectique, nous avons estimé le temps de solidification de l'océan de magma lunaire. Ce temps dépend principalement de trois paramètres : la composition initiale en anorthite, qui contrôle l'épaisseur de la croûte, la composition eutectique, qui contrôle l'apparition de l'anorthite dans la séquence de cristallisation, et la conductivité thermique de la croûte. Nous montrons que le temps de solidification est compris 45 et 240 millions d'années (Ma). En particulier, une croûte épaisse et une faible conductivité thermique augmentent le temps de solidification. De même, un océan de magma plus épais à la fin de la première étape de cristallisation augmente ce temps de solidification. Ainsi, à partir de ce modèle, nous posons des contraintes sur l'âge de la Lune compris entre 4400 et 4560 Ma. Par ailleurs, nous avons étudié comment la présence d'un retournement, modélisé par une décroissance exponentielle du flux de chaleur dans les cumulats peut affecter significativement ce temps de cristallisation. Un retournement rapide, d'une durée inférieure à 5 Ma, tend à réduire le temps de solidification. Au contraire un retournement long, d'une durée supérieure à 5 Ma, augmente le temps de cristallisation.

Comme le temps de solidification de l'océan de magma lunaire est long, il est possible que des instabilités thermiques se developpent avant la fin de la solidification de l'océan

de magma lunaire, voir avant que les phases denses ne cristallisent en haut des cumulats. Pour étudier cela, nous avons d'abord considéré un cas général. Nous avons aussi pris en compte les échanges possibles entre les cumulats et l'océan de magma. Nous imposons une condition aux limites mécanique permettant un échange de matière entre les cumulats et l'océan de magma, via des processus de fusion et de cristallisation. Pour étudier la convection dans les cumulats, nous avons utilisé une étude de stabilité linéaire ainsi que des simulations numériques directes. Ces approches nous ont d'une part permis de valider notre méthodologie, et d'autre part d'examiner l'influence d'une gravité variant linéairement avec le rayon (par rapport à une gravité uniforme), du rapport d'aspect de la coquille sphérique, et de courbure du profil initial de température.

Nous avons ensuite appliqué ces méthodes spécifiquement au cas lunaire, en utilisant comme état initial celui obtenu à l'issue du premier stade d'évolution de l'océan de magma lunaire dans notre modèle. L'étude de stabilité linéaire, couplée aux simulations numériques, permet d'extrapoler les résultats des simulations numériques directes à l'aide de lois d'échelle. Nous montrons qu'un retournement de degré un peut se développer avant la fin de la solidification de l'océan de magma lunaire, et avant la cristallisation des phases denses. Ce retournement de degré un est en partie favorisé par la condition aux limites de changement de phase. En effet, lorsque l'on impose une condition de changement de phase, la convection de degré un est préservée dans les cumulats lunaires même à fort nombre de Rayleigh. Nous montrons par ailleurs que, pour un nombre de Rayleigh relativement faible ($\mathcal{R}a < 10^6$) et un nombre de changement de phase Φ compris entre 10^{-1} et 14, le retournement atteint son maximum après plus de 5 Ma. Dans ce régime, un champ magnétique lunaire peut être généré, induit par l'extraction de chaleur du noyau vers le manteau. Un tel retournement, de durée relativement longue, pourrait également influencer la cristallisation de la croûte : d'une part en allongeant le temps de solidification de l'océan de magma, et d'autre part en contribuant à l'asymétrie crustale observée entre les faces visible et cachée de la Lune, du fait d'un apport de chaleur par les cumulats concentré dans un hémisphère.

Enfin, nous avons proposé d'appliquer notre modèle d'évolution thermique au cas de Mars, en utilisant le même diagramme de phase que celui employé pour la Lune. Sur Mars les gammes de pression sont supérieures à celle sur la Lune. À des pression de l'ordre de 7 GPa, la densité de l'olivine peut être inférieure à celle de l'océan de magma global. Cela a pour conséquence de diviser l'océan de magma en trois couches distinctes : un océan de magma basal, les cumulats, et un océan de magma supérieur. Nous proposons d'utiliser le modèle initial développé pour la Lune à l'océan de magma supérieur de Mars. En utilisant notre diagramme de phase, nous montrons que la pression atteinte à l'eutectique peut être inférieure à 1 GPa ce qui permet la cristallisation de l'anorthite. En supposant une

composition initiale en anorthite similaire à celle de la Lune hydratée, nous montrons qu'il est possible que les pressions atteintes à l'eutectique soient favorables à la cristallisation de l'anorthite. Ainsi, une croûte d'anorthite d'une épaisseur comprise entre environ 15 et 30 km peut se former sur Mars. Les temps nécessaires à la cristallisation de cette croûte sont compris entre 5 et 35 Ma.

Nous avons montré dans le chapitre 2 que les temps de solidification de l'océan de magma lunaire peuvent atteindre des temps importants, supérieurs à 150 Ma, et qu'un retournement purement thermique des cumulats lunaires peut se produire avant la fin de la solidification complète (chapitre 4). Un tel retournement influence non seulement le temps total de solidification de l'océan de magma, mais également l'évolution de la croûte. Nous nous interrogeons en particulier sur l'effet de ce retournement sur la cristallisation de la croûte. En effet, la perturbation de degré un peut persister suffisamment longtemps au sein des cumulats pour induire une perturbation analogue à la base de la croûte. Étant donné que la présence d'un changement de phase favorise l'établissement de la convection, il est légitime de se demander si la croûte elle-même peut entrer en convection, et si celle-ci prendrait la forme d'une harmonique sphérique de degré un. Par ailleurs, le flux thermique libéré lors du retournement est maximal sur un hémisphère et quasi nul sur l'autre. Une telle asymétrie conduit naturellement à s'interroger sur ses conséquences : un flux hémisphérique aussi contrasté pourrait-il, localement, engendrer une fusion partielle de la croûte ?

6.2 Perspectives

6.2.1 La croûte peut-elle convecter ?

Une des questions que nous pouvons nous poser concerne la possibilité du démarrage de la convection dans la croûte. En effet, il s'agit d'une configuration classique de convection de Rayleigh–Bénard, où l'instabilité peut se développer en raison du gradient de température entre la base de la croûte et sa surface. De plus, la base de la croûte est en contact avec l'océan de magma lunaire (LMO), et à l'interface ces deux couches sont en équilibre de phase. En considérant un changement de phase à l'interface LMO/croûte, le développement de la convection dans la croûte peut être facilité. Le gradient de température dans la croûte est important : sa base est à la température eutectique $T_{\mathrm{E}} = 1600\,\mathrm{K}$, tandis que sa surface est à la température d'équilibre $T_{\infty} = 270\,\mathrm{K}$. La viscosité dans la croûte varie fortement entre la base et le haut de la croûte du fait des fortes variations de température. Ceci ne facilite pas la convection et entraine la formation d'un couvercle stagnant au sein de la croûte. La viscosité adimensionnée avec la température de référence adimensionnée

T_{ref} en fonction du rayon dans la croûte s'écrit :

$$\eta(r) = \exp\left(2\log(R_\eta)\left[\frac{1}{T(r)+1} - \frac{1}{T_{ref}+1}\right]\right), \tag{6.1}$$

où R_η désigne le contraste de viscosité entre la base et la surface de la croûte. Par la suite, nous considérons T_{ref} et η_{ref} comme la température et la viscosité à la base de la croûte. Nous adoptons une valeur de $R_\eta = 10^6$, qui est d'un ordre de grandeur raisonnable pour un couvercle stagnant. Des valeurs plus proches de celles de la croûte réelle seraient plus difficiles à résoudre numériquement, ce qui justifie le choix de cette valeur de référence.

Équations de la convection dans la croûte

Étant donné le fort rapport d'aspect de la croûte ($\gamma \in [0,97; 0,99]$), nous choisissons d'adopter une géométrie cartésienne pour cette étude. La limite supérieure est notée z_o et la limite inférieure z_i. L'accélération de la gravité est supposée uniforme et dirigée vers le bas : $g(r) = -g_0\mathbf{e_z}$, où g_0 représente l'intensité de la gravité et $\mathbf{e_z}$ le vecteur unitaire dans la direction verticale. La croûte est considérée comme une couche flottante, avec une viscosité variable décrite par la relation eq. (6.1). Nous adoptons l'approximation d'un nombre de Prandtl infini, ainsi que le cadre de l'approximation de Boussinesq. Pour l'adimensionnement, nous utilisons les grandeurs suivantes : l'épaisseur maximale de la croûte $D = R_{\text{L}} - R_{\text{cr,max}}$, le temps diffusif $\tau = D^2/\kappa$ avec κ la diffusivité thermique, la température adimensionnée $\Theta = \dfrac{T - T_\infty}{\Delta T}$ avec $\Delta T = T_{\text{ref}} - T_\infty$; et η, la viscosité sans dimension. La profondeur adimensionnée z est définie dans l'intervalle $z \in \left[-\frac{1}{2}, \frac{1}{2}\right]$. Les équations de conservation de la masse, de la quantité de mouvement et de l'énergie, sous forme adimensionnée, s'écrivent alors :

$$\boldsymbol{\nabla} \cdot \boldsymbol{u} = 0 \tag{6.2}$$

$$0 = -\boldsymbol{\nabla} p + \boldsymbol{\nabla} \cdot \left(\eta\left(\nabla \boldsymbol{u} + \nabla^T \boldsymbol{u}\right)\right) + \mathcal{R}a\Theta\mathbf{e_z} \tag{6.3}$$

$$\frac{\partial \Theta}{\partial t} = \boldsymbol{\nabla}^2\Theta - \boldsymbol{u} \cdot \nabla\Theta \tag{6.4}$$

Le nombre de Rayleigh $\mathcal{R}a$ est calculé à partir de la viscosité de référence η_{ref} :

$$\mathcal{R}a = \frac{\alpha\rho g_0 \Delta T D^3}{\kappa\eta_{\text{ref}}}, \tag{6.5}$$

avec α le coefficient d'expansion thermique, et ρ la densité.

Conditions aux limites et conditions initiales

Pour les conditions aux limites thermiques, nous imposons des températures fixées à la base et à la surface de la croûte : la base est maintenue à la température eutectique, tandis que la surface est à la température d'équilibre. Cela conduit aux conditions aux limites thermiques adimensionnées suivantes :

$$T\left(z_o = \frac{1}{2}\right) = 0, \tag{6.6}$$

$$T\left(z_i = -\frac{1}{2}\right) = 1. \tag{6.7}$$

Comme dans les chapitres précédents, nous imposons une condition de changement de phase à l'interface LMO/croûte, qui correspond ici à la base du domaine. Pour la suite, nous détaillerons principalement les deux cas extrêmes : la condition perméable, correspondant à $\Phi = 10^{-2}$ et la condition imperméable correspondant à $\Phi \to \infty$. Nous considérons également des conditions de glissement sans frottement aux deux frontières (bas et haut du domaine), et une condition non pénétrative en haut de la croûte.

Pour l'étude de la convection dans la croûte, nous utilisons un profil initial de température qui satisfait l'équation de diffusion en régime stationnaire :

$$\nabla^2 T = 0. \tag{6.8}$$

En appliquant les conditions aux limites définies par eq. (6.6) et eq. (6.7), le profil initial de température adimensionné s'écrit (fig. 6.1) :

$$T(z) = -z + \frac{1}{2}. \tag{6.9}$$

Ce choix est motivé par le fait qu'il est proche du profil thermique résultant de la solidification du LMO (Colin et al., 2024, fig. 4) et assure une bonne cohérence avec l'adimensionnement utilisé.

Dans le cas de la croûte, nous nous limitons à une étude de stabilité linéaire. L'objectif est de déterminer si la croûte peut entrer en convection avant la fin de la solidification complète du LMO, en tenant compte d'une viscosité variable. Nous cherchons également à identifier le mode de convection le plus instable. Pour cette analyse de stabilité linéaire, nous utilisons l'outil numérique `StablinRB`, dont la méthode et les détails sont présentés au Chapitre 4. La principale différence ici avec les études décrites précédemment est que nous travaillons en géométrie cartésienne et que la viscosité varie avec la température.

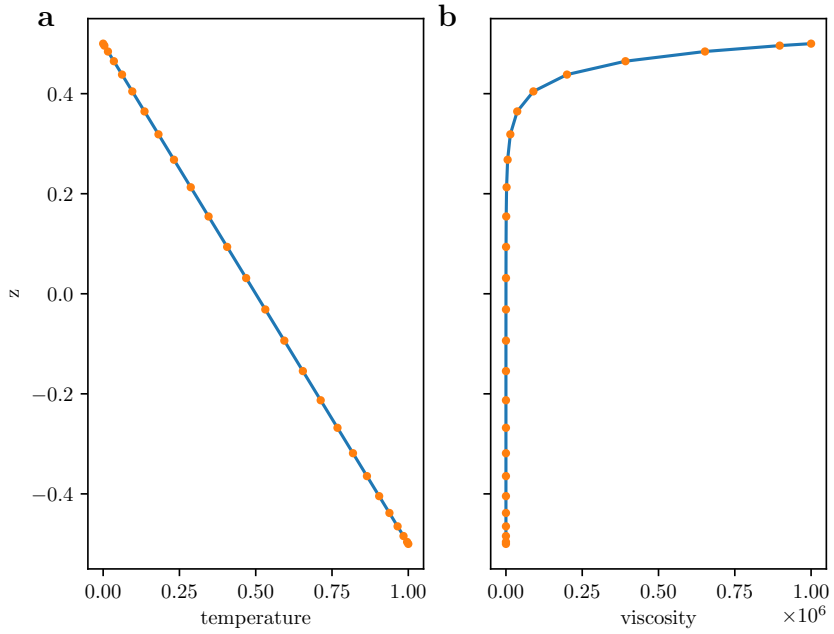

Figure 6.1: **a**- Profil initial de température et **b**- Profil de viscosité pour $R_\eta = 10^6$, les points oranges correspondent aux noeuds de Chebychev.

Conditions pour le démarrage de la convection

Dans cette section, nous présentons les résultats de l'analyse de stabilité linéaire en géométrie cartésienne, en tenant compte d'une viscosité variable dépendant de la température et d'une condition de changement de phase à l'interface LMO / croûte. Nous nous intéressons en particulier à la valeur du nombre de Rayleigh critique, $\mathcal{R}a_c$ (table 6.1), correspondant à la valeur minimale du nombre de Rayleigh nécessaire pour que la croûte puisse entrer en convection.

Table 6.1: Valeurs du nombre de Rayleigh critique pour différentes valeurs du nombre de changement de phase Φ.

Φ	$\mathcal{R}a_c$
∞	$1,5 \times 10^5$
10^3	$1,4 \times 10^5$
10^2	$1,1 \times 10^5$
10	$8,1 \times 10^4$
1	$7,7 \times 10^4$
10^{-2}	$7,6 \times 10^4$

Dans un premier temps, nous calculons le nombre de Rayleigh dans la croûte en fonction de son épaisseur pour plusieurs valeurs de viscosité de référence (fig. 6.2). En considérant une viscosité de référence à la base de la croûte η_{cr} comprise entre 10^{16} et 10^{21} Pa s, le nombre de Rayleigh associé varie entre 10^{-2} et 10^6 (fig. 6.2) pour une épaisseur de croûte comprise entre 5 et 45 km. Pour que la convection se mette en place, le nombre de Rayleigh de la croûte doit dépasser le nombre de Rayleigh critique, représenté en ligne pointillée grise

pour $\Phi = 10^{-2}$ et en ligne pointillée noire pour $\Phi \to \infty$ sur fig. 6.2. Les conditions permettant à la croûte de convecter sont donc relativement restreintes (fig. 6.2). Avec une conditions pénétrative ($\Phi = 10^{-2}$), la viscosité à la base de la croûte doit être inférieure à 4×10^{17} Pa s et l'épaisseur comprise entre 12 km (pour $\eta_{\mathrm{cr}} = 10^{16}$ Pa s) et 12 km (pour $\eta_{\mathrm{cr}} = 4 \times 10^{17}$ Pa s). Avec une condition non-pénétrative ($\Phi \to \infty$), ces conditions sont encore plus restreintes, η_{cr} doit être inférieure à 2×10^{17} Pa s et l'épaisseur de croûte nécessaire est de 15 km (pour $\eta_{\mathrm{cr}} = 10^{16}$ Pa s) à 34 km (pour $\eta_{\mathrm{cr}} = 2 \times 10^{17}$ Pa s). Dans le scénario de référence, cette épaisseur est atteinte entre quelques millions d'années et 50 Ma, soit bien avant la fin de la solidification de l'océan de magma, qui est de 172 Ma pour le cas de référence (*i.e.*, $C_0 = 0,075$, $C_E = 0,37$ et $k_{\mathrm{cr}} = 2\,\mathrm{W\,m^{-1}\,K^{-1}}$).

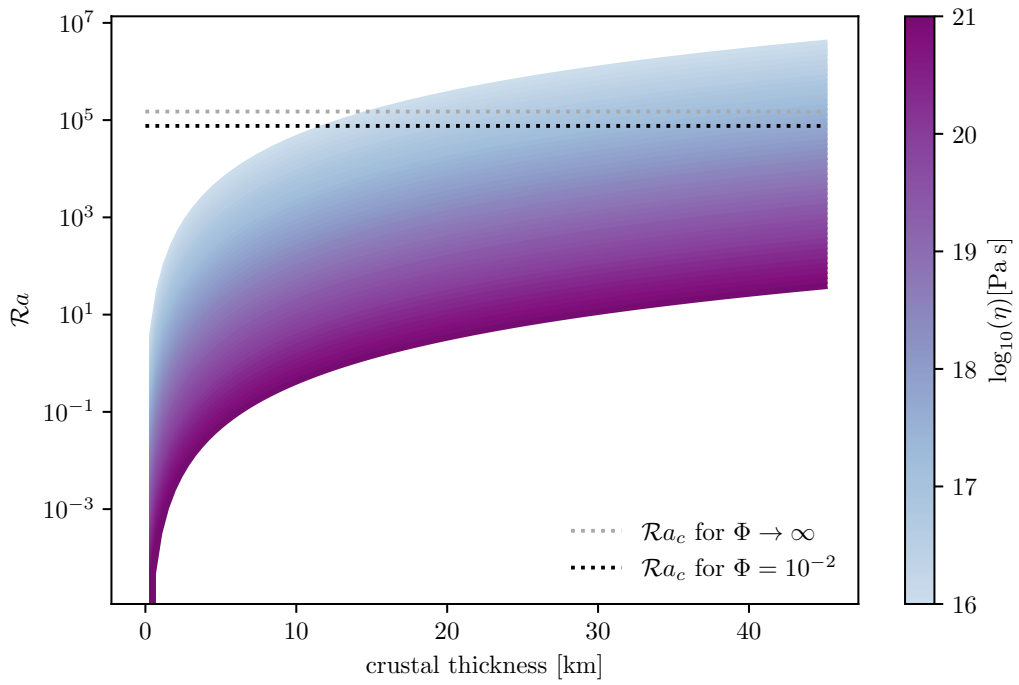

Figure 6.2: Evolution du nombre de Rayleigh dans la croûte en fonction de la viscosité de référence à la base de la croûte η_{cr} (colorbar). La ligne pointillée grise correspond à la valeur du nombre de Rayleigh critique pour $\Phi \to \infty$, et la ligne pointillée noire pour $\Phi = 10^{-2}$.

Le mode de convection dans la croûte présente une configuration typique de couvercle stagnant : les cellules de convection se développent uniquement à la base de la croûte, tandis que la partie supérieure reste quasi immobile, et les perturbations de température par rapport au profil de référence sont localisées sur la base de la croûte (fig. 6.1). Par ailleurs, une augmentation de la perméabilité de l'interface basal (c'est-à-dire une diminution de Φ) tend à favoriser légèrement des longueurs d'onde de convection plus grandes (fig. 6.3b), par rapport à des conditions imperméables (fig. 6.3a). De plus, dans le cas

d'une condition perméable, les lignes de courant sont ouvertes (fig. 6.3b).

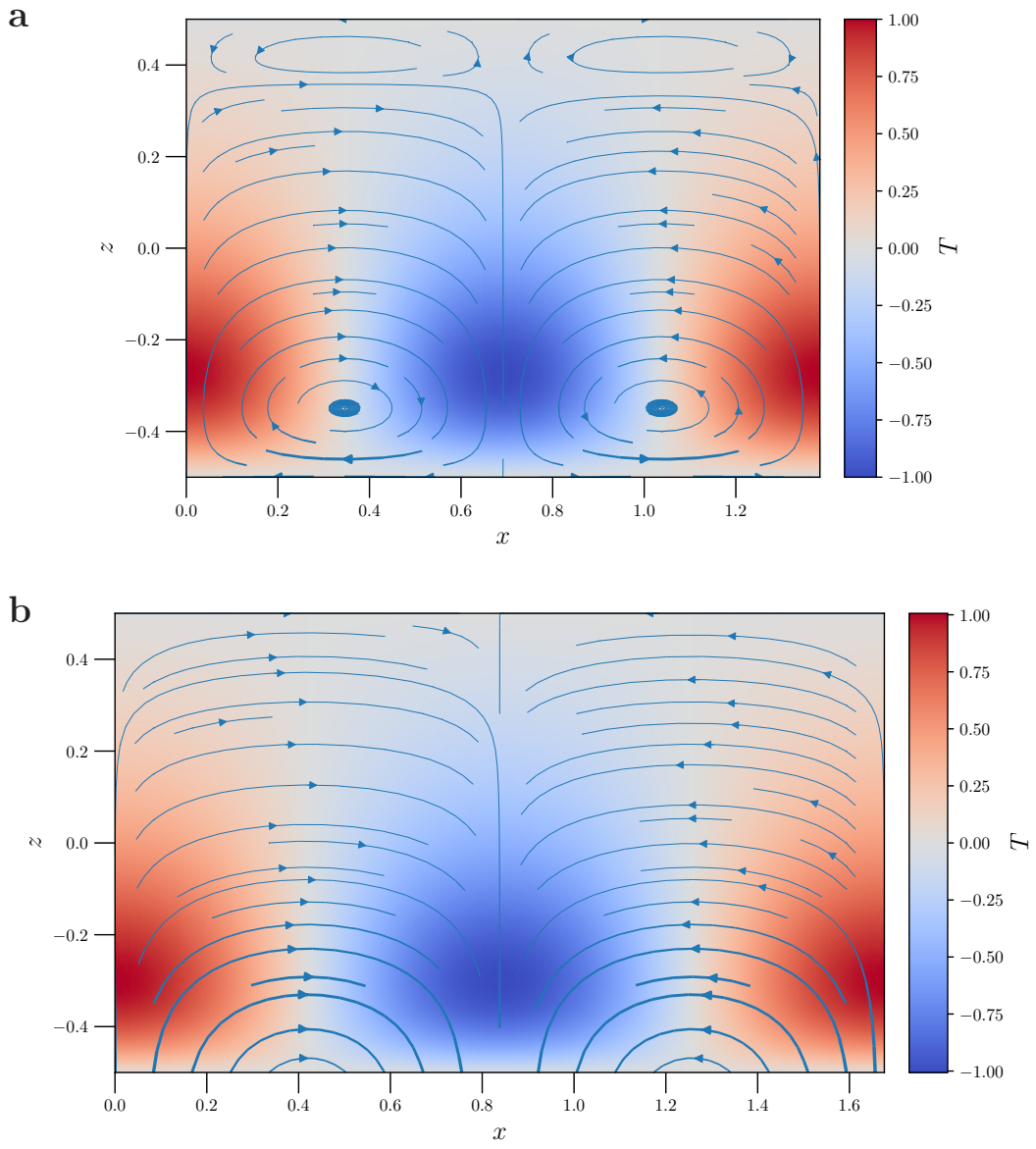

Figure 6.3: Perturbations de la température par rapport au profil de référence et lignes de courant pour $R_\eta = 10^6$, $\mathcal{R}a_c = 1,5 \times 10^5$. **a**- conditions aux limites imperméables, $\Phi \to \infty$ et **b**- conditions aux limites perméables $\Phi = 10^{-2}$.

Degré préférentiel de la convection

Nous avons montré que, pour des valeurs élevées du nombre de Rayleigh, la croûte peut entrer en convection. Étant donné qu'il s'agit d'une coquille sphérique très fine et que la convection se produit en régime stagnant, le mode préférentiel de la convection correspond à des longueurs d'onde courtes, c'est-à-dire à des modes de haut degré. Dans cette section, nous nous posons la question suivante : si le retournement du manteau lunaire

impose une perturbation de degré un à la base de la croûte, ce mode peut-il être favorisé en termes de taux de croissance par rapport au mode le plus instable identifié précédemment ? Pour y répondre, nous réalisons une analyse de stabilité linéaire similaire à celle présentée précédemment, mais cette fois en coordonnées sphériques, afin d'étudier le degré préférentiel de la convection dans une coquille très fine. L'objectif est de comparer le taux de croissance du mode de degré un à celui des autres modes.

Dans le cas d'une condition aux limites perméable le taux de croissance est négatif pour $l < 8$, et pour une condition imperméable le taux de croissance est négatif jusqu'à $l = 82$ (table 6.2). Dans les deux cas extrêmes de conditions aux limites (imperméable et perméable), les modes de faible degré ($l < 8$ pour $\Phi = 10^{-2}$ et $l = 82$ pour $\Phi \to \infty$) présentent un taux de croissance négatif (table 6.2). Il semble donc peu probable qu'un mode de convection de degré un puisse s'établir spontanément dans la croûte, même en présence d'un changement de phase à la base, en raison de la faible épaisseur de la coquille sphérique et de la variation importante de la viscosité entre le haut et le bas, et ce même si une perturbation de degré un est imposée. L'hypothèse d'une convection de degré un dans la croûte ne permet donc pas d'expliquer l'asymétrie observée dans la croûte lunaire. Il faut noter que ce résultat n'est valable que linéairement, si la pertubation venant des cumulats est importante, l'hypothèse linéaire n'est plus valide.

Table 6.2: Valeurs du taux de croissance en fonction de l et Φ. Le mode $l = 82$ correspond au plus petit mode où le taux de croissance est positif pour la condition imperméable ($\Phi \to \infty$).

Φ \ l	1	2	3	4	5	6	7	8	9	10	...	82
10^{-2}	σ=-8,8	σ=-8,3	σ=-7,5	σ=-6,4	σ=-4,9	σ=-3,2	σ=-1,2	σ=1,1	σ= 3,8	σ=6,7	...	σ=1054
∞	σ=-9,8	σ=-9,6	σ=-9,5	σ=-9,4	σ=-9,3	σ=-9,2	σ=-9,1	σ=-9,1	σ=-9,0	σ=-8,9	...	σ=0,1

6.2.2 Quels sont les effets d'un retournement du manteau lunaire sur la croûte ?

Nous avons montré qu'un retournement de degré un peut se produire dans les cumulats lunaires. Un tel comportement dynamique soulève naturellement la question de son impact sur la cristallisation de la croûte. En effet, si le flux thermique émis par les cumulats est intense, brutal, d'une durée inférieure à 5 Ma, et spatialement homogène, il peut entraîner la fusion complète de la croûte préexistante, comme nous l'avons montré dans le Chapitre 2. Dans ce cas, le système revient à une configuration classique de cristallisation,

dans laquelle aucun flux de chaleur additionnel ne provient des cumulats. Le temps de cristallisation du LMO est alors réduit à 160 Ma, contre 172 Ma pour le cas de référence (*i.e.*, $C_0 = 0,075$, $C_E = 0,37$ et $k = 2\,\mathrm{W\,m^{-1}\,K^{-1}}$). Au contraire, si ce retournement à une durée supérieure à 5 Ma, il peut augmenter le temps de solidification. Dans le Chapitre 5, nous montrons que le flux en haut des cumulats suite au retournement est spatialement variable. En particulier, dans le scénario d'un retournement de degré un, le flux thermique libéré par les cumulats est spatialement hétérogène : il atteint un maximum sur une portion restreinte de la surface et demeure nul ailleurs (fig. 6.4). De plus, nous montrons que le temps où survient le maximum de ce flux est supérieur à 5 Ma pour des valeurs de de $\mathcal{R}a < 10^6$ et des valeurs de Φ comprises entre 10^{-1} et 14. Nous pouvons supposer que le retournement peut affecter le temps de solidification, en particulier s'il dure longtemps. De plus, l'hétérogénéité de flux est susceptible d'affecter la dynamique de cristallisation de la croûte lunaire.

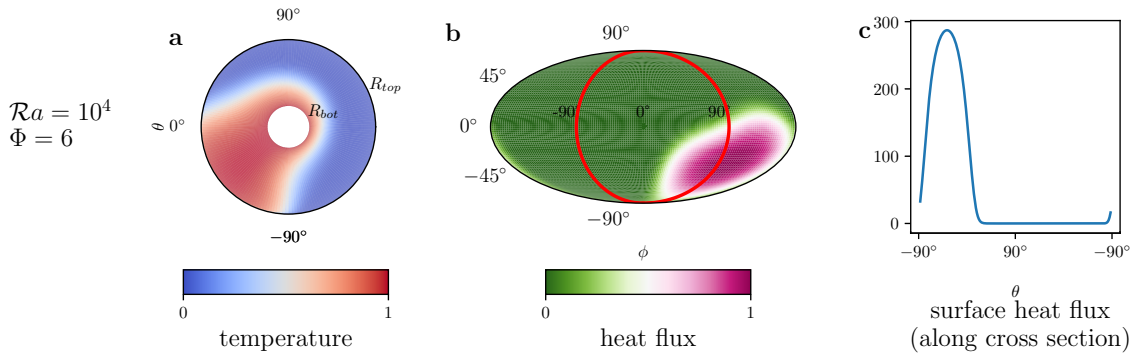

Figure 6.4: Extraits issus de simulations numériques pour le cas de référence ($\mathcal{R}a = 10^4$, $\Phi = 6$), à $t_{\max}$. **a**- champ de température dans une section transversale. **b**- flux de surface en haut des cumulats normalisé par le maximum du flux (projection de Mollweide). **c**- flux de surface le long du cercle correspondant à la section transversale normalisé par sa valeur extreme. La section transversale du champ de température est représentée par la ligne rouge sur le flux de surface (**b**).

Possibles conséquences d'un flux non homogène à la surface des cumulats

Pour étudier l'influence de la libération d'un flux non homogène à la surface des cumulats, nous nous appuyons sur l'étude de Bouffard et al. (2025). En effet, Encelade est une lune de Saturne qui présente une forte asymétrie dans l'épaisseur de sa couche de glace superficielle. Son épaisseur moyenne est de 20–30 km, avec des valeurs dépassant 30 km dans certaines régions équatoriales et inférieures à 5 km sous le pôle Sud. Dans leur travail, les auteurs explorent comment un flux hétérogène à la base de l'océan d'eau d'Encelade

peut influencer l'épaisseur et la structure de la couche de glace située au-dessus.

Dans un premier temps, nous voulons déterminer si leur approche peut être appliquée à la Lune. Pour cela, nous comparons plusieurs nombres sans dimension (table 6.3) afin de vérifier que la Lune se situe dans un régime dynamique similaire à celui d'Encelade. Comme la variation de température dans l'océan de magma est négligeable (l'ensemble de l'océan est à la température eutectique), nous définissons un nombre de Rayleigh basé sur le flux (Bouffard et al., 2025, eq. (1) Supplementary Materials). En particulier, nous utilisons la valeur du flux en haut de la croûte au début du second stade de cristallisation :

$$q_{\mathrm{cr}} = -k \left. \frac{\partial T}{\partial r} \right|_{r=R_L}, \tag{6.10}$$

avec k la conductivité thermique de la croûte. Le nombre de Rayleigh basé sur le flux pour le LMO est alors défini par :

$$\mathcal{R}a_o = \frac{\alpha g_0 q_{\mathrm{rad}} H^4}{\nu \kappa k}, \tag{6.11}$$

avec α le coefficient d'expansion thermique, g_0 l'accélération de gravité en surface, ν la viscosité cinématique, κ la diffusivité thermique et k la conductivité thermique dans le LMO. Nous utilisons aussi le nombre d'Ekman (Bouffard et al., 2025, eq. (4) Supplementary Materials):

$$Ek = \frac{\nu}{\Omega H^2}, \tag{6.12}$$

avec Ω, la vitesse de rotation. Dans le cas de la Lune, nous prenons la vitesse de rotation actuelle et celle pour une distance Terre-Lune de trois rayons terrestres (limite de Roche). Nous considérons ces deux valeurs extrêmes de vitesse de rotation en supposant qu'au début de la solidification de l'océan de magma, la Lune orbitait beaucoup plus proche de la Terre, et que sa vitesse de rotation était donc plus élevée qu'aujourd'hui.

Table 6.3: Nombres sans dimension et estimation de leur valeur pour Encelade d'après (Bouffard et al., 2025, tab. 1 Supplementary Materials) et la Lune.

Nombre sans dimension	Symbole	Encelade	Lune
Rapport d'aspect de l'océan	γ	0,8	0,9
Rayleigh (outer)	$\mathcal{R}a_o$	$9,2 \times 10^{24} - 2,8 \times 10^{25}$	$3,5 \times 10^{25}$
Ekmann	Ek	$2,2 \times 10^{-11}$	$8,3 \times 10^{-11} - 7,3 \times 10^{-9}$

Les valeurs de $\mathcal{R}a_o$ et Ek pour la Lune et Encelade sont du même ordre de grandeur. De plus, nous pouvons comparer le régime dans lequel se trouve ces deux satellites fig. 6.5. Dans le cas où la vitesse de rotation de la Lune est identique à l'actuelle, la Lune se trouve dans un régime non rotatif, ce qui indique que nous ne pouvons pas comparer Encelade et la Lune (étoiles violette et violette foncée sur fig. 6.5). Dans le cas où la vitesse de rotation

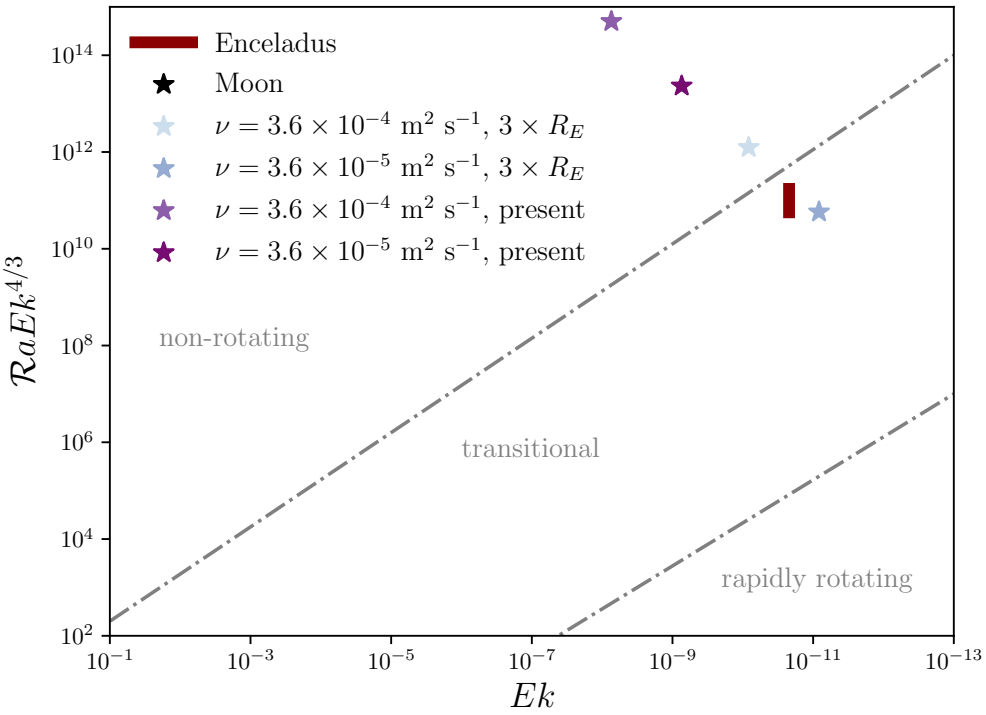

Figure 6.5: Diagramme de régime pour la convection océanique chauffée de manière hétérogène d'après (Bouffard et al., 2025, fig. 8 Supplementary Materials). Les valeurs pour Encelade sont représentées par la barre verticale rouge. Les valeurs pour la Lune sont représentées par les étoiles pour différentes valeurs de ν et de distance Terre-Lune. Les lignes grises en tirets-pointillés délimitent les différents régimes pour la convection dans l'océan.

correspond à la vitesse pour une distance Terre-Lune de trois fois le rayon terrestre, la Lune est dans un régime non rotatif si la viscosité cinématique dans l'océan de magma est $\nu = 3.6 \times 10^{-4}\,\mathrm{m^2\,s^{-1}}$ (ou $\eta = 1\,\mathrm{Pa\,s}$, étoile bleue claire sur fig. 6.5), et dans un régime transitionnel si la viscosité cinématique est $\nu = 3.6 \times 10^{-5}\,\mathrm{m^2\,s^{-1}}$ (ou $\eta = 1 \times 10^{-1}\,\mathrm{Pa\,s}$, étoile bleue foncée sur fig. 6.5). Dans ce dernier cas, la Lune se trouve dans le même régime qu'Encelade, ce qui nous permet d'appliquer les résultats de Bouffard et al. (2025) à la Lune.

À partir des simulations numériques directes, nous avons accès à la variation spatiale du flux à la base de l'océan de magma. Nous pouvons ainsi utiliser le critère d'hétérogénéité du flux à la base de l'océan q_i^* défini par Bouffard et al. (2025) :

$$q_i^* = \frac{q_{i,\max} - q_{i,\min}}{2\bar{q}_i}, \tag{6.13}$$

avec $q_{i,\max}$ le flux maximum, $q_{i,\min}$ le flux minimum, et $\bar{q}_i$ le flux moyen à la base du LMO.

Nous calculons ce critère pour l'ensemble des cas de nos simulations numériques directes dans lesquels nous sommes dans un scénario de retournement de degré un (table 6.4).

Table 6.4: Valeurs du facteur q_i^* en fonction de $\mathcal{R}a$ et Φ. Le symbole x signifie qu'il n'y a pas de valeur pour cette combinaison de paramètres.

$\mathcal{R}a$ \ Φ	**1**	**6**	**7**	**8**	**9**	**10**
$\mathbf{10^4}$	x	$q_i^* = 3,1$	$q_i^* = 3$	$q_i^* = 3$	$q_i^* = 3$	$q_i^* = 2,8$
$\mathbf{3 \times 10^3}$	x	$q_i^* = 4,9$	$q_i^* = 5,3$	$q_i^* = 5,5$	$q_i^* = 4,3$	x
$\mathbf{1,5 \times 10^3}$	x	$q_i^* = 4,3$	x	x	x	x
$\mathbf{5 \times 10^2}$	$q_i^* = 2,8$	x	x	x	x	x

Les résultats de nos simulations numériques montrent des valeurs de q_i^* comprises entre 2,8 et 5,5 au maximum (table 6.4). Bien que le flux maximum soit élevé, il est localisé sur une faible portion des cumulats, ce qui implique que le critère d'hétérogénéité q_i^* reste relativement faible. Dans Bouffard et al. (2025), les auteurs expliquent que pour des valeurs de $0 < q_i^* < 10$, le système se situe dans un régime transitoire où coexistent la convection en colonnes dans le LMO, dite « convection colonnaire » liée à la rotation, et le transport vertical lié aux flux provenant des cumulats. Dans ce régime, les effets d'un flux hétérogène à la base du LMO commencent déjà à se manifester sur la croûte. Pour les résultats des simulations numériques directes que nous avons réalisées, la valeur de q_i^* peut déjà être suffisante pour que le flux en surface des cumulats ait un impact sur la croûte (table 6.4) dans le cas où la Lune se trouve dans un régime transitionnel. La transmission du flux de la base vers la surface résulte d'une compétition entre la rotation et le transport vertical du flux. Dans le cas où la Lune se trouve dans un régime non rotatif, l'océan de magma est bien mélangé, et ce dans toutes les directions, nous pouvons supposer que le transport vertical peut être plus efficace. Il pourrait être intéressant d'explorer plus en profondeur cette question afin de déterminer, dans le cas de la Lune, comment est transmis verticalement le flux hétérogène à la base des cumulats.

Table 6.5: Liste des variables utilisées.

Symbole	Description	Valeur
R_{M}	rayon de la Lune	1737 km
R_{C}	rayon du noyau	390 km
R_{cr}	rayon de la croûte	0 - 45 km
R_{cr}	rayon des cumulats (durant la deuxième étape)	1612 - 1692km
H	épaisseur du LMO	125 - 0km
T_s	temperature de surface	1100 - 270K
ϵ	emissivité	1
σ	constante de Stafan-Boltzman	$5.67 \times 10^{-8}\,\mathrm{W\,m^{-2}\,K^{-4}}$
g_0	accélération de gravité en surface	$1.62\,\mathrm{m\,s^{-2}}$
c_p	capacité calorifique	$1 \times 10^{3}\,\mathrm{J\,kg^{-1}\,K^{-1}}$
ρ	densité du LMO	$3.3 \times 10^{3}\,\mathrm{kg\,m^{-3}}$
α	coefficient de dilatation thermique	$5 \times 10^{-5}\,\mathrm{K^{-1}}$
k	conductivité thermique du LMO	$4\,\mathrm{W\,m^{-1}\,K^{-1}}$
κ	diffusivité thermique du LMO	$1.4 \times 10^{-6}\,\mathrm{m\,s^{-1}}$
u_{LMO}	vitesse du LMO	$1\,\mathrm{m\,s^{-1}}$
η	viscosité dynamique du LMO	$1 \times 10^{-1}\,\mathrm{Pa\,s}$ to $1\,\mathrm{Pa\,s}$
ν	viscosité cinématique du LMO	$3.6 \times 10^{-5}\,\mathrm{m\,s^{-1}}$ to $3.6 \times 10^{-4}\,\mathrm{m\,s^{-1}}$
R_{Roche}	limite de Roche	$1.9 \times 10^{4}\,\mathrm{km}$
G	constante universelle de gravitation	$6.674 \times 10^{-11}\,\mathrm{m^3\,kg^{-1}\,s^{-2}}$
Ω	vitesse angulaire de rotation	$2,66 \times 10^{-6}$ - $2.4 \times 10^{-4}\,\mathrm{s^{-1}}$
q_{cr}	flux en surface de la croûte	$2.6\,\mathrm{W\,m^{-2}}$

Effets compositionnels

La prise en compte d'un changement de phase à l'interface entre les cumulats et l'océan de magma entraîne un échange de matière entre le LMO et les cumulats. Du côté du panache descendant, la température plus froide favorise la cristallisation des cumulats. La chaleur latente libérée est alors transportée dans l'océan de magma et permet la fusion des cumulats du côté du panache ascendant. Cette fusion peut avoir un effet compositionnel susceptible d'influencer directement la croûte. En fondant, les cumulats « relâchent » de l'olivine dans l'océan de magma, ce qui décale l'équilibre : l'océan de magma ne se trouve alors plus à l'eutectique. Dans ce cas, la cristallisation de la croûte ne peut pas être maintenue car les conditions d'équilibre ne sont plus réunies (fig. 6.6). Dans l'autre hémisphère, l'océan de magma reste à la composition eutectique, de sorte que les cumulats et la croûte continuent à cristalliser normalement. Il pourrait en résulter une configuration dans laquelle la croûte s'épaissit plus rapidement d'un côté que de l'autre, ce qui pourrait contribuer à expliquer l'asymétrie d'épaisseur crustale. Pour tester cette hypothèse, il serait nécessaire de modifier notre modèle d'évolution thermique et d'en faire un modèle

1,5D, dans lequel un hémisphère cristallise « normalement », tandis que l'autre autorise la fusion des cumulats en raison du retournement du manteau. Cela impliquerait que l'océan de magma atteigne l'eutectique, s'en écarte pendant la durée du retournement, puis retrouve l'eutectique une fois le retournement terminé.

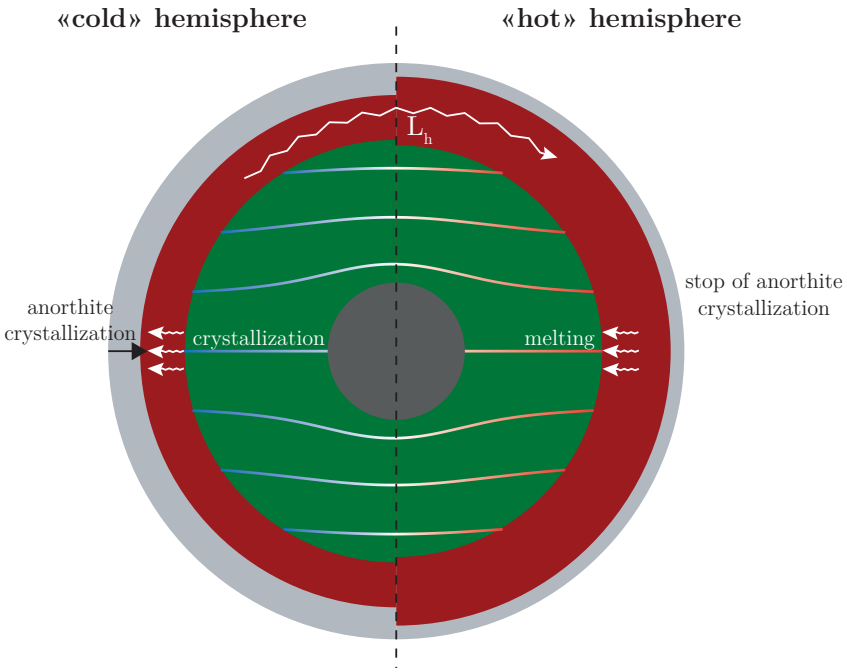

Figure 6.6: Schéma représentant un cristallisation différentielle entre l'hémisphère « froid » où les cumulats cristallisent du fait de la condition de changement de phase et l'hémisphère « chaud » où les cumulats fondent.

6.2.3 Améliorations possibles

Chauffage interne

Dans l'étude du retournement des cumulats lunaires, nous ne prenons pas en compte de chauffage interne dans les cumulats. En effet, en partant de l'hypothèse que ces éléments sont incompatibles, ils tendent à rester majoritairement dans le LMO. Cependant, dans le modèle d'évolution thermique de la solidification de l'océan de magma lunaire, nous avons montré qu'une partie des éléments producteurs de chaleur se trouvent dans les cumulats. Une amélioration possible serait la prise en compte d'un chauffage interne dans les cumulats. Cela tendrait à allonger la durée du retournement.

Dépendance temporelle de Φ

Dans notre modèle, nous considérons que l'efficacité du changement de phase ne varie pas au cours du temps. Cependant, à mesure que l'océan de magma se solidifie, son épaisseur diminue, ce qui peut affecter sa dynamique. La convection dans le LMO peut être moins vigoureuse donc le transport de chaleur latente dans le liquide devient moins efficace, ce qui affecte le temps nécessaire pour effacer la topographie. De plus, le profil de température évolue au cours du temps ce qui peut aussi avoir une influence sur le changement de phase. Pour prendre en compte ceci, il peut être envisagé de paramétriser le nombre de changement de phase pour prendre en compte sa dépendance temporelle au cours du temps.

Amélioration du modèle d'évolution thermique

Dans notre modèle d'évolution thermique (Chapitre 2), nous avons représenté le retournement par une décroissance exponentielle, où l'énergie stockée dans les cumulats est relâchée sur une période τ_{ov}. Une amélioration de ce modèle consisterait à utiliser directement les données des simulations numériques, dans le modèle d'évolution thermique en particulier utiliser le flux moyen pour simuler le retournement. La difficulté présente pour procéder est que nous n'avons pas identifié de lois d'échelle pour l'intensité maximale du retournement en fonction des nombres de Rayleigh et de changement de phase, ce qui nous obligerait à effectuer des estimations. En revanche, la forme de la courbe, ainsi que le temps de démarrage et la durée du phénomène, seraient alors mieux contraints. Il serait également intéressant de modifier le modèle pour permettre la fusion de la croûte, en particulier comment prendre en compte la composition en anorthite. Cela permettrait d'examiner son comportement dans le cas où le flux relâché est très intense et concentré sur une courte période.

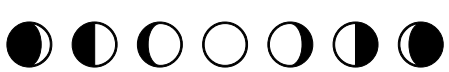

Bibliography

Aaboe, A., J. P. Britton, J. A. Henderson, O. Neugebauer, and A. J. Sachs (1991). *Saros Cycle Dates and Related Babylonian Astronomical Texts*. Vol. 81. 6. American Philosophical Society, 1–75. DOI: doi.org/10.2307/1006543.

Agee, C. B. and D. Walker (1988). Static compression and olivine flotation in ultrabasic silicate liquid. *J. Geophys. Res.* **93**:B4, 3437–3449. DOI: 10.1029/JB093iB04p03437.

Agrusta, R., A. Morison, S. Labrosse, R. Deguen, T. Alboussière, P. J. Tackley, and F. Dubuffet (2019). Mantle convection interacting with magma oceans. *Geophys. J. Int.* **220**: 1878–1892. DOI: 10.1093/gji/ggz549.

Alboussière, T., R. Deguen, and M. Melzani (2010). Melting-induced stratification above the Earth's inner core due to convective translation. *Nature* **466**:7307, 744–747. DOI: 10.1038/nature09257.

Alibert, C., M. D. Norman, and M. T. McCulloch (1994). An ancient Sm-Nd age for a ferroan noritic anorthosite clast from lunar breccia 67016. *Geochim. Cosmochim. Acta* **58**:13, 2921–2926. DOI: 10.1016/0016-7037(94)90125-2.

Banerdt, W. B., V. Dehant, R. Grimm, M. Grott, P. Lognonné, and S. E. Smrekar (2014). "Probing the interiors of planets with geophysical tools". *Encyclopedia of the Solar System*. Elsevier, 1185–1204.

Baratoux, D., H. Samuel, C. Michaut, M. J. Toplis, M. Monnereau, M. Wieczorek, R. Garcia, and K. Kurita (2014). Petrological constraints on the density of the Martian crust. *J. Geophys. Res. Planet* **119**:7, 1707–1727.

Binder, A. B. (1998). Lunar prospector: overview. *Science* **281**:5382, 1475–1476. DOI: 10.1126/science.281.5382.1475.

Borg, L. E. and R. W. Carlson (2023). The evolving chronology of moon formation. *Ann. Rev. Earth Planet. Sci.* **51**: 25–52. DOI: 10.1146/annurev-earth-031621-060538.

Borg, L. E., W. S. Cassata, J. Wimpenny, A. M. Gaffney, and C. K. Shearer (2020). The formation and evolution of the Moon's crust inferred from the Sm-Nd isotopic

systematics of highlands rocks. *Geochim. Cosmochim. Acta* **290**: 312–332. DOI: 10.1016/j.gca.2020.09.013.

Borg, L. E., A. M. Gaffney, T. S. Kruijer, N. A. Marks, C. K. Sio, and J. Wimpenny (2019). Isotopic evidence for a young lunar magma ocean. *Earth Planet. Sci. Lett.* **523**: 115706. DOI: 10.1016/j.epsl.2019.07.008.

Borg, L. E., G. A. Brennecka, and S. J. Symes (2016). Accretion timescale and impact history of Mars deduced from the isotopic systematics of martian meteorites. en. *Geochim. Cosmochim. Acta* **175**: 150–167. DOI: 10.1016/j.gca.2015.12.002.

Borg, L. E. and D. S. Draper (2003). A petrogenetic model for the origin and compositional variation of the martian basaltic meteorites. *Meteoritics & Planetary Science* **38**:12, 1713–1731. DOI: 10.1111/j.1945-5100.2003.tb00011.x.

Borg, L. E., A. M. Gaffney, and C. K. Shearer (2015). A review of lunar chronology revealing a preponderance of 4.34–4.37 Ga ages. en. *Meteoritics & Planetary Science* **50**:4, 715–732. DOI: 10.1111/maps.12373.

Borg, L., J. Connelly, M. Boyet, and R. Carlson (2011). "The age of lunar ferroan anorthosite 60025 with implications for the interpretation of lunar chronology and the magma ocean model". *42nd Annual Lunar and Planetary Science Conference*. Issue: 1608, 1171.

Bouffard, M., G. Choblet, H. Amit, G. Tobie, O. Čadek, and F. Terra-Nova (2025). Seafloor hydrothermal control over ocean dynamics in Enceladus. *Nat Astron*, 1–8. DOI: 10.1038/s41550-025-02490-1.

Boukaré, C.-E., E. Parmentier, and S. Parman (2018). Timing of mantle overturn during magma ocean solidification. *Earth Planet. Sci. Lett.* **491**: 216–225. DOI: 10.1016/j.epsl.2018.03.037.

Bouvier, L. C., M. M. Costa, J. N. Connelly, N. K. Jensen, D. Wielandt, M. Storey, A. A. Nemchin, M. J. Whitehouse, J. F. Snape, J. J. Bellucci, F. Moynier, A. Agranier, B. Gueguen, M. Schönbächler, and M. Bizzarro (2018). Evidence for extremely rapid magma ocean crystallization and crust formation on Mars. en. *Nature* **558**:7711, 586–589. DOI: 10.1038/s41586-018-0222-z.

Branlund, J. M. and A. M. Hofmeister (2012). Heat transfer in plagioclase feldspars. *American Mineralogist* **97**:7, 1145–1154. DOI: 10.2138/am.2012.3986.

Burns, K. J., G. M. Vasil, J. S. Oishi, D. Lecoanet, and B. P. Brown (2020). Dedalus: A flexible framework for numerical simulations with spectral methods. *Physical Review Research* **2**:2, 023068. DOI: 10.1103/PhysRevResearch.2.023068.

Cai, S. et al. (2025). Persistent but weak magnetic field at the Moon's midstage revealed by Chang'e-5 basalt. *Science Advances* **11**:1, eadp3333. DOI: 10.1126/sciadv.adp3333.

Canup, R. M. (2012). Forming a Moon with an Earth-like composition via a giant impact. *Science* **338**:6110, 1052–1055. DOI: 10.1126/science.1226073.

Carlson, R. W. (2019). Analysis of lunar samples: Implications for planet formation and evolution. *Science* **365**:6450, 240–243. DOI: 10.1126/science.aaw758.

Carter, J. and F. Poulet (2013). Ancient plutonic processes on Mars inferred from the detection of possible anorthositic terrains. *Nature Geosci.* **6**:12, 1008–1012. DOI: 10.1038/ngeo1995.

Charlier, B., T. L. Grove, O. Namur, and F. Holtz (2018). Crystallization of the lunar magma ocean and the primordial mantle-crust differentiation of the Moon. *Geochim. Cosmochim. Acta* **234**: 50–69. DOI: 10.1016/j.gca.2018.05.006.

Clauser, C. and E. Huenges (1995). Rock Physics and Phase Relations. A Handbook of Physical Constants. **3**: 105–126.

Colin, L., C. Michaut, S. Labrosse, and B. Bourdon (2024). Thermal evolution of the lunar magma ocean. *Earth Planet. Sci. Lett.* **648**: 119109. DOI: 10.1016/j.epsl.2024.119109.

Cournède, C., J. Gattacceca, and P. Rochette (2012). Magnetic study of large Apollo samples: Possible evidence for an ancient centered dipolar field on the Moon. *Earth Planet. Sci. Lett.* **331**: 31–42. DOI: 10.1016/j.epsl.2012.03.004.

Crawford, I. (2012). The scientific legacy of Apollo. *Astronomy & Geophysics* **53**:6, 6–24. DOI: 10.1111/j.1468-4004.2012.53624.x.

Ćuk, M. and S. T. Stewart (2012). Making the Moon from a fast-spinning Earth: a giant impact followed by resonant despinning. *Science* **338**:6110, 1047–1052. DOI: 10.1126/science.1225542.

Darwin, G. H. (1879). I. On the bodily tides of viscous and semi-elastic spheroids, and on the ocean tides upon a yielding nucleus. *Philosophical Transactions of the Royal Society of London* 170, 1–35.

Debaille, V., A. D. Brandon, Q. Z. Yin, and B. Jacobsen (2007). Coupled 142Nd–143Nd evidence for a protracted magma ocean in Mars. en. *Nature* **450**:7169, 525–528. DOI: 10.1038/nature06317.

Deguen, R. (2013). Thermal convection in a spherical shell with melting/freezing at either or both of its boundaries. *J. Earth Sci.* **24**:5, 669–682. DOI: 10.1007/s12583-013-0364-8.

Deguen, R., T. Alboussière, and P. Cardin (2013). Thermal convection in Earth's inner core with phase change at its boundary. *Geophysical Journal International* **194**:3, 1310–1334. DOI: 10.1093/gji/ggt202.

Drilleau, M., H. Samuel, R. F. Garcia, A. Rivoldini, C. Perrin, C. Michaut, M. Wieczorek, B. Tauzin, J. A. Connolly, P. Meyer, et al. (2022). Marsquake locations and 1-D seismic

models for Mars from InSight data. *J. Geophys. Res. Planet* **127**:9, e2021JE007067. DOI: 10.1029/2021JE007067.

Dwyer, C., D. Stevenson, and F. Nimmo (2011). A long-lived lunar dynamo driven by continuous mechanical stirring. *Nature* **479**:7372, 212–214. DOI: 10.1038/nature10564.

Elkins-Tanton, L. T., S. Burgess, and Q.-Z. Yin (2011). The lunar magma ocean: Reconciling the solidification process with lunar petrology and geochronology. *Earth Planet. Sci. Lett.* **304**:3-4, 326–336. DOI: 10.1016/j.epsl.2011.02.004.

Elkins-Tanton, L. T., P. C. Hess, and E. Parmentier (2005). Possible formation of ancient crust on Mars through magma ocean processes. *J. Geophys. Res. Planet* **110**:E12. DOI: 10.1029/2005JE002480.

Elkins-Tanton, L. T., J. A. Van Orman, B. H. Hager, and T. L. Grove (2002). Re-examination of the lunar magma ocean cumulate overturn hypothesis: melting or mixing is required. *Earth Planet. Sci. Lett.* **196**:3-4, 239–249. DOI: 10.1016/S0012-821X(01)00613-6.

Elkins-Tanton, L. T., E. M. Parmentier, and P. C. Hess (2010). Magma ocean fractional crystallization and cumulate overturn in terrestrial planets: Implications for Mars. *Meteoritics & Planetary Science* **38**:12, 1753–1771. DOI: 10.1111/j.1945-5100.2003.tb00013.x.

Evans, A. J. and S. M. Tikoo (2022). An episodic high-intensity lunar core dynamo. *Nat Astron* **6**:3, 325–330. DOI: 10.1038/s41550-021-01574-y.

Flahaut, J., V. Payet, F. Fueten, M. Guitreau, M. Barthez, G. Ito, and P. Allemand (2023). New Detections of Feldspar-Bearing Volcanic Rocks in the Walls of Valles Marineris, Mars. *Geophys. Res. Lett.* **50**:2, e2022GL100772. DOI: 10.1029/2022GL100772.

Fu, H., S. B. Jacobsen, and F. Sedaghatpour (2023). Moon's high-energy giant-impact origin and differentiation timeline inferred from Ca and Mg stable isotopes. *Commu Earth Environ* **4**:1, 307. DOI: 10.1038/s43247-023-00974-4.

Galilei, G. (1610). *Sidereus Nuncius, or the sidereal messenger.*

Garcia, R. F., J. Gagnepain-Beyneix, S. Chevrot, and P. Lognonné (2011). Very preliminary reference Moon model. *Phys. Earth Planet. Inter.* **188**:1-2, 96–113. DOI: 10.1016/j.pepi.2011.06.015.

Gastine, T., J. Wicht, and J. Aubert (2016). Scaling regimes in spherical shell rotating convection. *J. Fluid Mech.* **808**: 690–732. DOI: 10.1017/jfm.2016.659.

Glavin, D., J. Dworkin, M. Lupisella, G. Kminek, and J. Rummel (2004). Biological contamination studies of lunar landing sites: implications for future planetary protection and life detection on the Moon and Mars. *International Journal of Astrobiology* **3**:3, 265–271. DOI: 10.1017/S1473550404001958.

Goins, N. R., A. M. Dainty, and M. N. Toksöz (1981). Lunar seismology: The internal structure of the Moon. *J. Geophys. Res.* **86**:B6, 5061–5074. DOI: 10.1029/JB086iB06p05061.

Goossens, S., T. J. Sabaka, A. Genova, E. Mazarico, J. B. Nicholas, and G. A. Neumann (2017). Evidence for a low bulk crustal density for Mars from gravity and topography. *Geophysical research letters* **44**:15, 7686–7694. DOI: 10.1002/2017GL074172.

Greer, J., B. Zhang, D. Isheim, D. Seidman, A. Bouvier, and P. Heck (2023). 4.46 Ga zircons anchor chronology of lunar magma ocean. en. *Geochemical Perspectives Letters* **27**: 49–53. DOI: 10.7185/geochemlet.2334.

Gross, J., A. H. Treiman, and C. N. Mercer (2014). Lunar feldspathic meteorites: Constraints on the geology of the lunar highlands, and the origin of the lunar crust. *Earth Planet. Sci. Lett.* **388**: 318–328.

Hanan, B. and G. Tilton (1987). 60025: relict of primitive lunar crust? en. *Earth Planet. Sci. Lett.* **84**:1, 15–21. DOI: 10.1016/0012-821X(87)90171-3.

Hartmann, W. K. and D. R. Davis (1975). Satellite-sized planetesimals and lunar origin. *Icarus* **24**:4, 504–515. DOI: 10.1016/0019-1035(75)90070-6.

Harvey, B. (2007). The first cosmonauts to the moon. in: Soviet and Russian Lunar Exploration, 111–182. DOI: 10.1007/978-0-387-73976-2_5.

Hauri, E. H., A. E. Saal, M. J. Rutherford, and J. A. Van Orman (2015). Water in the Moon's interior: Truth and consequences. *Earth Planet. Sci. Lett.* **409**: 252–264.

Hauri, E. H., T. Weinreich, A. E. Saal, M. C. Rutherford, and J. A. Van Orman (2011). High Pre-Eruptive Water Contents Preserved in Lunar Melt Inclusions. en. *Science* **333**:6039, 213–215. DOI: 10.1126/science.1204626.

He, S., Y. Li, X. Zhu, J. Chen, Z. Li, T. Li, J. Zhong, J. Tan, Q. He, Z. Fu, Y. Zheng, J. Xing, and Z. Shi (2025). A relatively cool lunar farside mantle inferred from Chang'e-6 basalts and remote sensing. *Nature Geoscience* **18**:11, 1103–1108. DOI: 10.1038/s41561-025-01815-z.

Hess, P. C. and E. Parmentier (1995). A model for the thermal and chemical evolution of the Moon's interior: Implications for the onset of mare volcanism. *Earth Planet. Sci. Lett.* **134**:3-4, 501–514. DOI: 10.1016/0012-821X(95)00138-3.

Hummel, A. W. (1960). *Science and Civilisation in China. Volume III, Mathematics and the Sciences of the Heavens and the Earth. By Joseph Needham, with the collaboration of Wang Ling. (New York: Cambridge University Press. 1959. Pp. xlvii, 877. $27.50.)* Vol. 65. 3. _eprint: https://academic.oup.com/ahr/article-pdf/65/3/614/150896/65-3-614.pdf, 614–616. DOI: 10.1086/ahr/65.3.614.

Ivanov, M., H. Hiesinger, C. Van Der Bogert, C. Orgel, J. Pasckert, and J. Head (2018). Geologic history of the northern portion of the South Pole-Aitken basin on the Moon. *J. Geophys. Res. Planet* **123**:10, 2585–2612. DOI: 10.1029/2018JE005590.

Jacobson, S. A., A. Morbidelli, S. N. Raymond, D. P. O'Brien, K. J. Walsh, and D. C. Rubie (2014). Highly siderophile elements in Earth's mantle as a clock for the Moon-forming impact. *Nature* **508**:7494, 84–87. DOI: 10.1098/rsta.2013.0174.

Johnson, T., L. Morrissey, A. Nemchin, N. Gardiner, and J. Snape (2021). The phases of the Moon: Modelling crystallisation of the lunar magma ocean through equilibrium thermodynamics. en. *Earth Planet. Sci. Lett.* **556**: 116721. DOI: 10.1016/j.epsl.2020.116721.

Jolliff, B. L., J. J. Gillis, L. A. Haskin, R. L. Korotev, and M. A. Wieczorek (2000). Major lunar crustal terranes: Surface expressions and crust-mantle origins. *J. Geophys. Res. Planet* **105**:E2, 4197–4216. DOI: 10.1029/1999JE001103.

Jones, M. J., A. J. Evans, B. C. Johnson, M. B. Weller, J. C. Andrews-Hanna, S. M. Tikoo, and J. T. Keane (2022). A South Pole–Aitken impact origin of the lunar compositional asymmetry. *Science Advances* **8**:14, eabm8475. DOI: 10.1126/sciadv.abm8475.

Jung, J.-I., S. M. Tikoo, D. Burns, Z. Váci, and M. J. Krawczynski (2024). Assessing lunar paleointensity variability during the 3.9-3.5 Ga high field epoch. *Earth Planet. Sci. Lett.* **638**: 118757. DOI: 10.1016/j.epsl.2024.118757.

Kawamura, T., P. Lognonné, Y. Nishikawa, and S. Tanaka (2017). Evaluation of deep moonquake source parameters: Implication for fault characteristics and thermal state. *J. Geophys. Res. Planet* **122**:7, 1487–1504. DOI: 10.1002/2016JE005147.

Kelvin, W. T. (1863). On the secular cooling of the earth. *Transactions of the Royal Society of Edinburgh* **23**: 157–170.

Khan, A., D. Huang, C. Durán, P. A. Sossi, D. Giardini, and M. Murakami (2023). Evidence for a liquid silicate layer atop the Martian core. *Nature* **622**:7984, 718–723. DOI: 10.1038/s41586-023-06586-4.

Khan, A., K. Mosegaard, and K. L. Rasmussen (2000). A new seismic velocity model for the Moon from a Monte Carlo inversion of the Apollo lunar seismic data. *Geophys. Res. Lett.* **27**:11, 1591–1594. DOI: 10.1029/1999GL008452.

Knapmeyer-Endrun, B., M. P. Panning, F. Bissig, R. Joshi, A. Khan, D. Kim, V. Lekić, B. Tauzin, S. Tharimena, M. Plasman, et al. (2021). Thickness and structure of the martian crust from InSight seismic data. *Science* **373**:6553, 438–443. DOI: 10.1126/science.abf8966.

Konrad, W. and T. Spohn (1997). Thermal history of the Moon: Implications for an early core dynamo and post-accertional magmatism. *Advances in Space Research* **19**:10, 1511–1521. DOI: 10.1016/S0273-1177(97)00364-5.

Labrosse, S., A. Morison, R. Deguen, and T. Alboussière (2018). Rayleigh–Bénard convection in a creeping solid with melting and freezing at either or both its horizontal boundaries. en. *J. Fluid Mech.* **846**: 5–36. DOI: 10.1017/jfm.2018.258.

Laneuville, M., M. Wieczorek, D. Breuer, J. Aubert, G. Morard, and T. Rückriemen (2014). A long-lived lunar dynamo powered by core crystallization. *Earth Planet. Sci. Lett.* **401**: 251–260. DOI: https://doi.org/10.1016/j.epsl.2014.05.057.

Laneuville, M., M. Wieczorek, D. Breuer, and N. Tosi (2013). Asymmetric thermal evolution of the Moon. *J. Geophys. Res. Planet* **118**:7, 1435–1452. DOI: 10.1002/jgre.20103.

Lange, R. and I. S. Carmichael (1990). Thermodynamic properties of silicate liquids with emphasis on density, thermal expansion and compressibility. *Reviews in Mineralogy and Geochemistry* **24**:1, 25–64.

Langermann, Y. T. (1985). The Book of Bodies and Distances of Habash al-Hāsīb. *Centaurus* **28**:2, 108–128. DOI: 10.1111/j.1600-0498.1985.tb00831.x.

Latypov, R., S. Chistyakova, G. Costin, O. Namur, S. Barnes, and W. Kruger (2020). Monomineralic anorthosites in layered intrusions are indicators of the magma chamber replenishment by plagioclase-only-saturated melts. *Scientific Reports* **10**:1, 3839. DOI: 10.1038/s41598-020-60778-w.

Le Bars, M., M. A. Wieczorek, Ö. Karatekin, D. Cébron, and M. Laneuville (2011). An impact-driven dynamo for the early Moon. *Nature* **479**:7372, 215–218. DOI: 10.1038/nature10565.

Li, J., C. Beghein, P. Davis, M. A. Wieczorek, S. M. McLennan, D. Kim, V. Lekić, M. Golombek, M. Schimmel, E. Stutzmann, P. Lognonné, and W. B. Banerdt (2023). Crustal Structure Constraints From the Detection of the SsPp Phase on Mars. en. *Earth and Space Science* **10**:3, e2022EA002416. DOI: 10.1029/2022EA002416.

Li, Q.-L., Q. Zhou, Y. Liu, Z. Xiao, Y. Lin, J.-H. Li, H.-X. Ma, G.-Q. Tang, S. Guo, X. Tang, et al. (2021a). Two-billion-year-old volcanism on the Moon from Chang'e-5 basalts. *Nature* **600**:7887, 54–58. DOI: 0.1038/s41586-021-04100-2.

Li, Q.-L. et al. (2021b). Two-billion-year-old volcanism on the Moon from Chang'e-5 basalts. *Nature* **600**:7887, 54–58. DOI: 10.1038/s41586-021-04100-2.

Lin, Y., E. J. Tronche, E. S. Steenstra, and W. van Westrenen (2017). Evidence for an early wet Moon from experimental crystallization of the lunar magma ocean. *Nature Geosci.* **10**:1, 14–18. DOI: 10.1038/ngeo2845.

Lister, J. R. and B. A. Buffett (1995). The strength and efficiency of thermal and compositional convection in the geodynamo. *Phys. Earth Planet. Inter.* **91**:1-3, 17–30.

Lock, S. J., S. T. Stewart, M. I. Petaev, Z. Leinhardt, M. T. Mace, S. B. Jacobsen, and M. Cuk (2018). The origin of the Moon within a terrestrial synestia. *J. Geophys. Res. Planet* **123**:4, 910–951. DOI: 10.1002/2017JE005333.

Lock, S. J. and S. T. Stewart (2017). The structure of terrestrial bodies: Impact heating, corotation limits, and synestias. en. *J. Geophys. Res. Planet* **122**:5, 950–982. DOI: 10.1002/2016JE005239.

Lognonné, P. and C. Johnson (2015). "10.03 - Planetary Seismology". *Treatise on Geophysics (Second Edition)*. Ed. by G. Schubert. Second Edition. Oxford: Elsevier, 65–120. DOI: 10.1016/B978-0-444-53802-4.00167-6.

Lognonné, P. (2005). Planetary seismology. *Annu. Rev. Earth Planet. Sci.* **33**: 571–604.

Lognonné, P., J. Gagnepain-Beyneix, and H. Chenet (2003). A new seismic model of the Moon: implications for structure, thermal evolution and formation of the Moon. *Earth Planet. Sci. Lett.* **211**:1-2, 27–44. DOI: 10.1016/S0012-821X(03)00172-9.

Longhi, J. (2003). A new view of lunar ferroan anorthosites: Postmagma ocean petrogenesis. *J. Geophys. Res. Planet* **108**:E8.

Marks, N., L. Borg, C. Shearer, and W. Cassata (2019). Geochronology of an Apollo 16 clast provides evidence for a basin-forming impact 4.3 billion years ago. *J. Geophys. Res. Planet* **124**:10, 2465–2481. DOI: 10.1029/2019JE005966.

Maurice, M., N. Tosi, and C. Hüttig (2024). Small-scale overturn of high-Ti cumulates promoted by the long lifetime of the lunar magma ocean. *J. Geophys. Res. Planet* **129**:2, e2023JE008060. DOI: 10.1029/2023JE008060.

Maurice, M., N. Tosi, H. Samuel, A.-C. Plesa, C. Hüttig, and D. Breuer (2017). Onset of solid-state mantle convection and mixing during magma ocean solidification. *J. Geophys. Res. Planet* **122**:3, 577–598. DOI: 10.1002/2016JE005250.

Maurice, M., N. Tosi, S. Schwinger, D. Breuer, and T. Kleine (2020). A long-lived magma ocean on a young Moon. *Science advances* **6**:28, eaba8949. DOI: 10.1126/sciadv.aba8949.

McCallum, I. S. and H. E. O'Brien (1996). Stratigraphy of the lunar highland crust; depths of burial of lunar samples from cooling-rate studies. en. *American Mineralogist* **81**:9-10, 1166–1175. DOI: 10.2138/am-1996-9-1015.

McSween Jr, H. Y., T. L. Grove, R. C. Lentz, J. C. Dann, A. H. Holzheid, L. R. Riciputi, and J. G. Ryan (2001). Geochemical evidence for magmatic water within Mars from pyroxenes in the Shergotty meteorite. *Nature* **409**:6819, 487–490. DOI: 10.1038/35054011.

Michaut, C. and J. A. Neufeld (2022). Formation of the lunar primary crust from a long-lived slushy magma ocean. *Geophys. Res. Lett.* **49**:2, e2021GL095408. DOI: 10.1029/2021GL095408.

Michaut, C., M. Thiriet, and C. Thorey (2016). Insights into mare basalt thicknesses on the Moon from intrusive magmatism. *Phys. Earth Planet. Inter.* **257**: 187–192. DOI: 10.1016/j.pepi.2016.05.019.

Morison, A., S. Labrosse, R. Deguen, and T. Alboussière (2019). Timescale of overturn in a magma ocean cumulate. *Earth Planet. Sci. Lett.* **516**: 25–36. DOI: 10.1016/j.epsl.2019.03.037.

Morison, A. (2019). "Convection in the primitive mantle in interaction with global magma oceans". Theses. Université de Lyon.

Morison, A., S. Labrosse, R. Deguen, and T. Alboussière (2024). Onset of thermal convection in a solid spherical shell with melting at either or both boundaries. *Geophys. J. Int.* **238**: 1121–1136. DOI: 10.1093/gji/ggae208.

Nakajima, M. and D. J. Stevenson (2014). Investigation of the initial state of the Moon-forming disk: Bridging SPH simulations and hydrostatic models. *Icarus* **233**: 259–267. DOI: 10.1016/j.icarus.2014.01.008.

Nakamura, R., T. Matsunaga, Y. Ogawa, S. Yamamoto, T. Hiroi, K. Saiki, N. Hirata, T. Arai, K. Kitazato, H. Takeda, et al. (2009). Ultramafic impact melt sheet beneath the South Pole–Aitken basin on the Moon. *Geophys. Res. Lett.* **36**:22. DOI: 10.1029/2009GL040765.

Nakamura, Y., D. Lammlein, G. Latham, M. Ewing, J. Dorman, F. Press, and N. Toksöz (1973). New Seismic Data on the State of the Deep Lunar Interior. *Science* **181**:4094, 49–51. DOI: 10.1126/science.181.4094.49.

Nakamura, Y. (1983). Seismic velocity structure of the lunar mantle. *J. Geophys. Res.* **88**:B1, 677–686. DOI: 10.1029/JB088iB01p00677.

Nakamura, Y. (2005). Farside deep moonquakes and deep interior of the Moon. *Journal of Geophysical Research: Planets* **110**:E1. DOI: 10.1029/2004JE002332.

Nichols, C. I., B. P. Weiss, B. L. Getzin, H. H. Schmitt, A. Béguin, A. S. Rae, and J. Shah (2021). The palaeoinclination of the ancient lunar magnetic field from an Apollo 17 basalt. *Nat Astron* **5**:12, 1216–1223. DOI: 10.1038/s41550-021-01469-y.

Nozette, S., P. Rustan, L. Pleasance, J. Kordas, I. Lewis, H. Park, R. Priest, D. Horan, P. Regeon, C. Lichtenberg, et al. (1994). The Clementine mission to the Moon: Scientific overview. *Science* **266**:5192, 1835–1839. DOI: 10.1126/science.266.5192.183.

Nyquist, L., D. Bogard, A. Yamaguchi, C.-Y. Shih, Y. Karouji, M. Ebihara, Y. Reese, D. Garrison, G. McKay, and H. Takeda (2006). Feldspathic clasts in Yamato-86032: Remnants of the lunar crust with implications for its formation and impact history. *Geochim. Cosmochim. Acta* **70**:24, 5990–6015. DOI: 10.1016/j.gca.2006.07.042.

O'Driscoll, B., C. H. Emeleus, C. H. Donaldson, and J. S. Daly (2010). Cr-spinel seam petrogenesis in the Rum Layered Suite, NW Scotland: cumulate assimilation and in

situ crystallization in a deforming crystal mush. *Journal of Petrology* **51**:6, 1171–1201. DOI: 10.1093/petrology/egq013.

Ohtake, M. et al. (2009). The global distribution of pure anorthosite on the Moon. en. *Nature* **461**:7261, 236–240. DOI: 10.1038/nature08317.

Park, R. S., A. Berne, A. S. Konopliv, J. T. Keane, I. Matsuyama, F. Nimmo, M. Rovira-Navarro, M. P. Panning, M. Simons, D. J. Stevenson, and R. C. Weber (2025). Thermal asymmetry in the Moon's mantle inferred from monthly tidal response. *Nature* **641**:8065, 1188–1192. DOI: 10.1038/s41586-025-08949-5.

Parmentier, E., S. Zhong, and M. Zuber (2002). Gravitational differentiation due to initial chemical stratification: origin of lunar asymmetry by the creep of dense KREEP? *Earth Planet. Sci. Lett.* **201**:3-4, 473–480. DOI: 10.1016/S0012-821X(02)00726-4.

Perera, V., A. P. Jackson, L. T. Elkins-Tanton, and E. Asphaug (2018). Effect of reimpacting debris on the solidification of the lunar magma ocean. *J. Geophys. Res. Planet* **123**:5, 1168–1191. DOI: 10.1029/2017JE005512.

Phillips, M. S., C. E. Viviano, J. E. Moersch, A. D. Rogers, H. Y. McSween, and F. P. Seelos (2022). Extensive and ancient feldspathic crust detected across north Hellas rim, Mars: Possible implications for primary crust formation. *Geology* **50**:10, 1182–1186. DOI: 10.1130/G50341.1.

Plesa, A.-C., M. Wieczorek, M. Knapmeyer, A. Rivoldini, M. Walterova, and D. Breuer (2022). *Interior Dynamics and Thermal Evolution of Mars – a Geodynamic Perspective*. en. DOI: 10.48550/arXiv.2207.09283.

Prendergast, K. (2017). Knowth passage-grave in Ireland: An instrument of precision astronomy? *Journal of Lithic Studies* **4**:4, 67–76. DOI: 10.2218/jls.v4i4.1921.

Presnall, D. C., S. A. Dixon, J. R. Dixon, T. H. O'Donnell, N. L. Brenner, R. L. Schrock, and D. W. Dycus (1978). Liquidus phase relations on the join diopside-forsterite-anorthite from 1 atm to 20 kbar: Their bearing on the generation and crystallization of basaltic magma. *Contributions to Mineralogy and Petrology* **66**:2, 203–220. DOI: 10.1007/BF00372159.

Pritchard, M. and D. Stevenson (2000). Thermal aspects of a lunar origin by giant impact. *Origin of the Earth and Moon* **1**: 179–196.

Qin, C., A. C. Muirhead, and S. Zhong (2012). Correlation of deep moonquakes and mare basalts: Implications for lunar mantle structure and evolution. *Icarus* **220**:1, 100–105. DOI: 10.1016/j.icarus.2012.04.023.

Rapp, J. F. and D. S. Draper (2018). Fractional crystallization of the lunar magma ocean: Updating the dominant paradigm. en. *Meteoritics & Planetary Science* **53**:7, 1432–1455. DOI: 10.1111/maps.13086.

Reaves, G. and C. Pedretti (1987). Leonardo da Vinci's Drawings of the Surface Features of the Moon. *Journal for the History of Astronomy* **18**:1, 55–58. DOI: 10.1177/0021828687018001.

Roche, E. (1873). Essai sur la constitution et l'origine du système solaire. *Mémoires de la Section des sciences de l'Académie des sciences et lettres de Montpellier*.

Rogers, A. D. and W. H. Farrand (2022). Spectral evidence for alkaline rocks and compositional diversity among feldspathic light-toned terrains on Mars. *Icarus* **376**: 114883. DOI: 10.1016/j.icarus.2022.114883.

Roy, A., J. T. Wright, and S. Sigurðsson (2014). Earthshine on a young moon: explaining the lunar farside highlands. *ApJL* **788**:2, L42. DOI: 10.1088/2041-8205/788/2/L42.

Roy, D. J. W., J. D. Merriman, A. G. Whittington, and A. M. Hofmeister (2021). Thermal properties of carbonatite and anorthosite from the Superior Province, Ontario, and implications for non-magmatic local thermal effects of these intrusions. en. *International Journal of Earth Sciences* **110**:5, 1593–1609. DOI: 10.1007/s00531-021-02032-w.

Russell, S. S., K. H. Joy, T. E. Jeffries, G. J. Consolmagno, and A. Kearsley (2014). Heterogeneity in lunar anorthosite meteorites: implications for the lunar magma ocean model. *Philosophical Transactions of the Royal Society A: Mathematical, Physical and Engineering Sciences* **372**:2024, 20130241. DOI: 10.1098/rsta.2013.0241.

Saal, A. E., E. H. Hauri, M. L. Cascio, J. A. Van Orman, M. C. Rutherford, and R. F. Cooper (2008). Volatile content of lunar volcanic glasses and the presence of water in the Moon's interior. en. *Nature* **454**:7201, 192–195. DOI: 10.1038/nature07047.

Samuel, H., M. Drilleau, A. Rivoldini, Z. Xu, Q. Huang, R. F. Garcia, V. Lekić, J. C. Irving, J. Badro, P. H. Lognonné, et al. (2023). Geophysical evidence for an enriched molten silicate layer above Mars's core. *Nature* **622**:7984, 712–717. DOI: 10.1038/s41586-023-06601-8.

Schmidt, M. W. and G. Kraettli (2022). Experimental crystallization of the lunar magma ocean, initial selenotherm and density stratification, and implications for crust formation, overturn and the bulk silicate Moon composition. *J. Geophys. Res. Planet* **127**:5, e2022JE007187. DOI: 10.1029/2022JE007187.

See, T. (1909). Dynamical Theory of the Capture of Satellites and of rhe Division of Nebulae Under the Secular Action of a Resisting Medium. II. *Popular Astronomy, vol. 17, pp. 534-544* **17**: 534–544.

Shearer, C. K. (2006). Thermal and Magmatic Evolution of the Moon. en. *Reviews in Mineralogy and Geochemistry* **60**:1, 365–518. DOI: 10.2138/rmg.2006.60.4.

Shimizu, H., M. Matsushima, F. Takahashi, H. Shibuya, and H. Tsunakawa (2013). Constraint on the lunar core size from electromagnetic sounding based on magnetic field

observations by an orbiting satellite. *Icarus* **222**:1, 32–43. DOI: 10.1016/j.icarus.2012.10.029.

Snape, J. F., N. M. Curran, M. J. Whitehouse, A. A. Nemchin, K. H. Joy, T. Hopkinson, M. Anand, J. J. Bellucci, and G. G. Kenny (2018). Ancient volcanism on the Moon: Insights from Pb isotopes in the MIL 13317 and Kalahari 009 lunar meteorites. *Earth Planet. Sci. Lett.* **502**: 84–95. DOI: 10.1016/j.epsl.2018.08.035.

Snyder, G. A., L. A. Taylor, and C. R. Neal (1992). A chemical model for generating the sources of mare basalts: Combined equilibrium and fractional crystallization of the lunar magmasphere. *Geochim. Cosmochim. Acta* **56**:10, 3809–3823. DOI: 10.1016/0016-7037(92)90172-F.

Solomatov, V. (2015). "Magma Oceans and Primordial Mantle Differentiation". en. *Treatise on Geophysics*. Elsevier, 81–104. DOI: 10.1016/B978-0-444-53802-4.00155-X.

Solomatov, V. (1999). Fluid dynamics of magma oceans. *Origin of the Earth and Moon*, 323–328.

Spohn, T., W. Konrad, D. Breuer, and R. Ziethe (2001). The longevity of lunar volcanism: Implications of thermal evolution calculations with 2D and 3D mantle convection models. *Icarus* **149**:1, 54–65. DOI: 10.1006/icar.2000.6514.

Spudis, P. D., R. A. Reisse, and J. J. Gillis (1994). Ancient Multiring Basins on the Moon Revealed by Clementine Laser Altimetry. *Science* **266**:5192, 1848–1851. DOI: 10.1126/science.266.5192.1848.

Stegman, D. R., A. M. Jellinek, S. A. Zatman, J. R. Baumgardner, and M. A. Richards (2003a). An early lunar core dynamo driven by thermochemical mantle convection. *Nature* **421**:6919, 143–146. DOI: 10.1038/nature01267.

Stegman, D. R., A. M. Jellinek, S. A. Zatman, J. R. Baumgardner, and M. A. Richards (2003b). An early lunar core dynamo driven by thermochemical mantle convection. *Nature* **421**:6919, 143–146. DOI: 10.1038/nature01267.

Stooke, P. J. (1994). Neolithic Lunar Maps at Knowth and Baltinglass, Ireland. *Journal for the History of Astronomy*. DOI: 10.1177/002182869402500101O.

Sun, C., M. Graff, and Y. Liang (2017). Trace element partitioning between plagioclase and silicate melt: The importance of temperature and plagioclase composition, with implications for terrestrial and lunar magmatism. *Geochim. Cosmochim. Acta* **206**: 273–295. DOI: 10.1016/j.gca.2017.03.003.

Suzuki, A. and E. Ohtani (2003). Density of peridotite melts at high pressure. *Phys Chem Minerals* **30**: 449–456. DOI: 10.1007/s00269-003-0322-6.

Suzuki, A., E. Ohtani, and T. Kato (1998). Density and thermal expansion of a peridotite melt at high pressure. en. *Phys. Earth Planet. Inter.* **107**:1-3, 53–61. DOI: 10.1016/S0031-9201(97)00123-4.

Taylor, S. R. and S. McLennan (2009). *Planetary crusts: Their composition, origin and evolution*. Vol. 10. Cambridge University Press.

Taylor, S. R., G. J. Taylor, and L. A. Taylor (2006). The Moon: A Taylor perspective. *Geochimica et Cosmochimica Acta* **70**:24, 5904–5918. DOI: 10.1016/j.gca.2006.06.262.

Taylor, S. R. (1982). Lunar and terrestrial crusts: a constrast in origin and evolution. *Phys. Earth Planet. Inter.* **29**:3-4, 233–241.

Tikoo, S. M., B. P. Weiss, D. L. Shuster, C. Suavet, H. Wang, and T. L. Grove (2017). A two-billion-year history for the lunar dynamo. *Science Advances* **3**:8, e1700207. DOI: 10.1126/sciadv.1700207.

Turcotte, D. L. and G. Schubert (2002). *Geodynamics*. Cambridge university press.

Walker, D. and J. F. Hays (1977). Plagioclase flotation and lunar crust formation. *Geology* **5**:7, 425–428. DOI: 10.1130/0091-7613(1977)5<425:PFALCF>2.0.CO;2.

Warren, P. H. and J. T. Wasson (1979). The origin of KREEP. *Reviews of Geophysics* **17**:1, 73–88. DOI: 10.1029/RG017i001p00073.

Wasson, J. T. and P. H. Warren (1980). Contribution of the mantle to the lunar asymmetry. *Icarus* **44**:3, 752–771. DOI: 0.1016/0019-1035(80)90142-6.

Watson, C., J. A. Neufeld, and C. Michaut (2022a). Early asymmetric growth of planetary stagnant lids. *J. Fluid Mech.* **952**: A3. DOI: 10.1017/jfm.2022.864.

Watson, C., J. A. Neufeld, and C. Michaut (2022b). Early asymmetric growth of planetary stagnant lids. *J. Fluid Mech.* **952**: A3. DOI: 10.1017/jfm.2022.864.

Weber, R. C., P.-Y. Lin, E. J. Garnero, Q. Williams, and P. Lognonné (2011). Seismic detection of the lunar core. *Science* **331**:6015, 309–312. DOI: 10.1126/science.1199375.

Weill, D., J. Stebbins, R. Hon, and I. Carmichael (1980). The enthalpy of fusion of anorthite. *Contributions to Mineralogy and Petrology* **74**: 95–102. DOI: 10.1007/BF00375493.

Weiss, B. P. and S. M. Tikoo (2014). The lunar dynamo. *Science* **346**:6214, 1246753. DOI: 10.1126/science.1246753.

Wieczorek, M. A. (2009). The interior structure of the Moon: What does geophysics have to say? *Elements* **5**:1, 35–40. DOI: 10.2113/gselements.5.1.35.

Wieczorek, M. A., G. A. Neumann, F. Nimmo, W. S. Kiefer, G. J. Taylor, H. J. Melosh, R. J. Phillips, S. C. Solomon, J. C. Andrews-Hanna, S. W. Asmar, et al. (2013). The crust of the Moon as seen by GRAIL. *Science* **339**:6120, 671–675. DOI: 10.1126/science.1231530.

Wieczorek, M. A. et al. (2022). InSight Constraints on the Global Character of the Martian Crust. en. *J. Geophys. Res. Planet* **127**:5, e2022JE007298. DOI: 10.1029/2022JE007298.

Woo, J., D. Nesvornỳ, J. Scora, and A. Morbidelli (2024). Terrestrial planet formation from a ring: long-term simulations accounting for the giant planet instability. *Icarus*, 116109. DOI: 10.1016/j.icarus.2024.116109.

Wood, J. A. (1970). Petrology of the lunar soil and geophysical implications. *J. Geophys. Res.* **75**:32, 6497–6513. DOI: 10.1029/JB075i032p06497.

Wood, J. A., J. S. Dickey Jr, U. B. Marvin, and B. Powell (1970). "Lunar anorthosites and a geophysical model of the moon". *Geochimica et Cosmochimica Acta Supplement, Volume 1. Proceedings of the Apollo 11 Lunar Science Conference held 5-8 January, 1970 in Houston, TX. Volume 1: Mineraolgy and Petrology. Edited by AA Levinson. New York: Pergammon Press, 1970., p. 965.* Vol. 1, 965.

Wood, J. A. (1973). Bombardment as a cause of the lunar asymmetry. *The moon* **8**:1, 73–103. DOI: 10.1007/BF00562751.

Wray, J. J., S. T. Hansen, J. Dufek, G. A. Swayze, S. L. Murchie, F. P. Seelos, J. R. Skok, R. P. Irwin III, and M. S. Ghiorso (2013). Prolonged magmatic activity on Mars inferred from the detection of felsic rocks. *Nature Geosci.* **6**:12, 1013–1017. DOI: 10.1038/ngeo1994.

Yamamoto, S., R. Nakamura, T. Matsunaga, Y. Ogawa, Y. Ishihara, T. Morota, N. Hirata, M. Ohtake, T. Hiroi, Y. Yokota, et al. (2010). Possible mantle origin of olivine around lunar impact basins detected by SELENE. *Nature Geosci.* **3**:8, 533–536. DOI: 10.1038/ngeo897.

Yobregat, E., C. Fitoussi, and B. Bourdon (2024). Rb-Sr constraints on the age of Moon formation. en. *Icarus* **420**: 116164. DOI: 10.1016/j.icarus.2024.116164.

Zhang, B., Y. Lin, D. E. Moser, J. Hao, Y. Liu, J. Zhang, I. R. Barker, Q. Li, S. R. Shieh, and A. Bouvier (2021a). Radiogenic Pb mobilization induced by shock metamorphism of zircons in the Apollo 72255 Civet Cat norite clast. *Geochim. Cosmochim. Acta* **302**: 175–192. DOI: 10.1016/j.gca.2021.03.012.

Zhang, M., Y. Xu, and X. Li (2021b). Effect of crustal porosity on lunar magma ocean solidification. en. *Acta Geochimica* **40**:2, 123–134. DOI: 10.1007/s11631-020-00449-9.

Zhang, N., N. Dygert, Y. Liang, and E. Parmentier (2017). The effect of ilmenite viscosity on the dynamics and evolution of an overturned lunar cumulate mantle. *Geophys. Res. Lett.* **44**:13, 6543–6552. DOI: 10.1002/2017GL073702.

Zhong, S., E. Parmentier, and M. T. Zuber (2000a). A dynamic origin for the global asymmetry of lunar mare basalts. en. *Earth Planet. Sci. Lett.* **177**:3-4, 131–140. DOI: 10.1016/S0012-821X(00)00041-8.

Zhong, S., E. Parmentier, and M. T. Zuber (2000b). A dynamic origin for the global asymmetry of lunar mare basalts. *Earth Planet. Sci. Lett.* **177**:3-4, 131–140. DOI: 10.1016/S0012-821X(00)00041-8.

Ziethe, R., K. Seiferlin, and H. Hiesinger (2009). Duration and extent of lunar volcanism: Comparison of 3D convection models to mare basalt ages. *Planet. Spa. Sci.* **57**:7, 784–796. DOI: 10.1016/j.pss.2009.02.002.

Zuber, M. T., D. E. Smith, M. M. Watkins, S. W. Asmar, A. S. Konopliv, F. G. Lemoine, H. J. Melosh, G. A. Neumann, R. J. Phillips, S. C. Solomon, et al. (2013). Gravity field of the Moon from the Gravity Recovery and Interior Laboratory (GRAIL) mission. *Science* **339**:6120, 668–671. DOI: 10.1126/science.1231507.

Zuber, M. T., D. E. Smith, F. G. Lemoine, and G. A. Neumann (1994). The Shape and Internal Structure of the Moon from the Clementine Mission. *Science* **266**:5192, 1839–1843. DOI: 10.1126/science.266.5192.1839.

Résumé

La croûte lunaire est principalement composée d'anorthosite, une roche de faible densité qui cristallise à basse pression ($\sim 1\,\mathrm{GPa}$). L'enrichissement en anorthite de la croûte lunaire, mis en évidence grâce aux échantillons des missions Apollo, a apporté des preuves en faveur de la formation de la Lune par un impact géant entre la proto-Terre et un corps de la taille de Mars. De plus, la croûte lunaire présente une dichotomie marquée : sur la face visible, son épaisseur varie entre 20 et 30 km tandis que sur la face cachée elle atteint 50 à 60 km. À partir d'un simple diagramme de phase eutectique, nous avons développé un modèle décrivant la solidification de l'océan magmatique lunaire (LMO) en deux étapes de cristallisation. Ce modèle nous a permis d'estimer un intervalle de temps pour la solidification du LMO, en tenant compte de la teneur initiale en anorthite, de la composition eutectique et de la conductivité thermique de la croûte. En combinant cet intervalle avec les vitesses de refroidissement dérivées des roches lunaires, nous avons estimé une plage de temps pour la formation de la Lune comprise entre 4400 et 4560 Ma. Dans un second temps, nous avons étudié le retournement mantellique lunaire d'un point de vue thermique, lié au profil de température instable en fin de seconde étape de cristallisation. En supposant un changement de phase par fusion et/ou cristallisation à l'interface entre le manteau et le LMO, nous montrons qu'un retournement rapide de degré un peut survenir au début de la seconde étape. La présence de ce retournement pourrait affecter la cristallisation de la croûte par un flux thermique différentiel à la surface du manteau ou par la persistance d'une perturbation de degré un.

Abstract

The lunar crust is mostly composed of anorthosite, a low-density rock that crystallizes at low pressure ($\sim 1\,\mathrm{GPa}$). The enrichment in anorthite within the lunar crust, revealed by Apollo mission samples, provided evidence for the formation of the Moon through a giant impact between the proto-Earth and a Mars-sized body. Furthermore, the lunar crust is characterized by a significant dichotomy: on the near side, the crustal thickness ranges from 20-30 km, whereas on the far side it reaches 50-60 km. Using a simple eutectic phase diagram, we developed a model for the solidification of the Lunar Magma Ocean (LMO) in two stages of crystallization. With this model, we estimated a range for the solidification timescale of the LMO, taking into account the initial composition in anorthite content, the eutectic composition, and the thermal conductivity of the crust. Combining this timescale with cooling rates derived from lunar rocks, we estimated a range for the formation of the Moon between 4400 and 4560 Myr. Secondly, we investigated the lunar mantle overturn from a thermal perspective, driven by the unstable temperature profile at the end of the second crystallization stage. Assuming phase changes by melting and/or crystallization at the interface between the mantle and the LMO, we show that a rapid degree-one overturn can occur at the beginning of the second stage. The presence of such an overturn could affect crustal crystallization through differential heat flux at the surface of the mantle or through the persistence of degree-one perturbations.